EXPERIMENTAL STUDIES ON CRYSTAL POLYMORPHISM AND SELF-ASSEMBLED STRUCTURES IN SOFT MATTER

by

SUBHADIP GHOSH

A thesis submitted to
JAWAHARLAL NEHRU UNIVERSITY
for the award of the degree
of
DOCTOR OF PHILOSOPHY

November 2022



SOFT CONDENSED MATTER GROUP
RAMAN RESEARCH INSTITUTE
BANGALORE 560080

DECLARATION

I hereby declare that this thesis is composed independently by me at the Raman Research Institute, Bangalore, India, under the supervision of Prof. Arun Roy. The subject matter presented in this thesis has not previously formed the basis for the award of any degree, diploma, membership, associateship, fellowship or any other similar title of any other university or institution. I also declare that I have run it through the Turnitin plagiarism software.

Prof. Arun Roy **Subhadip Ghosh**

(Thesis Supervisor)

Soft Condensed Matter Group,

Raman Research Institute,

Bangalore 560080,

India.

THESIS CERTIFICATE

This is to certify that the thesis entitled ***Experimental studies on crystal polymorphism and self-assembled structures in soft matter*** submitted by **Subhadip Ghosh** for the award of the degree of **Doctor of Philosophy** of Jawaharlal Nehru University, New Delhi, India is his original work. This has not been published or submitted elsewhere for the award of any degree or diploma.

Prof. Tarun Souradeep
Director
Raman Research Institute,
Bangalore 560080,
India.

Prof. Arun Roy
(Thesis Supervisor)
Soft Condensed Matter Group,
Raman Research Institute,
Bangalore 560080, India.

Acknowledgments

First and foremost, I would like to express my sincere gratitude to my supervisor Prof. Arun Roy for his guidance, advice and help. I am deeply grateful for his unfailing support and encouragement which helped me to get motivated during my PhD tenure.

I am grateful to Prof. R. Prathibha, Prof. Reji Philip and Prof. Pramod A Pullarkat for their invaluable suggestions as my advisory committee members.

I thank Prof. Yashodhan Hatwalne, Prof. V A Raghunathan, Prof. Gautam Vivek Soni, Prof. Ranjini Bandyopadhyay, Prof. Dibyendu Roy and Prof. Sayantan Majumdar for the fruitful discussions during my PhD career.

I thank Ms. Vasudha K. N. for acquiring the XRD, DSC and UV-Visible data of our samples. I thank Mr. Yateendran for acquiring the SEM and confocal data of our samples. I am also grateful to Mr. Mani who helped to develop a birefringent measurement setup. I would like to express my sincere gratitude to Mr. Ram who helped to make the liquid crystal cells. I express my gratitude to Dr. Srinivasa H. T. for acquiring the TGA data of our samples. During my PhD tenure, the necessary glass items for experiments were made by Mr. Dason. I am very grateful to him and also to the other RRI workshop staff specially Mr. Ibrahim for their help and support.

I thank all of my group mates Dr. Deepshika, Saichand, Vishnu, Dipak, Swarnak and Susovan for their company, cooperation, fruitful discussion, help and many more.

During my PhD tenure, many times I had to take help from my chemistry lab mates Dr. Marichandran Vadivel, Dr. Ashwathanarayana Gowda, Dr. Anu Ranjith, Dr. Jagadeesh, Irla, Vanishree and Alaka. I am grateful to all these people for their help and technical assistance.

I thank other past and present students at RRI Dr. Meera Thomas, Dr. Sanjay Kumar Behera, Masesh, Manohar, Hari, Dr. Rajkumar Khan, Anindya, Sachidananda, Yogesh, Vaibhav, Deepak Mehta, Ashish, Dr. Kaushik, Maheswar, Subhajit, Nishant,

Dr. Adwaith, Dr. Nancy, Silpa, Shreyas, Rajkumar Biswas, Arsalan and Tanuman for their academic and non-academic interactions.

I am also grateful to the former secretaries of SCM group Mr. K. Radhakrishna, Ms. Amudha and the present SCM group secretary Ms. Chaithanya M.S. for their help in all the official works. I sincerely thank Mr. Raja J., Mr. Murali T. and Mr. Venkatesh V. for their support on a daily basis.

I express my sincere gratitude to all staff in RRI administration, computer department, canteen and hostels for their continuous support.

I thank Mrs. Supreeti Roy for her support and help especially in the covid pandemic periods. I really appreciate her friendly behaviour with me. I am also very grateful to Anusha and Susmit for those wonderful moments that we have spent together.

I am deeply grateful to my friends Dr. Shatruhan Singh Rajput, Dr. Arijit Singha Hazari, Vivakanand kumar, Purushottam Kumar and Dr. Sabyasachi Parida for their support and inspiration.

I have no words to express my gratitude to my parents, my late grandparents, my sister Ms. Debolina, my uncles, aunties and my cousin brother Mr. Sourav Basu for their continuous support, encouragement and motivation. I deeply thank to all of them.

Synopsis

The molecular self-organisation and the emergent physical properties of materials under different external conditions is an active field of research in soft condensed matter science. The supramolecular order leading to various advanced functional materials has attracted much attention due to their technological applications as well as for fundamental understanding of their properties. In this thesis, we report experimental investigations on two different types of soft materials exhibiting such self-assembled structures. The first system studied is a liquid crystal compound (8OCB) consisting of highly polar rod-like molecules. In the last few decades different phases of nOCB liquid crystal homologs have been investigated where n denotes the number of carbon atoms in the terminal aliphatic chain attached to one end of the rod like molecule. A nitrile (CN) head group attached to the other end of the molecule gives a strong dipole moment along its long axis. Various studies on this family of liquid crystals have established some unusual properties of their liquid crystalline phases such as intercalated organisation of molecules in their smectic A phase and the existence of reentrant nematic phase below the smectic A phase [1–3].

Interestingly these nOCB liquid crystals also exhibit various stable and metastable crystal phases [4, 5]. Although a large number of studies on the liquid crystalline phases of 8OCB compound have been reported, relatively few studies have been performed on its solid phases. In this thesis, we have studied the different crystalline polymorphs of 8OCB obtained by cooling the sample from its melt. We identify the metastable crystal state found in our sample as long parallelopiped or PP phase which transforms to stable commercial powder or CP phase on ageing at room temperature or by heating it above a certain temperature. Surprisingly, we have found that the stable CP crystal phase of 8OCB itself is a heterogeneous phase with the coexistence of fibrillar nano crystallites embedded in an amorphous solid phase. The existence of various metastable crystal phases and a heterogeneous phase as the stable ground state shows the remarkable complexity of the free energy landscape for this pure compound.

It is found that the CP phase of 8OCB grows as spherulites from its sufficiently supercooled melt. In spherulitic growth, the crystalline seed after nucleation grows with a spherical growth front in contrast to the growth dictated by the crystallographic symmetries. Though a variety of materials are now known to exhibit such spherulitic growth, the detail understating of the growth mechanism is still incomplete [6]. This kind of growth is often associated with the formation of many radially aligned fibrillar crystallites which branch non-crystallographically during its growth for filling the space. Furthermore, for some materials, the spherulitic growth is accompanied by a series of equidistant concentric bands and these type of spherulites are known as banded spherulite. In quasi two dimensional geometry, the banded spherulite domain appears as a flattened disk with circular boundary and these bands emerge as concentric circular rings. We have experimentally studied the spherulitic growth of CP phase of 8OCB from its melt. We find that the banded spherulite for this compound is formed by rhythmic growth of alternating concentric domains of crystal-rich and crystal-poor zones along radial direction. To the best of our knowledge this is the first report of a pure small molecular compound which produces banded spherulite entirely due to the rhythmic growth of two different zones.

The second soft material studied in thesis is the physical properties of starch gel. Starch apart from being the most consumable carbohydrates is also one of the largest polymer found in nature having application in biodegradable plastic and other industrial applications. In this thesis, we have experimentally studied the structural changes in a drying droplet of gelatinized starch solution drop-casted on a flat surface. We find that the homogeneous starch solution with time transforms to a gel state which on further drying acquires birefringence and partial crystallinity. After complete drying, these droplets transform to transparent circular films as biodegradable plastic. Using variety of experimental techniques, we explore the physical properties and the possible mechanisms of these transformations.

This thesis includes five chapters. In **Chapter 1**, we have given general in-

troductions to the different subjects relevant to the thesis. In **Chapter 2**, we have discussed briefly the various experimental techniques used in the thesis such as Polarising Optical Microscopy (POM), Field Emission Scanning Electron Microscopy (FESEM), Confocal Microscopy, Raman Spectroscopy (RS), X-ray Diffraction (XRD), UV-Vis Spectroscopy, Dielectric studies etc.

In **Chapter 3**, we have discussed the experimental studies performed on the crystalline polymorphs of 8OCB formed from its supercooled melt. Hori *et al.* first observed three different metastable crystal polymorphs of 8OCB obtained from solution crystallised samples and these phases are known as square-plate, needle phase and long parallelepiped or PP phase respectively [4]. It also forms a stable crystal phase known as commercial powder or CP phase. However, the crystal polymorphs of the pure compound obtained from its melt have not been studied in detail. We find two crystalline polymorphs of this compound most often forms on cooling the sample from its melt. These phases are characterised as the metastable PP phase and the stable CP phase respectively. The POM texture of this metastable PP phase shows a uniform birefringent texture which grows as a strip from the melt (fig. 1a). The unique Raman spectra of these individual phases helped us to identify these stable and metastable crystal phases as the CP and PP phase respectively. The metastable PP phase starts to transform to CP phase at room temperature after few days. It can also be transformed to CP phase by heating the sample above 312K. The POM texture of CP phase shows a nonuniform grainy texture indicating the presence of microscopic domains in this phase (fig. 1b). The FESEM studies

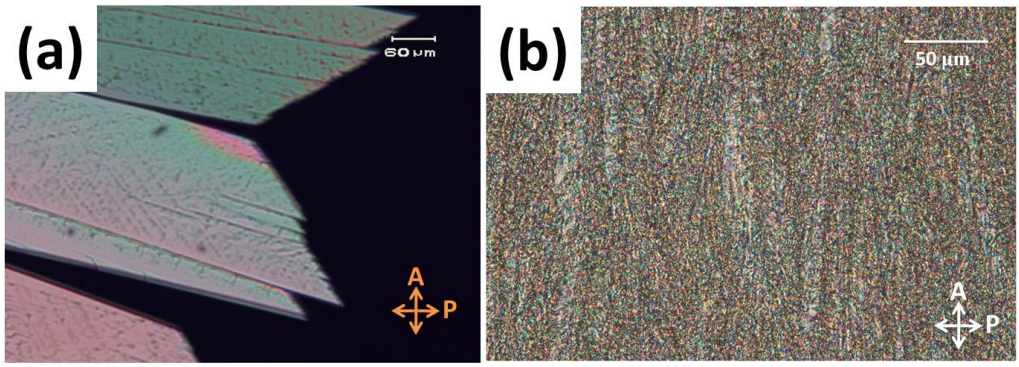


Figure 1: The POM textures of (a) PP phase and (b) CP phase of 8OCB.

of CP phase revealed the coexistence of myriad fibrillar nano crystalites embedded in an another solid phase. The XRD studies of CP phase showed that the fibrillar crystallites possess monoclinic lattice structure and no diffraction peaks were found for the other solid phase confirming its amorphousness. The Raman peak for stretching vibration of CN group of 8OCB molecules is quite sensitive to the local molecular environment. This peak is asymmetric in CP phase and was fitted with a prominent strong peak and a weak satellite peak at slightly lower Raman shift than the stronger one. The molecular environment of CN group is different in the amorphous and crystalline components of CP phase giving rise to these slightly different peak positions. The doublet structure of this CN peak in the CP phase can be attributed to the heterogeneous nature of this phase. During heating, this amorphous component melts to the smectic phase before the fibrillar crystallites giving rise to a pre-transitional increase in the dielectric constant before the melting point of CP phase. This pre-transitional effect has also been noticed in other experimental results. The coexistence of nano crystallites and the solid amorphous phase as the stable ground state and the existence of other metastable phases for this small molecular pure compound show the remarkable complexity of the free energy landscape of this system. We attribute this behavior to the strong dipole moment of the 8OCB molecules. The strongly dipolar nature of these molecules has been proposed to account for the reentrant nematic phase below its smectic phase under high pressure or in suitable mixtures with 6OCB [1, 2]. We are unable to isolate the amorphous component of the CP phase to clearly identify its structure. We speculate that the amorphous component of the CP phase may be the frozen reentrant nematic phase. Further experiments are required to reveal the detail structure of the CP phase and the possible origin of this heterogeneous ground state.

In **Chapter 4**, we have presented the experimental studies on the spherulitic growth of CP phase of 8OCB from its supercooled melt. The CP phase grows as both banded and non-banded spherulite depending on the supercooling temperature of the melt. The POM textures of the non-banded and banded spherulitic domains formed

between two coverslips are shown in fig. 2a and fig. 2b respectively. Both of these

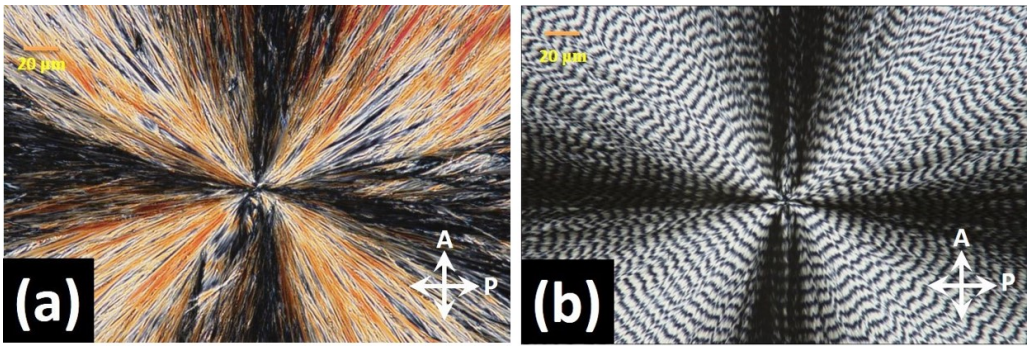


Figure 2: The POM textures of (a) non-banded and (b) banded spherulites of 8OCB CP phase.

textures have a Maltese cross with the black brushes always parallel to the polarisers. It signifies that one of the principle axes of effective refractive index ellipse lying on the sample plane is along the radial direction of the domains. The POM studies using a λ-plate were performed to determine the orientation of these axes. The minor axis of this refractive index ellipse was found to be aligned along the radial direction for both types of spherulite domains. Thus the spherulites of this compound are optically negative. The POM texture of banded spherulite domain shows concentric colour bands with periodic variation of colours. A periodic undulation of the effective birefringence along its radial direction gives rise to this colour variation. The SEM textures of this spherulitic domain also exhibit concentric bands where numerous fibrillar crystallites with their long axis along the radial direction were found to be embedded in an amorphous phase. The spherulitic bands arise from the periodic growth of crystallite-rich and crystallite-poor concentric zones during the formation of this domain. In crystallite-rich zones, the density of fibrillar domains is more whereas crystallite-poor zones are rich with amorphous phase. The resulting periodic change in effective birefringence along the radial direction produces the concentric interference colour bands between crossed polarisers. The asymmetric Raman peak envelope for CN stretching vibration observed in these domains can be fitted with two peaks with slightly different peak positions. The doublet structure of this peak indicates the coexistence of two different phases in these spherulitic domains. The

XRD studies showed that the fibrillar nano-crystallites possess monoclinic lattice structure whereas no XRD peak can be assigned to the other solid phase confirming its amorphousness. All these experimental results strongly support the existence of two different phases in banded and non-banded spherulites of this compound. We find that the rhythmic growth of crystal-rich and crystal-poor zones is the underlying physical mechanism for the formation this banded spherulite.

In **Chapter 5**, we have discussed the experimental studies on gelatinized starch solution and physical properties of dried starch films. We have studied the structural changes of drying gelatinized starch solution droplets on a flat surface. A sol-gel transition was observed in these droplets during drying. The cryo-SEM studies showed the presence of "cell-wall" like lamellar structures formed by the starch polymers inside these droplets in the gel phase. These lamellar structures produce a network in the starch solution giving rise to its gel property. During drying, the droplets start to acquire birefringence from its circular edge. After complete drying, these droplets form circular films which are transparent in visible light and also have partial crystallinity. The POM studies revealed that these films are optically biaxial except at its center where it is uniaxial. The optic axis at the center of these films is perpendicular to the film surface. In the biaxial part of these films, the conoscopic studies were performed to determine the orientation of the optic axes and their variation along the diameter of these films. We have measured the effective linear birefringence and its variation along the diameter of these films. The effective birefringence of the film is maximum at its peripheral region and it decreases towards its center. The structure and properties of these films have also been probed by XRD, Raman spectroscopy and SEM techniques. The results obtained from these studies have been used to account for the observed optical and other properties of the films.

List of publications

1. **Subhadip Ghosh** and Arun Roy, "Crystal polymorphism of 8OCB liquid crystal consisting of strongly polar rod-like molecules", RSC Adv., **11**, 4958 (2021).

2. **Subhadip Ghosh**, Dipak Patra and Arun Roy, "Observation of banded spherulite in a pure compound by rhythmic growth", Phys. Rev. Materials, **6**, 053401, (2022).

3. **Subhadip Ghosh** and Arun Roy, "Experimental studies of optical and structural properties of starch films formed on drying droplets of gelatinized starch solutions", *Manuscript is under preparation.*

Table of Contents

Declaration i

Thesis certificate iii

Acknowledgments v

Synopsis vii

List of publications xiii

List of tables and figures xix

1 Introduction 1

1.1 Liquid crystals . . . 1

1.1.1 Calamitic liquid crystal . . . 2

Nematic phase . . . 2

Smectic phase . . . 3

Reentrant phase . . . 4

1.1.2 Crystal polymorphism in calamitic liquid crystals . . . 5

1.2 Spherulitic growth . . . 6

1.2.1 Banded Spherulites . . . 7

1.3 Starch . . . 9

2 Experimental techniques 15

2.1 Polarising Optical Microscopy . . . 15

2.1.1 Conoscopic studies . . . 18

2.2 Confocal Microscopy . . . 22

2.3 Scanning Electron Microscopy . . . 24

2.3.1 Cryogenic-SEM . . . 25

2.4 UV-Visible Spectrophotometry 26
2.5 Raman Spectroscopy 27
2.6 X-ray Diffraction 29
2.7 Differential scanning calorimetry 30
2.8 Linear retardation measurement setup using photo elastic modulator . . 32
2.8.1 Photo elastic modulator (PEM) 32
2.8.2 Linear retardation measurement setup 33
2.9 Impedance analysis of samples 37
2.10 Making of Liquid crystal cells 40
2.11 Probe sonicator 42

3 Crystal polymorphism in 8OCB **45**

3.1 Introduction 45
3.2 Experimental Detail 47
3.2.1 Sample Description 47
3.2.2 Sample preparation 48
3.3 Results and Discussion 50
3.3.1 Polarising Optical Microscopy (POM) Study 50
3.3.2 Field Emission Scanning Electron Microscopy (FESEM) Study . . 54
3.3.3 Dielectric Studies 56
3.3.4 X-ray diffraction studies 59
3.3.5 Small angle X-ray diffraction studies 61
3.3.6 Raman spectroscopic studies 64
Raman peaks from 200 cm^{-1} to 900 cm^{-1} 64
Raman peaks from 200 cm^{-1} to 3200 cm^{-1} 67
3.4 Conclusion 74

4 Spherulitic growth in 8OCB **77**

4.1 Introduction 77
4.2 Experiment 79

4.3 Results and discussions 82
4.3.1 Polarising optical microscopy studies 82
Formation of continuous non-banded spherulite 87
POM studies of heating effects on the banded spherulite . . . 88
POM studies of aging effects on the banded spherulite 89
Core structure of the banded spherulites 91
4.3.2 Scanning electron microscopy studies 91
SEM studies of heating effect on banded spherulite 95
SEM studies of aging effect on banded spherulite 95
4.3.3 X-ray diffraction studies 96
4.3.4 Fluorescence microscopy studies 97
Fluorescence microscopy studies of heating effect on banded spherulite 98
Fluorescence microscopy studies of aging effect on banded spherulite 98
4.3.5 Raman studies in banded spherulite 100
4.3.6 Dielectric studies 103
Dielectric studies of heating and aging effect on banded spherulite 105
4.4 Conclusion 106

5 The optical & structural properties of starch films 109

5.1 Introduction 109
5.2 Sample Preparation 110
5.2.1 Extraction of potato starch 110
5.2.2 Preparation of gelatinized starch solutions and films 111
5.3 Experimental Results and discussions 113
5.3.1 Differential scanning calorimetry studies 113
5.3.2 Drying dynamics of starch solution droplets 114
5.3.3 The thickness profile of dried starch films 116
5.3.4 UV-Visible transmission spectroscopy studies 119

5.3.5 X-ray diffraction (XRD) studies 119
5.3.6 Raman spectroscopy studies 122
5.3.7 Polarising optical microscopy studies 124
Orthoscopy studies 124
Conoscopy studies 126
Determination of acute axial angle 129
5.3.8 Measurement of birefringence along the diameter of starch films . 132
Measurement of $(\beta - \alpha)$ 135
5.3.9 Scanning electron microscopy (SEM) studies 138
5.4 Conclusion 142

Summary **145**

List of tables and figures

Table 3.1 In-plane deformation of CH bonds of biphenyl moiety 69

Table 3.2 Combinational band for perpendicular deformations of CH_2 group 69

Table 3.3 Quadrant stretching mode of aromatic rings 69

Table 3.4 CN stretching vibration 70

Table 5.1 Starch content in water 112

Table 5.2 Observed Raman peaks for starch grains and films 123

Figure 1 The POM textures of (a) PP phase and (b) CP phase of 8OCB. . . ix

Figure 2 The POM textures of (a) non-banded and (b) banded spherulites of 8OCB CP phase. xi

Figure 1.1 Schematic diagram of molecular arrangement in nematic phase. **n** represents the director. 2

Figure 1.2 Schematic diagram of molecular arrangement in (a) smectic A_1, (b) smectic A_d and (c) smectic A_2 phases. **n**, d, **k** represent the director, layer spacing and layer normal respectively. 3

Figure 1.3 Schematic diagram of molecular arrangement in smectic C phase. **n**, d, **k** represent the director, layer spacing and layer normal respectively. 4

Figure 1.4 Schematic diagram of molecular arrangement in (a) smectic F and (b) smectic I phase. 5

Figure 1.5 SEM texture of potato starch grains. 9

Figure 1.6 Molecular structure of (a) amylose and (b) amylopectin. 10

Figure 1.7 POM texture of a starch grain (a) between crossed polarisers (b) after inserting λ-plate in the optical path between crossed polarisers. The bright field images of (c) a starch grain and (d) the remnant sack after gelatinization of the starch grain. 12

Figure 2.1 The polarising optical microscope. 16

Figure 2.2 The Michel-levy chart. 17

Figure 2.3 The ray diagram in conoscopic setup. 18

Figure 2.4 (a) [Down] The oblate indicatrix of an optically negative uniaxial sample. Principal indices in this indicatrix are n_e and n_o. [Up] The conoscopic figures of an optically uniaxial sample before [Left] and after [Right] inserting the λ-plate into the optical path when the optic axis of the sample is along the direction of propagation of light. (b) [Down] The prolate indicatrix of an optically positive uniaxial sample. Principal indices in this indicatrix are n_e and n_o. [Up] The corresponding conoscopic figures before [left side] and after [left side] inserting the λ-plate into the optical path when the optic axis of the sample is along the direction of propagation of light. The effective principal indices encountered by the light falling at different incident angle on the sample are shown in all these conoscopic figures. 19

Figure 2.5 [Left] The tilted optic axis of a uniaxial medium by an angle θ w.r.t. the direction of propagation of light along z axis. [Right] The conoscopic figures of this optically uniaxial sample at different angles (ϕ) of rotation of the sample on sample stage. 20

Figure 2.6 The index ellipsoid of an optically biaxial medium. 21

Figure 2.7 [Left] The indicatrix of an optically negative biaxial sample and the corresponding conoscopic figure when optic plane is parallel to the polariser and the direction of propagation of light. The effective principal indices encountered by the light falling at different incident angle on the sample are shown in this conoscopic figure. [Right] [Up] The conoscopic figures at +45° orientation of the optic plane w.r.t. polariser [Left] before and [Right] after inserting the λ-plate. [Down] The conoscopic figures at -45° orientation of the optic plane w.r.t. polariser [Left] before and [Right] after inserting the λ-plate. 22

Figure 2.8 [Left] The indicatrix of an optically positive biaxial sample. The corresponding conoscopic figure when optic plane is parallel to the polariser and the direction of propagation of light. The effective principal indices encountered by the light falling at different incident angle on the sample are shown in this conoscopic figure. [Right] [Up] The conoscopic figures at +45° orientation of the optic plane w.r.t. polariser [Left] before and [Right] after inserting the λ-plate. [Down] The conoscopic figures at -45° orientation of the optic plane w.r.t. polariser [Left] before and [Right] after inserting the λ-plate. 23

Figure 2.9 The ray diagram in confocal microscope. 24

Figure 2.10 The Raman Spectrometer. 29

Figure 2.11 The optical head of photo elastic modulator [PEM 100, Hinds instrument]. 32

Figure 2.12 The schematic diagram of linear birefringence measurement setup. 35

Figure 2.13 The schematic diagram of the dielectric measurement setup. . . . 38

Figure 2.14 (a) and (b) The etched ITO plates. (c) The liquid crystal cell formed by the etched plates. 40

Figure 2.15 The probe sonicator. 41

Figure 3.1 nOCB molecule. 46

Figure 3.2 XRD profile in smectic A phase of 8OCB. 48

Figure 3.3 The POM textures of (a) the stable CP phase and (b) PP phase growing from smectic A phase of 8OCB. 51

Figure 3.4 The POM textures of a strip of PP phase between crossed polarisers (a) without λ-plate (b) with the slow axis of the λ-plate parallel to the front edge and (c) with the slow axis of the λ-plate perpendicular to the front edge. The white double headed arrow indicates the major axis of the effective refractive index ellipse within the strip. (d) The schematic representation of the molecular organisation within the strip. . 52

Figure 3.5 The POM textures showing the transformation of PP phase to CP phase with increasing temperature. 53

Figure 3.6 PP phase to CP phase transition with time. 53

Figure 3.7 The SEM textures of (a) the CP phase, (b) the cross sectional view of the fibrillar nano crystallites in the CP phase and (c) PP phase. (d) shows the magnified view of the marked region of the PP phase in figure (c) indicating smooth homogeneous texture. 54

Figure 3.8 (a-i) The SEM textures at different temperature during heating the sample from PP phase. 55

Figure 3.9 The temperature variations of dielectric constant of 8OCB on heating the sample from its (a) PP phase and (b) CP phase. The inset in (a) shows the variation of the dielectric constant across the PP to CP phase transition in an expanded scale. (c) The temperature variation of dielectric constant of CP phase formed after 9 days from PP phase kept at room temperature. 58

Figure 3.10 The XRD profiles of (a) the CP phase in capillary at room temperature, (b) the capillary and (c) the CP phase on flat stage at room temperature. 60

Figure 3.11 The SAXS profiles of CP phase during heating in pre-transitional region before melting. $\Delta T = T - T_c$ is in K. 62

Figure 3.12 The temperature variation of intensity and FWHM of three crystalline peaks (a) (100), (b) (001), (c) $(10\bar{1})$ of CP phase and (d) (001) peak of smectic phase on heating the sample in the pre-transitional temperature range. Here $\Delta T = T - T_c$, where T and T_c denote the measured temperature and the complete melting temperature of CP phase respectively. 63

Figure 3.13 Raman spectra for (a) PP phase, (b) CP phase and (c) Needle phase. (d) The Raman spectra of 8OCB showing the variation with temperature across the transition from PP to CP phase. 65

Figure 3.14 Schematic free energy diagram of various phases of 8OCB with temperature variation. 67

Figure 3.15 Raman spectra in (a) PP phase, (b) CP phase, (c) Needle phase, (d) Smectic A, (e) Nematic and (f) Isotropic phase. 68

Figure 3.16 Raman peak for in-plane CH deformation in (a) PP phase, (b) Needle, (c) CP phase and (d) Smectic A phase. 71

Figure 3.17 Temperature variation of Raman peak position for in-plane CH deformation mode when initial phase was (a) PP phase, (b) CP phase. Temperature variation of Raman peak position for stretching vibration of CN group when initial phase was (c) PP phase, (d) CP phase. 72

Figure 3.18 Raman peak for CN stretching mode in (a) PP, (b) needle, (c) CP and (d) Smectic A phase. 73

Figure 3.19 The temperature variation of the Raman peak profile associated with the CN stretching vibration of 8OCB molecules in the pre-transitional temperature range of CP phase during heating the sample. $\Delta T = T - T_c$ in K denotes temperature difference from the complete melting temperature of CP phase. 74

Figure 4.1 The POM textures of banded spherulite of compound 8OCB at room temperature (a) between crossed polarisers, (b) between crossed polarisers and a λ plate, and (c) with only the polariser in the optical path. The white double-headed arrows in (b) indicate the orientations of major refractive index around the seed. (d) The POM texture of a banded spherulite domain between crossed polarisers for relatively thicker sample at room temperature. The insets show the variation of color in the bands in three different regions with slightly different sample thickness. (e) The same as in (d) with a red filter introduced in the optical path. The inset shows the variation of light intensity along the band normal which makes an angle γ with the polariser. (f) The variation of optical phase difference along the radial direction of the banded spherulite shown in (e). All scale bars are 20 μm. 83

Figure 4.2 (a) Growth velocity of banded spherulite at different supercooling. (b) The band spacing of banded spherulite formed at different supercooling. (c) Band spacing of banded spherulite of 8OCB at different spots along the length of a wedge cell. 84

Figure 4.3 The banded spherulite of 8OCB formed at ΔT = (a) 26 K, (b) 30 K, (c) 34 K, (d) 42 K. 86

Figure 4.4 The POM textures of the banded spherulite of 8OCB in a wedge shaped cell at spot number (a) 0, (b) 4, (c) 7 and (d) 11 along the increasing thickness of the cell. 87

Figure 4.5 Continuous non-banded spherulite formed at ΔT = 22.5 K (a) between crossed polarisers, (b) between crossed polarisers with λ-plate and (c) only polariser in the optical path. 88

Figure 4.6 The POM textures of (a) 8OCB banded spherulite between crossed polarisers. The POM textures of non-banded spherulite formed at 325 K (b) between crossed polarisers, (c) between crossed polarisers and the λ-plate and (d) only with a polarised in the optical path. All scale bars are 20 μm. 89

Figure 4.7 (a) 8OCB banded spherulite between crossed polarisers. The same spherulite after 73 days (b) between crossed polarisers, (c) between crossed polarisers and a phase plate and (d) with only a polarised in the optical path. All scale bars are 20 μm. 90

Figure 4.8 (a), (b) and (c) show the different morphologies of 8OCB banded spherulite. All scale bars are 20 μm. 91

Figure 4.9 The FESEM image of (a) the top surface of a banded spherulite and (b) the cross-sectional view of a banded spherulitic obtained from the cleaved surface showing the bulk structure. (c) The cross section of banded spherulite showing amorphous domain. (d) The cryo-SEM image of 8OCB banded spherulite formed after quenching the sample in isotropic phase. "A" and "B" zones represent the crystallite-rich and crystallite-poor concentric bands. (e) The cross section of fibrillar crystallites in banded spherulite. (f) The selected area in figure (e) with higher resolution. 93

Figure 4.10 Indicatrix ellipsoid in banded spherulite. The schematic representation of the variation of optical indicatrix along the radial direction of the banded spherulite of the compound 8OCB. The (a) top and (b) side views showing the uniaxial oblate indicatrix with radially oriented optic axes. 94

Figure 4.11 (a) The non-banded continuous spherulite formed after keeping the banded spherulite of 8OCB at 325 K for 1 hour followed by cooling it at room temperature. (b) The selected region in figure (a) with higher magnification. (c) Non-banded spherulite formed after keeping the banded spherulite for 73 days at room temperature. (d) The marked region in figure (c) in higher magnification. 96

Figure 4.12 XRD profile of banded spherulite of 8OCB. 97

Figure 4.13 (a) Fluorescent image of banded spherulite doped with rodamine 6G. (b) Fluorescent image of the non-banded spherulite formed after keeping the banded spherulite at 325 K for 10 minutes. (c) Fluorescent image of the banded spherulite after keeping it for 105 days at room temperature showing its transition to non-banded spherulite. 99

Figure 4.14 Raman specta of (a) the banded spherulite of 8OCB, (b) the non-banded spherulite formed after keeping the banded spherulite at 325 K for 10 minutes and (c) the non-banded spherulite formed after keeping the banded spherulite at room temperature for 73 days. 101

Figure 4.15 (a) The asymmetric Raman peak for CN stretching vibration in banded spherulite of 8OCB fitted by two Voigt functions. (b) The variation of intensity ratio of the fitted Raman peaks associated with the CN group of the molecules at few consecutive crystallite-rich and crystallite-poor bands along radial direction of the banded spherulite where r_0 is an initial point of measurement. 102

Figure 4.16 The temperature variation of dielectric constant of the banded spherulite during heating of the sample. The inset highlights the step change in dielectric constant at 318 K. 104

Figure 4.17 The temperature variation of dielectric constant of non-banded spherulite (a) formed after keeping banded spherulite of 8OCB at 325 K for 1 hour followed by cooling it at room temperature. (b) formed after keeping the banded spherulite at room temperature for 1 year. 105

Figure 5.1 Images of the sample (a) potatoes and (b) the extracted potato starch. 111

Figure 5.2 DSC thermogram of potato starch in excess water during heating at a rate of 5 K/min. The insets show the POM textures of a starch grain in water before and after gelatinization respectively. 113

Figure 5.3 (a) Variation of normalized diameter of a 150 μl starch solution droplet with 5.0 wt% starch concentration during its drying. The images show the droplet at different time intervals of its drying. The variation of weight and weight loss rate during drying of a 150 μl droplet of (b) 5.0 wt% of starch solution and (c) 9.5 wt% of starch solution and (d) pure water. 115

Figure 5.4 (a) The thickness profiles along a diameter of a starch films formed from different volume of starch solution droplets with 9.5 wt% initial starch concentration. (b) The corresponding normalized thickness profiles as a function of the normalized radial distance. (c) The thickness profiles along a diameter of a starch films formed from 300 μl droplets with different starch concentrations. (d) The corresponding normalized thickness profiles as a function of the normalized radial distance. 117

Figure 5.5 The image showing the transparency of a starch film of average thickness about 180 μm. 119

Figure 5.6 The UV-Visible transmission spectrum of starch film obtained on drying 600 μl droplet with 9.5 wt% starch concentration. 120

Figure 5.7 (a)The XRD profiles of starch grains and starch film formed from 600 μl droplet with 9.5 wt% of starch concentration. The profile for the film is shifted upward for clarity. (b) The XRD profiles at different times after dropcasting a 150 μl droplet with 9.5 wt% of initial starch concentration. The profiles at different times are shifted vertically for clarity of presentation. The insets show the images of the droplet at three different times after its dropcasting on a glass plate. 121

Figure 5.8 Raman spectra of (a) native potato starch grains and (b) starch film obtained on drying 600 μl droplet with 9.5 wt% starch concentration. 122

Figure 5.9 The POM images of the starch film (a) between crossed polarisers and (b) after inserting of a λ-plate with the slow axis at an angle of 45° with respect to the polariser. 125

Figure 5.10 (a)-(f) The POM textures of a section near the edge of a 150 μl droplet with 9.5 wt% of starch concentration at different time intervals after of its dropcasting on a glass substrate. (g) The variation of intensity at a 66 $\times$ 66 μm^2 spot at about 1 mm away from droplet edge. The red dot on the images indicates the spot where the intensity was calculated. 126

Figure 5.11 The conoscopic figures of starch film at its center (bottom row) and 3 mm away from its center (top row). The angle of the optic plane of the film with respect to the polariser and the presence of the λ-plate between the crossed polarisers are also indicated in the respective figures. 128

Figure 5.12 Schematic ray diagram of the conoscopic measurement setup. . . 129

Figure 5.13 Schematic diagram of a conoscopic figure having two uncrossed hyperbolic isogyres depicting the distances $2p$ and $2a$. 130

Figure 5.14 (a) Conoscopic figures at different positions along the radial direction of a starch film of radius about 8 mm formed from 600 μl starch solution with 9.5 wt% of starch concentration. The distance between two consecutive positions of measurement is 1 mm. (b) The variation of the optic axial angle ($2V$) along the radial direction of the film obtained from the conoscopic figures. 131

Figure 5.15 (a) The birefringence profile ($\gamma - \beta$) along the diameter of a starch film obtained from a 600 μl droplet with 9.5 wt% starch concentration. Its thickness profile has also given in this figure. (b) The birefringence profiles ($\gamma - \beta$) along the normalized radial direction of starch films formed from 300 μl droplets with different starch concentrations. (c) The birefringence profiles ($\gamma - \beta$) along the normalized radial direction of starch films obtained from different volumes of droplets with 6.5 wt% initial starch concentration. 133

Figure 5.16 The index ellipse on the optic plane of starch film. 135

Figure 5.17 The variation of ($\gamma - \beta$) and ($\beta - \alpha$) along the diameter of a starch film obtained on drying of 600 μl droplet with 9.5 wt% starch concentration. 136

Figure 5.18 [Left] The index ellipsoids along the diameter of starch film. [Right] The variation of index ellipse containing the principal indices α and β along the diameter of the film. 137

Figure 5.19 (a) Aluminum holder for cryo-SEM studies. (b) A schematic diagram showing the starch droplet in the aluminum holder. 139

Figure 5.20 The Cryo-SEM textures of cross section of a 300 μl droplet with 9.5 wt% starch concentration at different time after dropcasting. (a) The crust formed on the surface of the droplet after 10 minutes. (b) The cellular network structure inside the droplet after 10 minutes. (c) The texture near the contact line of the droplet after 14 hours showing the droplet surrounded by the dried film on the SEM holder. (d) The magnified view of the marked region 1 showing the smooth texture of the dried starch film. (e) The magnified view of the marked region 2 showing the thread like network structure inside the droplet edge. (f) The SEM texture near the interface of the droplet at its central region after 14 hours. (g) The magnified view of the marked region 3 showing the crust on top of the droplet and the thread like network below it. (h) The magnified view of the marked region 4 showing the cellular network structure well inside the droplet. 141

Figure 5.21 The schematic image of the droplet and droplet cross-section along with the peripheral film. 142

Chapter 1

Introduction

1.1 Liquid crystals

In general, a matter can exist in three different states which are solid, liquid and gas. Certain organic materials do not show a single transition from solid to liquid. In these cases, a few different phases can exist in between solid and isotropic liquid states. Some of the mechanical and symmetry properties of these in-between phases are similar to that found in isotropic liquid and solid phase. Therefore, these phases are often called as liquid crystal phases [7]. The liquid crystal was first discovered by Friedrich Reinitzer in 1888 [8].

The liquid crystal phases are viscous and can flow as liquids. In addition, these phases have optical birefringence, anisotropic behavior of their electrical conductivity and dielectric constant as usually found in crystal phases. The liquid crystalline phases are generally observed in compounds consisting of anisotropic molecules. The liquid crystalline phases are characterized by a long range orientational order of these anisotropic molecules. The molecules with rod, disc or bent-rod shaped structure are found to exhibit a variety of liquid crystal phases. Some of these liquid crystal phases also possess one or two dimensional positional order of molecules in addition to the orientational order.

The liquid crystals are divided into two major subcategories. These are thermotropic and lyotropic liquid crystals. In thermotropic liquid crystals, the behavior of liquid crystal phases and their transitions are controlled by temperature. On the other hand, liquid crystal phases in lyotropic systems are controlled by the concentration of amphiphilic molecules in solvents. In this thesis, we have worked on a

thermotropic liquid crystal consists of rod like molecules. This type of liquid crystal is also known as calamatic liquid crystal. A brief discussion on different liquid crystal phases for calamatic liquid crystals are given below.

1.1.1 Calamitic liquid crystal

The liquid crystals consist of rod-like molecules are called calamatic liquid crystals. This kind of liquid crystal consisting of achiral molecuels generally shows the following liquid crystal phases.

Nematic phase

This is the most simplest phase of liquid crystal. Here the molecules only have a long range orientational order but no transnational order. The long axis of molecules tend to aligned along a common axis known as director. The director is represented by an apolar unit vector $\mathbf{n}$ which means $\mathbf{n}$ and $-\mathbf{n}$ are indistinguishable. This phase belongs to $D_{\infty h}$ symmetry group (Schoenflies notation). A schematic representation of molecular arrangement in this phase is given in fig. 1.1. Nematic phase is usually an optically uniaxial medium with an optic axis parallel to the director. The birefringence of this phase is about 0.2 [9]. This phase is quite viscous with viscosity about 0.1 Poise which is about 10 times larger than that of water [7].

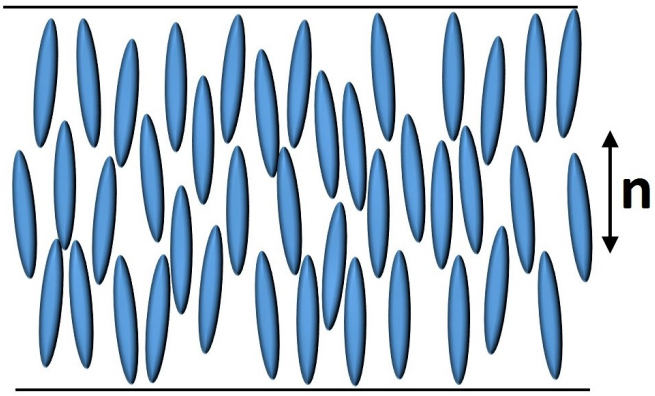


Figure 1.1: Schematic diagram of molecular arrangement in nematic phase. $\mathbf{n}$ represents the director.

Smectic phase

Molecules in smectic phase show both orientational and one dimensional positional order which arises due to the formation of lamellar structure. Inside each layer, molecules do not possess any long range positional order and hence in each layer molecules behave as two-dimensional liquid. The smectic phase is divided into the following subcategories,

Smectic A phase: In this phase, the molecules are arranged in liquid like layers with the director **n** along the layer normal. This phase is optically uniaxial and has $D_{\infty h}$ point symmetry. The layer spacing (d) in this phase is close to the molecular length (l) along its long axis. The XRD profile of smectic A phase gives a sharp peak in the small angle region corresponding to this layered structure and a wide hump at wide angle corresponding to the shorter correlation along the transverse direction of molecules.

For some strongly polar molecules, the measured layer spacing is found to vary between the molecular length (l) and twice this value. Fig. 1.2 gives the three different molecular arrangements as found in smectic A phase consisting of polar molecules. These smectic phases are known as monolayer smectic (SmA_1) (fig. 1.2a), partially bilayer smectic (SmA_d) (fig. 1.2b) and bilayer smectic (SmA_2) (fig. 1.2c) phase respectively [10]. The layer spacings (d) measured from the XRD profiles corresponding to these phases are l, l to $2l$ and $2l$ respectively.

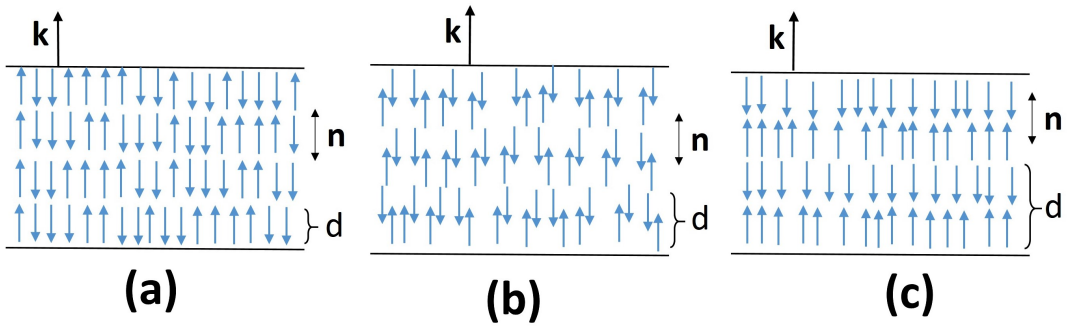


Figure 1.2: Schematic diagram of molecular arrangement in (a) smectic A_1, (b) smectic A_d and (c) smectic A_2 phases. **n**, d, **k** represent the director, layer spacing and layer normal respectively.

Smectic C phase: In this phase, the molecules are arranged in liquid like layers and the director makes a tilt angle θ with respect to the layer normal as shown in fig. 1.3. This phase has C_{2h} point symmetry.

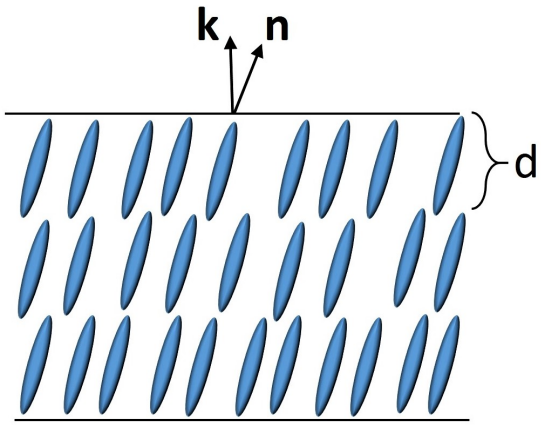


Figure 1.3: Schematic diagram of molecular arrangement in smectic C phase. **n**, d, **k** represent the director, layer spacing and layer normal respectively.

Hexatic smectic In this phase, the molecules in each layers are locally distributed on a triangular lattice. This positional order does not propagate over a distance larger than 100 Å but the bond orientatinal order of the haxagonal lattice structure extends over a large distance. When the long axes of molecules are on average aligned along the layer normal then the phase is called **hexatic smectic B** phase [7]. This phase has D_{6h} point symmetry. On the other hand, when the molecules are on average tilted towards a side of the hexagon as shown in fig. 1.4a, then the phase is called **smectic F** phase [7]. If theses molecules are tilted towards a vertex of this hexagon as shown in fig. 1.4b, then the phase is called **smectic I** phase [7]. The last two hexatic smectic phases have C_{2h} point symmetry.

Reentrant phase

The low temperate liquid crystal phases generally have higher order and hence lower symmetry than the phases formed at higher temperature. A calamatic liquid crystals often exhibit the phase sequence Isotropic → Nematic → Smectic → Crystal on decreasing temperature. However for some samples, a reentrant nematic phase is

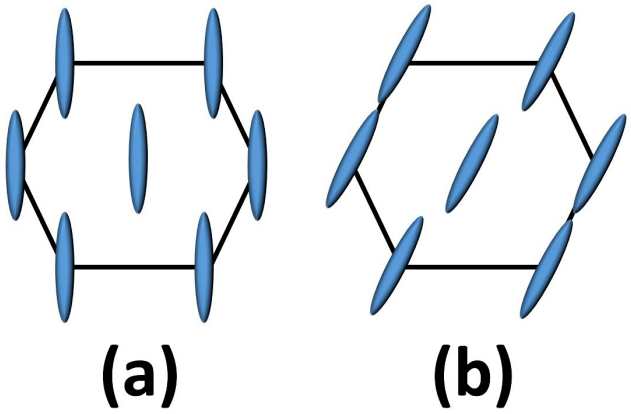


Figure 1.4: Schematic diagram of molecular arrangement in (a) smectic F and (b) smectic I phase.

found to appear below smectic phase on decreasing temperature. These types of samples generally show the following phase sequence on decreasing temperature.

$$\text{isotropic} \rightarrow \text{nematic} \rightarrow \text{smectic} \rightarrow \text{reentrant nematic} \rightarrow \text{crystal}$$

The reentrant nematic phase is also uniaxial in nature and has $D_{\infty h}$ point symmetry. This reentrant nematic phase was found to form in the mixture of two different homologs of cyano biphenyl compounds [1, 11]. The pure 8OCB compound also exhibits reentrant nematic phase at high pressure [2, 12].

1.1.2 Crystal polymorphism in calamitic liquid crystals

Crystal polymorphism of a compound describes the ability to form different crystal phases with dissimilar structures and properties. A subtle interplay between thermodynamic parameters and the growth kinetics of the crystalline domains gives rise to these polymorphic states. The calamatic liquid crystals are frequently found to form polymorphic solid states [4, 5, 13–18]. However, the polymorphic solid states of these calametic liquid crystals have not been studied in detail. In chapter 3, we have studied the properties of different crystal polymorphs of a calamatic liquid crystal. It has been found that the most stable solid state of this compound shows spherulitic growth from its melt. The experimental studies on this spherulitic growth have been discussed in chapter 4. In the following sections of this chapter,

the general properties of this growth phenomenon have been discussed.

1.2 Spherulitic growth

In general, growth of crystal domains shows discrete orientational symmetry. In some special cases, the solid phase after nucleation grows with a spherical growth front having continuous orientational symmetry. This growth phenomenon is known as spherulitic growth. In quasi-two-dimensional geometry, e.g. between two cover-slips, the spherulite domains have circular boundary. The spherulitic growth of solids is a ubiquitous phenomenon exhibited by many different types of materials such as polymers [19, 20], minerals [21–23], elements [24, 25], metals [6] and salts [26–28]. In 1937, H. F. Talbot observed spherulites of borax formed from phosphoric acid [6, 29]. These kind of circular crystal domains were named as "circular crystals" given by David Brewster [30]. Later the name changed to spherulite [6].

The radius of spherulitic domain increases linearly with time till its impingement with another crystal domain [31]. The spherulitic domains consist of radially aligned fibrillar crystallites which show non-crystallographic branching to fill the spherical volume of the domain [6, 31]. This non-crystallographic branching separates spherulites from other poly-crystalline aggregates. In crystallographic branching, long range positional order is maintained in branching. But in non-crystallographic branching this long range positional order is not maintained during branching. The misorientation of the newly formed crystallites typically varies from 0° to 15°.

In general, the diameter of needle shaped fibrillar domains in non-polymeric spherulite domains varies from 10^{-3} to 10^{-7} m [31]. But in spherulites of polymeric system, the thickness of ribbon-like fibrillar crystalline units varies in the range from 100 Å to 1000 Å and its width varies from 10^{-1} μm to 10 μm. The long chain polymer molecules fold back and forth regularly in these ribbon-like domains during crystallization [32].

Spherulites, depending on its morphology, are classified into compact and open spherulite respectively [6, 31]. The compact spherulites do not contain any free

space between the fibrillar crystallites as compared to the open or spiky spherulites. The outer boundary of the compact spherulite domain is smooth and width of the fibrils are less to that found in open spherulites.

Spherulites, consisting of birefringent fibrillar crystallites, produce Maltese cross between crossed polarisers. In general, the black brushes of Maltese cross in birefringent spherulite domain are parallel to the polarisers' pass axis and it remains invariant on sample rotation. This implies that the major refractive index on the sample plane is either along the radial or azimuthal direction of the circular spherulite domain. The spherulites with major refractive index parallel to its radial direction are optically positive [6, 19]. On the other hand, optically negative spherulites have major refractive index along its azimuthal direction. The optical sign of spherulites can be determined by noting the change of interference colors of the sample after inserting a λ-plate in the optical path.

1.2.1 Banded Spherulites

A large sub-group of spherulite with concentric banded structure is known as banded spherulite. In quasi-two-dimensional geometry, the banded spherulite domain appears as a flattened disk with circular boundary and these bands appear as concentric circular rings. The polarising optical microscopic textures of these spherulites show concentric bands with periodic variation of interference color. This kind of ring banded spherulites are generally found to form during polymer crystallization [19, 20]. In addition, some small molecular compounds also form banded spherulites [33–40]. A coherent twisting of the birefringent ribbon-like polymer crystallites along the radial direction of the spherulite domain changes the orientation of indicatrix ellipsoid periodically along the same direction. This modulates the effective birefringence periodically along the radial direction of the domain which gives rise to the concentric colour banded structure with a periodic variation of colours between crossed polarisers. The twisting of optically uniaxial crystallites with optic axis perpendicular to the radial direction gives rise two consecutive black bands in

π rotation of indicatrix. In these black bands the effective birefringence is zero. These kind of spherulites are known as single-banded spherulite [19]. On the other hand, optically biaxial crystallites are associated with an indicatrix ellipsoid having three different principal indices along three mutually orthogonal directions. If the optic plane is perpendicular to the long axis of these crystallites then the coherent twisting of crystallites along the radial direction produces two circular black bands in each π rotation of the indicatrix. These are called double-banded spherulites [19].

The proposed mechanisms to account for the twist in the ribbon-like crystallites are broadly divided into two categories [20]. Some of these mechanisms relate twisting of the crystallites with the growth kinetics. The self induced concentration field during lamellar growth was proposed as the reason behind lamellar twisting [41]. The other proposed mechanisms relate the morphological features of lamellae to its twisting. There are mainly two different kinds of morphological features of lamellae have been proposed for lamellar twisting [20]. Few groups of researchers have introduced screw dislocation to account for lamellar twisting [42–44]. The other proposals relate twisting to the structural difference in folding conformation at two opposite fold surfaces of the lamellar crystal. Keith and Padden emphasized this structural difference in folding conformation to account for the twisting in polyethylene lamellar crystal [32]. Latter Lotz and Cheng advocated this proposal for other polymeric systems [20]. In addition, another mechanism was proposed to account for lamellar twisting which is known as autodeformation [6].

The diffusion controlled growth mechanism sometimes produces rhythmic change in supply of materials at the growth front of solid domains growing from its solutions [45–53]. This mechanism ultimately gives rise to the periodic height modulation of the free surface along the radial direction of the solid domain and produces concentric ring banded structure. This ring banded structures only have been observed in solid thin films with one free surface. It does not have any general applicability in the bulk crystallization of samples and hence is not considered as banded spherulite [20].

1.3 Starch

Starch is a natural source of polysaccharide. The starch grains are found in fruits, roots, stems, seeds and leaves of different plants and trees. The starch grains may have spherical, elliptical or polygonal shapes [54]. The size of the insoluble starch grains varies from 1 to 100 μm [55]. The ellipsoidal and spherical potato starch grains used in our experiments is shown in fig. 1.5. The starch grains are made of two different kind of polysaccharides named as amylose and amylopectin. The amylose is mostly linear and possesses $\alpha(1\rightarrow4)$ glycosidic linkage between D-glucose units as shown in fig. 1.6a. The degree of polymerization found in amylose chains is about 600. Most of the native starches contain 20% – 30% amylose. On the other hand, amylopectin is one of the largest branched bio-polymer found in nature containing both $\alpha(1\rightarrow4)$ and $\alpha(1\rightarrow6)$ glycosidic linkages between D-glucose units as shown in fig. 1.6b. The $\alpha(1\rightarrow6)$ glycosidic linkage is only found at the branch points of side chains. The molecular weight of amylopectin is in the range between (50–500) $\times$ 10^6 [54]. It is the major component found in starch grains.

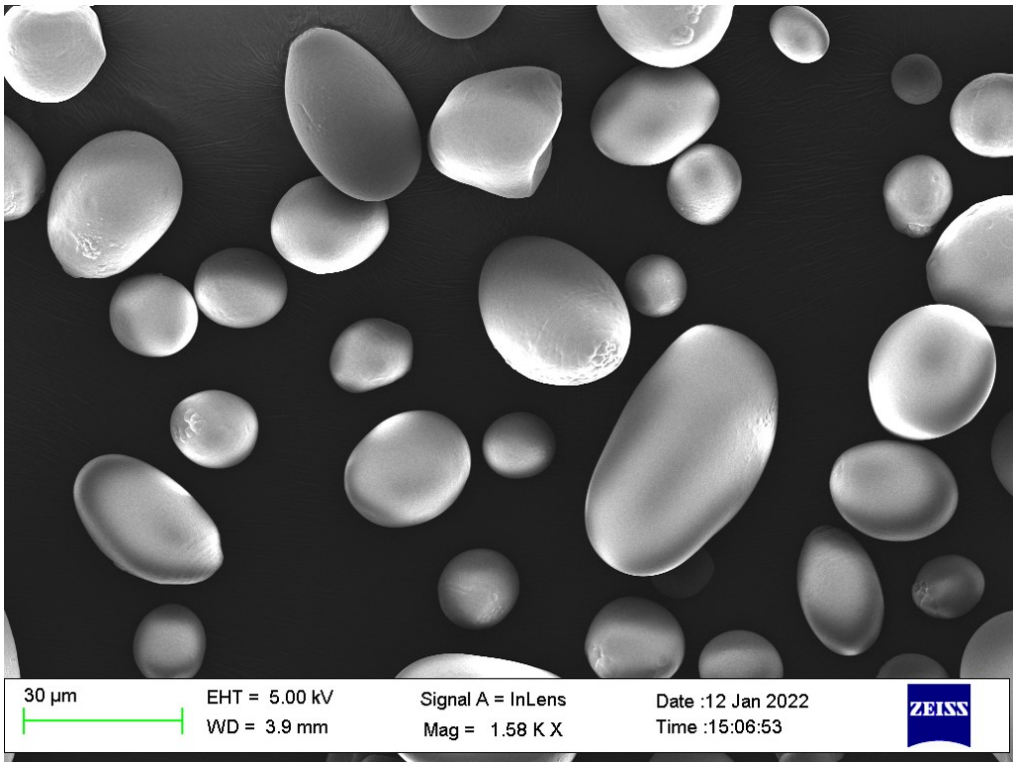


Figure 1.5: SEM texture of potato starch grains.

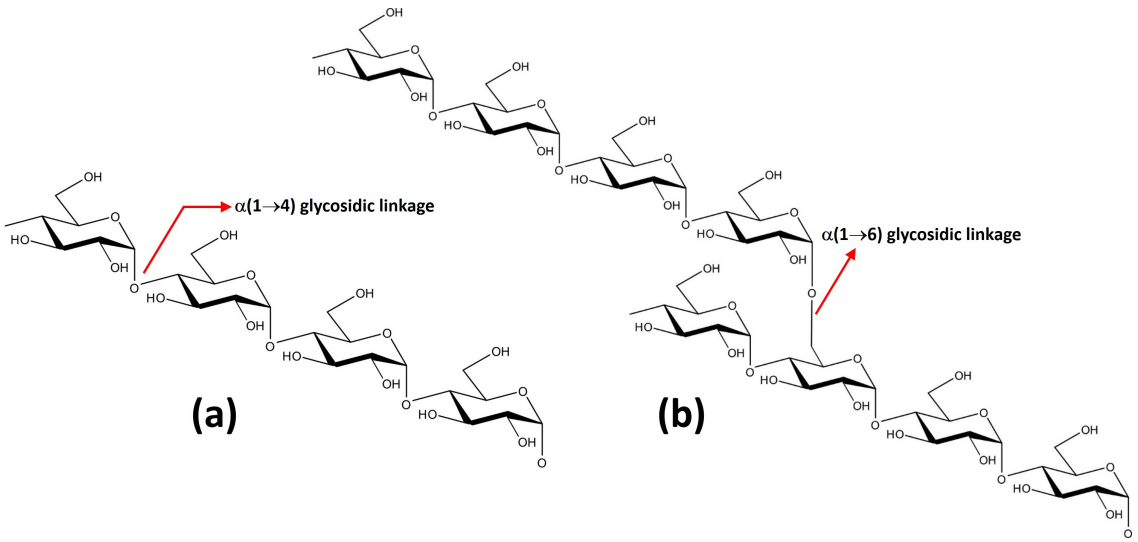


Figure 1.6: Molecular structure of (a) amylose and (b) amylopectin.

Starch grains have hierarchical structure. It consists of alternating amorphous and crystalline shell-like domains referred to as "growth rings" which surround an amorphous core known as hilum [55]. The thickness of these growth rings varies between 100 – 500 nm [55]. The crystalline domains consist of blocklets of size 50 – 500 nm [56]. The smaller blocklets of size about 20 – 50 nm are found in amorphous domains [57]. The size and distribution of these blocklets play an important role for resisting gelatinization and enzymatic degradation. Inside these blocklets, alternating crystalline and amorphous lamellae with the period of about 9–11 nm are found to form by amylopectin molecules [54]. The amylopectin molecules which take part for constructing crystalline lamellae are found to form cluster of double helical chains in these lamellae [54, 57]. The branch points for amylopectin side chains are found in amorphous lamellae [57].

The crystallinity of native starch grains varies from 15% to 45% [55]. There are mainly two different kinds of crystal polymorphs found in starch grains. One of them known as A-type polymorph shows compact nature of amylopectin double helices. This type of polymorph is mostly found in cereal starch grains. The other one which shows relatively less compact structure of amylopectin double helices in crystalline lamellae is known as B-type polymorph. This type of polymorph is mostly found in tuber and root starches [55]. A mixture of both of these types of crystallinity has

been found in starch grains from legumes, some roots and fruits. This type of crystal polymorph is known as C-type polymorph. It was proposed that in C-type grains, the B-type of polymorphs are placed at the central region surrounded by A-type of polymorphs [58–60]. Although the reverse situation has also been observed in high-amylose mutant rice starch [61].

The structure of A-type polymorph was determined by the analysis of the results from the electron diffraction studies, decomposing the x-ray powder diffraction profiles into individual peaks, x-ray fiber diffraction studies and the molecular modeling [62]. The intra and inter molecular interaction energy calculation show that the amylopectin chains form left handed parallel double helical strands in the crystalline lamellae. Each single helix with pitch length 2.138 nm is related to the other one of the double stranded structure by a two fold axis of rotation. Therefore the apparent fiber distance in double helix along its axis is 1.069 nm. The two polymer chains in a double stranded helix are bound by hydrogen bonds. This structure is very compact and no other molecules are present in between these two component helices. The double helices in the crystalline lamellae form monoclinic lattice structure with lattice parameters a = 2.124 nm, b = 1.172 nm, c = 1.069 nm and $\beta = 123.5^\circ$ [62]. There are four water molecules found in an unit cell which can not be extracted before crystal disruption. The double stranded helices are bound by hydrogen bonds directly or through the water molecules.

The structure of B-type of polymorph was also determined by the analysis of the results from electron diffraction studies, x-ray powder diffraction studies, x-ray fiber diffraction studies and the molecular modeling [63]. The left handed parallel stranded double helices formed by amylopectin chains in the crystalline lamellae produce the hexagonal lattice structure. The corresponding lattice parameters are a = b = 1.85 nm and c = 1.04 nm where c-axis is along the long axis of double stranded helix. The single helix in a double strand has a pitch length of 2.08 nm and it is related to the other conjugated helix by a two fold axis of rotation. Therefore the apparent repetition along c-axis in a double stranded conformation is 1.04 nm.

The double helices are bound with each other by hydrogen bonds and produce a channel bound by the hexagonal arrangement. The channel in a hexagonal unit cell contains 36 number of water molecules.

The starch grains are birefringent. Fig. 1.7a shows the image of a starch grain between crossed polarisers. The black brushes of Maltese cross in this POM texture remain invariant on rotating the sample stage. These black brushes with an intersection point at the hilum divide the whole grain into four quadrants. The interference colour of the starch grain belongs to the first order of Levy chart. The insertion of a λ-plate in the optical path changes the colour of first and third quadrants into blue whereas the second and four quadrants turn into yellow as shown in fig. 1.7b. So, an effective addition and subtraction of optical path differences occur in these respective places. This implies that the major index of the index ellipse is along the radial direction of the domain.

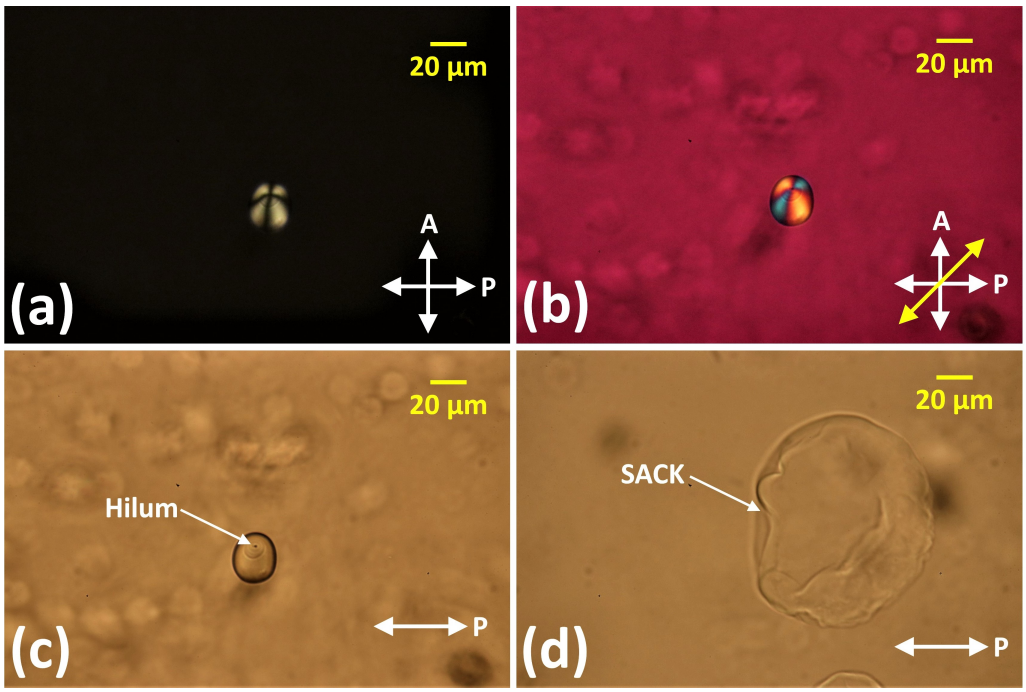


Figure 1.7: POM texture of a starch grain (a) between crossed polarisers (b) after inserting λ-plate in the optical path between crossed polarisers. The bright field images of (c) a starch grain and (d) the remnant sack after gelatinization of the starch grain.

Fig. 1.7c shows the bright field image of a potato starch grain with only the polariser in the optical path. The hilum of this grain appears as a dark spot as

shown in this figure. The starch grains swell to some extent when kept in water at room temperature. However on heating in excess water, above a certain temperature the starch grains absorb water which gives rise to a pressure in the grains and disrupts it. This irreversible transition is known as starch gelatinization [64]. After gelatinization, starch grains loose its crystallinity [65] and birefringence [66]. An unwinding of starch bio-polymers also occurs in this irreversible transition [67]. The starch bio-polymers come out from grains and make the solution viscous. After complete gelatinization, the residues of starch grains are known as "ghost" or "sack" as shown in fig. 1.7d [68, 69]. Based on experimental studies, a few models on the gelatinization mechanism of starch grains have been proposed [64, 65, 67, 70, 71].

The dispersed starch biopolymers in gelatinized starch solution form ordered network structure on aging which is known as retrogradation [56]. The retrograded starch containing certain percentage of water generally possess B-type of crystal polymorph [56]. The crystalline structure in retrograded starch sample develops when water content in gelatinized starch solution lies in the range from about 20% to 90% [72, 73]. In this continuously ongoing retrogradation process, amylose molecules develop a network structure relatively faster than that of amylopectin molecules [56, 74]. The gelatinised starch sample becomes turbid with aging due to the continuously developing network structure of starch biopolymers inside it [56, 75, 76]. Initially the turbidity increases relatively faster due to the fast formation of amylose network [56, 74]. After a certain time from gelatinization, the turbidity of sample increases slowly for the slow development of amylopectin networks.

The transparent biodegradable films are obtained on drying a gelatinized starch solution [77–79]. In recent years starch based bio-plastics have attracted much attention as a replacement of synthetic polymer films in plastic industries [80]. In chapter 5, we have studied the properties of starch films formed on drying of gelatinized potato starch solution droplets.

Chapter 2

Experimental techniques

2.1 Polarising Optical Microscopy

The polarising optical microscopy (POM) is a very common and versatile technique used to investigate birefringent samples. This microscope is equipped with a polariser and an analyser placed before the condenser and after the objective lens respectively as shown in fig. 2.1. The birefringent samples are generally studied between these polarisers with their pass axis at right angle to each other known as crossed position. The birefringent and optically isotropic specimens generally appear bright and dark respectively between crossed polarisers. The POM studies of our samples were performed by using the Olympus BX50 polarizing optical microscope equipped with digital camera (Canon 80D) and a microscope hot stage (Linkam LTS420E) placed on the sample stage (see fig. 2.1).

The refractive index of a birefringent sample is represented by an ellipsoid which is known as indicatrix ellipsoid. For isotropic samples, all the principal indices are same and the indicatrix becomes a spheroid. The cross section of this indicatrix normal to the direction of propagation of light effectively determine the birefringence of the sample. For an optically isotropic system this cross section is always circular and hence the effective birefringence is zero. Therefore after passing through the optically isotropic system, the light does not change its state of polarisation. Therefore, the isotropic sample looks dark between crossed polarisers. On the other hand for an optically anisotropic medium, the cross section of the indicatrix is generally an ellipse known as index ellipse. After passing through this sample, the state of polarisation of light in general changes and therefore the sample appears bright

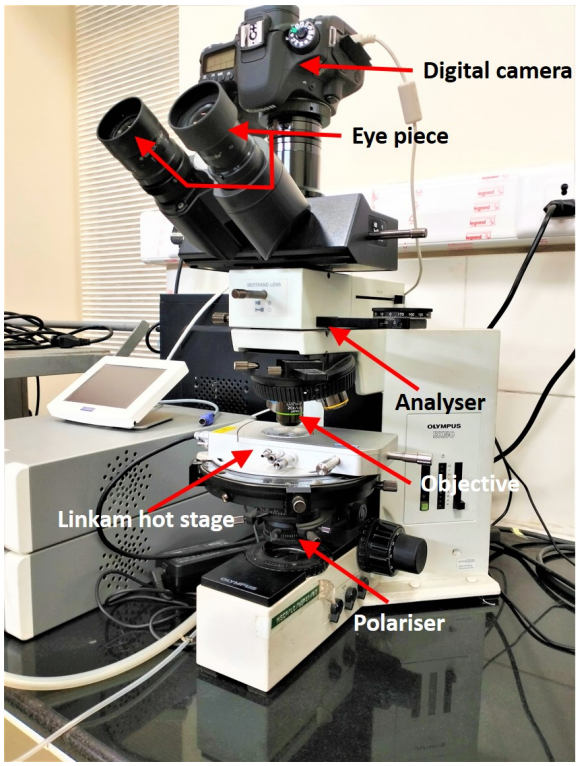


Figure 2.1: The polarising optical microscope.

between crossed polarisers. The state of polarization depends on the optical path difference encountered by the light during passing through the sample and also the wavelength of the light. Therefore depending on the effective phase retardation, the sample produces images with different colours when it is illuminated by white light. The variation of interference colour on varying the optical path difference in the specimen illuminated by white light is depicted in Michel-Levy chart as shown in fig. 2.2.

The transmitted intensity for a given wavelength of light passing through a sample between crossed polarisers can be written as,

$$I = I_0 \times sin^2(2\phi) \times sin^2(\delta/2) \tag{2.1}$$

Here I and I_0 are the intensities after the analyser and polariser respectively. ϕ is the angle between one of the principal axes of the effective index ellipse and the polariser. The phase difference $\delta = (2\pi d\Delta n)/\lambda$, where d is the thickness of the sample, Δn is the effective birefringence of the sample and λ is the the wavelength

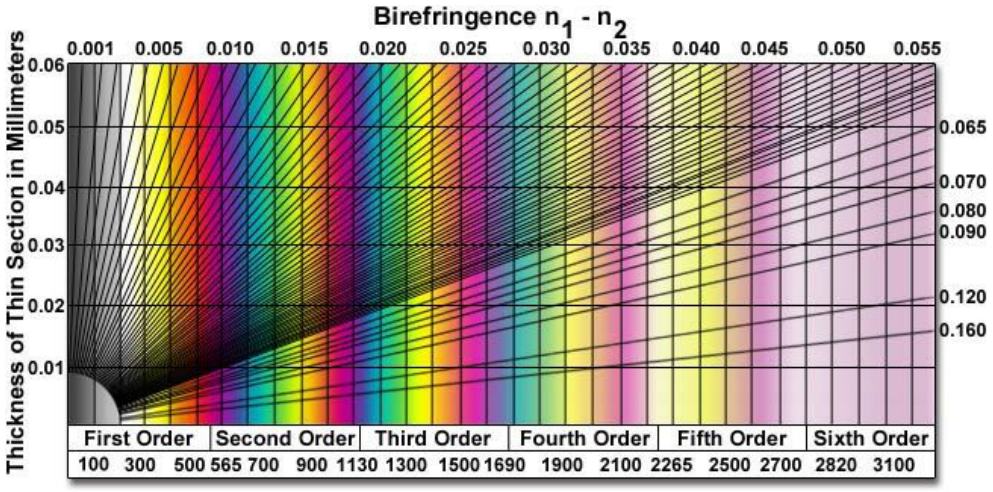


Figure 2.2: The Michel-levy chart.

of the light. It can be seen from eqn. 2.1 that when one of the principal axes of the index ellipse is parallel to the polariser i.e. $\phi = 0$ or $\pi/2$ then the sample appears dark. Therefore, there are four extinction positions which appear on 360° rotation of the sample. The sample becomes brightest when these principal axes make $\pm 45°$ angle with respective to the polariser.

The orientation of the major principal axis of the effective index ellipse can be determined at these brightest positions using a λ-plate in the optical path of the microscope. The λ-plate for a given wavelength with a known slow axis is generally introduced after the objective lens of the microscope. In our setup, a λ-plate for wavelength of 530 nm is used with its slow axis at an angle of 45° with respect to the polariser. The introduction of this phase plate in the optical path turns the dark regions of the sample to magenta whereas the bright regions change to other colours depending on the effective addition and subtraction of the optical path differences occurred in the sample and the λ-plate respectively. These studies can be performed easily when the interference colour of the sample is grey-white which belongs to the first order region of the Levy chart. In case of effective addition of path differences, the colour of the sample changes from gray-white to blue (see the Levy chart in fig. 2.2) which implies that the slow axis of the λ-plate and the major axis of index ellipse are parallel to each other. On the other hand, when these are perpendicular to each other then the interference colour turns to yellow due to the subtractive

nature of the respective path differences.

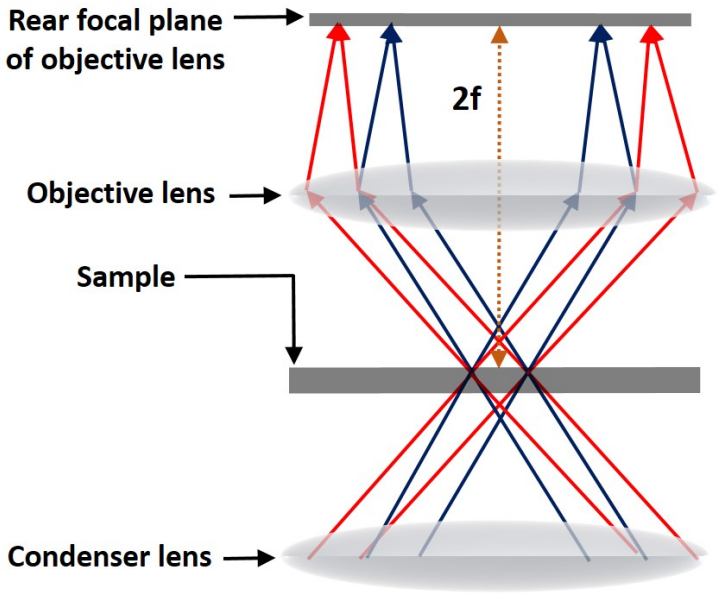


Figure 2.3: The ray diagram in conoscopic setup.

2.1.1 Conoscopic studies

The conoscopic studies are performed on birefringent samples to determine their optical anisotropy. A condenser lens with high numerical aperture concentrates the light into a cone and illuminates the sample. After passing through the sample, the light is focused on the back focal plane of the objective lens as shown in fig. 2.3. To see the conoscopic figure, the Bertrand lens attached with POM should be inserted into the optical path. The conoscopic studies on our samples were performed by using an objective lens with 50X magnification and 0.5 numerical aperture.

An optically uniaxial system has a single optic axis and can be either optically positive ($n_e > n_0$) or negative ($n_e < n_0$). These uniaxial systems possess prolate and oblate shaped indicatrix ellipsoid respectively as shown in fig. 2.4. When the optic axis is parallel to the direction of propagation of light, then the conoscopic figures of the uniaxial samples have a crossed isogyres as shown schematically in fig. 2.4. The intersection point of the crossed isogyres remains invariant on rotation of the sample. The cross isogyres divide the field of view into four quadrants with equal areas as shown in fig. 2.4. The colour of these quadrants is gray-white for retardation in the

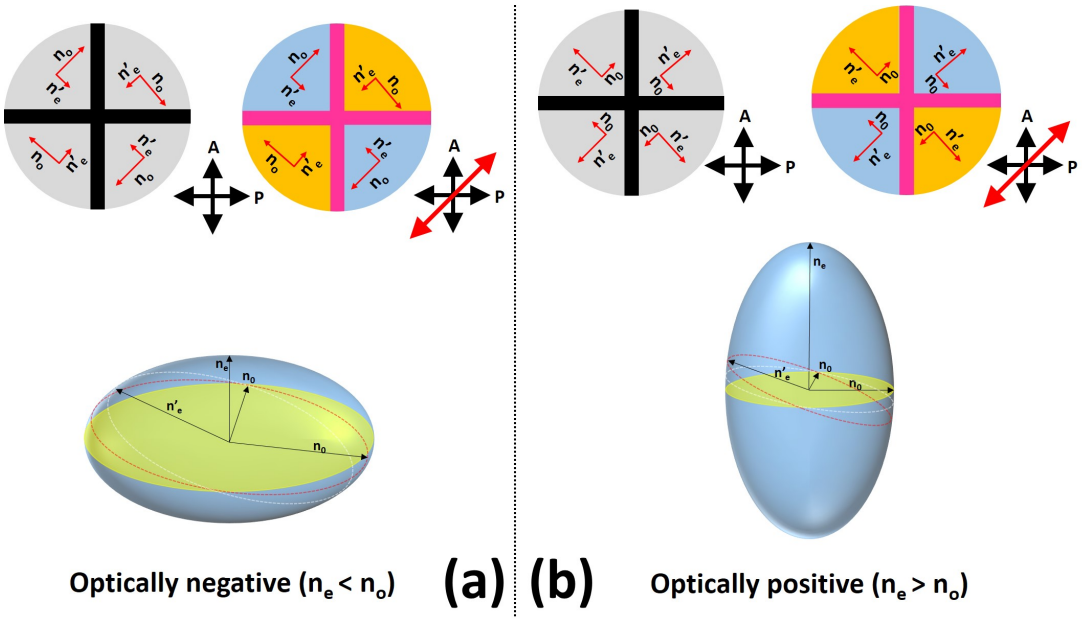


Figure 2.4: (a) [Down] The oblate indicatrix of an optically negative uniaxial sample. Principal indices in this indicatrix are n_e and n_o. [Up] The conoscopic figures of an optically uniaxial sample before [Left] and after [Right] inserting the λ-plate into the optical path when the optic axis of the sample is along the direction of propagation of light. (b) [Down] The prolate indicatrix of an optically positive uniaxial sample. Principal indices in this indicatrix are n_e and n_o. [Up] The corresponding conoscopic figures before [left side] and after [left side] inserting the λ-plate into the optical path when the optic axis of the sample is along the direction of propagation of light. The effective principal indices encountered by the light falling at different incident angle on the sample are shown in all these conoscopic figures.

first order region of the Levy chart. For highly birefringent samples, the concentric isochromes can also be found. However, the starch samples studied in this thesis have low birefringence and the isochromes were not observed in the conoscopic figures. For an optically negative uniaxial sample with low retardation in the first order region of the Levy chart, introduction of the λ-plate changes the colour of the first and third quadrants to yellow and second and fourth quadrants to blue as shown in fig. 2.4a. The optical path differences in these pairs of quadrants show subtractive and additive nature respectively. On the other hand, for an optically positive uniaxial sample, the first and third quadrants change to blue whereas second and fourth quadrants change to yellow. The nature of the optical anisotropy of the uniaxial medium can be determined from these colour variations. If the optic axis is slightly tilted with respect to the direction of propagation of light then the intersection point rotates

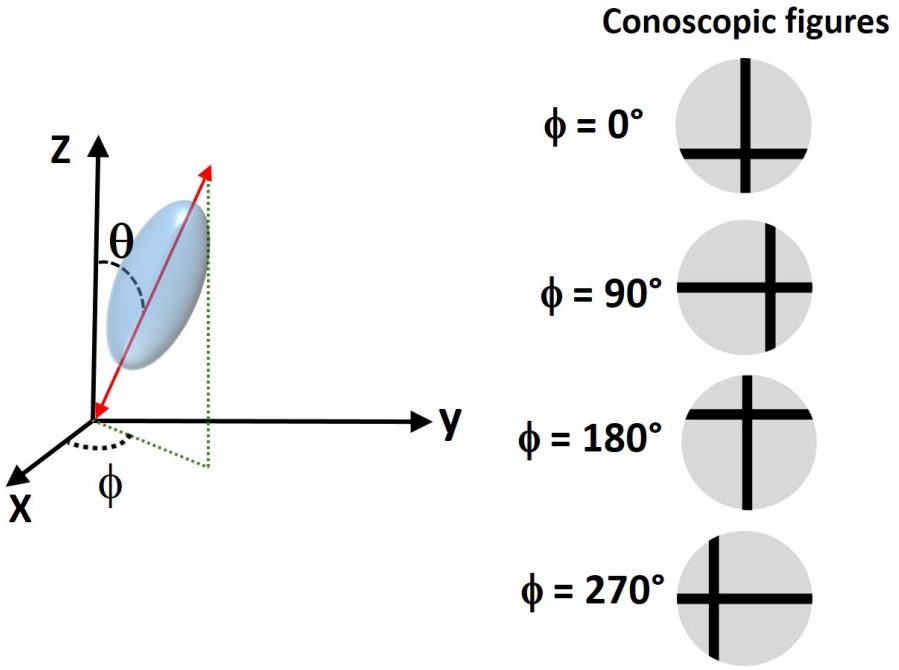


Figure 2.5: [Left] The tilted optic axis of a uniaxial medium by an angle θ w.r.t. the direction of propagation of light along z axis. [Right] The conoscopic figures of this optically uniaxial sample at different angles (ϕ) of rotation of the sample on sample stage.

around the center of the field of view on rotating the sample as shown in fig. 2.5.

For a biaxial medium, all the three principal indices α, β and γ are different ($\alpha < \beta < \gamma$) as shown in fig. 2.6. These mediums have two optic axes and they lie on the plane containing the major and minor principal axes i.e. α-γ plane. This plane is called optic plane. The acute angle between these optic axes is known as acute axial angle ($2V$). The biaxial sample is optically negative when the minor principal axis of the indicatrix is the bisectrix of the acute axial angle (see fig. 2.7). On the other hand, when the major principal axis is the bisectrix of this acute axial angle, then the biaxial sample is optically positive (see fig. 2.8).

Fig. 2.7 and fig. 2.8 show the schematic conoscopic figures for the optically negative and optically positive biaxial samples respectively. In these cases the acute bisectrix is along the direction of propagation of light. Therefore the optic plane is also parallel to the direction of propagation of light. The conoscopic figures in these cases show the crossed isogyres when the optic plane is either parallel or perpendicular to the polariser. The intersection point of crossed isogyres remains

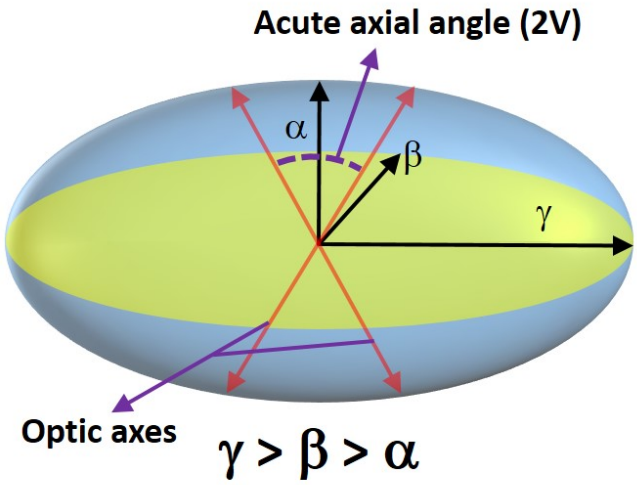


Figure 2.6: The index ellipsoid of an optically biaxial medium.

at the center of the field of view. For other orientations of the optic plane with respect to the polariser, the isogyres become uncrossed. At ±45° orientation of the optic plane with respect to the polariser, the conoscopic figures show the uncrossed hyperbolic isogyres as shown in the right side of fig. 2.7 and fig. 2.8. In these figures, the poles of the optic axes appear on the apex of the hyperbolic isogyres with zero effective birefringence. These poles are also called melatope. The convex sides of these uncrossed hyperbolic isogyres are always directed towards the acute bisectrix.

The interference colour of the areas in the schematic conoscopic figures bound by the convex side and concave side of the uncrossed hyperbolic isogyres is gray-white (see the right side of fig. 2.7 and fig. 2.8). This colour belongs to the first order region of the Levy chart. For the optically negative biaxial sample, introduction of the λ-plate changes the colour of the areas bound by the convex and concave side of isogyres to blue and yellow respectively at +45° orientation of the optic plane as shown in right side top row of fig. 2.7. The optical path differences in these bound regions show the additive and subtractive nature respectively. At -45° orientation of the optic plane, the colours of these respective regions interchange as shown in right side bottom row of fig. 2.7. On the other hand, for the optically positive biaxial sample, the opposite nature of these colour variations should be observed as shown in right side of fig. 2.8. Therefore, these colour variations after introducing the λ-

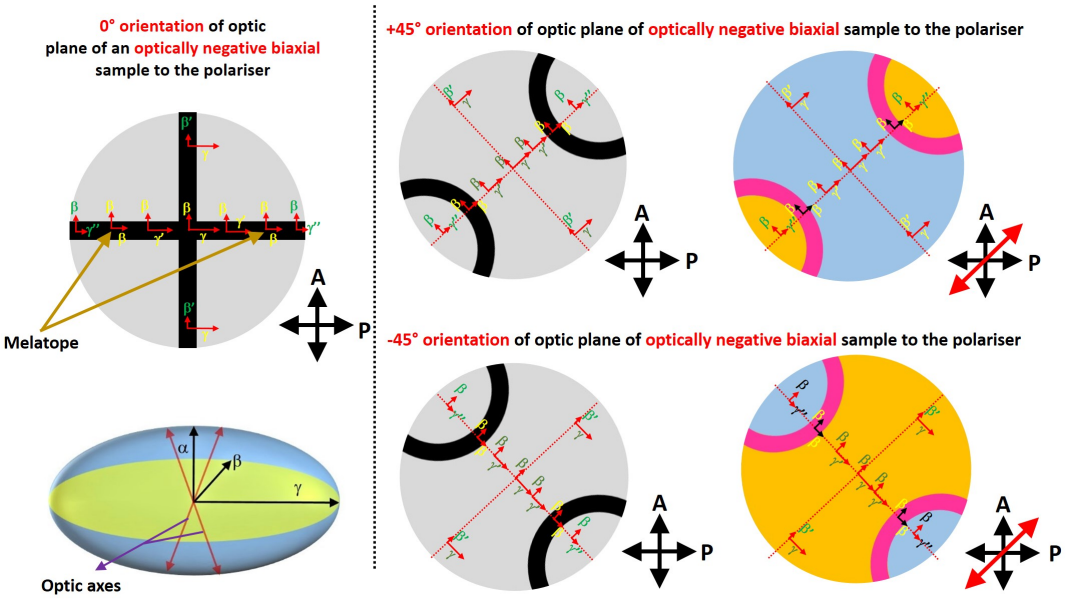


Figure 2.7: [Left] The indicatrix of an optically negative biaxial sample and the corresponding conoscopic figure when optic plane is parallel to the polariser and the direction of propagation of light. The effective principal indices encountered by the light falling at different incident angle on the sample are shown in this conoscopic figure. [Right] [Up] The conoscopic figures at +45° orientation of the optic plane w.r.t. polariser [Left] before and [Right] after inserting the λ-plate. [Down] The conoscopic figures at -45° orientation of the optic plane w.r.t. polariser [Left] before and [Right] after inserting the λ-plate.

plate in the optical path can be used to determine the optical nature of a biaxial medium.

2.2 Confocal Microscopy

Confocal microscope has some advantages over the wide field fluorescent microscope. This microscopy studies are capable to collect the fluorescent signal from a particular optical section of the sample without any disturbances from the other optical sections. The samples doped with fluorescent dye molecules can only be studied in this microscopy technique. In the laser scanning confocal microscope, a beam of light with wavelength λ is focused on the sample. The emitted fluorescent signal from the sample passes through the dichromatic mirror and falls on the aperture of a pinhole placed before the photo-multiplier detector as shown in fig. 2.9. The dichromatic mirror blocks the exciting beam to pass through it. This pinhole aperture is at the

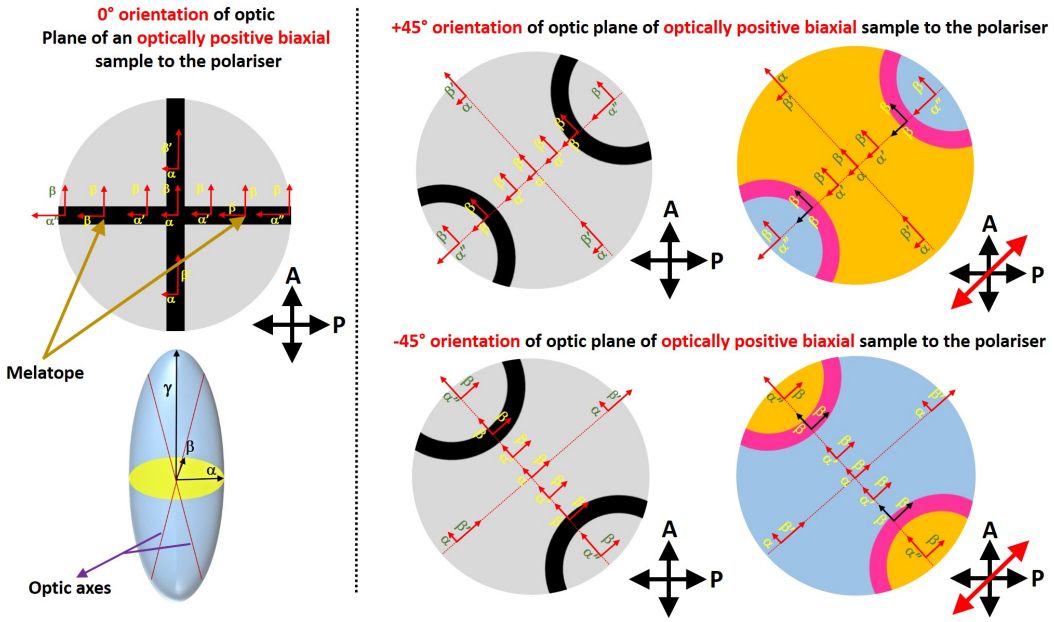


Figure 2.8: [Left] The indicatrix of an optically positive biaxial sample. The corresponding conoscopic figure when optic plane is parallel to the polariser and the direction of propagation of light. The effective principal indices encountered by the light falling at different incident angle on the sample are shown in this conoscopic figure. [Right] [Up] The conoscopic figures at +45° orientation of the optic plane w.r.t. polariser [Left] before and [Right] after inserting the λ-plate. [Down] The conoscopic figures at -45° orientation of the optic plane w.r.t. polariser [Left] before and [Right] after inserting the λ-plate.

conjugate plane to front focal plane of the objective lens. At this aperture, the illuminated point of the specimen on the focal plane of the objective produces an airy disc. The fluorescent signal coming from other optical sections at different depth of the sample produces extended airy discs on the same pinhole aperture. These extended airy discs do not contribute to the formation of the fluorescent image. The lateral XY scanning along with the axial (along z-axis) scanning of the specimen by the focused laser beam produces the complete confocal fluorescent image of the specimen.

In our experiment, the confocal images of the sample were taken by Leica SP8 confocal microscope equipped with different lasers. An Argon gas laser of wavelength 514 nm was used as an exciting beam which was focused on the sample by the objective lens of the microscope. The back scattered fluorescent signal from the sample was collected through the same objective lens. A prism dichroic is equipped

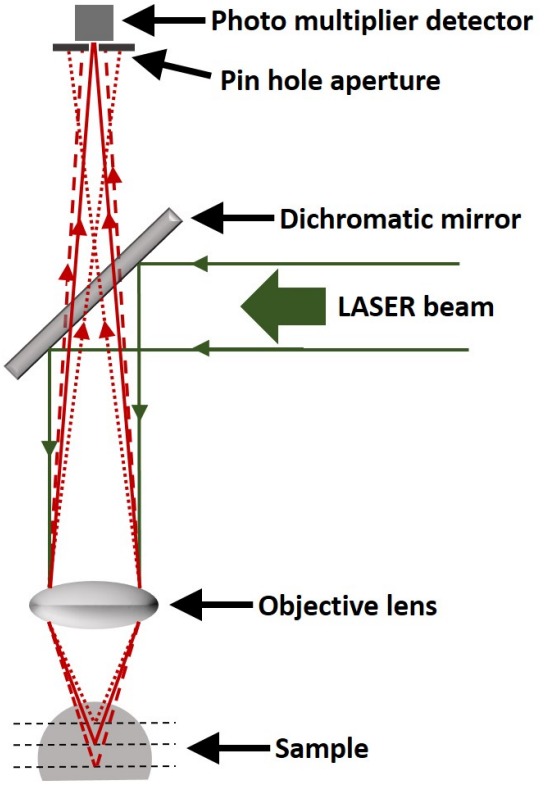


Figure 2.9: The ray diagram in confocal microscope.

with this setup to select a particular bandwidth of the fluorescent signal to pass through it. In our experiments, the bandwidth of the fluorescent signal detection was set as 550 nm to 630 nm. An oil immersion objective with 100X magnification and numerical aperture 1.25 was used for acquiring the confocal images of our samples. The refractive index of the oil used for this purpose was 1.4.

2.3 Scanning Electron Microscopy

Scanning electron microscope is used to probe the sample topography in high resolution which is beyond the resolution of optical microscope. We used Carl Zeiss (Ultra Plus model) scanning electron microscope for SEM studies of our samples. Here, the field emission electron gun is used as a source of electron beam. The electron beam after emission is accelerated by an applied accelerating voltage. This

beam is focused by electromagnetic lenses on the sample. The bombardment of accelerated electrons on the conducting samples emits secondary electrons from it. These secondary electrons are detected by the detector and produces the image of sample surface.

Generally, the yield of secondary electrons from electrically non-conducting samples is relatively less. In addition, it also accumulates charges due to the bombardment of the incident electron beam. The localization of the accumulated charges on the sample disturb the secondary electron trajectories which perturbs the image of the sample surface. To overcome these difficulties, a thin metallic coating is made on the surface of the electrically non-conducting samples. Our samples were also non-conducting. Therefore the surface of the solid phases of our compound was sputter coated with platinum [QUORUM (Q150R S)] before the SEM studies. The coating thickness was mostly kept around 2 nm. The solid phases of our compound were formed on the conducting surface of ITO coated glass plates. An electrical connection was made between this conducting surface to the metallic sample stage by using conducting silver paste. In this way the sample surface was always grounded. The metallic coating produces high yield of secondary electrons after bombarding it by the incident electron beam. It also conducts charges and makes the sample surface electrically neutral during imaging. The electrically conducting samples usually do not need such treatment for their SEM studies. In this case, the sample is usually kept on a double sided conducting tape to attach it with the metallic sample stage.

2.3.1 Cryogenic-SEM

The liquids with boiling points below 183 K are known as cryogenic liquids. We use liquid nitrogen with boiling point about 77 K as a cryogenic liquid. The sample kept in a holder is dipped in the liquid nitrogen for quenching it to low temperature. The quenched sample is then transferred to the cryo-preparation chamber attached with the field emission SEM (FESEM) system. The sample stage in this chamber is already cooled to 103 K by liquid nitrogen circulation and the vacuum maintained

in this chamber is in the range between 10^{-4} and 10^{-5} mbar. After transferring the sample to the cryo-preparation stage, it is heated to 183 K to make it relatively soft. The top part near the interface of this relatively soft sample is cut by a knife. After cutting the sample, it is kept at this temperature for 15 minutes. In this time period, ice sublimates from the top surface of the sample. This sublimation process is generally needed for water based samples. Then the electrically non-conducting surface of the sample is sputter coated with platinum for 60 sec. which produces approximately 6 nm thick platinum film on the top of the sample. After completing all these processes, the sample temperature is again brought down to 103 K and then it is transferred to the microscope stage. This stage is already kept at 83 K by liquid nitrogen circulation and the pressure maintained in the sample chamber is about 10^{-6} mbar.

2.4 UV-Visible Spectrophotometry

The UV-Visible transmission spectroscopy studies of samples were performed by using Lamda 35 Perkin Elmer spectrophotometer. It is a scanning double beam spectrophotometer. The main parts of this machine are source of light, monochromator and a detector. The tungsten and deuterium lamp sources are used to cover the whole scanning wavelength range from 190 nm to 1100 nm. The sources switch automatically during the monochromator skewing. The light from the source passes through an entrance slit and then falls on a grating which disperses the beam into its components. The exit slit after the grating allows a particular band of wavelength of the dispersed beam to pass through it at a time. This spectral bandwidth is 1 nm and it depends on the exit slit width which is changeable in this setup. The scanning of sample is performed for the whole wavelength range by skewing of this grating. The exit beam after the slit falls on a beam splitter which splits the beam into two equal intensity components. These two beams pass through the sample and the reference respectively and ultimately collected by two different photodiodes placed at the end of the optical paths. In this double beam spectrophotometer, the

transmittance is calculated from the ratio of measured intensities of sample beam and the reference beam respectively. At the beginning, the machine performs a blank measurement where it measures both the intensities of sample beam (S_{blank}) and reference beam (R_{blank}) simultaneously for the full wavelength range in absence of sample and reference in optical paths. It then performs the same task in presence of both the sample (S_{meas}) and the reference (R_{meas}) in the respective optical paths. We used this setup for acquisition of the UV-Visible spectra of starch films as discussed in chapter 5. In these measurements, we placed the starch film at the sample stage and took air as reference. The transmittance (T) of the sample film is measured from the following relation,

$$T = \frac{S_{meas}}{R_{meas}} \times \frac{R_{blank}}{S_{blank}} \times 100\% \tag{2.2}$$

2.5 Raman Spectroscopy

In general, a radiation with frequency ω after falling on an object can be transmitted, absorbed and scattered from the object. The scattering of radiation with same frequency as that of the incident radiation is known as Rayleigh scattering. It is an elastic scattering which means that no energy exchange occurs during interaction between radiation and the interacting molecules. On the other hand, in Raman scattering, the scattered wavelength ($\omega \pm \omega_M$) is different than that of the incident radiation. Hence Raman scattering is an inelastic scattering. In this inelastic process, an exchange of energy between molecule and the incident radiation changes the final state of the molecule from its initial one. This final state of the molecule is either more or less energetic than its initial state. Therefore, the energy of scattered radiation shifts from that of the incident radiation. This shift is generally represented in terms of wave number shift expressed in cm^{-1} unit and called as Raman shift.

The Raman bands with negative and positive Raman shifts are called Stokes and anti-Stokes bands respectively. The less energetic Stokes bands appear when

molecules absorb energy from the incident radiation and finally reach to the higher energetic state. On the other hand, anti-Stokes bands appear when molecules release energy and go to the less energetic states. At room temperature, the probability of finding molecules in ground state is much higher than that of its other excited states. These ground state molecules can participate in inelastic scattering by shifting themselves to the higher energy states. This eventually increases the intensity of Stokes bands compared to that of the anti-Stokes bands. Therefore, Stokes bands are usually considered in Raman spectroscopic analysis.

The Raman spectroscopic studies of our samples were performed by using Horiba Jabin-Yvon T64000 (see fig. 2.10) micro Raman spectrometer attached with an air cooled argon laser and a He-Ne laser. The wavelength of the exciting radiations coming from argon and He-Ne laser is 514 nm and 633 nm respectively. During data acquisition process, one of these laser beams is used to focus on the sample by the objective lens of a microscope. The spot of illumination on the sample is selected by looking its image on a dedicated computer screen. These images are taken by a digital camera attached to the microscope of this system. The radius (r) of the focused laser spot on the sample depends on the numerical aperture ($N.A.$) of the objective lens and the used wavelength (λ) of illumination as $r = 0.61 \times \lambda/N.A.$ We used an objective lens with 50X magnification and $N.A.$ of 0.75 to focus the laser beam on the sample. Hence the calculated spot size produced by this lens for the exciting beam with wavelengths 633 nm and 514 nm is less than 1 μm.

The back-scattered light from the sample is collected by the same objective lens and passes through a dichoric mirror to the spectrometer. The dichoric transmits only the wavelengths higher than the exciting wavelength. Inside the spectrometer, the signal gets dispersed by a grating (1800 groves/mm) and then focused on a peltier cooled CCD camera. This device transforms the light signal to the electrical signal which is again converted to the digital signal by analog to digital converter. At last, the profile of the spectrum is observed in the computer monitor screen. This profile shows an intensity plot verses Raman shift in cm^{-1}. The resolution of this

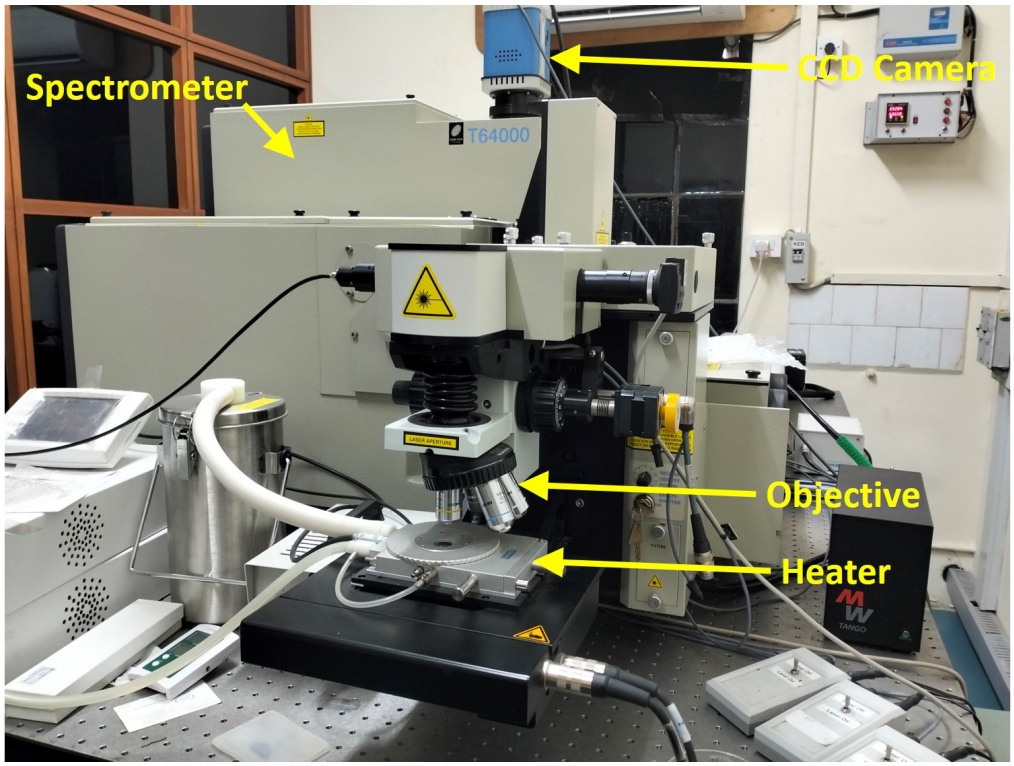


Figure 2.10: The Raman Spectrometer.

profile for 514 nm exciting wavelength is about 0.5 cm^{-1} per pixel.

The system is equipped with a Linkam hot stage placed on the sample stage. The temperature range in this hot stage varies from -196°C to 600°C. The temperature resolution of this setup is 0.1°C. To acquire the Raman spectra from the samples during heating, an objective with 50X magnification and long working distance is used. Prior to taking the Raman spectra of the sample, the spectrometer is calibrated using 520.7 cm^{-1} line of silicon.

2.6 X-ray Diffraction

X-ray diffraction technique is a powerful tool to detect the positional order of molecular organization. The characteristic lengths of separation between atoms or molecules in a lattice structure is determined by Bragg's law as given below

$$2d_{hkl}sin\theta = \lambda \tag{2.3}$$

where d_{hkl} is the distance between lattice planes with Miller indices (hkl), 2θ is the scattering angle and λ is the wavelength of the incident x-ray beam.

A DY 1042-Empyrean (PANalytical) x-ray diffractometer with a PIXcel 3D detector was used to acquire the wide angle x-ray scattering (WAXS) profiles of our samples using CuK_α radiation of wavelength 1.54 Å. Small-angle x-ray scattering (SAXS) studies were performed using a HECUS S3 Microsystem fitted with a copper anode x-ray generator (Genix) and a 1D position-sensitive detector.

The samples in its liquid state are filled in Lindemann capillaries (outer diameter 1.0 mm). The filled capillaries are flamed sealed. These samples are used for the SAXS and WAXS studies. The XRD profiles of the samples are acquired during transmission of x-ray beam through the samples in capillaries. A hot stage (Linkam) is used to maintain the temperature of the samples in WAXS machine. The temperature resolution in this hot stage is 0.1°C. On the other hand in SAXS machine, a Peltier-controlled stainless steel holder is used for controlling the temperature of the samples.

The Lindemann capillary itself shows a wide hump at wide angle of its own diffraction profile. Therefore this profile interferes with that of the sample inside the capillary. To avoid this disturbance, samples are kept on a silicon made flat sample stage of the wide angle x-ray diffractometer. The silicon flat stage shows a flat XRD profile which does not interfere with that coming from the sample. In this arrangement, the XRD studies are performed in the grazing angle of incidence of the x-ray beam. The XRD studies of the samples on the flat stage can only be performed at room temperature.

2.7 Differential scanning calorimetry

Differential scanning calorimetry (DSC) studies is an indispensable technique for measuring the first order phase transitions of the samples. A power compensation DSC setup was used to study of our samples. Here, the difference in flow rate of heat to (or rate of heat released from) the sample and the reference is measured during

heating (or cooling) of both of them simultaneously in controlled rate of temperature variation. The sample is kept in an aluminum crucible whereas the other reference aluminum crucible remains empty. During heating or cooling of both these crucibles, the rate of change of temperature is kept same for both of them.

The DSC thermogram of a sample gives the profile of the difference between the rates of heat flow to (or heat released from) the sample and the reference respectively during varying the temperature of both of these systems in same rate. During a first order phase transition of the sample, the rate of supplied (or released) heat to (or from) the sample varies continuously till its complete transition whereas the same remains constant for the reference in this period of transition. This variation gives rise to a transition peak in the corresponding DSC thermogram of the sample. The first order phase transitions can either be endothermic or exothermic. In these transitions, the necessary latent heat is absorbed and released from the sample respectively which gives rise to the corresponding endothermic and exothermic peaks in DSC thermograms.

The total area enclosed by an exothermic (or endothermic) peak within the temperature range from T_a to T_b gives the total heat released (or absorbed) by the sample during the corresponding phase transition. The DSC studies are performed at an environment of constant pressure on the samples. Therefore, the thermodynamic relations imply that the heat (dQ) supplied (or released) to (or from) the sample in changing its temperature by an amount dT is equal to the change in enthalpy (dH) of the sample. Therefore, the area under the transition peak is also equal to the total change of the enthalpy of the sample in the corresponding phase transition as given in the following relation.

$$\Delta H = \int_{T_a}^{T_b} \left(\frac{dH}{dT}\right)_p dT = \int_{T_a}^{T_b} \left(\frac{dQ}{dT}\right)_p dT = \Delta Q \tag{2.4}$$

Here p denotes pressure. The specific enthalpy during first order phase transition of a sample is calculated from the ratio of measured enthalpy and the weight of the studied sample.

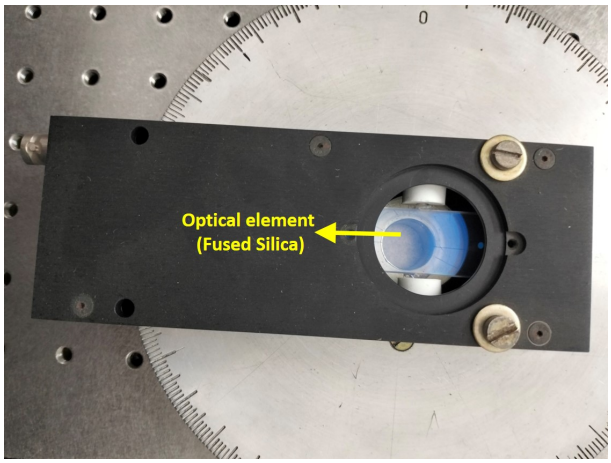


Figure 2.11: The optical head of photo elastic modulator [PEM 100, Hinds instrument].

METTLER TOLEDO DSC 3 machine was used to acquire the DSC thermograms of our samples. The lowest and highest limits of the range of temperature variation in this machine are -40°C and 600°C respectively. The rate of heating or cooling the sample in this setup can be varied from 0.01°C/minute to 200°C/minute. The resolution of the flow rate of heat in this setup is 0.05 mJ/sec.

2.8 Linear retardation measurement setup using photo elastic modulator

2.8.1 Photo elastic modulator (PEM)

Photo elastic modulator is a resonant polarization modulator of light passing through it. In this device the mechanism of photo elastic effect is used to modulate linear retardation of an optical element. We have used (Model PEM 100, Hinds instrument) photo elastic modulator in our setup. In this device a rectangular fused silica bar is used as the optical element which is softly bonded with a quartz transducer. This optical element is transparent in visible wavelength range and optically isotropic in stress free condition. This optical element acquires linear optical birefringence when a strain is induced into it. The quartz transducer attached with this optical element transforms the ac electrical signal to a periodic mechanical distortion with

a frequency of 50 KHz. It is equal to the fundamental frequency of mechanical distortion of the optical element. Hence the oscillation of the transducer establishes a distortion in optical element at its fundamental frequency. As a consequence of this, an induced sinusoidal strain in the optical element leads to a sinusoidal variation of linear retardation in the optical element. The maximum amplitude of sinusoidal modulation of optical path difference is called peak retardation. The peak retardation in our setup can reach upto quarter wave for 170 nm to 2 μm wavelength range and half wave for 170 nm to 1 μm wavelength range.

2.8.2 Linear retardation measurement setup

A He-Ne laser beam (5 mW) with wavelength 633 nm was used for this setup. The beam first passes through a Glan-Thomson polariser with a pass axis at 0° orientation. After that the beam passes through the photo elastic modulator (PEM) with its axis set at an angle of 45° to the polariser. The beam then falls on the sample normally and passes through it. The sample is kept in such a way that the major axis of the effective index ellipse is at ±45° to the polariser. After passing through the sample, the beam falls on the Glan-Thomson analyser with the pass axis perpendicular to that of the initial polariser. The laser beam after the analyser, falls on a photo diode where the optical signal transforms to the electrical signal. This electrical signal contains both ac and dc parts. The ac signal is separated from the dc signal by a signal controlling unit (SCU 100, Hinds instrument) and sent to the lock-in amplifier (SR 830). The rms amplitude of the ac signal corresponding to the first and second harmonics is measured by the lock-in amplifier which is fed with a reference signal of 50 KHz frequency from the PEM controller. This is also the frequency of modulation of birefringence in the PEM. The ratio of the rms amplitudes gives the retardation of the sample. The whole setup is shown schematically in fig. 2.12.

The intensity at photo diode is calculated by using Jones calculus. The Jones matrix corresponding to the polariser with 0° orientation of its pass axis is $P =$

$\begin{pmatrix} 1 & 0 \\ 0 & 0 \end{pmatrix}$. The Jones matrix corresponding to the analyser with 90° orientation of its pass axis is $A = \begin{pmatrix} 0 & 0 \\ 0 & 1 \end{pmatrix}$. Now the Jones matrix for a linear retardation plate with 0° orientation of its slow axis is $\begin{pmatrix} e^{-i(\delta/2)} & 0 \\ 0 & e^{i(\delta/2)} \end{pmatrix}$. Here, $\delta = (2\pi/\lambda)(n_e - n_o)d$ is the phase difference introduced by the retarder where n_e and n_o are the refractive indices encountered by e-ray and o-ray respectively on normal incidence of light to the retardation plate. Therefore $(n_e - n_o)$ is the birefringence of the retardation plate in case of normal incidence of light. The thickness of this plate is d and λ is the wavelength of the light passing through it. When this slow axis makes a positive angle ρ to the polariser, then the Jones matrix for the retarder becomes,

$$\begin{pmatrix} cos\rho & -sin\rho \\ sin\rho & cos\rho \end{pmatrix} \begin{pmatrix} e^{-i(\delta/2)} & 0 \\ 0 & e^{i(\delta/2)} \end{pmatrix} \begin{pmatrix} cos\rho & sin\rho \\ -sin\rho & cos\rho \end{pmatrix}$$

$$= \begin{pmatrix} cos^2\rho\ e^{-i(\delta/2)} + sin^2\rho\ e^{i(\delta/2)} & sin\rho\ cos\rho\ (e^{-i(\delta/2)} - e^{i(\delta/2)}) \\ sin\rho\ cos\rho\ (e^{-i(\delta/2)} - e^{i(\delta/2)}) & sin^2\rho\ e^{-i(\delta/2)} + cos^2\rho\ e^{i(\delta/2)} \end{pmatrix} \tag{2.5}$$

where $\begin{pmatrix} cos\rho & sin\rho \\ -sin\rho & cos\rho \end{pmatrix}$ is the rotational matrix.

Now for PEM, $\rho = 45°$ and the retardation is being modulated as $\delta = \delta_R = \delta_R^0 sin(\omega t)$. Here, δ_R^0 and ω are the peak retardation and frequency of modulation of retardation in the PEM. Hence the Zones matrix for PEM as calculated from eqn. 2.5 is,

$$M = \begin{pmatrix} cos(\delta_R/2) & -isin(\delta_R/2) \\ -isin(\delta_R/2) & cos(\delta_R/2) \end{pmatrix} \tag{2.6}$$

The normally incident laser beam on the sample encounters the index ellipse perpendicular to its direction of propagation. Therefore, for an effective birefringence δ and an orientation angle ρ of the major axis of index ellipse, the Jones matrix

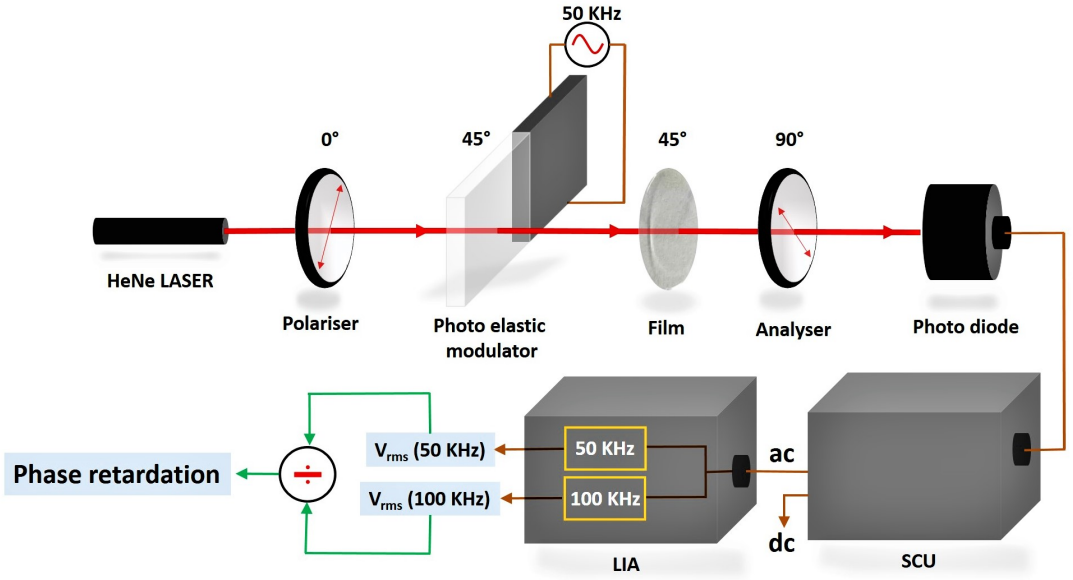


Figure 2.12: The schematic diagram of linear birefringence measurement setup.

corresponding to the sample is,

$$S = \begin{pmatrix} cos^2\rho\ e^{-i(\delta/2)} + sin^2\rho\ e^{i(\delta/2)} & sin\rho\ cos\rho\ (e^{-i(\delta/2)} - e^{i(\delta/2)}) \\ sin\rho\ cos\rho\ (e^{-i(\delta/2)} - e^{i(\delta/2)}) & sin^2\rho\ e^{-i(\delta/2)} + cos^2\rho\ e^{i(\delta/2)} \end{pmatrix} \tag{2.7}$$

The laser beam after passing through the polariser becomes linearly polarised and the Jones vector corresponding to this polarised light beam is, $J = \begin{pmatrix} E_x \\ 0 \end{pmatrix}$, where E_x is the component of electric vector of the polarised light parallel to the polariser.

The laser beam after polariser is passing through the PEM, sample and analyzer respectively before falling on the photodiode. Hence the Jones vector representing light at photodiode is,

$$J_{final} = A\ S\ M\ J \tag{2.8}$$

This matrix multiplication ultimately gives, $J_{final} = \begin{pmatrix} E_x^{final} \\ E_y^{final} \end{pmatrix}$, where

$E_x^{final} = 0$,

$E_y^{final} = -iE_x \times [cos(\delta_R/2) \times sin(2\rho) \times sin(\delta/2) + sin(\delta_R/2)\{sin^2\rho\, e^{-i(\delta/2)} + cos^2\rho\, e^{i(\delta/2)}\}]$.

Hence the intensity of the light falling on the photodiode is,

$$I = J_{final}^{\dagger}\ J_{final} \tag{2.9}$$

or,

$$\boxed{I = I_0[cos(\delta_R) \times sin^2(2\delta) \times sin^2(\delta/2) + sin^2(\delta_R/2) + \frac{1}{2}sin(\delta_R) \times sin(\delta) \times sin(2\rho)]} \tag{2.10}$$

The light intensity as given in eqn. 2.10 falls on the photodiode and produces a voltage signal as given in the following equation,

$$\boxed{V = V_0[cos(\delta_R) \times sin^2(2\delta) \times sin^2(\delta/2) + sin^2(\delta_R/2) + \frac{1}{2}sin(\delta_R) \times sin(\delta) \times sin(2\rho)]} \tag{2.11}$$

The magnitude of dc component, the coefficient of 1st and 2nd harmonics of the voltage signal after expressing the eqn. 2.11 in Fourier series are given as follows,

dc signal:

$$(V_0/2)[1 + J_0(\delta_0^R)\{2sin^2(2\rho) \times sin^2(\delta/2) - 1\}] \tag{2.12}$$

Coefficient of 1st harmonic:

$$V_0[J_1(\delta_0^R) \times sin(\delta) \times sin(2\rho)] \tag{2.13}$$

Coefficient of 2nd harmonic:

$$V_0[J_2(\delta_0^R)\{1 - 2sin^2(2\rho) \times sin^2(\delta/2)\}] \tag{2.14}$$

where $J_0(\delta_0^R)$, $J_1(\delta_0^R)$ and $J_2(\delta_0^R)$ are the Bessel functions of first kind. The peak retardation δ_0^R of the PEM for 633 nm wavelength is kept at 2.405 radians. Hence $J_0(\delta_0^R) = 0, J_1(\delta_0^R) = 0.5191,\ J_2(\delta_0^R) = 0.4317$. The effective major index on the

plane of starch film studied in this thesis was along -45° to the polariser, therefore ρ = -45°. So, the amplitude of the first and second harmonic signals will be modified as,

$$V_{1f} = sin\delta \times 0.5191 \times V_0 \tag{2.15}$$

and

$$V_{2f} = cos\delta \times 0.4317 \times V_0 \tag{2.16}$$

Hence,

$$\boxed{tan\delta = \frac{0.4317}{0.5191} \times \frac{V_{1f}}{V_{2f}}} \tag{2.17}$$

Now in the lock-in amplifier (SR830), the rms voltage corresponding to the different harmonics is measured. As δ is measured from the ratio of the amplitudes of the first and second harmonics as given in eqn. 2.17, therefore the relation will remain same even for the ratio of rms amplitudes of the voltage signals corresponding to the first and second harmonics. Hence,

$$\boxed{tan\delta = \frac{0.4317}{0.5191} \times \frac{V_{rms}^{1f}}{V_{rms}^{2f}}} \tag{2.18}$$

where V_{rms}^{1f} and V_{rms}^{2f} are the rms amplitudes of first and second harmonics.

2.9 Impedance analysis of samples

Pure liquid crystals are generally dielectric materials with very high resistivity. But the synthesized liquid crystal samples often contain some ionic impurities which make them not perfect dielectric. Therefore, the liquid crystal cells filled with the sample can be considered as a capacitor with capacitance C_s) and a resistor with resistance R_s in parallel as shown in fig. 2.13. The size of the effective electrode area in these cells is generally 5–10 mm and the thickness of these cells is about 5–20 μm. To measure the impedance of these filled cells, it is connected in series with a known resistance R_m = 1 kΩ. The end points of this circuit is connected with the output of the ac power supply from the lock-in amplifier (Stanford Research System, model

no. SR830). The frequency (ω) and rms amplitude (V_0) of the applied ac voltage are set to 5641 Hz and 0.5 volt respectively.

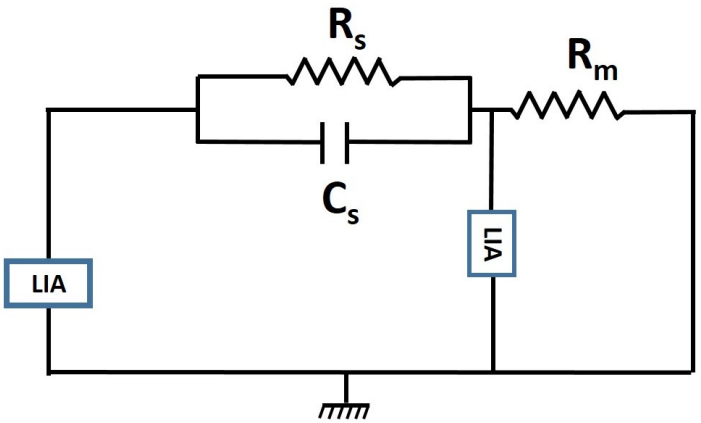


Figure 2.13: The schematic diagram of the dielectric measurement setup.

The impedance of the cell is,

$$Z_s = \frac{R_s(1 - j\omega C_s R_s)}{(1 + \omega^2 C_s^2 R_s^2)} \tag{2.19}$$

So, the total impedance including the series resistance R_m is,

$$Z_T = Z_s + R_m = \frac{R_s(1 - j\omega C_s R_s)}{(1 + \omega^2 C_s^2 R_s^2)} + R_m \tag{2.20}$$

Therefore, the total current supplied by the source is,

$$I_T = \frac{V_0 e^{i(\omega t + \phi_0)}}{Z_T} \tag{2.21}$$

where ϕ_0 is the phase of the applied voltage. So, the measured voltage across R_m is

$$V_m = R_m \times I_T \tag{2.22}$$

After using the relations in eqn. 2.20 and eqn. 2.21 in eqn. 2.22, V_m becomes,

$$V_m = \frac{R_m(1 + \omega^2 C_s^2 R_s^2) V_0 e^{i(\omega t + \phi_0)}}{R_m + R_s + \omega^2 C_s^2 R_s^2 R_m - j\omega C_s R_s^2} \tag{2.23}$$

Here V_m is a complex quantity. Hence, comparing the real part and the imaginary part of the both sides of the eqn. 2.23, the following relations can be found.

$$V_m^0 cos(\omega t+\phi_m) = \frac{V_0 R_m[\{R_s + R_m + \omega^2 C_s^2 R_s^2 R_m\}cos(\omega t + \phi_0) - \omega C_s R_s^2 sin(\omega t + \phi_0)]}{(R_s + R_m)^2 + R_m^2 R_s^2 C_s^2 \omega^2} \tag{2.24}$$

and

$$V_m^0 sin(\omega t+\phi_m) = \frac{V_0 R_m[\omega C_s R_s^2 cos(\omega t + \phi_0) + \{R_s + R_m + \omega^2 C_s^2 R_s^2 R_m\}sin(\omega t + \phi_0)]}{(R_s + R_m)^2 + R_m^2 R_s^2 C_s^2 \omega^2} \tag{2.25}$$

where, ϕ_m and V_m^0 are the absolute phase and rms amplitude of the measured signal across R_m respectively. After solving eqn. 2.24 and eqn. 2.25, one can find that

$$\boxed{R_s = R_m \left[\frac{(V_m^0 - V_0)(V_m^0 + V_0)}{V_m^0\{V_m^0 - V_0 cos(\phi_m - \phi_0)\}} - 2\right]} \tag{2.26}$$

and

$$\boxed{C_s = \left[\frac{V_m^0 V_0 sin(\phi_m - \phi_0)}{R_m \omega\{{V_m^0}^2 + {V_0}^2 - 2V_m^0 V_0 cos(\phi_m - \phi_0)\}}\right]} \tag{2.27}$$

The amplitude (V_m^0) and phase difference ($\phi_m - \phi_0$) of the voltage drop across the resistance R_m are measured by the same lock-in amplifier (SR830). The whole experimental setup is automated by interfacing it with a personal computer using LabVIEW software.

The dielectric constant of the sample inside the cell is measured by taking the ratio of filled cell capacitance (C_s) and empty cell capacitance (C_0). On the other hand, the conductivity of the samples is measured from the relation,

$$\sigma = \frac{d}{R_s \times A} \tag{2.28}$$

where d is the sample thickness and A is the effective area of electrode. To study the temperature variation of impedance of samples, a microscope hot stage (Instec) is used where the temperature variation of the samples is performed in a controlled way. The resolution of temperature measurement in this hot stage is 0.1°C.

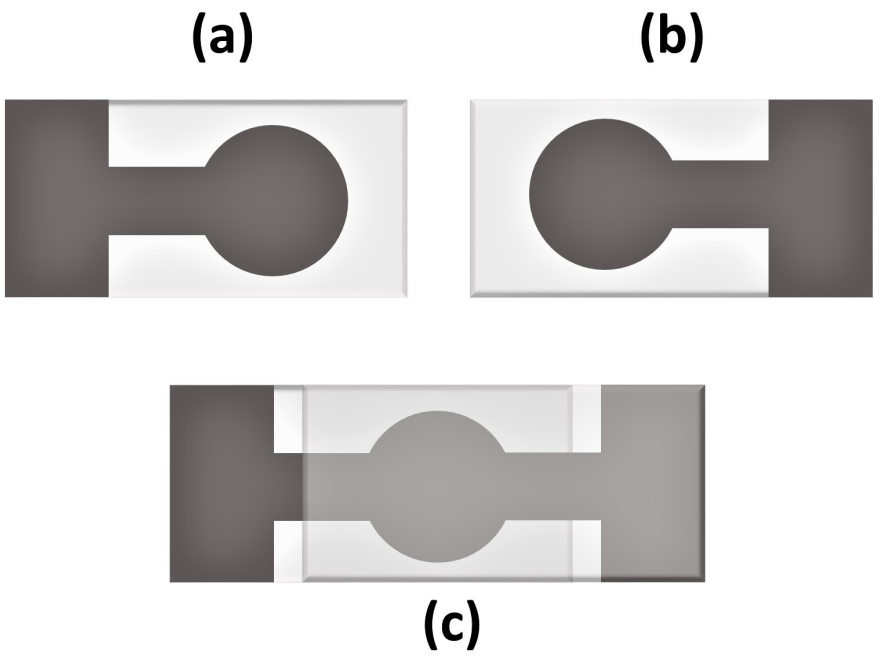


Figure 2.14: (a) and (b) The etched ITO plates. (c) The liquid crystal cell formed by the etched plates.

2.10 Making of Liquid crystal cells

The liquid crystal cells are made of two ITO coated glass plates. A circular pattern of ITO coating is formed by etching on both plates to get an active electrode area of diameter 8 mm (see fig. 2.14). Sometimes rectangular pattern of electrodes are also used. The etched glass plates are glued together using an epoxy glue with a small gap between the plates. The ITO electrodes are on the inside surface of the cell and also the effective electrode areas are overlapping on each other. The cells are cured at 150°C for one and half hours after the glue is applied at the side edges of the plates. The thickness of the empty cells is measured by an interferometric technique using Ocean optics spectrometer. The empty capacitance of cell is measured before filling the cell with the sample. After that the cells are filled with the sample in its isotropic phase by capillary action. In these cells with parallel electrodes, the empty capacitance is,

$$C_0 = \frac{\epsilon_0 A}{d} \tag{2.29}$$

where ϵ_0 is the dielectric constant of the cell without sample, A and d are the effective electrode area and the distance between them respectively. This relation is only valid when the electrode diameter is large compared to the sample thickness d. After filling the sample, the capacitance of the cell becomes,

$$C_s = \frac{\epsilon_0 \epsilon_r A}{d} \tag{2.30}$$

where ϵ_r is the dielectric constant of the sample. After measuring capacitance of the cell before and after filling it with the sample, the dielectric constant of the sample can be determined as,

$$\epsilon_r = \frac{C_s}{C_0} \tag{2.31}$$

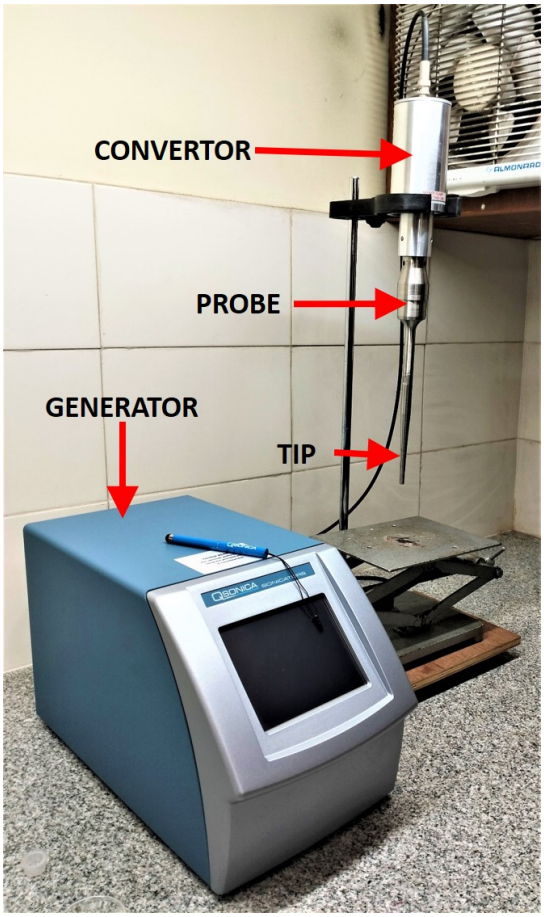


Figure 2.15: The probe sonicator.

2.11 Probe sonicator

The probe sonicator transforms the electrical signal to the mechanical vibration. The whole machine is divided into three parts and these are generator, converter and probe (see fig. 2.15). The generator transforms the supplied ac line power (220 volt rms amplitude, 50 Hz) to an electrical signal of 20 KHz frequency. The converter as a transducer transforms the 20 KHz ac signal to the mechanical vibration with same frequency. This vibration is transferred to the probe attached with the transducer. A tip which is attached down to the probe vibrates longitudinally with the same frequency as supplied by the converter.

The tip of the sonicator is dipped into the liquid samples. The longitudinal vibration of the tip produces a periodic cycle of compression and rarefaction in liquids which causes cavitation into it. During rarefaction, a large number of micro-voids are generated inside the liquid samples. These micro-voids are called cavitation bubbles. During compression in liquids, these micro-bubbles collapse and release tremendous energy in the cavitation field which drives the mechanism of fluid processing.

The effect of sonication depends on diameter of tip, volume of sample, shape of sample container, amplitude of vibration of the tip and sample temperature. The tips with lesser diameter deliver high intensity of sonication for a given percentage of its amplitude of vibration, although the corresponding field of cavitation covers lesser volume of the sample down to the tip. The diameter of the sample container should be less such that the sample should not escape far from the tip during sonication. The intensity of sonication increases with increasing the amplitude of vibration of the tip which is controlled from the generator of this setup. More amplitude of vibration of the tip enhances the sample temperature during sonication which increases the possibility of degradation of samples. Moreover, increasing the temperature of sample enhances vapor pressure. Therefore, more vapor occupies the volume of micro-cavities which blast less violently during liquid compression. This reduces the the efficiency of sonication. To reduce these difficulties, the sample

container is advised to keep in a heat sink during sonication. In addition, the pulsed mode of vibration is also suggested rather than a continuous mode of vibration in the probe sonication.

The Qsonica sonicator (QSONICA 700) was used to sonicate the gelatinized starch solutions as discussed in chapter 5. The microtips with 6 mm diameter were used for sonication. The amplitude of vibration was always kept at 40%. The sonication was performed on samples in pulse mode of vibration to control the temperature of samples.

Chapter 3

Crystal polymorphism in 8OCB

3.1 Introduction

Molecules having strong electric dipole moment can exhibit rich variety of phases on changing the temperature. The long range dipole-dipole interactions between the molecules compared to the van der Waals interactions play important role in stabilizing different phases. The strong dipolar association contributes to the complexity in the self-organisation of the molecules giving rise to interesting physical properties in their liquid and solid phases [81, 82]. In the last few decades different phases of dipolar nOCB liquid crystal homologs (see fig. 3.1) have been investigated where n denotes the number of carbon atoms in the terminal aliphatic chain attached to one end of the biphenyl core of the molecule [1, 2, 11, 12, 83–85]. These rod-like molecules have strong dipole moment along their long axis due to the presence of the nitrile (CN) group attached to the other end of the biphenyl core of each molecule [1]. In this family of liquid crystals, the compounds 8OCB (4´-octyloxy-4-cyanobiphenyl) and 9OCB (4´-nonyloxy-4-cyanobiphenyl) with intermediate chain length show both smectic A and nematic phases. The lower homologs exhibit only nematic and higher homologs exhibit only smectic A phase [4]. In the smectic A phase, the rod-like molecules are arranged in layers with their long axes on average parallel to the layer normal and the layer spacing is same as the molecular length (l) [7]. But the nOCB homologues exhibit an intercalated smectic A (SmA_d) phase with layer spacing as $1.4l$ [1, 12, 85]. Moreover at higher pressure and in mixtures of different homologous compounds, a remarkable reentrance phenomena with reentrant nematic phase has been observed [1, 2, 11]. The intercalated nature

of smectic A phase and the reentrant phenomena thought to arise from the strong dipolar association of the molecules forming dynamic pairs in their liquid crystalline phases [1, 12].

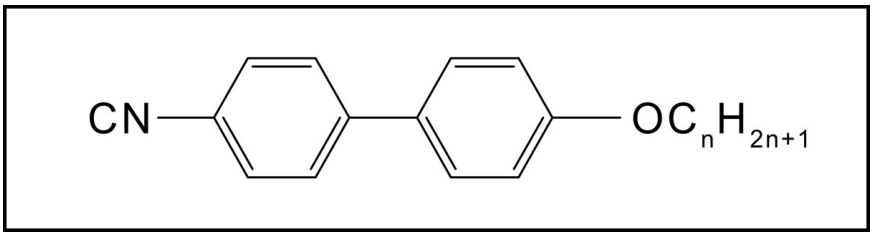


Figure 3.1: nOCB molecule.

Interestingly these nOCB liquid crystals also exhibit various stable and metastable crystalline phases [4, 5, 13, 18, 86, 87]. Hori *et al.* first observed three different metastable crystal polymorph of 8OCB grown from its solution and these phases were square-plate, needle phase and long parallelepiped (PP) phase respectively [4]. They found that the square-plate phase was too unstable to probe experimentally. With the help of X-ray diffraction studies, it has been shown that the needle and PP metastable phases have triclinic and monoclinic lattice structures respectively. The lattice parameters for needle phase are $a = 12.71$ Å, $b = 20.41$ Å, $c = 7.32$ Å, $\alpha = 99.86°$, $\beta = 99.44°$, $\gamma = 92.55°$. On the other hand, the lattice parameters for the PP phase are $a = 8.55$ Å, $b = 36.14$ Å, $c = 5.85$ Å, $\beta = 95.09°$. The molecules in the needle phase form tetramers by CN...CN interaction whereas the CN...biphenyl intermolecular interaction plays dominant role in stabilising the monoclinic crystal structure of the PP phase. In addition to these metastable crystal phases, 8OCB has a stable crystal phase which is known as commercial powder (CP) phase. The lattice structure of the CP phase is monoclinic with $a = 30.56 - 30.62$ Å, $b = 7.39 - 7.44$ Å, $c = 25.43 - 25.52$ Å, $\beta = 107.3° - 107.8°$, but the detail molecular arrangement is still not well understood [83, 88]. Most of the previous studies on stable and metastable crystal phases of 8OCB were carried out on solution crystallised samples. Jackli *et al.* studied a metastable crystal state of 8OCB obtained by cooling the sample from its melt and identified the observed metastable phase as needle crystal phase [15]. After that the temperature variation of dielectric constant of a metastable state of

8OCB doped with graphene nano platelets has been reported [89]. Recently, a glassy state of 8OCB on fast cooling of the sample from its melt has been observed [90].

Though a large number of studies on the liquid crystalline phases of nOCB molecules have been reported, relatively few studies are performed on the solid phases of this system. In this chapter, we report detail experimental studies on the different crystal polymorph of 8OCB obtained by cooling the sample from its melt. We identify the metastable crystal state often found in our sample as PP phase which transforms to stable CP phase on aging at room temperature or by heating it above 312 K. Based on our experimental results, we have found that the stable CP crystal phase of 8OCB is a heterogeneous phase with the coexistence of fibrillar nano crystallites embedded in an amorphous phase. In this chapter we also discuss that this amorphous phase melts first during heating which causes a pre-transitional phenomenon before complete melting of stable CP phase. The existence of various metastable crystal phases and a heterogeneous phase as the stable ground state show remarkable complexity of the free energy landscape for this type of pure compound consisting of relatively small rod-like molecules with strong dipole moment along their long axis.

3.2 Experimental Detail

3.2.1 Sample Description

Here, we have studied the crystal polymorphism of 4´-octyloxy-4-cyanobiphenyl (abbreviated as 8OCB) thermotropic liquid crystal compound. It contains molecules with polar cyanobiphenyl head group attached with an aliphatic tail through an oxygen atom. The molecular structure is given in fig. 3.2. The dipole moment of each molecule and the molecular weight of this compound are 3.5 debye and 307.434 respectively [1]. The compound melts at 327.5 K to smectic A phase. Further heating transforms the smectic A phase to nematic and then isotropic phase at 340 K and 353 K respectively. On cooling, the sample shows a large supercooling

effect ($\approx 30-35$ K) during smectic A to crystal transition. The detail XRD studies performed on the smectic A phase reveal that the layer spacing is 31.7Å as shown in fig. 3.2. However, The reported molecular length of this compound is 24 Å [1]. Based on these observations, an intercalated organization of molecules (see inset of fig. 3.2) in the layer have been proposed by Cladis *et al.* [1]. The polar molecules form dynamic intercalated pairs in their liquid crystal phases giving rise to layer thickness as 31.7 Å in smectic A phase as shown in fig. 3.2.

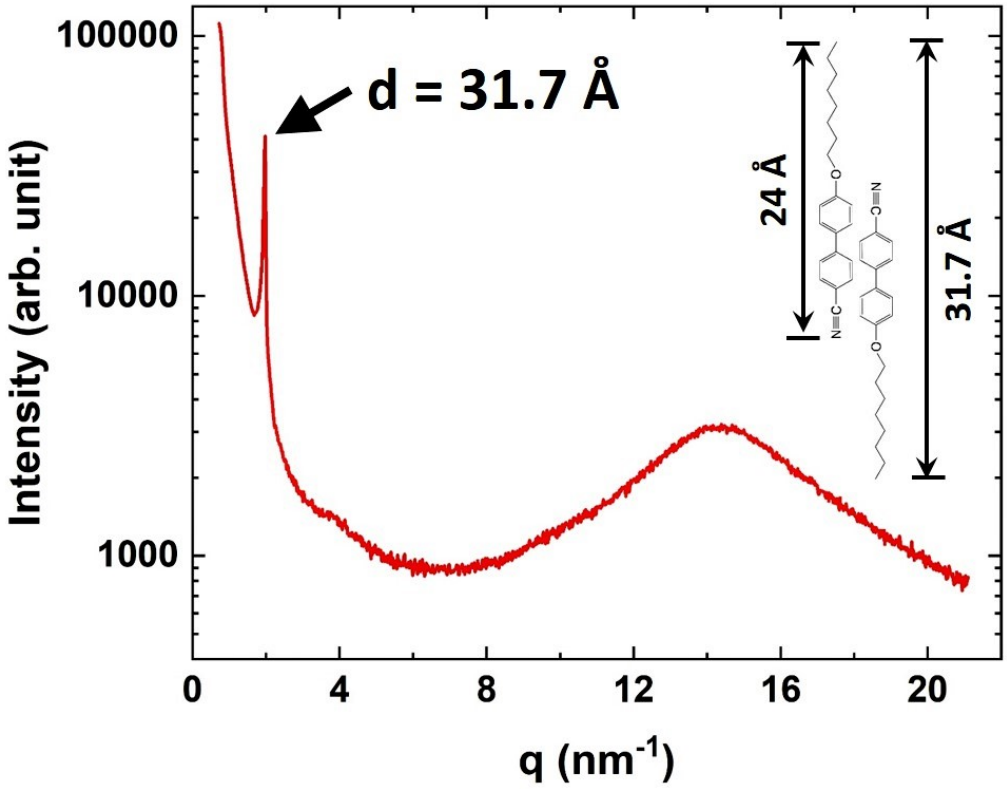


Figure 3.2: XRD profile in smectic A phase of 8OCB.

3.2.2 Sample preparation

The commercially available liquid crystalline sample 4´-Octyloxy-4-cyanobiphenyl (8OCB) was used in all the experimental studies. Sample sandwiched between two cleaned coverslips was used for Raman Spectroscopy (RS) and polarised optical microscopy (POM) studies. A coverslip was heated to 373 K by keeping it on a

hot stage and then small amount of 8OCB sample was placed on it. The sample transformed to isotropic state at that temperature. Then another coverslip was carefully placed on top of the sample. The sample sandwiched between the coverslips was then allowed to cool to obtain different crystal polymorph. Raman spectra were obtained using laser micro-Raman spectrometer (Jabin-Yvon T64000) equipped with a microscope hot stage and a temperature controller (Linkam T95). The Raman signal from the back scattered light was detected using cooled CCD camera. Prior to taking the Raman spectra of the sample, the spectrometer was calibrated using 520.7 cm^{-1} line of silicon. The POM studies of the sample were carried out on a polarized optical microscope (Olympus BX 50) equipped with a hot stage (Linkam).

X-ray diffraction (XRD) studies were performed on samples filled in Lindemann capillaries (outer diameter 1.0 mm) with CuK_α radiation of wavelength 1.54 Å using DY 1042-Empyrean (PANalytical) x-ray diffractometer comprising a programmable divergence slit and PIXcel 3D detector. For grazing incidence studies, the crystal phase was formed on a coverslip and the identity of the phase was confirmed by POM studies. The sample was then scrapped off from the coverslip and placed on the silicon flat stage attached with the x-ray setup. The silicon flat stage was used as its XRD profile gives a flat background and does not interfere with sample's profile. Small-angle x-ray scattering (SAXS) studies were performed using a HECUS S3 Microsystem fitted with a copper anode x-ray generator (Genix) and a 1D position-sensitive detector. The sample was taken in Lindemann capillary tube (outer diameter 1.0 mm). A Peltier-controlled stainless steel holder was used to maintain the sample temperature.

Field Emission Scanning Electron Microscopy (FESEM) studies were performed by using CARL ZEISS (ULTRA PLUS model) system to probe the surface morphology of the samples. For FESEM studies, a small amount of sample was kept on a cleaned thin aluminium foil and it was cooled to the desired phases from its isotropic phase. Sometimes the indium tin oxide (ITO) coated glass plates were used as substrate for visibility of the sample under microscope. The sample was then coated

with platinum [QUORUM (Q150R S)] to probe the surface morphology.

The dielectric measurements in metastable crystalline state were performed by using home made liquid crystal (LC) cells. The LC cells were made by using clean ITO coated glass plates with a circular electrode area of diameter 8 mm. For probing the dielectric constant of stable crystal phase, commercially available LC cells (INSTEC Inc.) of sample thickness 9 μm were also used. The sample was filled in the LC cells in its isotropic state by capillary action using a hot stage. The measurements of dielectric constant as a function of temperature were performed on a homemade experimental setup discussed in chapter 2. A sinusoidal ac voltage of frequency 5641 Hz and rms amplitude 0.5 volts was used for this measurement.

3.3 Results and Discussion

3.3.1 Polarising Optical Microscopy (POM) Study

The POM studies of the sample were carried out on a polarized optical microscope (Olympus BX 50) equipped with a Linkam hot stage (LTS420E) controlled by Linkam T95 controller. Two types of crystal phases of 8OCB were most often observed on cooling the sample from its melt. One of them was the stable commercial powder or CP crystal phase. The other phase was the long parallelepiped or PP crystal phase which transformed irreversibly to the CP crystal phase at higher temperature or even at room temperature after few days. Hence the PP crystal phase is metastable in nature. The POM textures of the CP phase and the PP phase are shown in fig. 3.3a and fig. 3.3b respectively.

The stable CP crystal phase grew from its melt as spherulites and showed a nonuniform grainy texture (fig. 3.3a) between crossed polarisers. The nonuniform texture indicates the presence of many submicroscopic domains coexisting in this phase. The metastable PP phase grew from its melt as flat strips with a smooth homogeneous texture (fig. 3.3b). Interestingly, the growing front edge of a strip was found to be tilted with respect to the growth direction by an acute angle of about

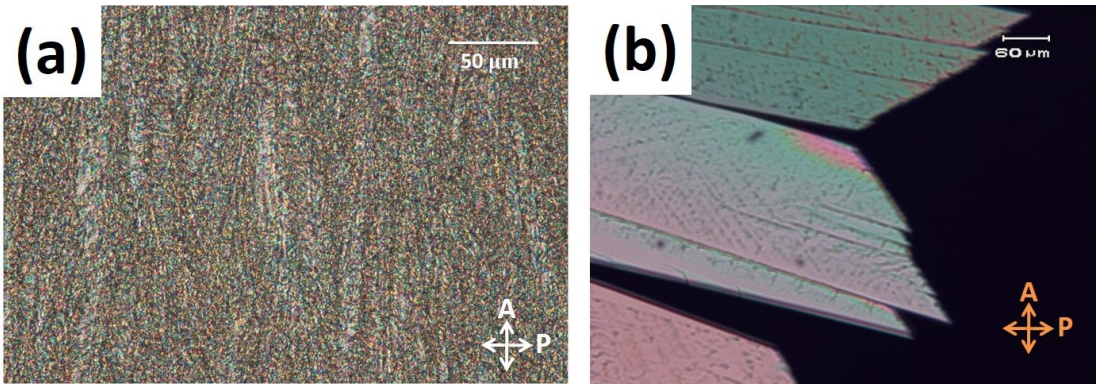


Figure 3.3: The POM textures of (a) the stable CP phase and (b) PP phase growing from smectic A phase of 8OCB.

±40°. When a strip was rotated by 360° between crossed polarisers, four extinction positions with a difference of 90° were always found. This indicates that a strip of PP phase has an uniform orientational order. The uniform extinction of a strip occurred when its front edge was made parallel or perpendicular to the polariser axis. It implies that the major or minor axis of the effective refractive index ellipse is parallel to the front edge of the strip. The POM studies using a λ-plate were performed to determine the direction of the major axis of this refractive index ellipse within a strip of PP phase. The used λ-plate was a positive birefringent crystal plate with a known direction of its slow axis. A sample strip of lower thickness with the birefringence colour in first order region of Levy chart (see fig. 3.4) was chosen for this purpose to clearly identify the colour changes of the sample on inserting the λ-plate in the light path. The strip was kept at its brightest positions at angle ±45° respectively with respect to one of its four extinction positions i.e. the front edge of the strip was making angle ±45° respectively with respect to the polariser. At these two brightest positions, the colour variations of the strip were noticed (see fig. 3.4b and fig. 3.4c) by introducing the λ-plate in the optical path of the microscope. When front edge of the strip was parallel to the slow axis of the λ-plate, the strip appeared blue (fig. 3.4b) indicating the effective addition of optical path differences between the ordinary and extraordinary rays on passing through the sample and the λ-plate. On the other hand, when the front edge of the strip was perpendicular to the slow axis of λ-plate then the strip appeared dark yellow (fig. 3.4c) due to the effective

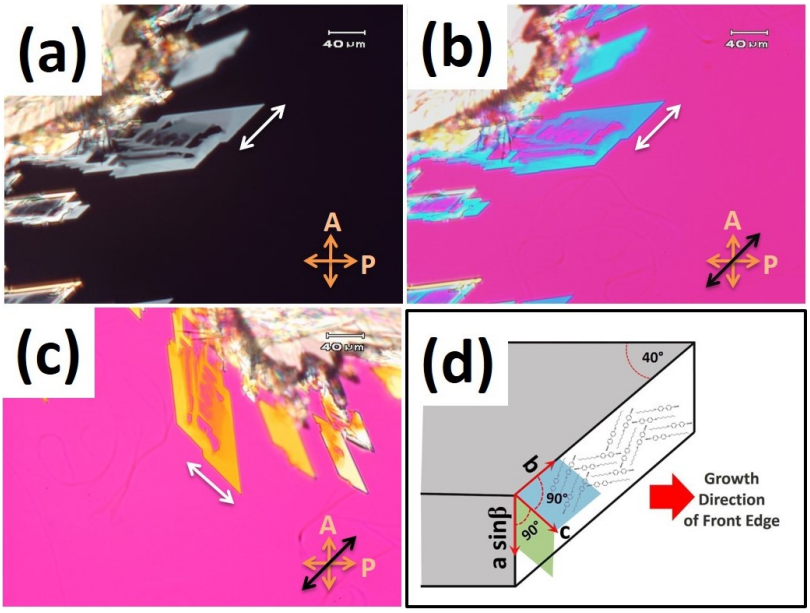


Figure 3.4: The POM textures of a strip of PP phase between crossed polarisers (a) without λ-plate (b) with the slow axis of the λ-plate parallel to the front edge and (c) with the slow axis of the λ-plate perpendicular to the front edge. The white double headed arrow indicates the major axis of the effective refractive index ellipse within the strip. (d) The schematic representation of the molecular organisation within the strip.

subtraction of these optical path differences. These observations illustrate that the effective refractive index parallel to the front edge (white double headed arrow in fig. 3.4) of the PP strip is larger than that perpendicular to the growing front plane of the strip.

Fig. 3.4d shows a possible schematic organisation of the 8OCB molecules within the strip taking into account the reported monoclinic lattice structure of the PP phase [4]. The b-axis of the monoclinic lattice having maximum component of the refractive index is parallel to the front edge of the strip while the c-axis is perpendicular to the growing front plane. The molecules lie parallel to this front plane of the growing strip as shown in fig. 3.4d. This organisation of the molecules can account for slightly higher birefringence of PP phase compared to that of smectic A phase in a planner aligned sample. This model also perhaps explain slightly higher dielectric constant of PP phase in a non-aligned liquid crystal cells compared to that in the CP crystal phase as discussed later.

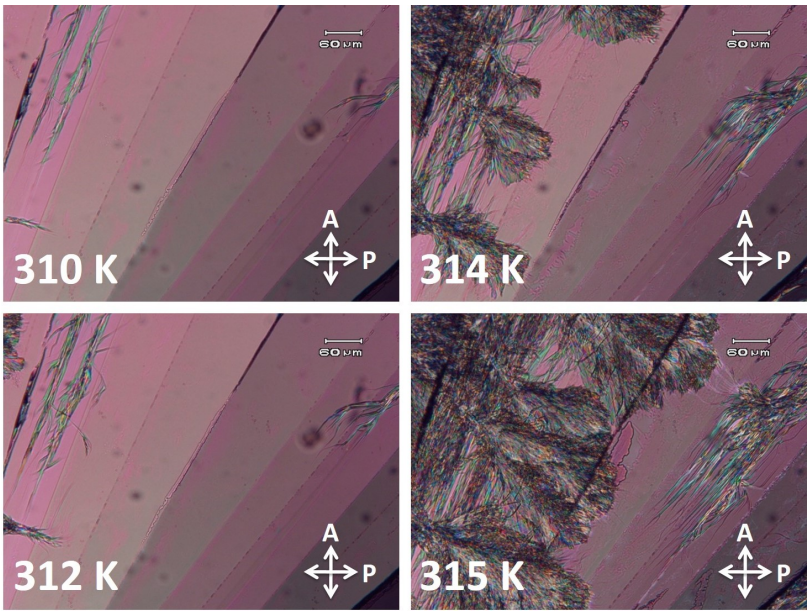


Figure 3.5: The POM textures showing the transformation of PP phase to CP phase with increasing temperature.

The metastable PP phase transforms to the stable CP phase on increasing the temperature of the sample. Fig. 3.5 shows the POM textures of the growth of CP phase into the PP phase during heating it with 1 K/min rate. The CP phase appeared from the top left corner of the visible area of the sample at 312 K. This agrees with the reported transition temperature of solution crystallised PP phase of 8OCB [5]. Therefore, we conclude that the metastable phase observed in our sample on cooling from its melt is the PP phase.

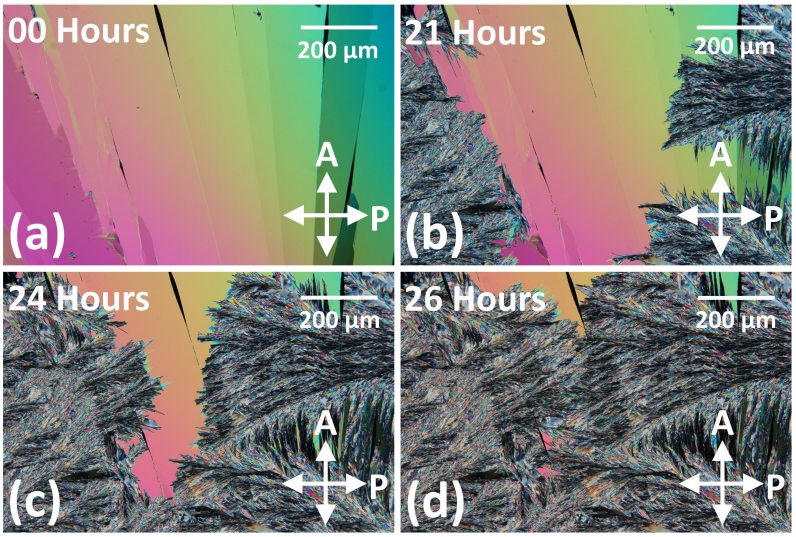


Figure 3.6: PP phase to CP phase transition with time.

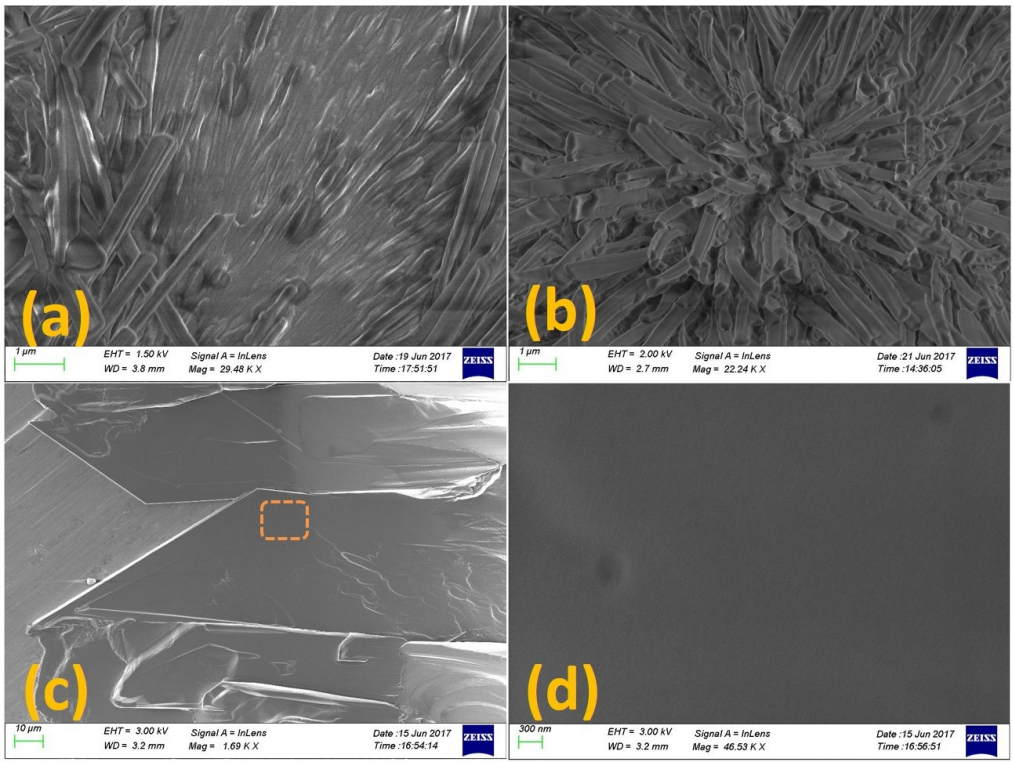


Figure 3.7: The SEM textures of (a) the CP phase, (b) the cross sectional view of the fibrillar nano crystallites in the CP phase and (c) PP phase. (d) shows the magnified view of the marked region of the PP phase in figure (c) indicating smooth homogeneous texture.

The metastable PP phase also transforms to CP phase at room temperature within few days. Fig. 3.6 shows this transition at different intervals of time. The transition mostly starts to occur from the grain boundaries between the strips.

3.3.2 Field Emission Scanning Electron Microscopy (FE-SEM) Study

Field Emission Scanning Electron Microscopy (FESEM) studies were performed by using CARL ZEISS (ULTRA PLUS model) system. The detail of this microscopic technique has been discussed in chapter 2. The FESEM studies were performed to investigate the structure of the crystalline phases of 8OCB at higher resolution. Fig. 3.7 shows the FESEM photomicrographs of the sample in these crystal phases. The FESEM texture of the CP phase (fig. 3.7a) shows the presence of numerous fibrillar nano crystallites embedded in an noncrystalline amorphous phase. Fig. 3.7b

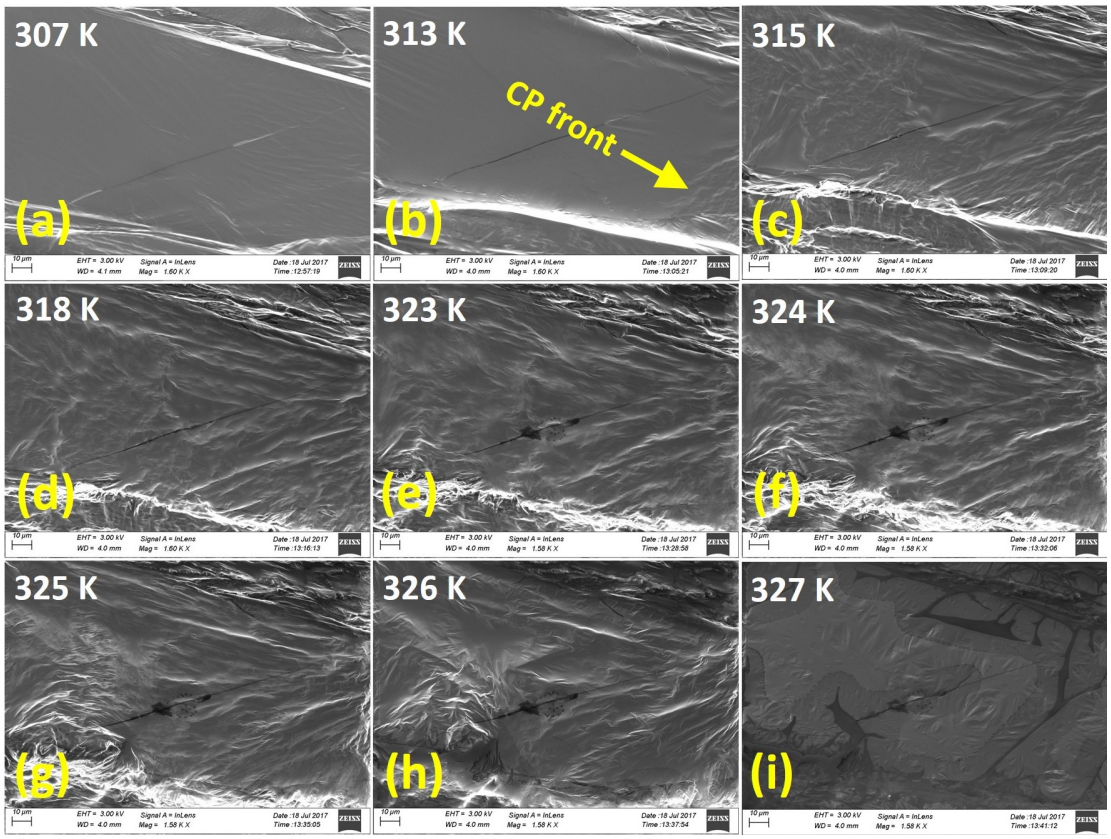


Figure 3.8: (a-i) The SEM textures at different temperature during heating the sample from PP phase.

shows the cross section of these nano crystallites in the transverse direction which appears either rectangular or elliptical in shape. The nano crystallites have long fibrillar shape of length $5 - 7$ μm and width about $100 - 400$ nm. Therefore, the FESEM studies clearly reveal that the stable CP crystal phase of 8OCB is a heterogeneous phase consisting of two sub-phases coexisting together.

Fig. 3.7c shows the FESEM texture of the PP phase. The sharp front edge of a strip in the PP phase with a 40° tilt to its growth direction is also clearly visible here. Fig. 3.7d shows the magnified view of the marked position in fig. 3.7c. The uniform FESEM texture of metastable PP phase indicates the homogeneity of this phase unlike the CP phase.

The POM studies discussed earlier reveal that the PP phase transforms to CP phase at 312 K. This transition was also verified by FESEM studies as shown in fig. 3.8. Fig. 3.8a shows the SEM texture of PP phase at 307 K. It transforms to CP phase at 313 K on heating the sample on the specimen stage of the SEM setup.

The growing front of CP phase has been marked in fig. 3.8b. Fig. 3.8c to 3.8i show the subsequent changes in the SEM textures of the CP phase during heating the sample till its melting at 327 K. The texture of the sample starts to change from 324 K (see fig. 3.8f) and the smectic domains become visible at 326 K as shown in fig. 3.8h. Fig. 3.8i shows the SEM textures of the sample after complete melting to the smectic A phase. Therefore SEM studies clearly show the pre-transitional effect of melting of the sample from the CP phase to the smectic A phase.

3.3.3 Dielectric Studies

Dielectric measurements on the sample were performed with increasing temperature to detect the various phase transitions as shown in fig. 3.9. In these measurements, the heating rate was always kept at 1 K/min. One advantage of our technique is that the state of the sample can be observed during the measurement of dielectric constant using POM. As 8OCB forms different stable and metastable crystal phases during cooling from its melt, this measurement technique enable us to ensure the state of the sample being probed using microscopic observations. Once the phase of the sample is formed inside the liquid crystal cell, it does not need to be displaced to other specimen stage for characterization unlike in DSC studies. Therefore, a disturbance free measurement of dielectric constant especially in metastable phases is possible in this setup. All the measurements were carried out during heating of the sample either from the metastable PP phase (see fig. 3.9a) or from stable CP phase (see fig. 3.9b). The transition from the PP phase to the CP phase at 312 K was clearly detected as shown in fig. 3.9a. A step decrease in dielectric constant is clearly visible at this transition (see inset in fig. 3.9a). On further heating, the melting transition from CP to smectic A phase at 327.5 K was observed which agrees with the reported melting point of solution crystallised CP phase [5]. Interestingly, a prominent pre-transitional effect in which the dielectric constant of the sample increasing continuously from 321 K was observed (see fig. 3.9). Further studies discussed in the coming sections of this chapter showed that this pre-transitional effect arose due to

the changes occurring in the heterogeneous CP phase in this temperature range. The amorphous component of the CP phase starts to transform below the melting point of the nano crystallites at 327.5 K giving rise to this pre-transitional behavior. The monotonic increase of the dielectric constant in the smectic A phase above 327.5 K on heating was due to the gradual change from planner to homeotropic alignment of molecules in the LC cells. The dielectric constant parallel to the director in the homeotropic configuration is much larger than that of the perpendicular component in planner configuration due to the strong longitudinal dipole moment of the 8OCB molecules [91]. The dielectric constant then again decreased in the nematic phase as the nematic to isotropic transition temperature was approached due to the decrease in the orientational order of the sample.

The frequency dependent dielectric studies were performed in the solid and liquid mesophases of the sample. We did not find any dielectric relaxation for all these phases till 100 KHz. The dielectric constant in the solid phases of the sample is relatively low compared to its perpendicular component ($\epsilon_{\perp}$) in the liquid mesophases of the compound. This is perhaps due to the lower contribution of the orientatinal polarization to the dielectric constant in these solid phases compared to that in the liquid mesophases.

As mentioned earlier, the metastable PP phase transforms to CP phase after few days at room temperature. This transition was confirmed using dielectric measurement of the sample. The PP phase was formed in a home made cell with planner alignment which was identified by POM observations. The sample was then kept at room temperature for 9 days. In this period of time, the PP phase was found to transform to CP phase as confirmed from the POM observations. The dielectric measurement on heating the sample from the CP phase obtained in this way was performed as shown in fig. 3.9c. The dielectric profile shows very similar trend as that found for CP phase obtained by directly cooling the sample from its melt (see fig. 3.9b). This result implies that the metastable PP phase transforms only to CP phase at room temperature. The presence of other metastable phases after

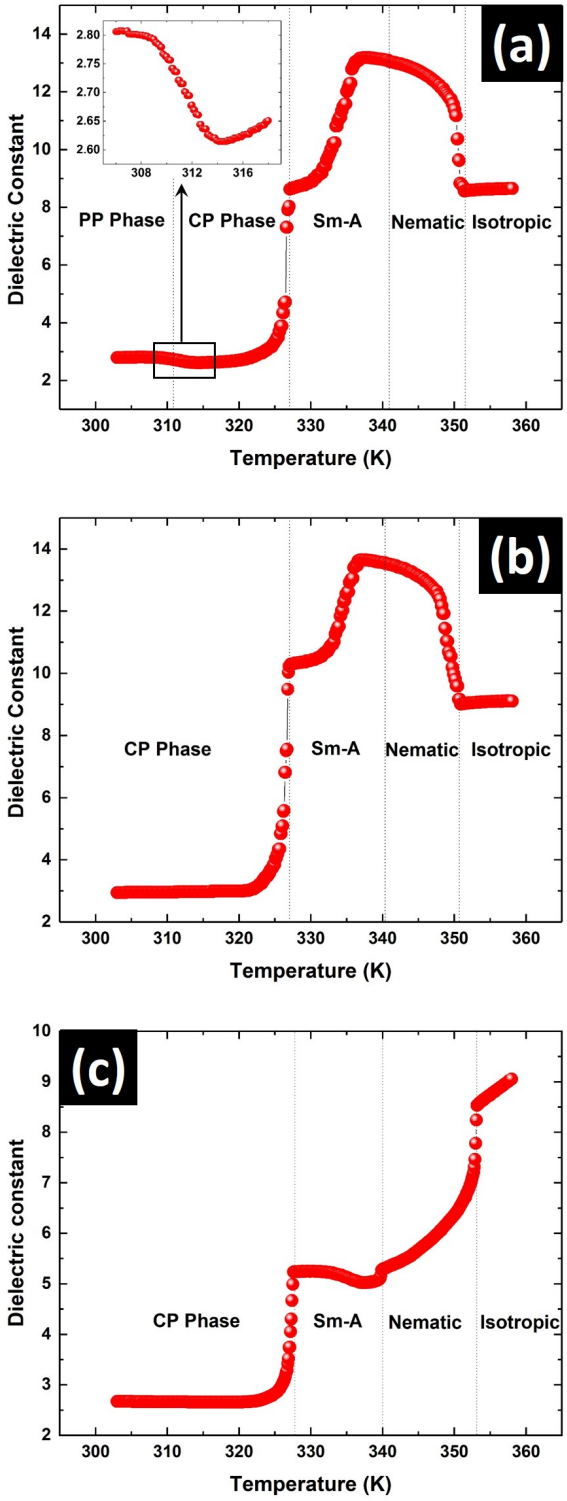


Figure 3.9: The temperature variations of dielectric constant of 8OCB on heating the sample from its (a) PP phase and (b) CP phase. The inset in (a) shows the variation of the dielectric constant across the PP to CP phase transition in an expanded scale. (c) The temperature variation of dielectric constant of CP phase formed after 9 days from PP phase kept at room temperature.

this transition were not found. This was also confirmed by Raman studies discussed later.

3.3.4 X-ray diffraction studies

The powder x-ray diffraction (XRD) studies of the sample filled in Lindemann capillary tubes were performed to characterise the crystallographic structure of the CP phase. The XRD intensity profile obtained in the CP phase as a function of the scattering vector q is shown in fig. 3.10a. The prominent diffraction peaks obtained in the CP phase can be indexed with the Miller indices of a monoclinic lattice structure as indicated in fig. 3.10a. The lattice parameters obtained for this monoclinic structure are a = 30.72 Å, b = 7.47 Å, c = 25.58 Å and $\beta = 107.7°$. These parameters were calculated by using the following relation for monoclinic lattice structure

$$\frac{1}{d_{hkl}^2} = \frac{1}{sin^2\beta}\left[\frac{h^2}{a^2} + \frac{k^2 sin^2\beta}{b^2} + \frac{l^2}{c^2} - \frac{2hlcos\beta}{ac}\right], \tag{3.1}$$

where d_{hkl} $(= 2\pi/q)$ is the lattice spacing between two consecutive lattice planes with Miller index (hkl). The lattice parameters are obtained by solving eqn. 3.1 using the d_{hkl} values corresponding to the peaks with Miller indices (100), (001), $(10\bar{1})$, $(10\bar{2})$ respectively. Hori *et al.* also reported about the monoclinic lattice structure of CP phase of 8OCB compound grown from its solution. The reported lattice parameters are in the range a = 30.56 Å - 30.62 Å, b = 7.39 Å - 7.44 Å, c = 25.43 Å - 25.52 Å and $\beta = 107.3°$ - $107.8°$ [88]. Therefore, the reported lattice structure of solution crystallized CP phase of 8OCB matches very well with that of the CP phase formed from the melt.

The Lindemann capillary itself produces an XRD profile with a broad hump at wide angle (see fig. 3.10b) which interferes with that coming from the sample. FESEM studies of CP phase clearly reveal the coexistence of fibrillar crystallites embedded in an amorphous solid phase. This amorphous phase shows a broad hump at wide angle with similar range of scattering angle as that shown by the

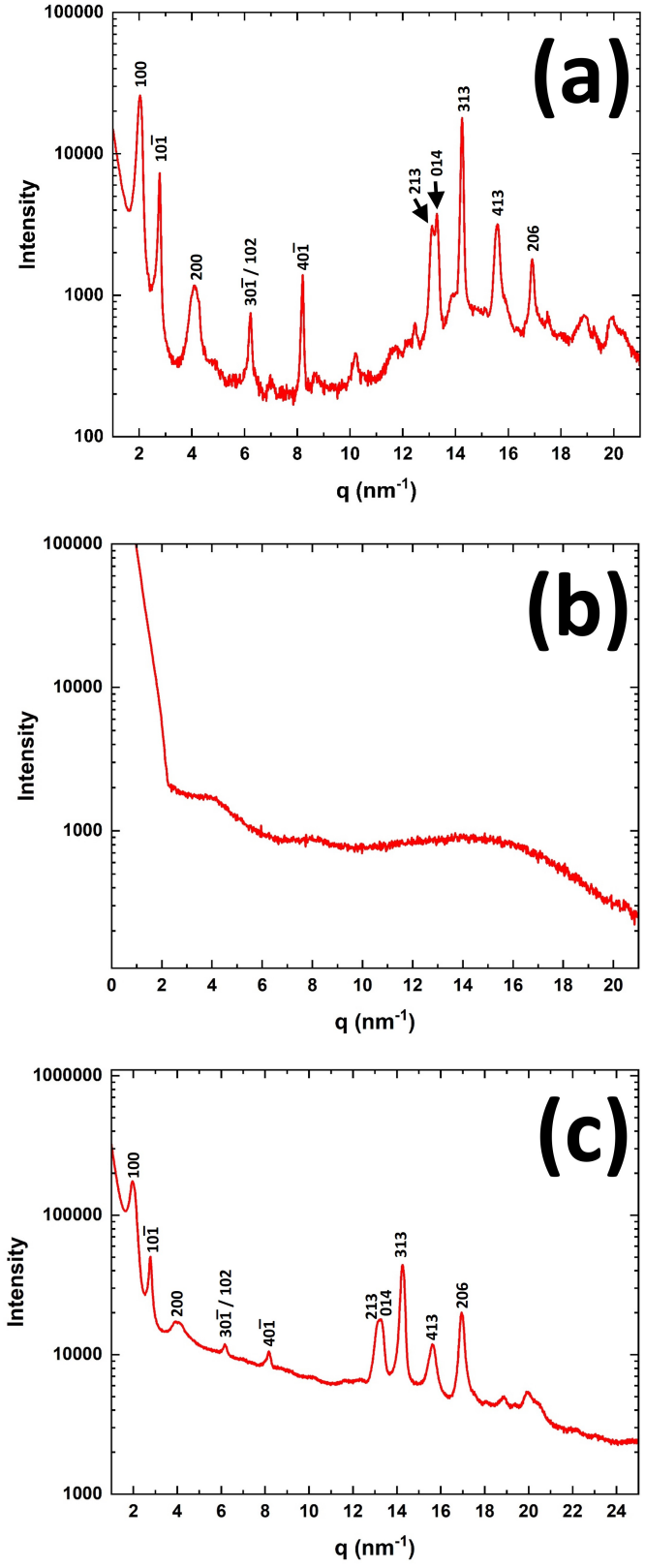


Figure 3.10: The XRD profiles of (a) the CP phase in capillary at room temperature, (b) the capillary and (c) the CP phase on flat stage at room temperature.

Lindemann capillary itself. Therefore, the amorphous hump from the sample with relatively less intensity is masked by the hump produced by the capillary tube. This difficulty was overcome by taking the XRD profile of the sample in the grazing mode of x-ray incidence on a flat silicon specimen stage. The silicon stage has a flat XRD profile which does not interfere with that coming from the sample.

The CP phase was formed on a cleaned coverslip which was identified by POM observations. The sample was then scraped off from the coverslip and placed on the silicon flat stage for XRD studies. The total acquisition time of the XRD profile in the range from q $\approx$ 0.7 nm^{-1} to 28 nm^{-1} with 0.001 nm^{-1} step size was set to 180 minutes. The range of 2θ values corresponding to the above range of q values is $1^\circ - 40^\circ$. Fig. 3.10c shows the XRD profile of this sample where a small broad hump in the range from about 11 nm^{-1} to 21 nm^{-1} was found. This broad hump arises due to the amorphous component of the sample in the CP phase. Therefore, we conclude from XRD and FESEM studies that the nano crystalline component of the CP phase has monoclinic lattice structure while the other component, which did not exhibit any sharp peak in the XRD profile is in the noncrystalline amorphous state.

3.3.5 Small angle X-ray diffraction studies

It was observed that the diffraction peak for smectic phase at 1.98 nm^{-1} appeared before complete melting of CP phase during heating. To quantify the structural changes in the CP phase during heating in the pre-transitional temperature range from 321 K to 327.5 K the small angle x-ray scattering (SAXS) studies of the sample were performed. In the scattering vector (q) range from 1.40 nm^{-1} to 3.20 nm^{-1} ($2\theta = 2^\circ$ to 4.5°) in the SAXS profile, three peaks at 2.14 nm^{-1} (100), 2.58 nm^{-1} (001) and 2.80 nm^{-1} ($10\bar{1}$) corresponding to the monoclinic lattice structure of CP phase were found (see fig. 3.11). These peaks were fitted with three different Gaussian functions to accurately determine their intensities, positions and the full widths at half maxima (FWHM). The intensity profiles of these fitted peaks as function of

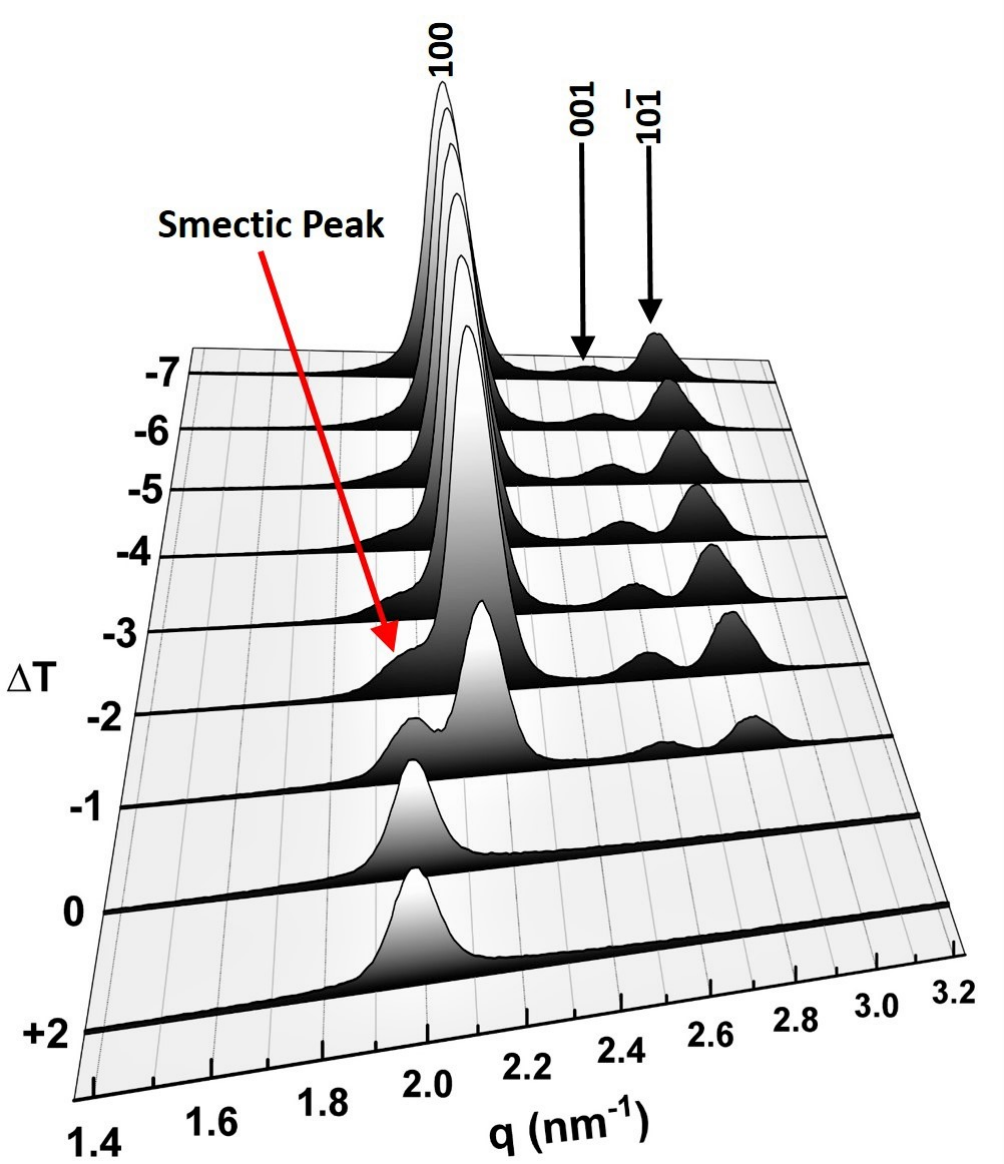


Figure 3.11: The SAXS profiles of CP phase during heating in pre-transitional region before melting. $\Delta T = T - T_c$ is in K.

the wave vector q at different temperatures are shown in the fig. 3.11. Fig. 3.12 shows the variation of the intensity and FWHM of these peaks with temperature difference $\Delta T = T - T_c$, where T and T_c denote the measured temperature and the transition temperature from CP to smectic phase respectively. The intensity of all these peaks either increased or remained almost same with increasing temperature till $\Delta T = -2$ K and then started to decrease till the complete melting of CP phase at T_c. The FWHM of all these peaks decreased till T_c. The Debye Scherrer equation says that the FWHM of the diffracted peaks is inversely proportional to the

mean size of the ordered domains. Hence reducing FWHM of these peaks in the pre-transitional temperature range implies that the dimensions of nano crystalline domains increase during heating the sample before melting. Above T_c, only one peak at 1.98 nm^{-1} corresponding to the layer spacing in the smectic phase was observed. Interestingly, this smectic peak started to grow from 5 K below T_c and became prominent with further heating (see fig. 3.12). The SAXS results therefore indicate that both the nano crystalline component of CP phase and the smectic phase grew at the expanse of the amorphous component of the CP phase during heating it in this pre-transitional region.

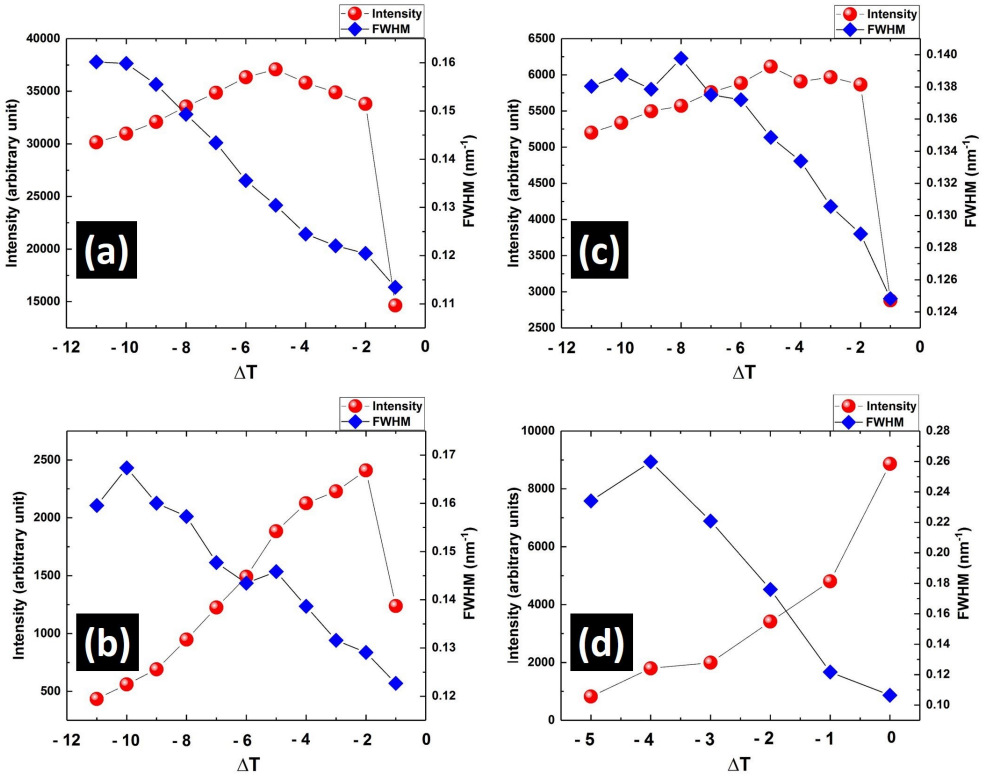


Figure 3.12: The temperature variation of intensity and FWHM of three crystalline peaks (a) (100), (b) (001), (c) $(10\bar{1})$ of CP phase and (d) (001) peak of smectic phase on heating the sample in the pre-transitional temperature range. Here $\Delta T = T - T_c$, where T and T_c denote the measured temperature and the complete melting temperature of CP phase respectively.

This was also confirmed by studying the SEM texture of CP phase which was cooled to the room temperature after keeping it at 325 K for 1 hour. This texture showed that the size of the fibrillar nano crystallites in the CP phase became larger compared to that obtained on cooling from its melt (see fig. 4.11a,b in chapter 4).

It implies that the fibrillar nano crystallites in CP phase grew at the expense of the amorphous phase in the pre-transitional temperature range and their size was preserved on subsequent cooling to room temperature. Hence the morphological changes occurring in the pre-transitional region during heating of CP phase gave rise to the continuous increase in the dielectric constant of sample before its complete melting.

3.3.6 Raman spectroscopic studies

The Raman spectroscopic studies of the sample were performed to characterize the observed crystal phases obtained from its melt. This spectroscopic technique is an indispensable tool to identify the crystal phases of 8OCB. In this section, a few of the characteristic peaks in the range from 200 cm^{-1} to 900 cm^{-1} which allowed us to identify the different solid phases of the compound, have been discussed. In addition, four prominent peaks in the range between 200 cm^{-1} to 3200 cm^{-1} were studied at different phases of this compound as discussed below.

Raman peaks from 200 cm^{-1} to 900 cm^{-1}

Fig. 3.13a and fig. 3.13b show the Raman spectra of the sample in its PP and CP phase respectively in the range of 200 cm^{-1} to 900 cm^{-1}. In addition to the PP phase, 8OCB also forms two other metastable crystal phases from its solution known as needle phase and square-plate phase respectively [4]. Though, the needle crystal phase known to be formed very less frequently, we incidentally found the needle crystal phase once on cooling the sample from the smectic phase. Fig. 3.13c shows the Raman spectra of the needle crystal phase in the range between 200 cm^{-1} to 900 cm^{-1}.

It can be seen that two closely spaced peaks at about 400 cm^{-1} are almost invisible (fig. 3.13a) for the metastable PP phase but are prominent for the CP and needle phase respectively (fig. 3.13b, 3.13c). These pairs of peaks at 399 cm^{-1} and 414 cm^{-1} in the CP phase and 406 cm^{-1} and 420 cm^{-1} in needle phase respectively

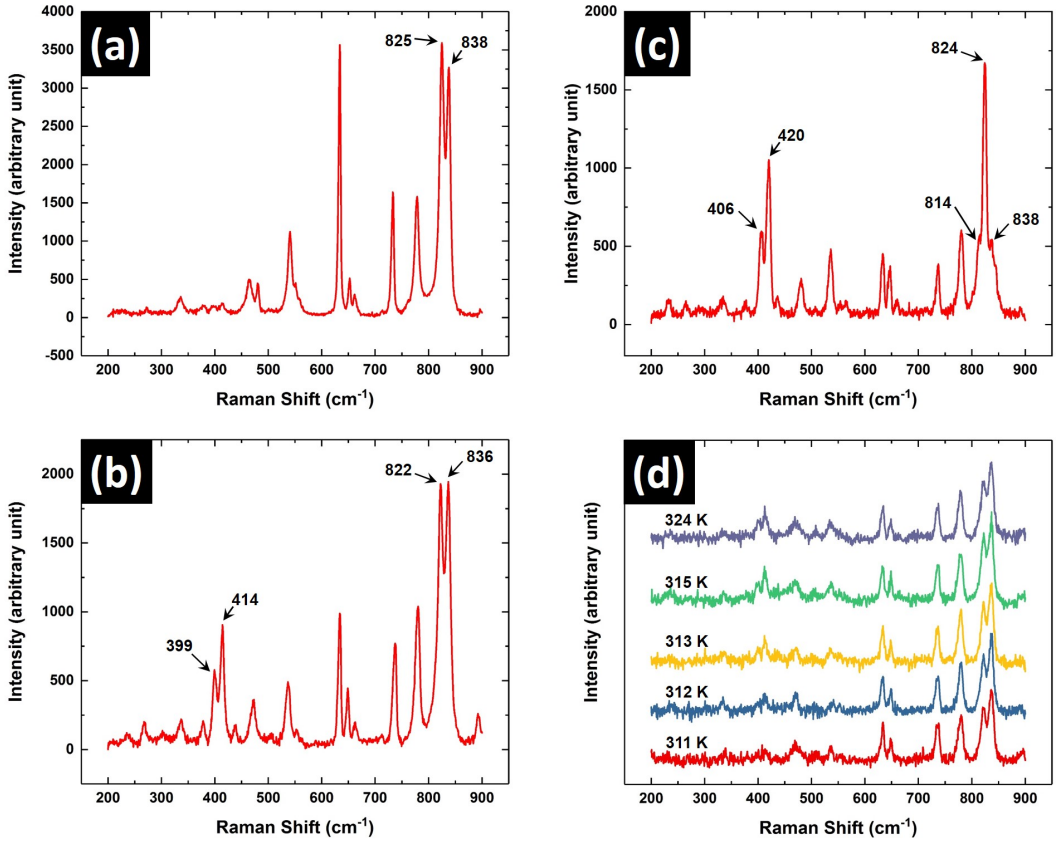


Figure 3.13: Raman spectra for (a) PP phase, (b) CP phase and (c) Needle phase. (d) The Raman spectra of 8OCB showing the variation with temperature across the transition from PP to CP phase.

have been assigned to the stretching vibrations of twisted biphenyl link [88]. The intensities of these peaks are reported to be quite sensitive to the dihedral or twist angle of the biphenyl moiety of the 8OCB molecules [92]. This dihedral angle varies in the different crystalline states of 8OCB. The reported twists of biphenyl moiety of 8OCB molecules in PP phase and needle phase are 2.2° and about 38° respectively [4]. Although there is no report for it in CP phase but the value was expected to be high [88]. The low value of the twist angle in the PP phase accounts for the absence of the doublet peaks at 400 cm^{-1} while these peaks are prominent in other crystalline phases of 8OCB. The absence of these peaks for the metastable PP crystal phase observed in our experiments on cooling the sample from its melt therefore confirms its identity. The Raman spectroscopic signature of the transition from PP to CP phase is shown in fig. 3.13d where the doublet peak near 400 cm^{-1} started to appear

from 312 K on heating.

Another doublet peak were found for PP phase near 800 cm^{-1}. The position of the component peaks is 825 cm^{-1} and 838 cm^{-1} respectively (fig. 3.13a). The same peaks were also observed for CP phase at 822 cm^{-1} and 836 cm^{-1} respectively (fig. 3.13b). In needle crystal, these peaks are positioned at 824 cm^{-1} and 838 cm^{-1} respectively (fig. 3.13c). These peaks are associated with two different perpendicular deformation modes of CH bonds linked with the phenyl rings of the 8OCB molecule [93]. For PP and CP phase these two peaks have similar intensity but in case of needle phase the peak at 824 cm^{-1} is highly intense than the other one. Hori *et al.* reported similar results for solution crystallized needle phase of 8OCB [88]. Therefore, the needle phase was identified from the nature of these two peaks. In our sample, the intensity profile of these two peaks do not change across PP to CP phase transition as shown in fig. 3.13d which implies that the needle phase does not form across this transition. Hori *et al.* reported that in most cases, the PP phase grown from 8OCB solution transformed to CP phase in slow heating [88]. Occasionally, they found traces of needle phase coexisting with CP phase after the transition. However, from micro-Raman studies we did not detect any trace of the needle phase on slow heating (1 K/min) of the PP phase above 312 K.

The stability and the transition between smectic and these solid phases can be understood using the schematic energy diagram as shown in fig. 3.14 [5]. At room temperature, the CP phase is most stable and the lowest energy state of 8OCB. The metastable PP phase is the next lowest energy state compared to the other phases of 8OCB as shown in fig. 3.14. Thus, the metastable PP phase tends to transform to the stable CP phase. However at room temperature, this transition takes few days to complete, possibly due to the high energy barrier between these two states. On increasing the temperature, this barrier height decreases and also the metastable needle phase becomes of lower energy than the PP phase above 312 K. Therefore, the PP phase becomes more unstable towards the formation of CP and needle phase. It is our conjecture that perhaps above 312 K, the energy barrier between PP and

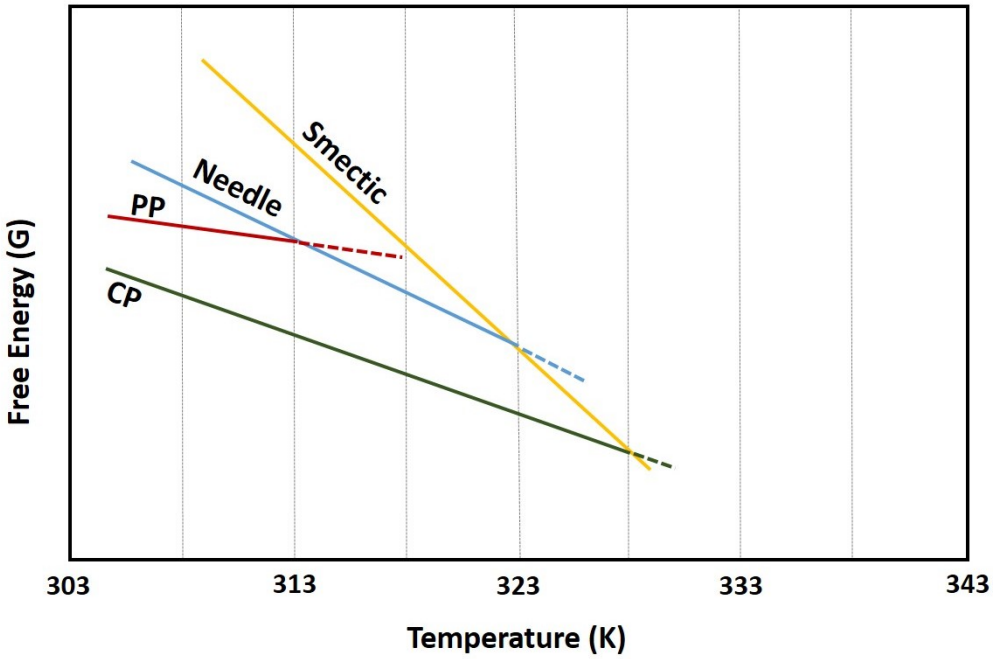


Figure 3.14: Schematic free energy diagram of various phases of 8OCB with temperature variation.

needle phase is comparatively larger than that between PP and CP phase. Hence the transition probability of unstable PP phase to most stable CP phase is much larger than that to the needle phase. This explains the absence of needle phase in our sample above this transition though, Hori *et al.* occasionally found traces of needle phase above this transition of solution crystallized PP phase [88].

Raman peaks from 200 cm^{-1} to 3200 cm^{-1}

In the range between 200 cm^{-1} to 3200 cm^{-1}, four prominent Raman peaks were found for all phases of the compound as shown in fig. 3.15. In this subsection, we have studied the properties of these peaks at different phases of 8OCB. These four peaks are positioned at about 1185 cm^{-1}, 1285 cm^{-1}, 1605 cm^{-1} and 2230 cm^{-1} respectively. The first one is associated with in-plane deformation of CH bonds of the biphenyl moiety [93]. The second one is a combinational band of symmetric and asymmetric out of plane deformations of CH_2 group in the aliphatic chain [93]. The third peak is for quadrant vibration of aromatic rings and the last one is for CN stretching vibration respectively [93, 94]. Besides these, the peaks in the range

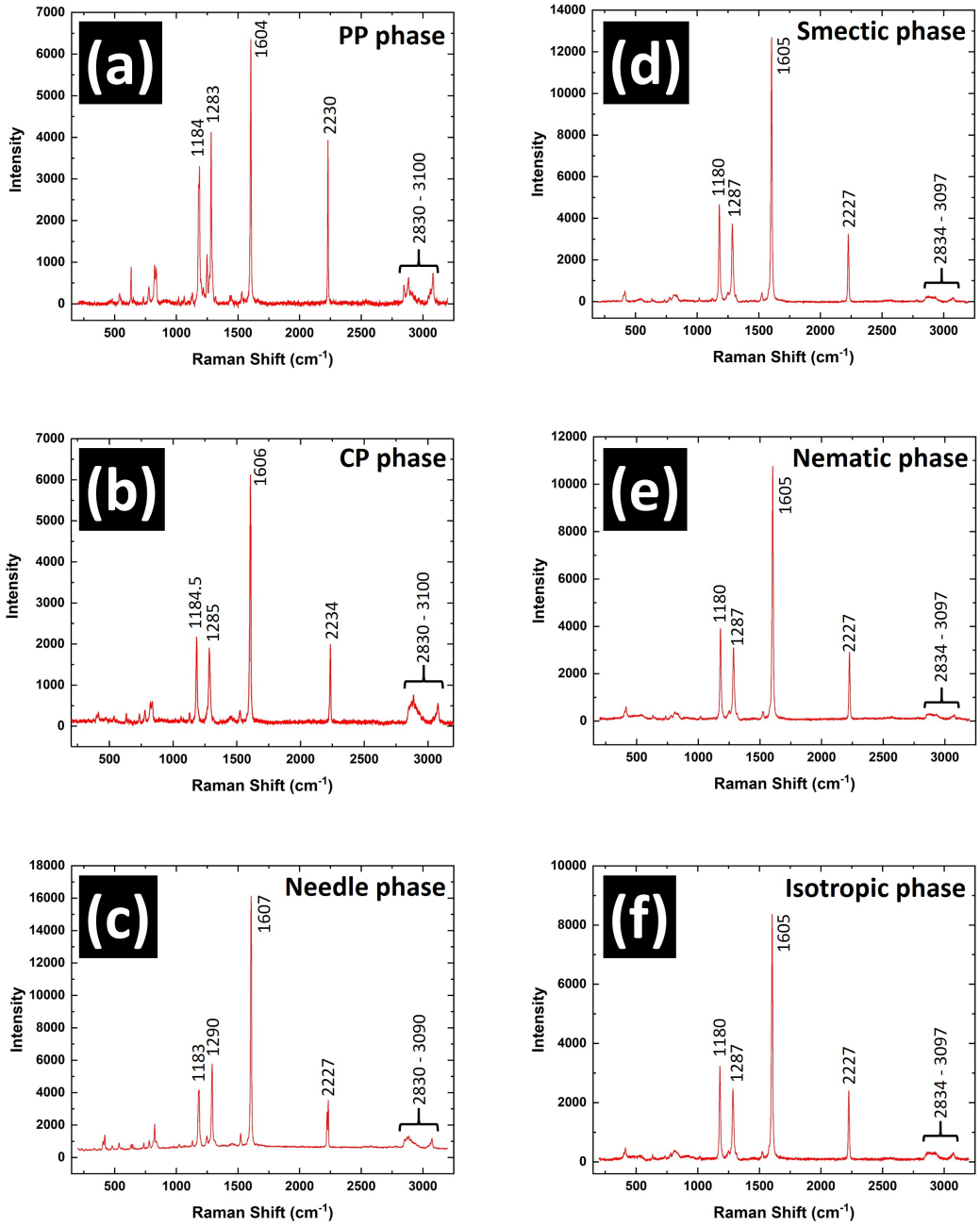


Figure 3.15: Raman spectra in (a) PP phase, (b) CP phase, (c) Needle phase, (d) Smectic A, (e) Nematic and (f) Isotropic phase.

between 2830 cm^{-1} to 3100 cm^{-1} in all phases come from CH stretching vibrations [84].

All these prominent peaks were fitted with Voigt functions using Origin software to resolve the component peaks and accurately determine the peak positions at different phases. The Voigt function can be obtained by convoluting a suit-

able Gaussian and a Lorentzian function respectively. The fitting processes were performed after subtracting an appropriate baseline from the data. The detail of these four intense peaks after fitting in different phases of the compound is given in table 3.1, table 3.2, table 3.3 and table 3.4 respectively.

Table 3.1: In-plane deformation of CH bonds of biphenyl moiety

Name of Phase	**Nature of peak**	**Raman Shift**
PP phase	Doublet	Component peaks are at 1181 cm^{-1} and 1188 cm^{-1}
Needle phase	Doublet	Component peaks are at 1180 cm^{-1} and 1186 cm^{-1}
CP phase	Symmetric	1185 cm^{-1}
Smectic A	Symmetric	1180 cm^{-1}
Nematic	Symmetric	1180 cm^{-1}
Isotropic	Symmetric	1180 cm^{-1}

Table 3.2: Combinational band for perpendicular deformations of CH_2 group

Name of Phase	**Nature of peak**	**Raman Shift**
PP phase	Asymmetric	1283 cm^{-1}
Needle phase	Asymmetric	1290 cm^{-1}
CP phase	Asymmetric	1284.5 cm^{-1}
Smectic A	Symmetric	1287 cm^{-1}
Nematic	Symmetric	1287 cm^{-1}
Isotropic	Symmetric	1287 cm^{-1}

Table 3.3: Quadrant stretching mode of aromatic rings

Name of Phase	**Nature of peak**	**Raman Shift**
PP phase	Asymmetric	1604 cm^{-1}
Needle phase	Asymmetric	1607 cm^{-1}
CP phase	Asymmetric	1606 cm^{-1}
Smectic A	Symmetric	1605 cm^{-1}
Nematic	Symmetric	1605 cm^{-1}
Isotropic	Symmetric	1605 cm^{-1}

The Raman peak for in-plane deformation of CH bonds attached with biphenyl moiety shows doublet structure in PP and needle phase. These peaks were fitted with two Voigt functions in the PP and needle phase as shown in fig. 3.16a and fig. 3.16b respectively. For PP phase, the component peaks are positioned

Table 3.4: CN stretching vibration

Name of Phase	**Nature of peak**	**Raman Shift**
PP phase	symmetric	2230 cm^{-1}
Needle phase	Doublet	The component peaks are at 2222 cm^{-1} and 2233 cm^{-1}
CP phase	Asymmetric	The peak at 2233 cm^{-1}, the component peaks are at 2227 cm^{-1} and 2234 cm^{-1}
Smectic A	Symmetric	2227 cm^{-1}
Nematic	Symmetric	2227 cm^{-1}
Isotropic	Symmetric	2227 cm^{-1}

at 1180 cm^{-1} and 1186 cm^{-1} respectively whereas for needle phase these are at 1181 cm^{-1} and 1188 cm^{-1} respectively. In other phases the peak envelope is symmetric (see fig. 3.16c,d).

The positions of these peaks did not vary appreciably during heating of PP phase as shown in fig. 3.17a. Across the transition from the PP to CP phase at 312 K, the doublet peaks transformed to a single symmetric peak centered at 1185 cm^{-1} which signifies the presence of only CP phase after this crystal to crystal phase transition. The position of this symmetric peak started to decrease continuously on heating above 323 K (fig. 3.17a). This type of pre-transitional effect near the melting point of CP phase was also observed in the XRD and dielectric studies. The position of this peak remained almost constant in all the liquid phases with increasing temperature. The temperature variation of this peak position was also studied on heating the sample which was initially in its stable CP phase rather than metastable PP phase. Again a totally symmetric singlet peak was observed in the whole temperature range of CP phase. The variation of this peak position with temperature is shown in fig. 3.17b. The clear match between peak positions in the CP phase with temperature for both cases signifies that the PP phase transformed to the CP phase at 312 K on heating.

The Raman peak at 1283 cm^{-1} in PP phase is a combination band of symmetric and asymmetric perpendicular deformations of CH_2 group attached to the aliphatic chain. It showed a small jump towards higher Raman shift across the PP to CP phase

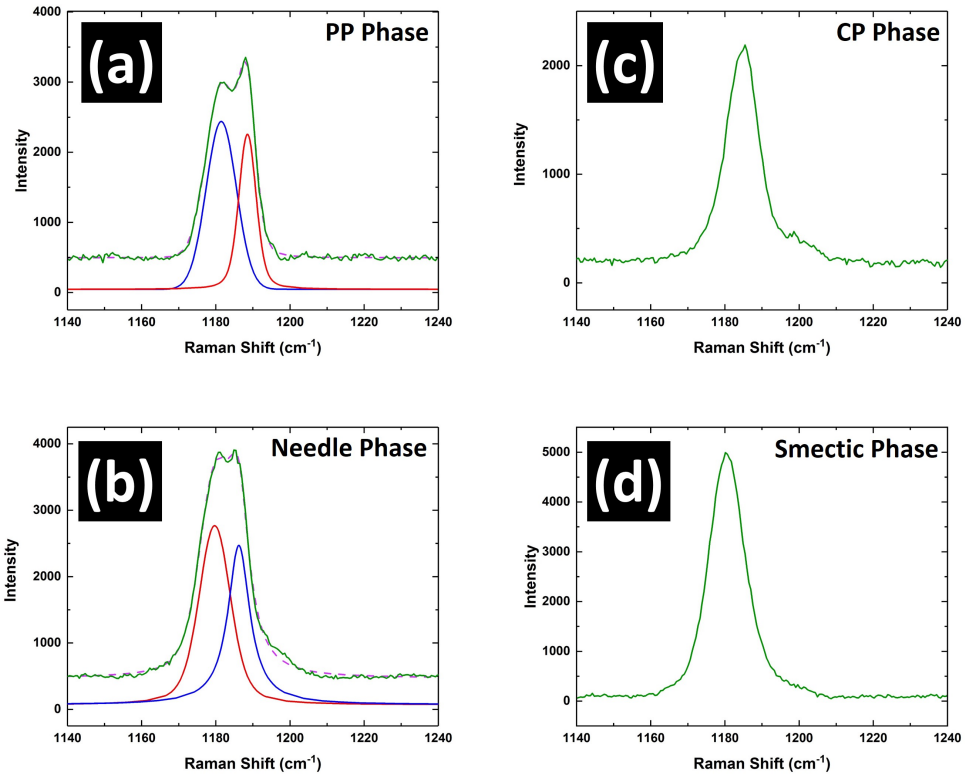


Figure 3.16: Raman peak for in-plane CH deformation in (a) PP phase, (b) Needle, (c) CP phase and (d) Smectic A phase.

transition. Near CP to smectic phase transition, the position changed gradually towards higher Raman shift till the complete melting of CP phase. In liquid phases, the peak position remained invariant with increasing temperature.

The Raman peak for quadrant stretching mode of aromatic rings positioned at 1604 cm^{-1} in PP phase is asymmetric in nature. It is also asymmetric in needle and CP phase. Across PP to CP phase transition, this peak remains asymmetric and shifts to the higher wave number. This peak becomes symmetric in the liquid phases and the position of the peak remains constant with increasing temperature.

The Raman peak for CN stretching vibration is quite sensitive to the electron density of CN group [83]. This electron density depends on the local molecular environment around the CN group in different phases of 8OCB and hence sensitive to these phases. The CN stretching vibration gives rise to a symmetric singlet peak at 2230 cm^{-1} in the PP phase (fig. 3.18a). The closer proximity between the CN group of a molecule with the biphenyl moiety of the neighboring molecule in the

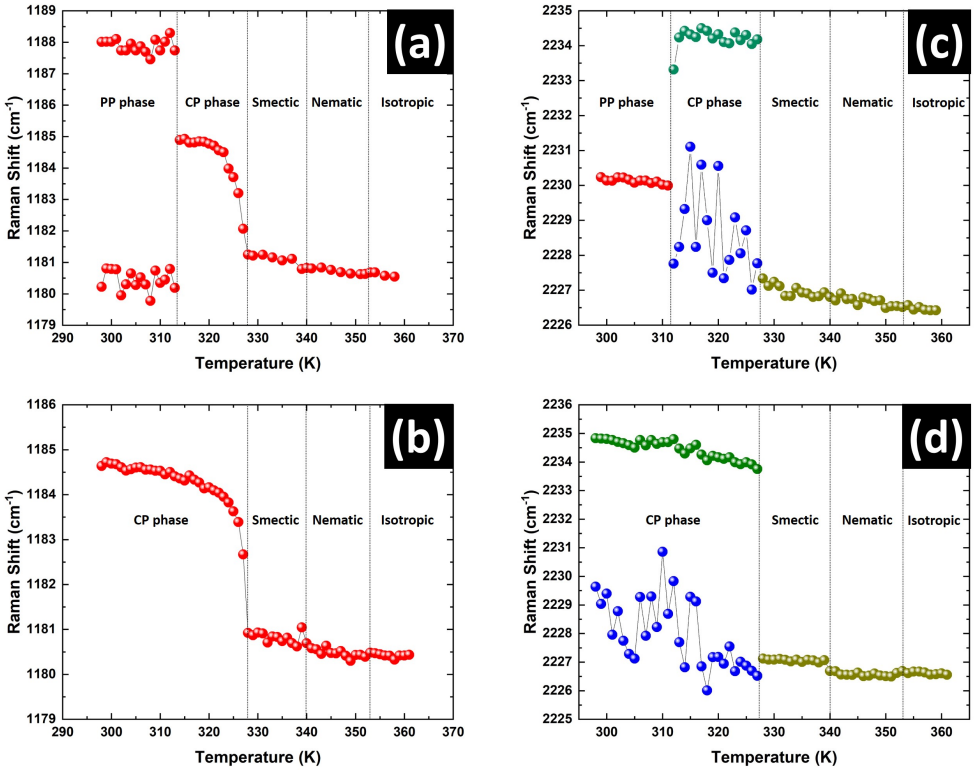


Figure 3.17: Temperature variation of Raman peak position for in-plane CH deformation mode when initial phase was (a) PP phase, (b) CP phase. Temperature variation of Raman peak position for stretching vibration of CN group when initial phase was (c) PP phase, (d) CP phase.

monoclinic structure of PP phase manifests itself in giving rise to this peak [4]. This peak shows doublet structure at needle phase and fitted with two Voigt functions. The fitted component peaks at 2222 cm^{-1} and 2233 cm^{-1} respectively are shown in fig. 3.18b. This splinting comes possibly due to the dipolar interaction among neighboring CN groups [87]. In CP phase, this peak becomes asymmetric and was fitted (Voigt fitting) with a prominent strong peak positioned at 2235 cm^{-1} and a weak satellite peak at 2226 cm^{-1} (see fig. 3.18c). In liquid phases, it remains symmetric at 2227 cm^{-1} (see fig. 3.18d).

The temperature variation of Raman peak position for CN stretching vibration is shown in fig. 3.17c and fig. 3.17d when initial phase was PP and CP phase respectively. No change in peak position was noticed during heating the sample in PP phase. Across PP to CP transition the peak became asymmetric. The fitted intense peak position remained invariant during heating till melting of this phase. The less

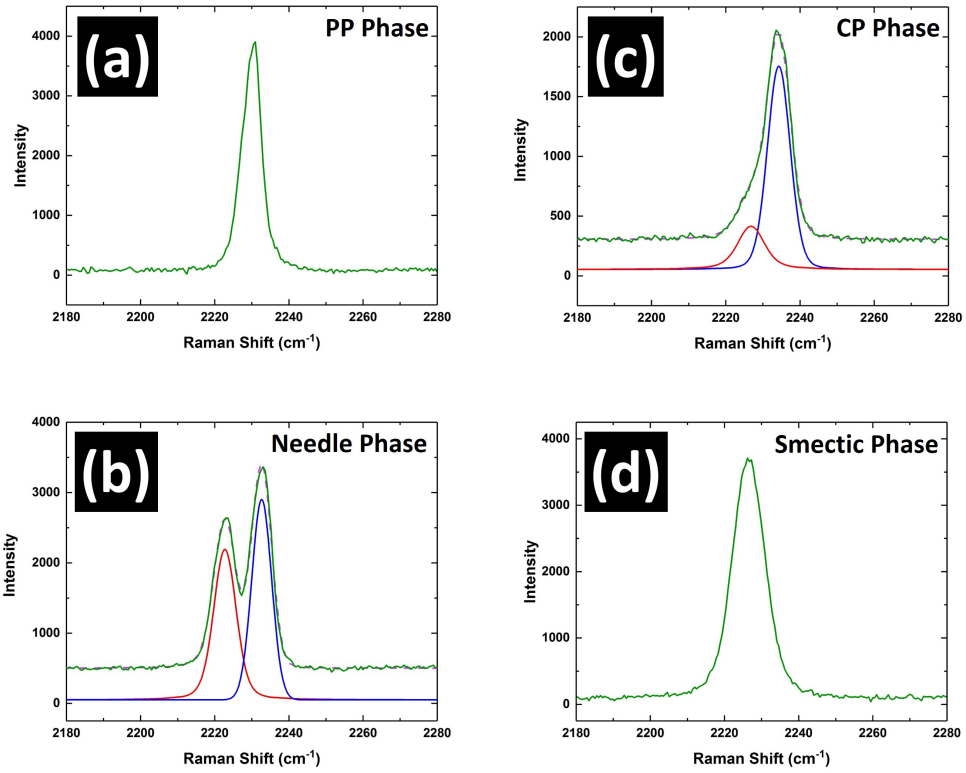


Figure 3.18: Raman peak for CN stretching mode in (a) PP, (b) needle, (c) CP and (d) Smectic A phase.

intensity of shoulder peak causes a fitting error in evaluating its exact peak position at different temperatures. In liquid phases, the peak position remained invariant with increasing temperature. The similar behavior was also found when the sample was heated from the initial CP phase.

The molecular environment of CN group is different in the amorphous and crystalline components of CP phase giving rise to a slightly different peak positions. Hence the doublet nature of the CN peak in the CP phase can be attributed to the heterogeneous nature of this phase. The fitted strong and weak peaks are associated with the nano crystalline and amorphous components of the CP phase respectively. This was inferred from the pre-transitional variation of these peaks near the CP to smectic phase transition as shown in fig. 3.19. The intensity and position of the strong peak remained almost constant with increasing temperature in the pre-transitional range and it disappeared on melting of the nano crystallites at T_c. On the other hand, the intensity and the position of weak peak started to change in

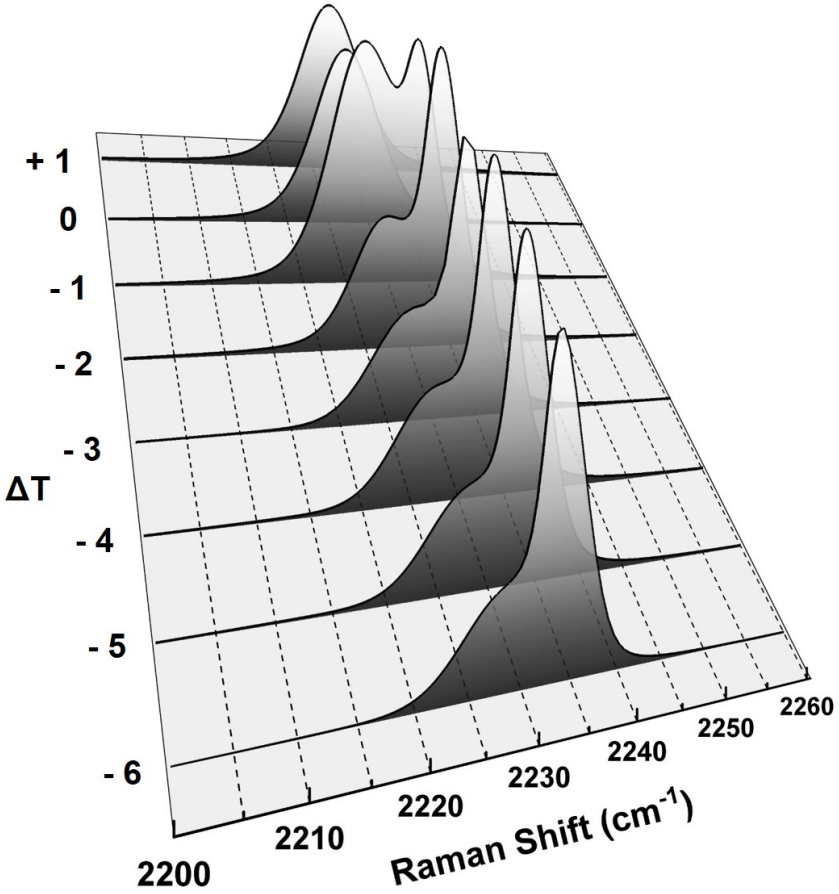


Figure 3.19: The temperature variation of the Raman peak profile associated with the CN stretching vibration of 8OCB molecules in the pre-transitional temperature range of CP phase during heating the sample. $\Delta T = T - T_c$ in K denotes temperature difference from the complete melting temperature of CP phase.

this temperature range due to the transformation of the amorphous component to smectic below T_c and only this peak remained after transition to the smectic phase at T_c.

3.4 Conclusion

Two different crystalline states of 8OCB are observed on cooling the sample from its melt. One of them is the metastable long parallelepiped or PP crystal phase. The other one is the stable crystal phase known as the commercial powder or CP phase. The metastable PP phase transforms to the stable CP phase on aging at room temperature or by heating it above 312 K. Though the PP phase is a homogeneous crystal phase, the SEM studies show that the stable CP phase is actually

heterogeneous in nature with two sub-phases coexisting together. Here numerous fibrillar nano crystallites are found to be embedded in an amorphous matrix. The XRD studies on the CP phase show that the fibrillar nano crystallites have monoclinic lattice structure while no lattice structure is found corresponding to the amorphous component. This signifies that there is no long range positional order in the amorphous component of the CP phase. The CP phase shows a prominent pre-transitional effect close to its melting point during heating. This effect arises due to the transition of amorphous part of CP phase that starts before than the melting point of nano crystallites at 327.5 K. Such coexistence of crystalline and amorphous states is generally observed for large molecular weight polymeric systems or in mixtures of incompatible molecules [31, 95]. The coexistence of nano crystallites and the amorphous phase in the stable ground state has not been observed for this type of small molecular weight liquid crystals. We attribute this behaviour to the strong dipole moment of the 8OCB molecules. This strongly polar 8OCB compound is known to exhibit reentrant nematic phase below its smectic phase under high pressure or in suitable mixtures with 6OCB [1, 2]. Thus, it is our expectation that this amorphous component may be the frozen reentrant nematic phase. We are unable to isolate the amorphous component of the CP phase to clearly identify its structure. Further experiments are required to reveal the detail structure of the CP phase and the possible origin of the heterogeneous ground state.

Chapter 4

Spherulitic growth in 8OCB

4.1 Introduction

The spherulitic growth of solids is a ubiquitous phenomenon exhibited by many different types of materials such as polymers [19, 20], minerals [21–23], elements [24, 25], metals [6] and salts [26–28]. It is also found in biological materials like coral skeletons [96], kidney stones [97], proteins [98–100] and urinary sediments [101]. In spherulitic growth, the solid phase after nucleation grows with a spherical growth front with continuous orientational symmetry in contrast to the growth of a crystal having discrete orientational symmetries. The spherulites were initially named as "circular crystals" for its circular boundary in quasi-two-dimensional geometry which was changed later to spherulite [30]. In spite of research on it for over a century, the detailed understanding of the mechanism of this abundantly found natural growth phenomenon is still incomplete [6]. The spherulitic growth morphology is often associated with the formation of many radially aligned fibrillar crystallites which branch non-crystallographically for filling space during the growth [31]. The misorientations of the lattice planes between parent and daughter crystallites in spherulite domain vary between 0° to 15° in contrast to the crystallographic branching where the crystal orientation remains preserved during branching as generally seen in dendritic growth [6].

Depending upon morphology, spherulites are classified into two categories named as compact or closed and open spherulite [6]. In compact spherulites, the width of fibrillar crystallites is comparatively lesser than the open spherulites. The fibrillar density in compact spherulite is higher than open spherulite.

In some materials, the spherulitic growth is accompanied by a series of equidistant concentric bands and is known as banded spherulite. In quasi-two-dimensional geometry, the banded spherulite domain appears as a flattened disk with circular boundary and these bands appear as concentric circular rings. The polarising optical microscopic textures of these spherulites show concentric bands with periodic variation of interference color. Polymers generally form this kind of banded spherulite [6, 19, 20, 32]. Some small molecular systems also produce banded spherulites [33–40]. An organized periodic twist of radially aligned fibrillar crystallites in the banded spherulitic domain has been observed to generate a periodic change of effective birefringence along the radial direction. This undulation in the birefringence gives rise to concentric interference colour bands with periodic variation of colors when viewed through crossed polarisers. The mechanism of twist of the fibrils are still a debated subject. The proposed mechanisms are broadly divided into two categories [20]. In first category, the twisting is related with growth kinetics of fibrillar crystallites whereas the second category relates twisting with the lamellar structure itself. Keith and Padden advocated that the twisting in polyethylene lamellae forms due to the unbalanced surface stress at its opposite surfaces [32]. Later Lots and Chen continued this argument for other chiral polymers [20]. In contrast, some multi-component blends of materials form banded spherulites by rhythmic deposition of host and additive materials [95, 102, 103]. Even in some of these cases, twist order of fibrils has been found to contribute to the modulation of effective birefringence along the radial direction. So the organized twisting of the fibrillar crystallites is considered to be a primary mechanism for the formation of the banded spherulites.

Besides banded spherulite, the rhythmic growth of ring banded structures formed on thin films with one free surface has been reported [45–53]. The periodic height modulation of the free surface gives rise to the ring banded structure in these systems. The effective birefringence in these cases may also vary periodically depending on the periodic orientational change of lamellar building blocks. The diffusion controlled growth mechanism produces a rhythmic variation of material supply near

the growth front of the solid phase which leads to this height modulation. These types of ring banded structures are found only in thin films and are very different from the banded spherulites formed in three-dimensional bulk systems [20].

In this chapter, we report the formation of banded spherulite by pure 4′-octyloxy-4-cyanobiphenyl liquid crystalline compound consisting of relatively small rodlike molecules with 24 Å molecular length. We show that the rhythmic growth of concentric crystallite-rich and crystallite-poor zones is the underlying mechanism for the formation of banded spherulites of this compound contrary to the organized twisting of the fibrillar crystallites. The crystallite-rich zones have higher density of radially aligned fibrillar nano-crystallites while crystallite-poor zones are rich in the solid amorphous state of the compound. The alternation of these concentric regions changes the effective birefringence periodically along the radial direction of the spherulite giving rise to the concentric interference color bands between crossed polarisers.

4.2 Experiment

The commercially available liquid crystalline compound 4′-octyloxy-4-cyanobiphenyl (8OCB) was used with 99% purity. The sample shows a melting transition to the smectic-A phase at 327.5 K on heating from its most stable crystal phase known as the commercial powder or CP phase. On further heating, the compound transforms to the nematic and to the isotropic liquid phase at 340 K and 353 K respectively. The sample exhibits a large range of supercooling from its smectic A phase. The supercooling $\Delta T = T_c - T$, where T is temperature below the melting point T_c. The banded spherulitic domains are formed on supercooling the smectic phase by at least 22.5 K below the melting temperature. The probability of getting the banded spherulites increases with higher supercooling. For spherulitic growth, the sample sandwiched between two cleaned coverslips in its isotropic phase was cooled to a desired temperature (T) below its melting point (T_c) using a microscope hot stage (Linkam). The spherulitic domains grown in this way were used for polaris-

ing optical microscope (POM) observations and Raman spectroscopic studies. The spacing between the spherulitic bands was determined by taking photographs using a digital camera (Canon EOS 80D) attached to the polarising microscope (Olympus BX50) followed by analysis of the images using the imageJ software. The velocity of the growth front in isothermal condition was calculated by analyzing the videos of spherulitic growth of the compound taken at different supercooling.

The micro-Raman spectroscopic studies of the spherulite domain were performed using a Raman spectrometer (Jabin Yvon T64000) equipped with a nanopositioning stage. An air-cooled argon laser (Melles Griot) beam of wavelength 514 nm was used as an excitation source. An objective lens with 50X magnification and 0.75 numerical aperture was used to focus the beam on the sample. The Raman spectra of the sample were recorded from the backscattered light. The theoretically estimated diameter of the focused spot is less than 1 μm.

The field emission scanning electron microscopy (FESEM) studies of the spherulite domain were conducted using the CARL ZEISS (ULTRA PLUS model) system. The banded spherulites of the sample were formed from its melt on cleaned ITO-coated glass plates at room temperature. The free surface of these samples was sputter coated with platinum [QUORUM (Q150R S)] for FESEM imaging. For the cross-sectional view of the domain, the spherulites formed on coverslips were cleaved in the middle and then the cross-sectional areas were sputter coated with platinum for FESEM imaging.

For cryo-SEM imaging, a small brass container was filled with the sample above its clearing temperature using a hot stage. After that it was dipped in liquid nitrogen for fast cooling which produced the banded spherulites. It was then transferred to the cryo-sample preparation chamber (Quorum Technologies PP3000T) of the FESEM system maintained at a temperature of 103 K. The sample was then heated to 183 K to make it soft and the upper portion of the sample was scraped off for removing the ice content. The newly opened sample surface was then sputter coated with platinum and transferred to the main unit for SEM imaging where the sample

was maintained at 83 K.

The fluorescent dye (rhodamine 6G) was mixed with the 8OCB sample at $1{:}10^4$ wt/wt ratio. The mixture was stirred for 3 hours above the clearing temperature of 8OCB for homogeneous mixing. The sample was then sandwiched between two coverslips and supercooled to room temperature to form the banded spherulites. The fluorescent images of the spherulite domain were captured by a confocal microscope (Leica SP8) equipped with an argon gas laser. The exciting wavelength was 514 nm.

A DY 1042-Empyrean (PANalytical) x-ray diffractometer with a PIXcel 3D detector was used to acquire the x-ray diffraction (XRD) profiles of the sample using CuK_α radiation of wavelength 1.54 Å. The banded spherulites were formed on a cleaned coverslip on cooling the sample to room temperature from its isotropic phase and its formation was confirmed by POM observation. The sample was then scraped off this substrate and placed on a silicon plate. The XRD measurements were performed in the grazing angle of incidence of the x-ray beam. The silicon plate has a flat XRD profile which does not interfere with that from the sample.

The temperature variation of the dielectric constant of the sample was measured using a homemade setup. The detail of this setup has been discussed in chapter 2. Two different kind of commercially available liquid crystal cells (INSTEC Inc.) were used for dielectric measurement. One of them had planner alignment with 5×5 mm^2 electrode area and 5 μm sample thickness. Another one had homeotropic alignment with 10×10 mm^2 electrode area and 9 μm sample thickness. Prior to filling the sample, the capacitance of both the empty cells was measured. The cells were then filled with the sample in its isotropic phase by capillary action on a hot stage. After that, it was supercooled to the lower temperature to form banded spherulite domains. The formation of the banded spherulites was confirmed using POM observation of the sample. A sinusoidal voltage of rms amplitude 0.5 V and frequency 5641 Hz was used for the dielectric measurements. The ratio of the capacitance of the filled cell to the empty cell gives the dielectric constant of the sample.

4.3 Results and discussions

4.3.1 Polarising optical microscopy studies

Fig. 4.1a shows a polarising optical microscope (POM) texture of the banded spherulite of 8OCB liquid crystal formed between two coverslips at room temperature. The POM texture of this banded spherulites shows four black brushes parallel to the polarisers forming a Maltese cross in addition to the concentric interference color bands with periodic variation of colors. These color bands arise from the periodic variation of the effective birefringence in the sample along the radial direction. The black and white appearance of the interference color bands in this texture is due to relatively lower thickness of the sample with phase retardation in the first-order region of the Levy chart. The dark arms of the Maltese cross remain invariant on rotating the sample between crossed polarisers. This implies that the major axis of the effective refractive index ellipse in the plane perpendicular to the light path lies parallel or perpendicular to the radial direction of the spherulitic domain.

The POM studies using a λ-plate of path difference 530 nm were performed to determine the orientation of this major axis. Fig. 4.1b is the POM image after introducing the phase plate in the optical path of the microscope. The yellow double-headed arrow shows the orientation of the slow axis of the phase plate with respect to the orientations of the crossed polarisers. It can be inferred from the Levy chart that there is effective addition and subtraction of path differences due to the sample and the λ-plate in the blue and yellow colored regions of the texture respectively. This observation clearly indicates that the major axis is oriented parallel to the azimuthal direction of the banded spherulite. The spherulites with major index along the radial and azimuthal direction of the domain are optically positive and negative respectively [6, 19]. Hence the spherulite observed for this sample is optically negative. The white double-headed arrows in fig. 4.1b show the orientation of the major axis around the seed of this spherulite domain.

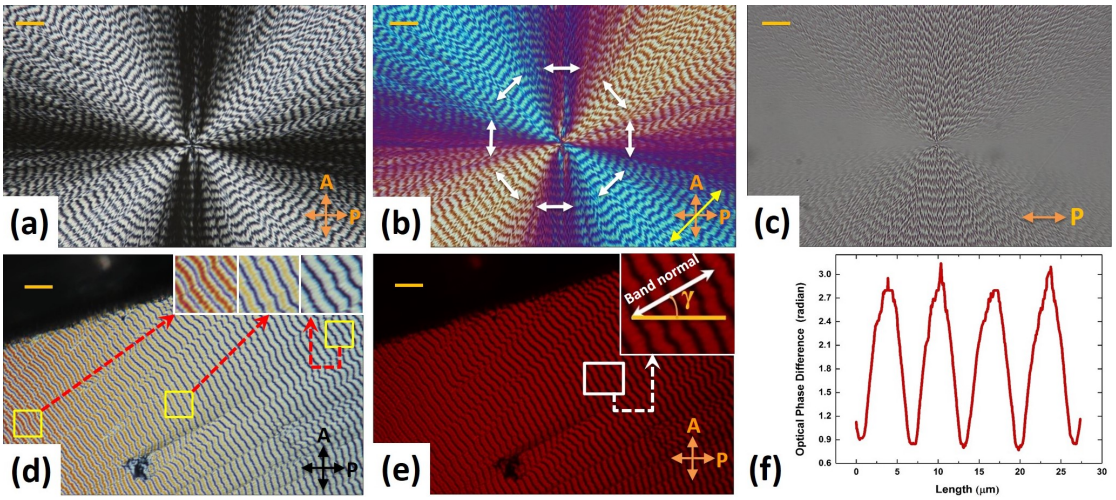


Figure 4.1: The POM textures of banded spherulite of compound 8OCB at room temperature (a) between crossed polarisers, (b) between crossed polarisers and a λ plate, and (c) with only the polariser in the optical path. The white double-headed arrows in (b) indicate the orientations of major refractive index around the seed. (d) The POM texture of a banded spherulite domain between crossed polarisers for relatively thicker sample at room temperature. The insets show the variation of color in the bands in three different regions with slightly different sample thickness. (e) The same as in (d) with a red filter introduced in the optical path. The inset shows the variation of light intensity along the band normal which makes an angle γ with the polariser. (f) The variation of optical phase difference along the radial direction of the banded spherulite shown in (e). All scale bars are 20 μm.

The bright-field image of the sample is shown in fig. 4.1c with only the polariser in the light path. In this figure, the bands have low (high) optical contrast where band normal is parallel (perpendicular) to the polariser. This observation indicates that the radial component of refractive index does not vary appreciably along the radial direction. The strong variation of the azimuthal component along the radial direction produces the undulation of the birefringence in the banded spherulite.

For relatively thicker sample, there are multiple interference color rings in a given spherulitic band as shown in fig. 4.1d. The insets in fig. 4.1d are the magnified view of these interference color rings in three regions with slightly different sample thickness. The variation of phase retardation in the texture can be measured from the intensity variation by introducing a red filter in the light path of the POM. Fig. 4.1e is the POM image of the spherulite domain with a periodic variation of intensity along the radial direction of the spherulite. The inset in fig. 4.1e depicts the magnified view of the marked region of this domain where the band normal

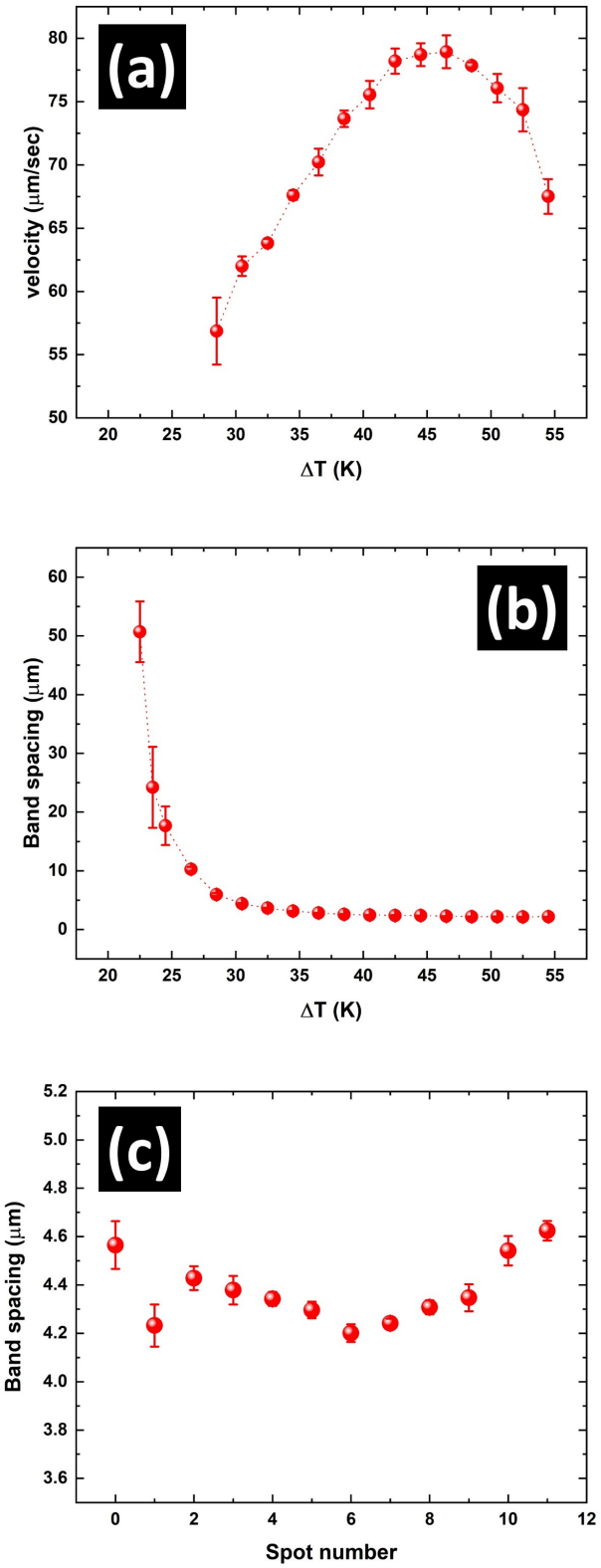


Figure 4.2: (a) Growth velocity of banded spherulite at different supercooling. (b) The band spacing of banded spherulite formed at different supercooling. (c) Band spacing of banded spherulite of 8OCB at different spots along the length of a wedge cell.

makes an angle $\gamma = 30.5^{\circ}$ with respect to the polariser. Using this known value of γ, the phase retardation introduced by the sample can be calculated from the following formula,

$$I = I_0 sin^2(2\gamma) sin^2(\phi/2) + I_d, \tag{4.1}$$

where I_0, I and I_d are the incident, measured and the dark background intensities with crossed polarisers respectively. The phase retardation $\phi = 2\pi d\Delta n/\lambda$, where d is the sample thickness, Δn is the effective linear birefringence of the sample and λ is the wavelength of incident light. At first, the dark background intensity was measured in the sample free area of the cell and it was subtracted from the intensity profile. As the interference colors of bands (without red filter) belong to the first order of Levy chart hence at maximum intensity (with red filter) along the band normal, $\phi = \pi$. This allows us to calculate I_0. The known I_0 was used further to calculate the variation of retardation along the band normal from the measured intensity profile along the same direction as shown in fig. 4.1f. The variation of sample thickness for the selected small region shown in the inset of fig. 4.1e is negligible. Therefore, the oscillation of phase retardation across the bands mainly arises due to the variation of the birefringence in the sample.

The velocity of the growth front of the banded spherulite formed in isothermal condition at different supercooling is shown in fig. 4.2a. This velocity increases initially with increasing supercooling. After reaching around 80 μm/sec, it starts to fall with further supercooling. This kind of temperature variation of growth velocity has also been found in spherulitic growth of polymeric systems [19]. In these systems, growth velocity is controlled by the driving force for nucleation and the transportation of polymeric chains to the growth front. With increasing supercooling, this driving force increases whereas the mobility of polymeric chain diminishes simultaneously. Hence at lower supercooling, the growth velocity of polymeric spherulite is dominated by nucleation process which increases with increasing supercooling. On the other hand at higher supercooling, this growth phenomenon is dominated by transportation of polymer chains which decreases with increasing supercooling. The

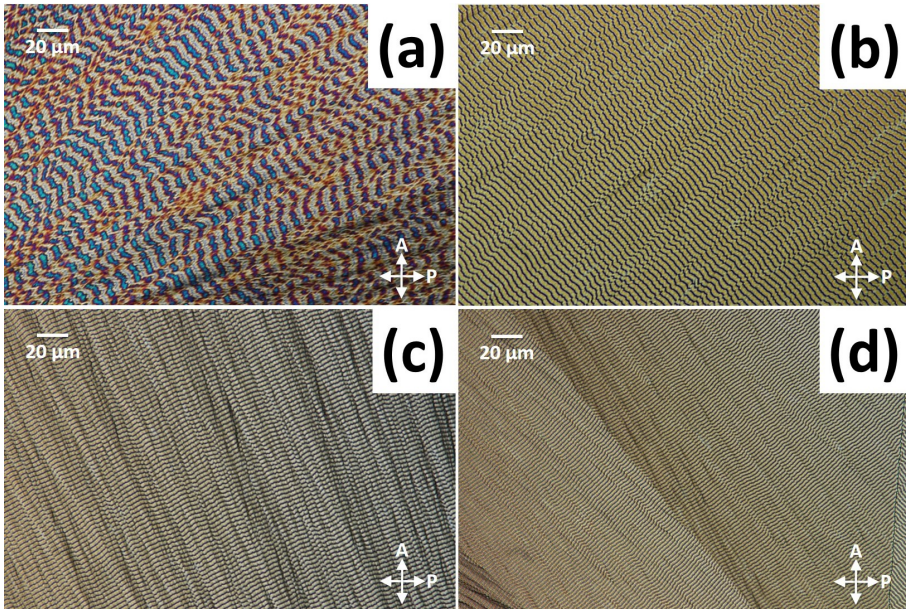


Figure 4.3: The banded spherulite of 8OCB formed at ΔT = (a) 26 K, (b) 30 K, (c) 34 K, (d) 42 K.

competing effects of these two process can give rise a non-monotonic variation with a peak of the growth velocity as a function of supercooling. The non-monotonic variation of growth velocity with supercooling observed in our sample can perhaps be explained using similar mechanisms proposed for the polymeric systems.

The spacing between successive bands depends on supercooling ($\Delta T = T_c - T$) of the sample as shown in fig. 4.2b. The banded spherulite in our sample was found to form for supercooling of at least 22.5 K below the melting point. Fig. 4.3 shows POM textures of banded spherulite of 8OCB formed at different supercooling. The band spacing at higher supercooling ($\Delta T \sim$ 35 K - 55 K) is around 3-4 μm which tends to diverge on approaching ΔT = 22.5 K from above.

To study the variation of band spacing with thickness of the sample, the banded spherulite of the compound was formed in a wedge shaped cell. The interference colour of bands near the thinner edge of the cell belongs to the first order of Levy chart whereas near the opposite edge of the cell, this colour belongs to the higher order of Levy chart as shown in fig. 4.4. This signifies an increasing sample thickness along the 11 mm length of the wedge shaped cell. We measured the band spacing of the sample at few equidistant spots along the length of the wedge as shown in

fig. 4.2c. The distance between two successive spots was 1 mm and the spots were counted from the thinner edge of the sample. As can be seen from fig. 4.2c, the band spacing of the spherulite is independent of the thickness of the sample.

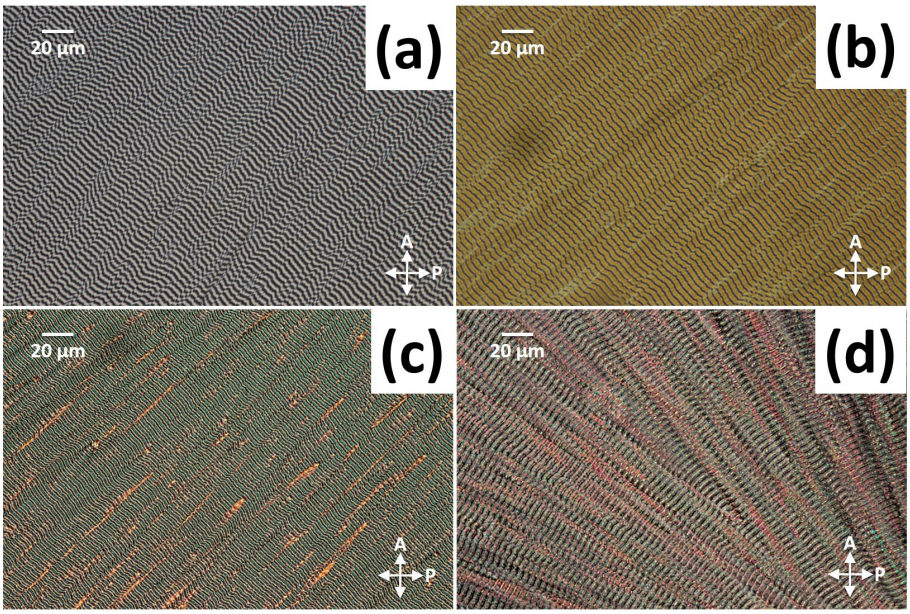


Figure 4.4: The POM textures of the banded spherulite of 8OCB in a wedge shaped cell at spot number (a) 0, (b) 4, (c) 7 and (d) 11 along the increasing thickness of the cell.

Formation of continuous non-banded spherulite

As mentioned earlier, the banded spherulite does not form for $\Delta T < 22.5$ K. Instead a non-banded continuous spherulites were found to be formed for lower values of supercooling of the sample. Fig. 4.5a shows the POM texture of a continuous spherulite of the compound formed from its melt sandwiched between two coverslips at ΔT = 22.5 K. The black brushes of the Maltese cross parallel to the polarisers remain invariant on rotating the sample on the microscope stage. The interference colours of this continuous spherulite domain belong to the first order of the Levy chart. After introducing the phase plate, the colour of the first and third quadrant remained in first order of Levy chart whereas the colour of second and fourth quadrant was changed to the second order of Levy chart as shown in fig. 4.5b. An effective subtraction and addition of optical path differences in sample and the phase plate respectively transformed the colour of these pairs of quadrants accordingly. Hence

the major index on the sample plane is along the azimuthal direction as shown by the yellow double headed arrows around the seed of the domain (fig. 4.5b). Therefore, this continuous spherulite of the compound is also optically negative. Fig. 4.5c shows the bright field image of this continuous spherulite where only a polariser was inserted in the optical path. Here the texture of the domain has clear contrast along the direction perpendicular to the polariser's pass axis. But the contrast is relatively low along the direction of polariser. Similar behaviour was also observed for banded spherulite of this compound as discussed earlier.

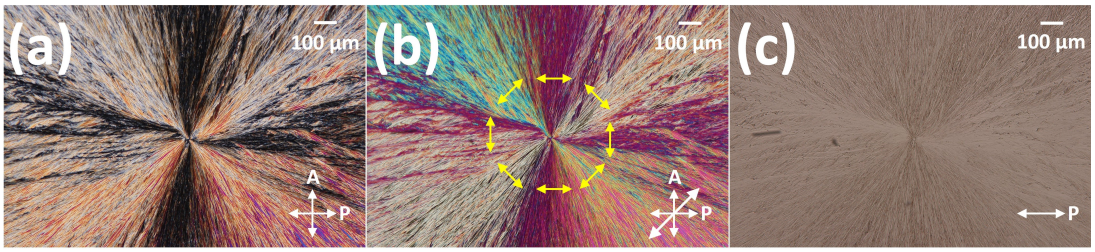


Figure 4.5: Continuous non-banded spherulite formed at $\Delta T = 22.5$ K (a) between crossed polarisers, (b) between crossed polarisers with λ-plate and (c) only polariser in the optical path.

POM studies of heating effects on the banded spherulite

The banded spherulite of 8OCB was found to transform irreversibly to non-banded continuous spherulite on heating. Fig. 4.6 shows the textural changes of a banded spherulite across such transformation. Fig. 4.6a shows the POM texture of the banded spherulite initially formed at room temperature. This sample was then heated to 325 K and held at that temperature for 1 hour which transformed the banded spherulite to a non-banded one. The non-banded spherulite texture persists on subsequent cooling of the sample to the room temperature. Fig. 4.6b shows the POM texture of this continuous spherulite. The interference colour of this spherulite belongs to the first order of the Levy chart. The black brushes of the Maltese cross parallel to the polarisers remain invariant on sample rotation. It indicates that the major index on the sample plane is either parallel or perpendicular to the radial direction of the domain. After introducing the phase plate in the optical path, the

colour of the first and third quadrants changed to orange whereas second and fourth quadrants changed to blue (see fig. 4.6c). These interference colours belonging to first and second order of Levy chart respectively indicate that the optical path differences at sample and phase plate show an additive and subtractive nature at these respective pairs of quadrants. Hence the major index on sample plane is lying along the azimuthal direction of the domain same as the banded spherulite domain. Fig. 4.6d shows the bright field image of this continuous spherulite domain after introducing a polariser before the sample. Here, the domain along its radial direction perpendicular to the direction of incident polarisation of light has clear contrast than that parallel to the direction of polarisation. This is also same as found in the bright field image the banded spherulite shown in fig. 4.1c.

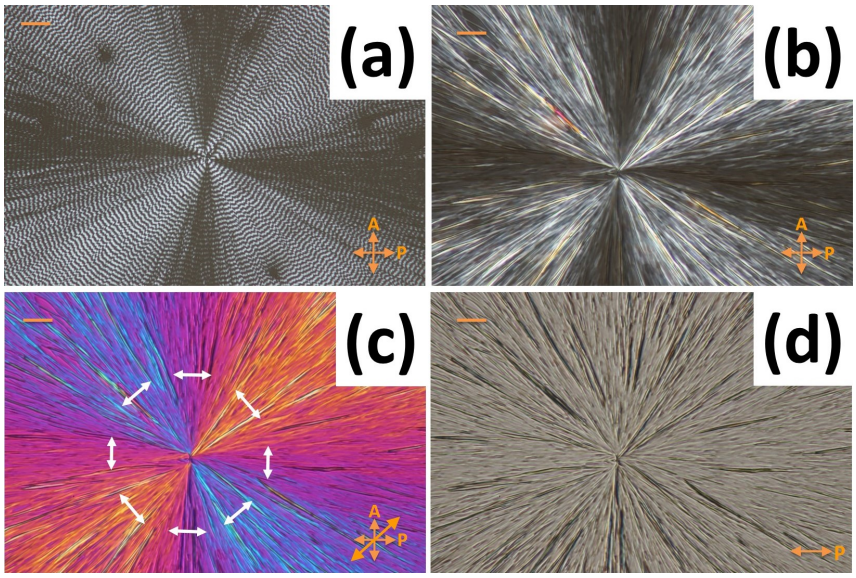


Figure 4.6: The POM textures of (a) 8OCB banded spherulite between crossed polarisers. The POM textures of non-banded spherulite formed at 325 K (b) between crossed polarisers, (c) between crossed polarisers and the λ-plate and (d) only with a polarised in the optical path. All scale bars are 20 μm.

POM studies of aging effects on the banded spherulite

The banded spherulite structure in our sample is found to be metastable in nature. It slowly transforms to the non-banded continuous spherulite with time. Fig. 4.7a shows the POM texture of the banded spherulite of 8OCB just after its formation between two coverslips at room temperature. The sample was then kept

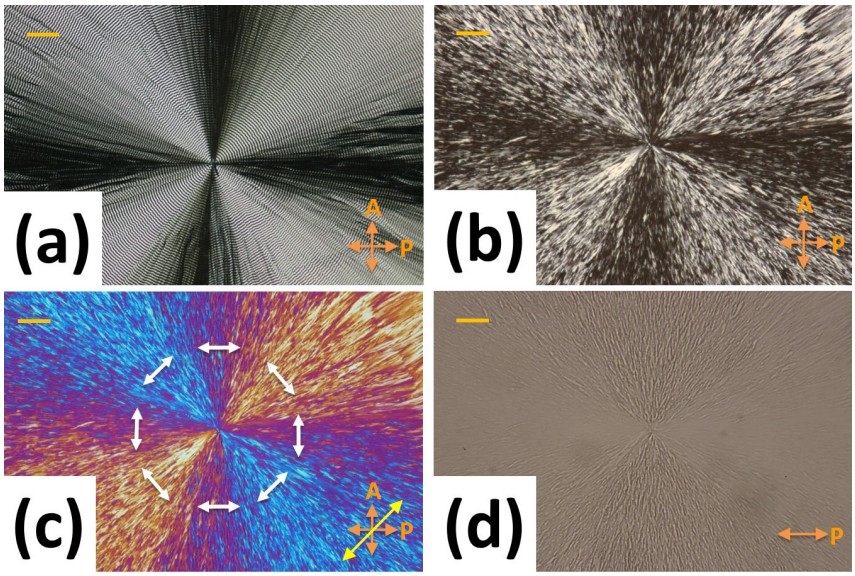


Figure 4.7: (a) 8OCB banded spherulite between crossed polarisers. The same spherulite after 73 days (b) between crossed polarisers, (c) between crossed polarisers and a phase plate and (d) with only a polarised in the optical path. All scale bars are 20 μm.

at room temperature for 73 days. The POM texture of this spherulite after 73 days is shown in fig. 4.7b. On ageing, the banded structure of the spherulite changed to the non-banded continuous spherulite. The black brushes of the Maltese cross in this texture always remain parallel to the polarisers on rotating the sample. It implies that the major index is either parallel to the radial or azimuthal direction of the domain. The interference colour of the four quadrants formed by Maltese cross in this transformed continuous spherulite belongs to the first order of Levy chart. On introducing a phase plate in the optical path, the colour of the first and third quadrants was changed to orange whereas second and fourth quadrants were changed to blue (see fig. 4.7c). These colours belong to the first and second order of Levy chart respectively which indicates that in these pair of quadrants the path differences show subtractive and additive nature respectively. Therefore, the major index lying on the sample plane is along the azimuthal direction of the domain as shown by the double headed white arrows in fig. 4.7c. The bright field image of this non-banded continuous spherulite with only a polariser in the optical path is shown in fig. 4.7d. The texture has clear contrast along the radial direction of the domain perpendicular to the polariser's pass axis whereas in the parallel direction

the domain has less contrast. This is also observed in the case of banded spherulite of the compound.

Core structure of the banded spherulites

The spherulite starts to grow from a point giving rise to a defect core structure. The different types of core structures have been observed. Fig. 4.8a shows a point like core structure observed in the banded spherulite of our sample. Sometimes the core region of banded spherulite shows sheaf like or double leaf like structure as shown in fig. 4.8b. The bands in the spherulites of our sample generally form concentric rings although the formation of spiral bands has also been noticed as shown in fig. 4.8c.

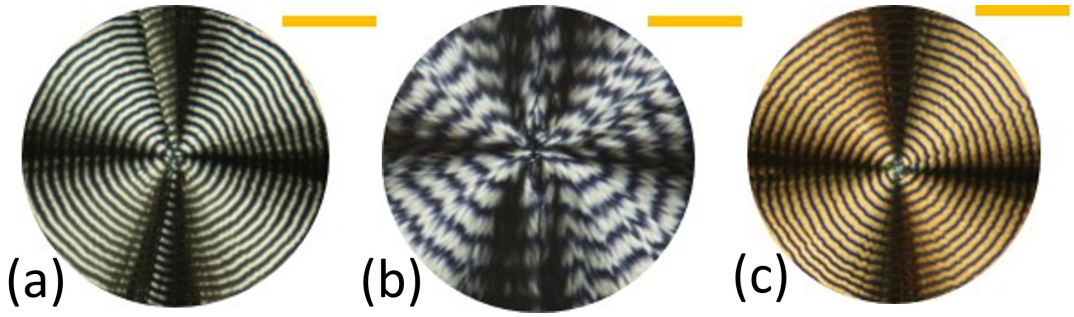


Figure 4.8: (a), (b) and (c) show the different morphologies of 8OCB banded spherulite. All scale bars are 20 μm.

4.3.2 Scanning electron microscopy studies

Scanning electron microscopy studies are performed to observe the surface topography of the samples beyond the optical resolution limit. The POM studies of banded spherulite as discussed above show that a periodic variation of birefringence along its radial direction gives rise to the concentric interference colour bands between crossed polarisers. The detail of structural variation giving rise to the bands in the spherulite can not be probed by optical microscopes due to its limited resolution. Therefore, SEM studies were performed on these banded spherulite to observe the structural variation. The FESEM studies of the banded spherulite domain showed a coexistence of two different phases. Here, fibrillar crystallites oriented along the

radially outward direction of the spherulite domain are embedded in a solid amorphous phase as shown in fig. 4.9a. This figure also shows concentric bands with same periodicity as that found in POM studies. The bands in the spherulite arise from the periodic growth of crystallite-rich and crystallite-poor concentric zones as indicated by "A" and "B" respectively in fig. 4.9a. In crystallite-rich bands, the composition of fibrillar crystallites are more than that of the amorphous component whereas crystallite-poor bands are rich with amorphous phase. Similar repetitive structure was also found in the FESEM texture of the cross-sectional surface area of the sample (fig. 4.9b) showing its bulk nature. The FESEM texture of the cross-sectional area of this banded spherulite shown in fig. 4.9c exhibits a clear evidence of amorphous phase present in this domain. The crystallites have length similar to the periodicity of the bands while its width varies from 100 nm to 300 nm.

The cryo-SEM studies of the sample was carried out on quenching it from its isotropic liquid phase. In this process, the sample in its isotropic liquid phase was immediately dipped in liquid nitrogen and then it was transferred to the cryo-preparation chamber of the SEM setup for further processing which has been discussed in section 4.2. Fig. 4.9d shows the cryo-SEM image of the banded spherulite formed in the quenched sample. It can be seen from this picture that the composition of nano-fibrils in this spherulite is relatively lesser than that found in banded spherulite of the sample formed at room temperature. On the other hand, the composition of amorphous phase is relatively higher in this quenched sample than that found in normal spherulites. These give rise to a relatively smooth textured banded spherulite than that shown in fig. 4.9a and fig. 4.9b.

Some polymers and a few small molecular systems exhibit concentric color banded spherulites in which organized twisting of fibrillar units along their long axis has been observed as the mechanism of the band formation [6, 19, 20, 32–37]. In some small molecular systems, a periodic variation of orientation of individual crystallites has been reported to produce concentric color bands [104, 105]. But in our sample, neither twist nor periodic change of orientation of fibrillar crystal-

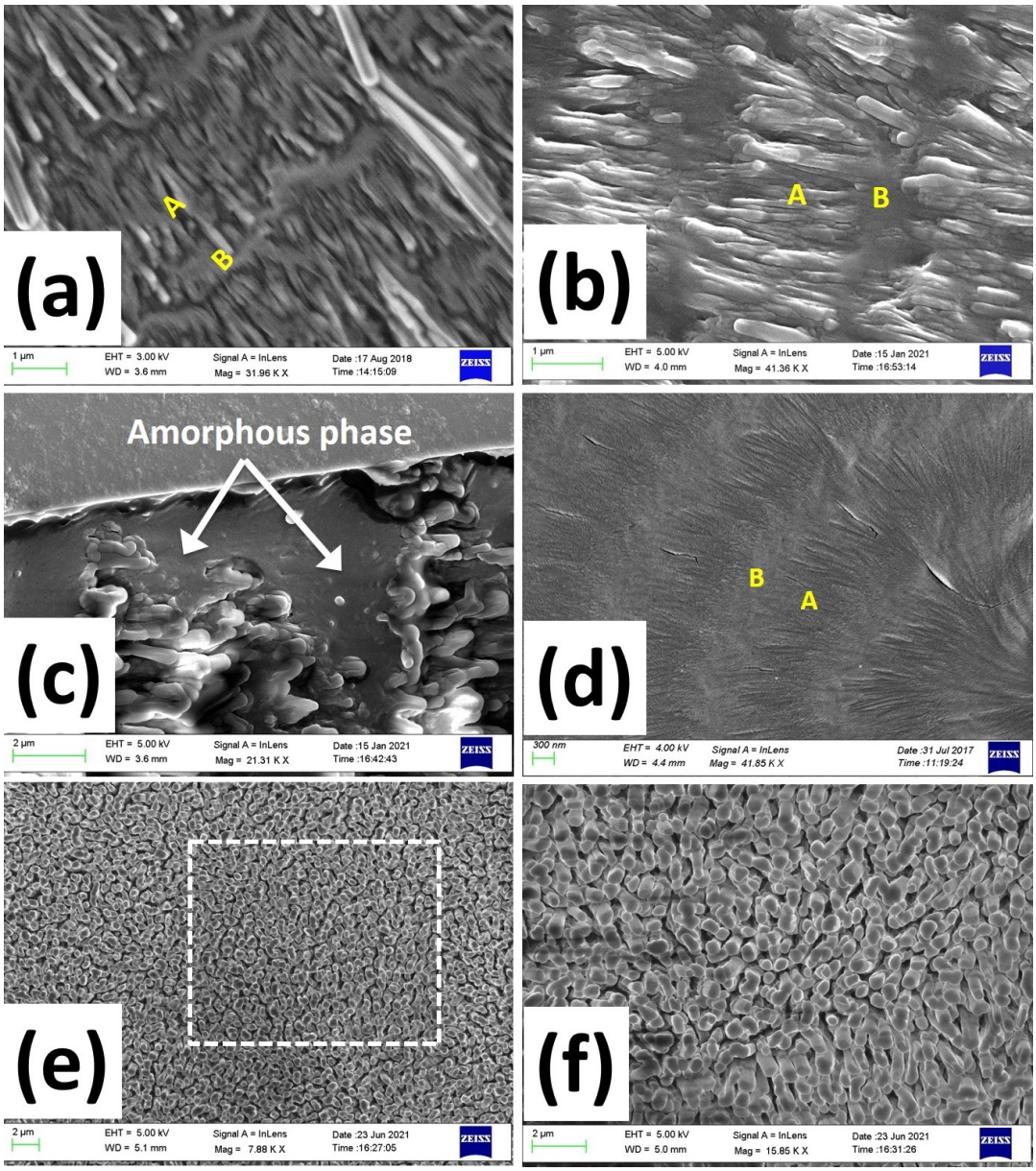


Figure 4.9: The FESEM image of (a) the top surface of a banded spherulite and (b) the cross-sectional view of a banded spherulitic obtained from the cleaved surface showing the bulk structure. (c) The cross section of banded spherulite showing amorphous domain. (d) The cryo-SEM image of 8OCB banded spherulite formed after quenching the sample in isotropic phase. "A" and "B" zones represent the crystallite-rich and crystallite-poor concentric bands. (e) The cross section of fibrillar crystallites in banded spherulite. (f) The selected area in figure (e) with higher resolution.

lites is found. The FESEM studies depict that the rhythmic growth of concentric crystallite-rich and crystallite-poor zones produces the banded spherulite of 8OCB. The periodic change in birefringence along the radial direction due to these concentric zones gives rise to the interference color bands observed between crossed

polarisers. The crystallite-poor regions possess least birefringence due to their predominant amorphous nature while the crystallite-rich zones have larger birefringence due to the presence of a large number of radially aligned crystallites.

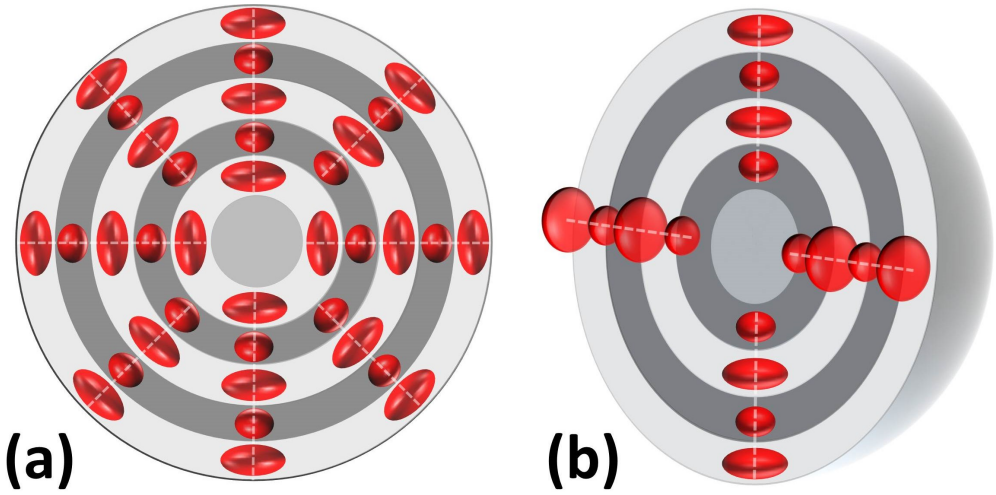


Figure 4.10: Indicatrix ellipsoid in banded spherulite. The schematic representation of the variation of optical indicatrix along the radial direction of the banded spherulite of the compound 8OCB. The (a) top and (b) side views showing the uniaxial oblate indicatrix with radially oriented optic axes.

Fig. 4.10 shows the schematic representation of the variation in the refractive index ellipsoid along the radial direction of the banded spherulite. The FESEM studies revealed that the elliptical or rectangular cross sections of radially aligned fibrillar crystallites are oriented randomly about their long axis (see fig. 4.9e,f) giving rise to a uniaxial structure about the radial direction. The POM studies showed that the azimuthal component of the refractive index is larger than the radial component in the spherulite. Hence, the banded spherulite of 8OCB possesses a uniaxial oblate indicatrix with a radially oriented optic axis as shown in fig. 4.10. The radial component of the refractive index does not vary appreciably along the radial direction but the periodic variation of the transverse component gives rise to the modulation in the birefringence of the sample as observed in fig. 4.1c. This birefringence modulation causes the concentric interference colour bands as shown schematically in fig. 4.10.

As can be seen from fig. 4.1c, the bands illuminated by plane polarised light exhibit less contrast when band normal is parallel to the direction of polarisation whereas they acquire good contrast when their normal is perpendicular to the direction of polarisation. This observation can be explained by assuming that the refractive index of the amorphous domain is close to that along the longitudinal direction of the fibrillar crystallites whereas its transverse component of refractive index is different from that of amorphous phase. The same arguments can be used to explain the bright field images of non-banded continuous spherulites of this compound with only the polariser in the optical path as discussed above.

SEM studies of heating effect on banded spherulite

The 5 μl of 1 wt% 8OCB solution in chloroform was dropcasted on an ITO coated glass plate and it was left for complete solvent evaporation. The sample was then kept at 333 K for 10-15 minutes which evaporates unwanted residue of solvent present in the sample. The sample was then cooled to room temperature to produce banded spherulite. To study the effect of heating on the this banded spherulite, it was held at 325 K below its melting point (327.5 K) for 1 hour followed by cooling it to room temperature. The POM studies of this sample confirmed that the concentric banded structure had completely transformed to the non-banded continuous spherulite. Fig. 4.11a,b show the SEM textures of this non-banded spherulite which also confirm the absence of bands. The length of the radially aligned fibrillar crystallites in this non-banded spherulite has increased compared to that found prior to this heat treatment. There was no twist in these crystallites.

SEM studies of aging effect on banded spherulite

The banded spherulites on ITO coated glass plates were formed by the same method as discussed above and kept for 73 days at room temperature. On aging, the banded spherulites were found to transform to the non-banded spherulite as confirmed from POM studies. The FESEM studies were also performed to confirm these obser-

vations. Fig. 4.11c,d show the FESEM textures of a domain of these non-banded spherulites where no bands were found. The radially aligned fibrillar crystallites has increased longitudinally by many times of its initial length. Any twist in these extended fibrillar crystallites was not found.

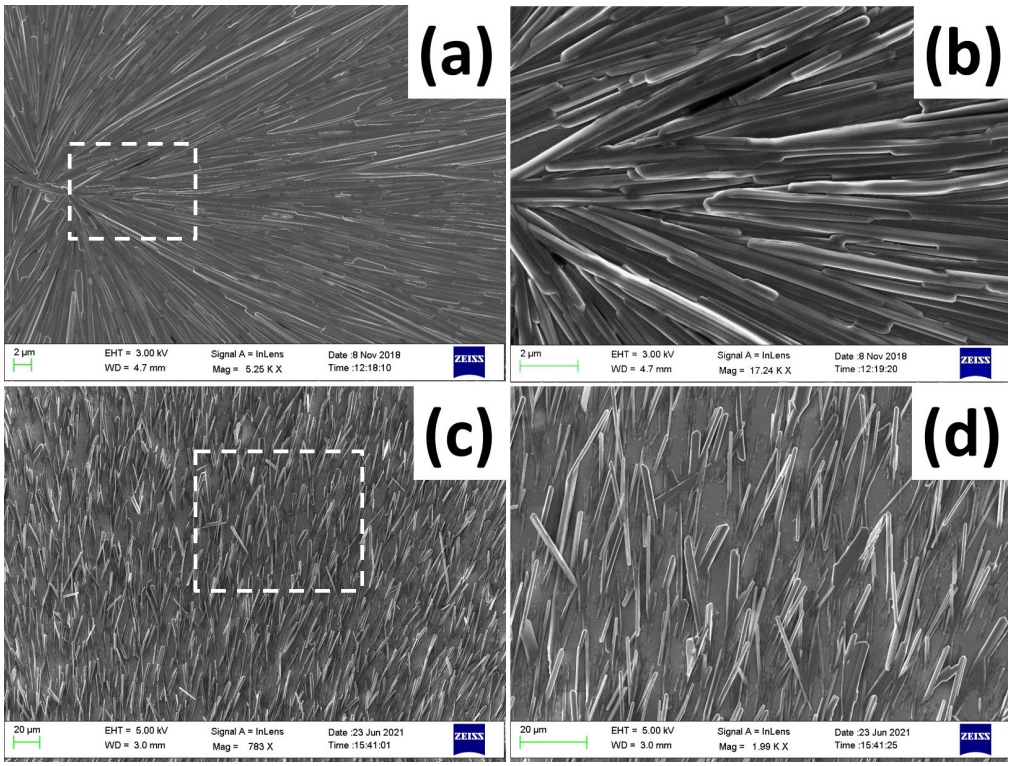


Figure 4.11: (a) The non-banded continuous spherulite formed after keeping the banded spherulite of 8OCB at 325 K for 1 hour followed by cooling it at room temperature. (b) The selected region in figure (a) with higher magnification. (c) Non-banded spherulite formed after keeping the banded spherulite for 73 days at room temperature. (d) The marked region in figure (c) in higher magnification.

4.3.3 X-ray diffraction studies

The x-ray diffraction studies were performed to identify the crystal structure of the banded spherulite of 8OCB. The XRD profile of the banded spherulite as shown in fig. 4.12 is identical to that of the commercial powder or CP crystal phase of 8OCB. As discussed in chapter 3, the CP crystal phase of the compound is composed of fibrillar nano-crystallites embedded in its own amorphous solid state. All the peaks observed in the XRD profile of the banded spherulite match with those of the CP crystal phase of this compound. These XRD peaks with the corresponding Miller

indices are associated with the monoclinic crystal structure of the nano-crystallites. The amorphous component shows only a broad hump from 11 nm^{-1} to 21 nm^{-1} in this XRD profile. Thus the XRD studies confirm that the banded spherulite of the compound has similar composition as that of its CP crystal phase. The bands are formed due to the periodic variation of composition of nano-crystalites and the amorphous state.

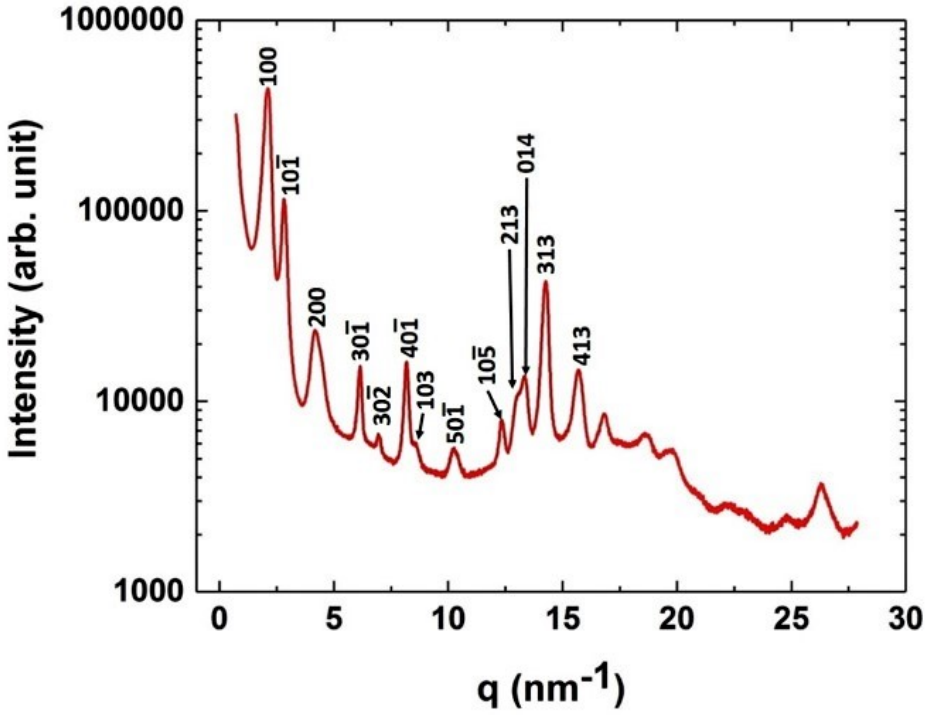


Figure 4.12: XRD profile of banded spherulite of 8OCB.

4.3.4 Fluorescence microscopy studies

The fluorescent image of a banded spherulite domain [see fig. 4.13a] was obtained by doping the sample with a fluorescent dye (rhodamine 6G). It shows a periodic variation of dye concentration along the radial direction of the spherulite domain. The crystallite-rich zones are found to have higher concentration of dye molecules compared to the crystallite-poor zones which makes these zones brighter and darker respectively in the fluorescent image. The advection of the dye molecules during the growth of crystallite-rich and crystallite-poor zones perhaps can explain their

distribution in the banded spherulite of the sample. The density in crystallite-rich zones is higher compared to that in crystallite-poor regions. Thus the growth of a crystallite-rich band produces a diffusive current which advects the dye molecules from the leading edge of the growth front that gives rise to the higher density of the dye molecules in this band. The depletion of molecular density promotes the formation of crystallite-poor zones with lower density of the dye molecules. The repetition of these processes leads to the formation of banded spherulite in this sample. Therefore, the fluorescent microscopy studies support the rhythmic growth mechanism of formation of banded spherulite in our sample.

Fluorescence microscopy studies of heating effect on banded spherulite

The transformation of banded spherulite to non-banded structure as found in SEM studies was also probed using fluorescent microscopy studies. The fluorescent dye (rhodamine 6G) doped banded spherulite of the compound was formed at room temperature between two coverslips. The sample was then kept at 325 K for 10 minutes followed by cooling it to room temperature. The POM studies on this sample showed absence of banded texture thus confirming the complete transformation of banded spherulite to the non-banded continuous one. Fig. 4.13b shows the fluorescent image of this continuous spherulite where no periodic distribution of dye molecules was found. Hence the fluorescent microscopy studies also confirm the destruction of the band structure on heating the sample to its pre-transitional temperature region giving rise to the continuous spherulite.

Fluorescence microscopy studies of aging effect on banded spherulite

As discussed above, the banded spherulite was also found to transform to the non-banded spherulite on aging the sample at room temperature. To study this effects using fluorescent microscopy, the dye doped banded spherulite was formed at room temperature between two coverslips. This sample was then kept at room temperature for 105 days. Fig. 4.13c depicts the fluorescent image of this aged spherulitic

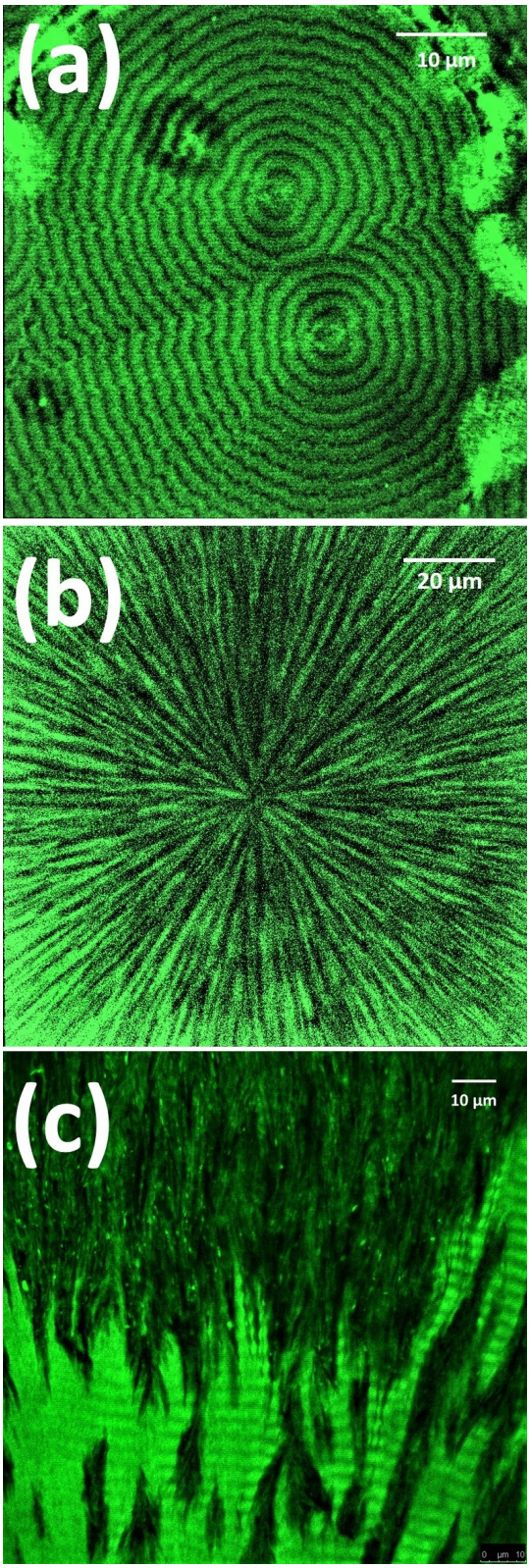


Figure 4.13: (a) Fluorescent image of banded spherulite doped with rodamine 6G. (b) Fluorescent image of the non-banded spherulite formed after keeping the banded spherulite at 325 K for 10 minutes. (c) Fluorescent image of the banded spherulite after keeping it for 105 days at room temperature showing its transition to non-banded spherulite.

domain showing the transformation of the banded spherulite to non-banded structure. As can be seen from this figure, the non-banded texture with uniform distribution of dye molecules grows at the expanse of the banded texture with periodic variation in the dye density. Therefore, the distribution of the dye molecules in the sample changes with changing morphology of the banded structure.

4.3.5 Raman studies in banded spherulite

Raman spectroscopic studies were performed to characterize the banded spherulite of 8OCB obtained from its melt. The Raman spectrum of the banded spherulite is shown in fig. 4.14a. The four intense Raman peaks were found in the wave number range 200–3200 cm^{-1}. These peaks are positioned at 1185 cm^{-1}, 1285 cm^{-1}, 1607 cm^{-1} and 2234 cm^{-1} respectively. The first peak is associated with in-plane deformation of CH bonds attached with biphenyl moiety [93]. Second peak is a combination band of symmetric and asymmetric perpendicular deformations of CH_2 group attached in aliphatic chain [93]. The third peak is for quadrant stretching vibration associated with biphenyl moiety and the last one is for CN stretching vibration respectively [93, 94]. The position of all these peaks are same as that found in CP phase of 8OCB discussed in chapter 3. The doublet peak near 400 cm^{-1} as shown in the inset of fig. 4.14a is for the stretching vibration of the twisted biphenyl moiety [88]. The pair of component peaks positioned at 822 cm^{-1} and 836 cm^{-1} is associated with two different perpendicular deformation modes of CH bonds linked with the phenyl rings of the 8OCB molecule [93]. The peaks from 2830 cm^{-1} to 3100 cm^{-1} are associated with CH stretching vibration [84]. All these peak positions are same as found in CP phase of the compound. Hence the Raman spectrum of banded spherulite confirms that the banded spherulite structure of the sample has the same composition as that found in the CP phase of the compound.

A sample with banded spherulite structure was heated to 325 K and kept for 1 hour at this temperature followed by cooling it to room temperature. This process transformed the sample to the non-banded continuous spherulite. Fig. 4.14b shows

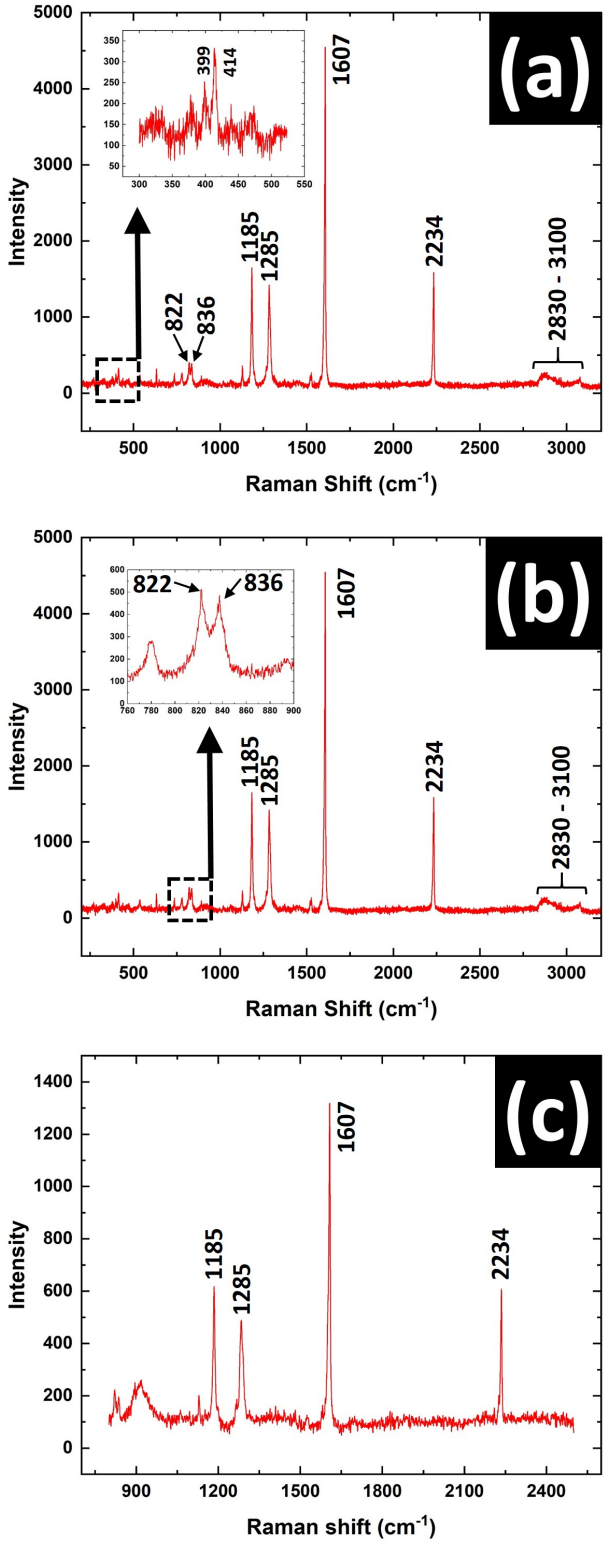


Figure 4.14: Raman specta of (a) the banded spherulite of 8OCB, (b) the non-banded spherulite formed after keeping the banded spherulite at 325 K for 10 minutes and (c) the non-banded spherulite formed after keeping the banded spherulite at room temperature for 73 days.

the Raman spectrum of this continuous non-banded spherulite. All the Raman peaks as mentioned above are observed at the same positions as found in the Raman spectrum of banded spherilite. This implies that the phase of the sample remains the same in this banded to non-banded spherulite transformation during heating.

To study ageing effects, a banded spherulite of the sample was kept at room temperature for 73 days. The POM studies of this aged sample confirmed the transformation of banded spherulite to non-banded continuous spherulite. Fig. 4.14c shows the Raman spectrum of this transformed non-banded spherulite. All the Raman peaks observed for the banded spherulite are also found in the continuous spherulite domain at the same positions. This result implies that the composition of continuous spherulite obtained on aging the sample is same as the composition of banded spherulite of the CP phase.

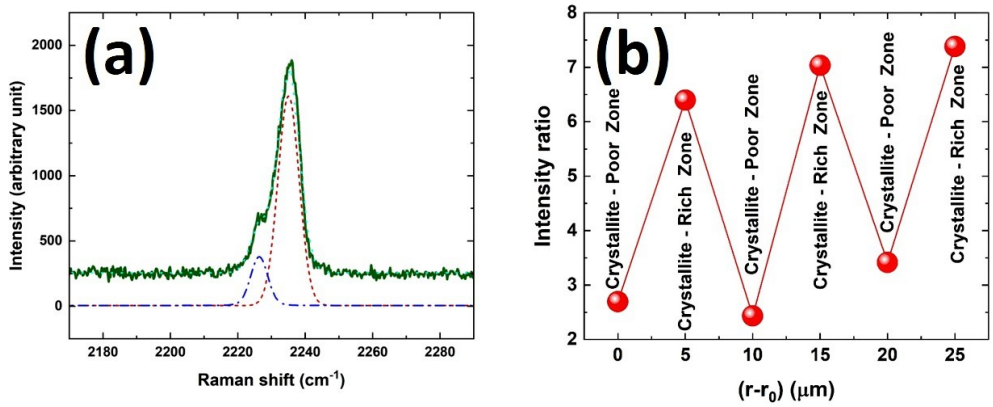


Figure 4.15: (a) The asymmetric Raman peak for CN stretching vibration in banded spherulite of 8OCB fitted by two Voigt functions. (b) The variation of intensity ratio of the fitted Raman peaks associated with the CN group of the molecules at few consecutive crystallite-rich and crystallite-poor bands along radial direction of the banded spherulite where r_0 is an initial point of measurement.

The Raman peak for stretching vibration of nitrile group (CN) of 8OCB is reported to be quite sensitive to the local molecular environment [83]. This Raman peak is asymmetric in the banded and non-banded spherulites and can be fitted by two closely spaced peaks as shown in fig. 4.15a. The fitted intense peak at 2235 cm^{-1} is due to the fibrillar crystallites whereas the shoulder peak at 2226 cm^{-1} arises from the solid amorphous phase of the spherulite same as found in the CP

phase (see chapter 3). These peaks for stretching vibration of CN bond were used to examine the spatial variation of composition of two different phases along the radial direction of the banded spherulite domain of the compound. The ratio of the intensities of these peaks obtained in the crystallite-rich and crystallite-poor zones along the radial direction of the banded spherulite is shown in fig. 4.15b. The higher and lower values of this intensity ratio at crystallite-rich and crystallite-poor zones respectively indicate the periodic variation of the compositions along the radial direction of the banded spherulite.

4.3.6 Dielectric studies

The temperature variation of dielectric constant of the banded spherulite sample is shown in fig. 4.16. The thickness of the sample was 5 μm and it was formed at room temperature in a commercially available planner aligned liquid crystal cell (Instec Inc). The dielectric measurements were carried out on heating the sample from its solid phases. The compound forms various stable and metastable solid phases from its melt during cooling. Hence the determination of the initial solid phase under study is necessary for proper interpretation of the experimental results. Our dielectric measurement setup has an advantage of examining the phase of the sample by looking it simultaneously under microscope. This phase determination is not possible in differential scanning calorimetry studies which probes the first order transitions with high accuracy.

In the dielectric profile, a sudden change of slope was observed at 318 K indicating a transformation in the sample [see inset in fig. 4.16]. But no change in the POM textures of the banded spherulites was found at this temperature. We attribute it to the softening of the amorphous component of the sample. On further heating, the bands started to become blurred irreversibly at 321 K and the texture transformed completely to non-banded spherulite at 325 K. The FESEM studies of this non-banded spherulite revealed that the length of the radially aligned fibrillar crystallites was increased and their distribution was uniform along the radial direction giving

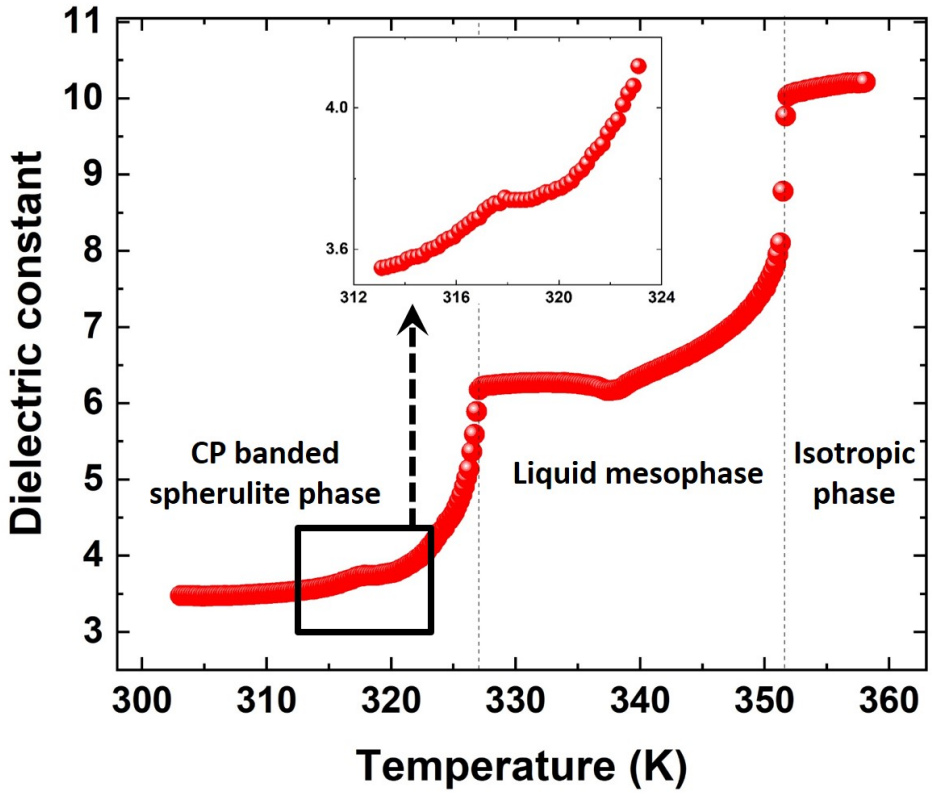


Figure 4.16: The temperature variation of dielectric constant of the banded spherulite during heating of the sample. The inset highlights the step change in dielectric constant at 318 K.

rise to the non-banded texture (see fig. 4.11a). Thus the amorphous component after softening gradually transforms to the crystallites and smectic phase on heating as discussed in chapter 3. This accounts for the observed increase in dielectric constant with increasing temperature before complete melting of the sample to the smectic phase at 327.5 K.

After this transition, the dielectric constant remains almost constant in smectic phase. Its value in the planner configuration gradually increases with temperature after smectic to nematic phase transition due to the decrease in the orientational order till the nematic to isotropic phase transition at 353 K. Above this transition, molecules do not possess any long range order in the isotropic phase and the value of dielectric constant remain almost constant on further heating.

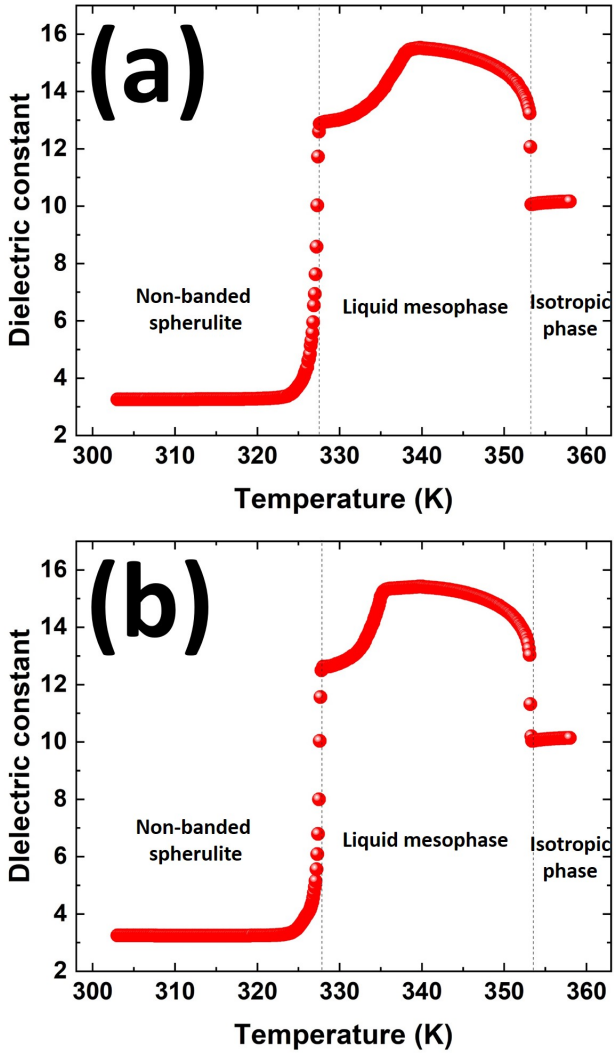


Figure 4.17: The temperature variation of dielectric constant of non-banded spherulite (a) formed after keeping banded spherulite of 8OCB at 325 K for 1 hour followed by cooling it at room temperature. (b) formed after keeping the banded spherulite at room temperature for 1 year.

Dielectric studies of heating and aging effect on banded spherulite

The banded spherulite of the compound formed in a homiotropic liquid crystal cell (Instec Inc.) was heated to 325 K and kept at that temperature for 1 hour. The sample was then cooled to room temperature. The POM studies confirmed that the banded spherulite in this process changed to non-banded continuous spherulite. The temperature variation of dielectric constant of this sample during heating is shown in fig. 4.17a. The dielectric profile obtained for this sample is very similar to that

found in CP phase of the compound (see fig. 3.9b in chapter 3). This result indicates that the non-banded spherulite is basically the CP phase of the compound.

The dielectric properties of the aged banded spherulite of the sample was also studied using commercially available homeotropic liquid crystal cell. The banded spherulite of the compound formed in the LC cell was kept for one year at room temperature for aging. After one year, the banded spherulite was completely transformed to non-banded continuous spherulite as confirmed from the POM studies. The temperature variation of dielectric constant of this transformed sample during heating is shown in fig. 4.17b. Similarity of this profile with that found in CP phase (see fig. 3.9b in chapter 3) of this compound confirms its identity.

4.4 Conclusion

We have studied the banded spherulitic growth of the most stable solid phase of pure 8OCB liquid crystalline compound from its melt during cooling. A variety of experimental techniques such as POM, XRD, SEM, Raman spectroscopy etc. were used to characterise the sample. The compound exhibits coexistence of fibrillar nano-crystallites and an amorphous phase in its most stable solid state at room temperature. The banded spherulites are formed due to the rhythmic generation of crystallite-rich and crystallite-poor concentric zones on supercooling the smectic phase of the compound. In crystallite-rich zones, the density of fibrillar crystallites are more and crystallite-poor zones are rich with amorphous phase. This produces the modulation in birefringence which gives rise to the concentric interference color bands with periodic variation of colours observed between crossed polarisers. Generally banded spherulites in other compounds are found to form by coherent twisting of fibrillar crystallites. It changes the effective birefringence periodically along the radial direction of the domain and ultimately produces concentric interference colour bands between crossed polarisers. However, we have not found any twist in these fibrillar crystallites embedded in the solid amorphous phase of the banded spherulite. To the best of our knowledge, this is the first report of the banded spherulite formed

by periodic variation of composition of two different solid phases of a pure compound without any twist order in the crystallites.

Chapter 5

The optical & structural properties of starch films

5.1 Introduction

The drying dynamics of a solution droplet casted on a flat substrate and the structure of the deposited film produced after drying for various solute substances such as polymers [106–108], DNA [109, 110], nanotubes [111–114], nanorods [115, 116], liquid crystals [117, 118], colloids [119–122], surfactants [123, 124], salts [125, 126] and biological materials [127–130] are an active field of research during last two decades. The most spectacular phenomenon found in deposited solute films after drying a solution droplet is the coffee ring effect where a circular stain is found to form due to the capillary flow of solute particles towards the pinned edge of the droplet. Interestingly, self-assembled structure of solute ingredients has also been found in some cases which makes the deposited thin film birefringent [109, 113, 114, 117].

The drying dynamics of droplets of polymer solutions in some cases exhibit different behavior than the usual coffee ring effect. The droplets with high concentration of polymer and high contact angle with the substrate produce films with distorted surface profiles after drying [108, 131–133]. In these cases, an elastic or glassy but solvent permeable skin forms on top of the droplets during its drying [134–136]. Further drying decreases the enclosed droplet volume which buckles the skin and produces varieties of surface distortion in the deposited film.

Starch, the most abundant and consumable carbohydrates, is the source of large polysaccharides found in nature. Starch naturally occurs in the form of grains and

is made of amylose and amylopectin which are generally linear and branched polymers respectively. The starch grains on heating in excess water swell and rapture irreversibly by imbibing water above a certain temperature which allows the starch polysaccharides to disperse in water. This phenomenon is known as starch gelatinization [55]. The gelatinized starch solution casted on flat surface produces transparent biodegradable starch films after drying [77–79]. In recent years starch based bioplastics have attracted much attention as a replacement of synthetic polymer films in plastic industries [80].

In this chapter, we describe the detail studies on the properties of the biodegradable potato starch films formed after drying of the gelatinized starch solution droplets casted on a plastic substrate. We study the drying dynamics of these droplets of gelatinized starch solution and find that the circular films produced after drying are optically biaxial except at its center. The film is uniaxial at the center with an optic axis normal to its flat surface. The polarised optical microscopy studies establish that in the biaxial region of the circular films, the three principal refractive indices are along radial, azimuthal and perpendicular directions respectively. We measure the variation of birefringence along the diameter of the film. This is equivalent to the variation of orientational order of starch bio-polymers along same direction of the film obtained on drying of droplets. The microscopic studies in drying droplets were performed to find a possible reason behind the acquisition of birefringence and its variation along the diameter of starch films.

5.2 Sample Preparation

5.2.1 Extraction of potato starch

The starch grains were extracted from the potatoes procured locally from the market. At first potatoes were peeled and washed thoroughly in water to remove the soil and skin. The peeled potatoes were then grated gently and mixed with excess water at room temperature. This mixture was then stirred properly to extract the starch

grains from the grated potato into the water. The water with the dispersed starch grains was then separated from the remnants of the grated potato by using a sieve. In this way, the starch grains dispersed in water become separated from the remaining parts of potatoes. The dispersed starch grains being of slightly higher density than water precipitate after few minutes. After complete precipitation, the excess water on top of the sediment was decanted and the sedimented starch content was dried in air at room temperature for 3–4 days. The potato starch sample after complete drying appeared as white powder as shown in fig. 5.1.

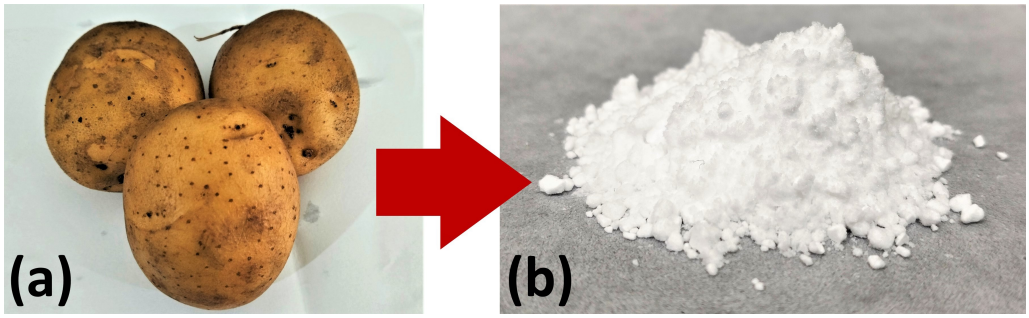


Figure 5.1: Images of the sample (a) potatoes and (b) the extracted potato starch.

5.2.2 Preparation of gelatinized starch solutions and films

The gelatinized starch solutions with different starch concentrations in water were prepared using the following method. A chosen amount M g of starch sample was dispersed in a given amount W g of water in a 50 ml beaker. The concentration C of starch in wt% in the gelatinized starch solution was calculated by using the following equation

$$C = \frac{M}{(M+W)} \times 100 \tag{5.1}$$

The beaker containing starch grains dispersed in water was closed tightly by using aluminum foil and kept at 363 K for 1.5 hours with continuous stirring of the sample using magnetic stirrer. At this temperature, the starch grains become gelatinized. The gelatinized starch solution was then kept at room temperature for 10 minutes in a water bath producing a highly viscous sample. The presence of large interlinked starch polysaccharides and the remnant structures of the gelatinized starch grains

in the solution make it highly viscous and inhomogenious. The sample was then homogenized using a ultrasonic probe sonicator (QSONICA Q700). The 17 ml of the starch solution was taken in a 20 ml glass vowel and sonicated in pulsed mode (2 sec./4 sec. on/off) for 10 minutes with 40% amplitude of vibration using a 6 mm diameter tip. The sonicated starch solution was then cooled to room temperature by keeping it in a water bath for 5 minutes.

The Potato starch was dispersed in water to prepare the gelatinized starch solutions with five different starch concentrations following the method as described above. The details of these mixtures are given in table 5.1.

Table 5.1: Starch content in water

Sample no.	added starch grains (grams)	added water (ml)	added water (grams)	starch concentration (wt%)
1	3.5	30	28.805	10.8
2	2.5	25	23.930	9.5
3	2.5	30	28.805	8.0
4	2.0	30	28.805	6.5
5	1.5	30	28.805	5.0

The solutions with different starch concentrations as described above were drop-casted on flat plastic substrates by using a micro-pipette. These solution droplets were kept at room temperature and ambient humidity for its complete drying. The droplets on complete drying produce the starch films on the substrate. It is found that the films produced in this way can be easily removed from plastic substrates for further studies whereas the films formed on glass plates are firmly attached to the substrate. It is hard to detach them from the glass plates for further characterizations.

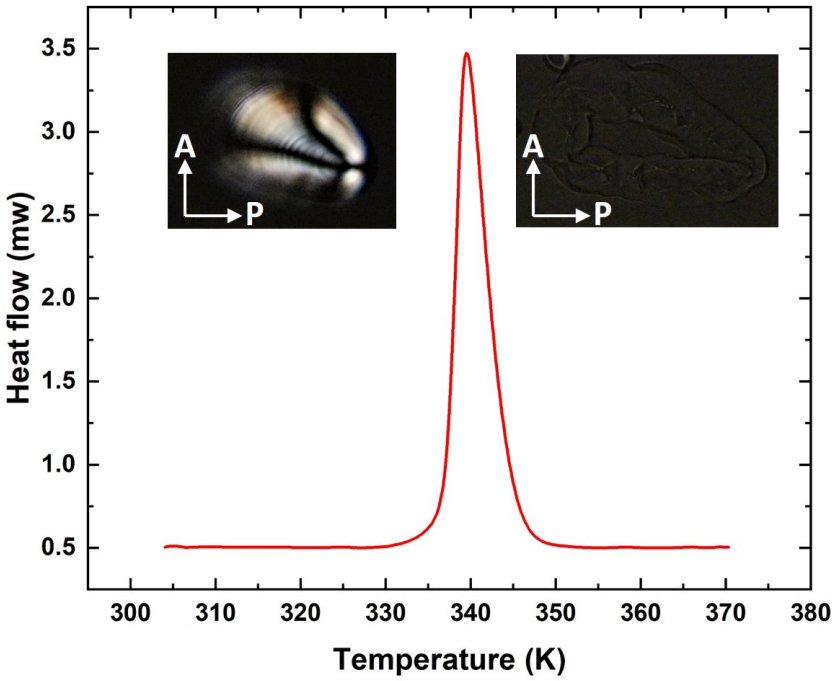


Figure 5.2: DSC thermogram of potato starch in excess water during heating at a rate of 5 K/min. The insets show the POM textures of a starch grain in water before and after gelatinization respectively.

5.3 Experimental Results and discussions

5.3.1 Differential scanning calorimetry studies

The native starch grains on heating in excess water swell and get disrupted on absorbing water above a certain temperature. This irreversible transition is known as starch gelatinization which shows an endothermic peak in the DSC thermogram [64, 137, 138]. The native starch grains are semi-crystalline and birefringent in nature which appear bright between crossed polarisers. The grains loose both of their crystallinity and birefringence across this transition. Fig. 5.2 shows the DSC thermogram of the potato starch when heated in excess water as found in our experiments. In these experiments, about 11 mg of native potato starch was mixed with about 22 μl water in a DSC cup. This cup was then completely sealed for measuring the DSC thermogram of the sample on heating at the rate of 5 K/min.

The sample gives a single endothermic gelatinization peak at about 340 K as shown in fig. 5.2. The specific enthalpy of transition calculated from the peak is about 5.13 J/gm. The inset pictures at left and right sides of the endothermic peak show the POM textures of a starch grain in water before and after gelatinization respectively. The birefringent starch grain looks bright between crossed polarisers before its gelatinization and it becomes dark after its gelatinization.

5.3.2 Drying dynamics of starch solution droplets

The weight loss during drying of a starch solution droplet was measured using a quartz crystal micro-balance with precision of 10^{-4} g. The 150 μl of starch solution was dropcasted on the flat surface of a plastic petridish using a micro-pipette. This droplet was then allowed to dry in air at room temperature (about 25°C) and humidity in the range 53%–55%. The petridish was kept on the micro-balance and the weight of the droplet was measured in 5 minutes interval till its complete drying. The experiment was repeated for other droplets with same initial volume but different starch concentrations.

Fig. 5.3a shows the images of a 150 μl droplet with 5 wt% starch concentration at different time intervals of its drying. The initial diameter of this droplet was about 11 cm. Initially, the droplet dries with its edge pinned to the substrate. After about 170 minutes, the droplet edge starts to recede towards the center with the formation of a peripheral film from the initial pinned edge of the droplet. Further drying reduces the diameter of the droplet. The time variation of the diameter of the circular droplet edge normalized by its initial diameter is shown in fig. 5.3a. Initially, the normalized diameter remain constant with value one and started to decrease after about 170 minutes. The complete drying of this droplet gives rise to a circular starch film with diameter same as that of the initial droplet.

The variation of the weight of this drying droplet with time is shown in fig. 5.3b. Initially, the weight of the droplet decreases linearly due to constant rate of evaporation of water. The height of the droplet perhaps reduces gradually with time during

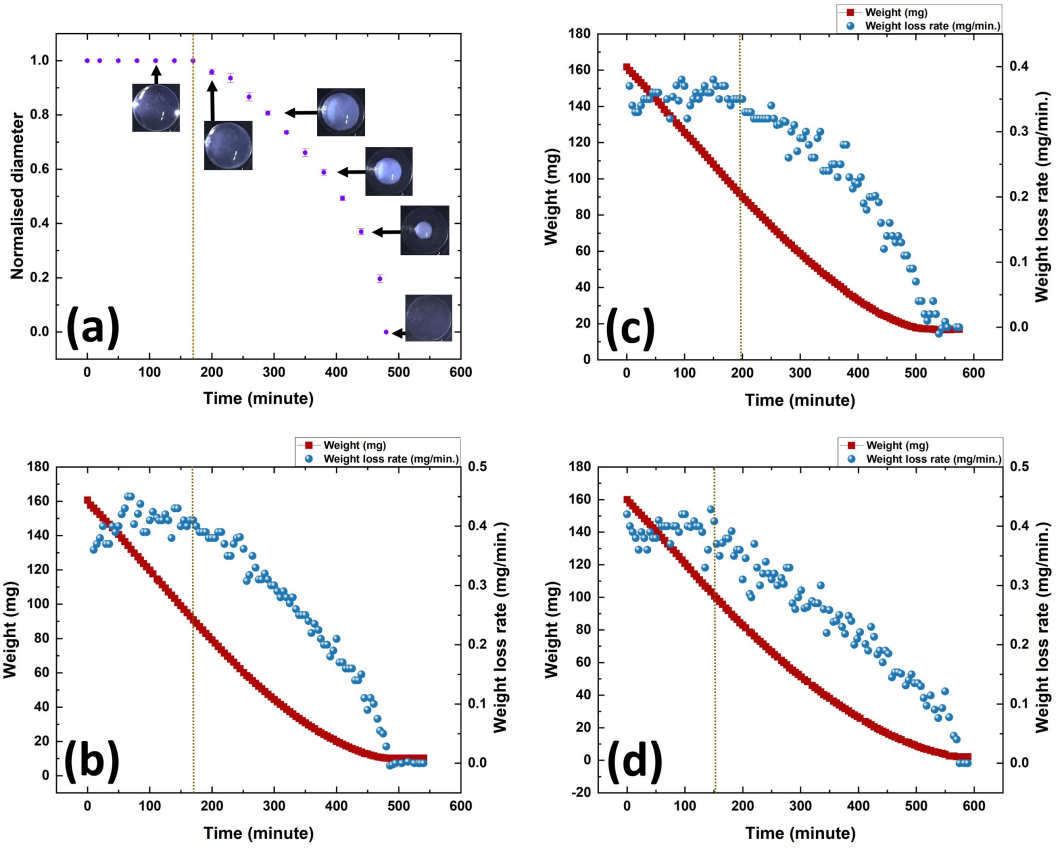


Figure 5.3: (a) Variation of normalized diameter of a 150 μl starch solution droplet with 5.0 wt% starch concentration during its drying. The images show the droplet at different time intervals of its drying. The variation of weight and weight loss rate during drying of a 150 μl droplet of (b) 5.0 wt% of starch solution and (c) 9.5 wt% of starch solution and (d) pure water.

this phase as a consequence of water evaporation keeping its circular edge pinned as shown in fig. 5.3a. The rate of weight loss starts to decrease continuously after about 170 minutes till its complete drying. The sample does not show any weight loss after its complete drying.

The similar dynamics was also found for other starch solution droplets with same initial volume but different starch concentrations. The weight loss curve of a 150 μl droplet with 9.5 wt% starch concentration is shown in fig.5.3c. For this concentration, the rate of weight loss starts to decrease after about 190 minutes when the circular edge of the droplet starts to recede towards the center. The SEM studies as discussed in section 5.3.9 show the developed gel network in the droplet with 9.5 wt% of initial starch concentration after about 10 minutes of its

dropcasting. Therefore, the decrease in the rate of weight loss of the droplet on drying is independent of sol-gel transition as claimed in a previous report [126].

The drying dynamics of a pure 150 μl water droplet on the same petridish was also investigated to compare it with that of starch droplets as discussed above. The variation of its weight with time is shown in fig. 5.3d. Initially, the rate of weight loss of this droplet is constant till about 150 minutes from its dropcasting. The diameter of the circular droplet edge did not change during this period of time. The droplet diameter started to reduce gradually after about 150 minutes showing simultaneous decrease in the rate of weight loss till its complete drying. Therefore, the dynamics of drying for starch solution droplets is very similar to that of pure water droplets. This result again confirms that the decrease in rate of weight loss is due to the receding of the droplet edge during drying.

5.3.3 The thickness profile of dried starch films

The starch solution droplets on drying produce circular films on the substrate. These circular films have azimuthal symmetry with a radial variation of its thickness. The thickness profiles along the diameter of these films were measured to elucidate their morphology. These films were cut along their diameter and the images of their cross sections were taken by using a microscope (Olympus BX50) attached with a digital camera (Canon 80D). These images were then analyzed by using digital image processing software (imageJ, NIH) to obtain the thickness profiles. Fig. 5.4a shows the variation of thickness along the diameter of different starch films formed after drying of different volume of droplets with 9.5 wt% of initial starch concentration. It is found that all these profiles show a sharp increase near the edge of these films and a dimple at their center giving rise to a M-shaped thickness profile. The films have a maximum thickness h_{max} and radius r_0 depending on the initial volume of the corresponding droplets. The normalized thickness profiles (h/h_{max}) of these films when plotted with their normalized radial distance (r/r_0), collapse to a single curve as shown in fig. 5.4b. Therefore, the scaled thickness profile (h/h_{max}) is a function

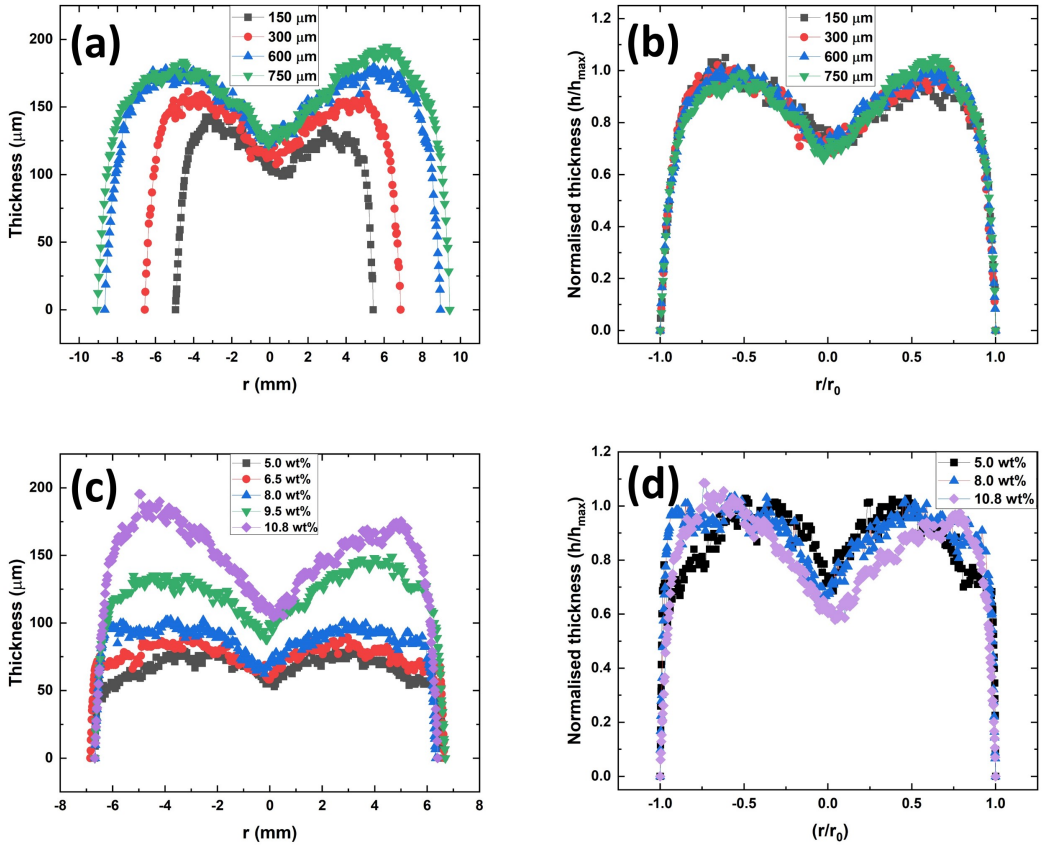


Figure 5.4: (a) The thickness profiles along a diameter of a starch films formed from different volume of starch solution droplets with 9.5 wt% initial starch concentration. (b) The corresponding normalized thickness profiles as a function of the normalized radial distance. (c) The thickness profiles along a diameter of a starch films formed from 300 μl droplets with different starch concentrations. (d) The corresponding normalized thickness profiles as a function of the normalized radial distance.

of the scaled radial distance (r/r_0) only when other experimental parameters remain same.

The SEM studies as discussed in section 5.3.9 show the cellular network of starch bio-polymers inside the droplets which causes gelation. In addition, an elastic water permeable solid crust was also found to form on these drying droplets. The evaporation of water near the interface of drying droplets leads to the formation of this elastic crust. The evaporation rate of water near the circular contact edge of droplet is highest [120]. Therefore, a flow of water towards the edge of droplets gives rise to a compressive stress on the gel network along the radially outward direction. On the other hand, reducing volume of the drying droplet enclosed by the solid crust

produces a stress on it. These two dynamic effects perhaps concurrently lead to the formation of M-shaped thickness profile of the film.

Fig. 5.4c depicts the thickness profiles of starch films formed from 300 μl droplets for different initial starch concentrations. The maximum thickness of these films with similar diameter increases on increasing the initial starch concentration. The maximum thickness of the film for 5.0 wt% initial starch concentration occurs closer to the center of the film which moves towards the edge of the film on increasing the initial starch concentration.

The normalized thickness profiles (h/h_{max}) as a function of normalized radial distance (r/r_0) of the data shown in fig. 5.4c is plotted in fig. 5.4d. The dimple at the center of the film from the droplet with 10.8 wt% initial starch concentration is dipper and wider compared to that of the film formed from the droplet with 5.0 wt% initial starch concentration. The droplet with higher concentration of starch takes relatively less time to form a thicker crust on its surface. This perhaps leads to a dipper and wider dimple in the film formed from more concentrated starch solution droplet. Therefore, the variation of h/h_{max} with r/r_0 of the films depends on the initial starch concentration of the droplets.

A circular coffee stain is generally found to form on drying dilute solution droplets for various kind of solutes [119, 120]. During this drying process, the solute particles are piled towards the pinned edge of the droplet and are ultimately deposited near the edge. Therefore, the thickness profiles along the diameter of dried solute films show the highest thickness near the edge which diminishes towards the center. This thickness variation along the radial direction is reduced on increasing the initial solute concentration in droplets [108]. In our experiments, the dimple at the center of starch films becomes dipper and wider on increasing the initial starch concentration of the droplets. Therefore, the mechanism of the formation of the dimple in starch films is not similar to the formation of coffee rings.

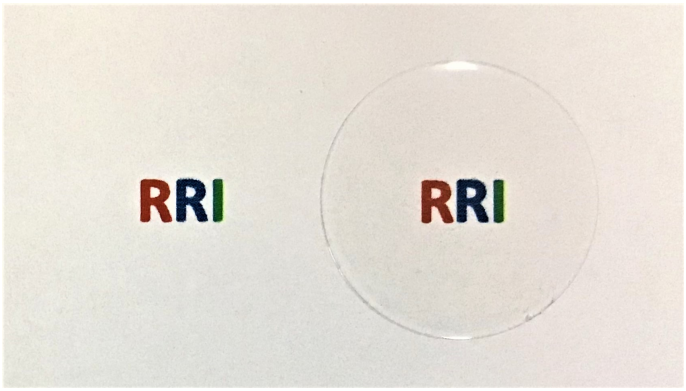


Figure 5.5: The image showing the transparency of a starch film of average thickness about 180 μm.

5.3.4 UV-Visible transmission spectroscopy studies

The dried starch films are transparent in visible light as shown in fig. 5.5. For more quantitative measurements, the UV-Visible spectroscopic studies of the starch films were performed by using Lamda 35 Perkin Elmer spectrophotometer. Fig. 5.6 shows the UV-Visible spectrum of a starch film formed after complete drying of 600 μl droplet with 9.5 wt% of starch concentration. The transmittance of this film of thickness about 180 μm is 95% in 400 nm to 1100 nm wavelength range. The absorption in the film starts to increase with decreasing wavelength below 400 nm in the UV range. A shoulder peak in the transmittance spectrum is found at wavelength of about 250 nm. The origin of this peak is not clear even in the literature.

5.3.5 X-ray diffraction (XRD) studies

The XRD measurements of starch grains and starch films were performed to determine their crystalline structure. All these measurements were performed in the grazing angle of incidence of the x-ray beam. The samples were kept on a flat silicon stage which gives flat XRD profile and hence it does not interfere with the profiles from samples. The XRD profile of starch grains in our sample is shown in fig. 5.7a. The profile exhibits peaks on top of a broad amorphous hump. This indicates that the grains are semi-crystalline in nature. The peak positions in the XRD profile of these grains is similar to that found for the potato starch grains having B-type of

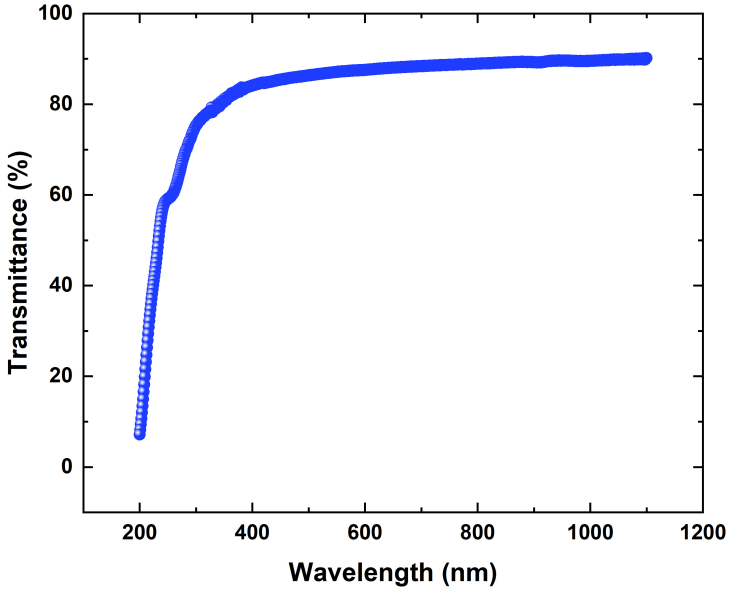


Figure 5.6: The UV-Visible transmission spectrum of starch film obtained on drying 600 μl droplet with 9.5 wt% starch concentration.

crystal polymorphism [55, 139–141]. The B-type crystal polymorph has the hexagonal lattice structure with lattice parameter $a = b = 1.85\ nm$, $c = 1.04\ nm$ and $\gamma = 120^{\circ}$ [63]. The broad hump in this diffraction profile represents the amorphous parts of the grains coexisting with crystalline parts.

The XRD profile of starch film formed from 600 μl droplet with 9.5 wt% starch concentration is also shown in fig. 5.7a. The diffraction peaks on a broad hump in this profile indicate that the film has semi-crystalline structure with coexistence of both crystalline and amorphous domains. The similarity of this diffraction profile to that found for starch grains indicates that the film also has B-type of crystal structure.

The starch solution droplets do not possess any crystalline structure just after its dropcasting. The XRD studies at different times after dropcasting were performed to investigate the development of crystalline order on drying. The XRD profiles were measured on a 150 μl droplet with 9.5 wt% starch concentration during its drying on a glass plate. These measurements were performed in the grazing angle of incidence of the x-ray beam. The baseline corrections for all these profiles were performed by

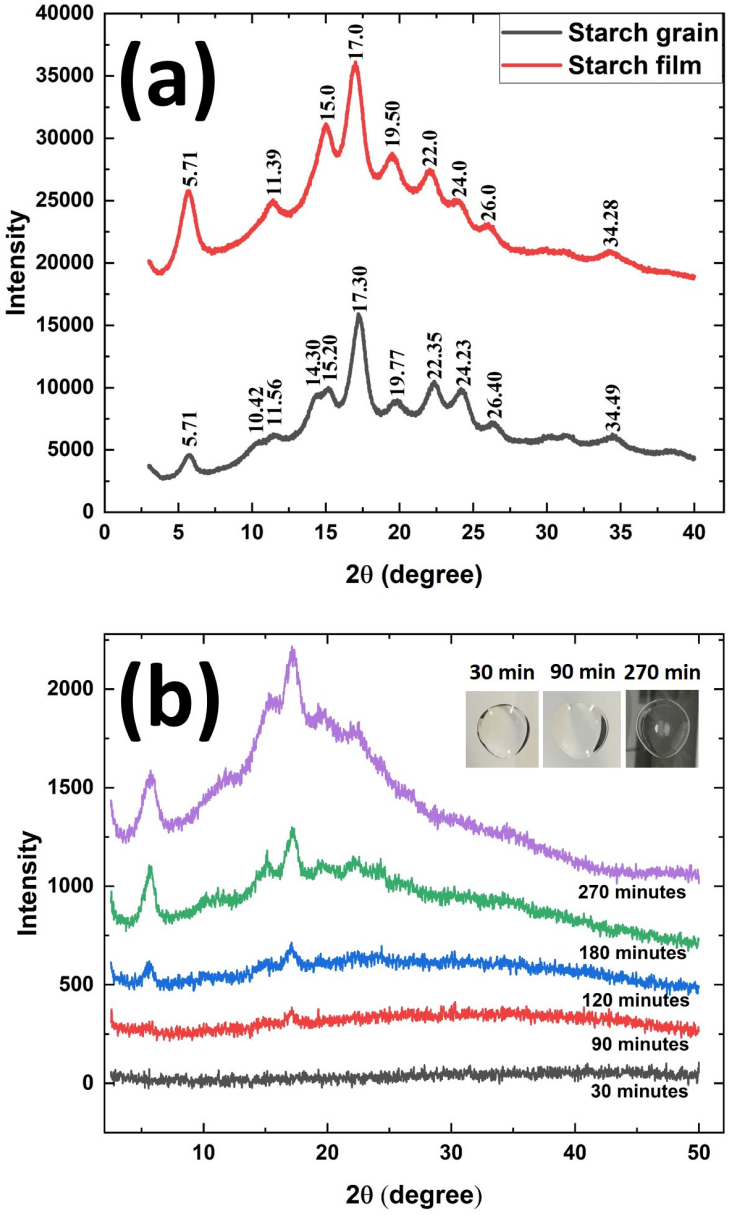


Figure 5.7: (a)The XRD profiles of starch grains and starch film formed from 600 μl droplet with 9.5 wt% of starch concentration. The profile for the film is shifted upward for clarity. (b) The XRD profiles at different times after dropcasting a 150 μl droplet with 9.5 wt% of initial starch concentration. The profiles at different times are shifted vertically for clarity of presentation. The insets show the images of the droplet at three different times after its dropcasting on a glass plate.

subtracting the profiles from that of the empty glass plate. The XRD profiles of this droplet at different times after dropcasting are shown in fig. 5.7b. It can be seen from the figure that the droplet did not have any crystalline order at 30 minutes after of its dropcasting. The sample started to acquire the crystalline order after 90 minutes

when it started to dry from its edge as shown in the inset of fig. 5.7b. The SEM studies as discussed in section 5.3.9 below indicate that the starch solution develop gel structure almost immediately after its preparation. Therefore, the absence of crystalline structure even after 30 minutes of its dropcasting indicates that the gel network inside the droplet does not possess crystalline order. The crystalline order which develops after 90 minutes arises due to the dried starch film forming at the periphery of the droplet. The peaks of the XRD profile along with a broad hump intensify on further drying till the complete drying.

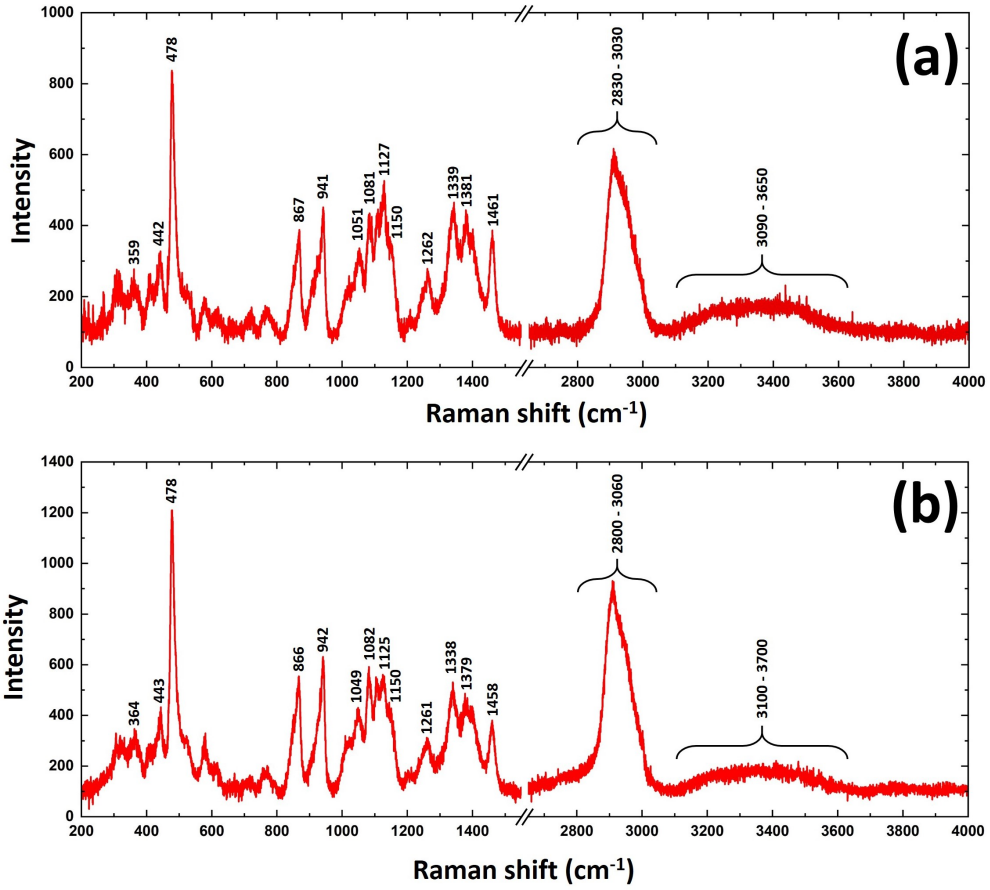


Figure 5.8: Raman spectra of (a) native potato starch grains and (b) starch film obtained on drying 600 μl droplet with 9.5 wt% starch concentration.

5.3.6 Raman spectroscopy studies

The Raman spectroscopy is a non-invasive technique used to characterize a variety of samples. Raman spectroscopy studies on the native potato starch grains and the

Table 5.2: Observed Raman peaks for starch grains and films

Serial no.	Raman peaks for starch grain (cm^{-1})	Raman peaks for starch film (cm^{-1})	Vibrational modes
1	359	364	Skeletal mode of pyranose ring
2	442	443	Skeletal mode of pyranose ring
3	478	478	Skeletal mode of pyranose ring
4	867	866	ν_s(C_1-O-C_5), δ(C-H), δ(CH_2)
5	941	942	ν_s(C_1-O-$C_{4'}$)
6	1051	1049	ν(C-OH), δ(C-OH), ν(C-C)
7	1081	1082	δ(C-OH) bending
8	1127	1125	ν(C-OH), δ(C-OH), ν(C-O)
9	1150	1150	ν_s(C_1-O-$C_{4'}$)
10	1262	1261	CH_2OH related modes
11	1339	1338	δ(CH_2) twisting, δ(C-OH) bending
12	1381	1379	δ(C-OH), δ(CH) bending, δ(CH_2 scissoring)
13	1461	1458	δ_s(CH_2) twisting, C-H bending
14	2830 – 3030	2800 – 3060	ν(C-H)
15	3090 – 3650	3100 – 3700	ν(O-H)

starch films obtained on drying starch solution droplets were carried out to compare their structural features. Fig. 5.8a show the Raman spectrum in the range between 200 cm^{-1} and 4000 cm^{-1} for starch grains while fig. 5.8b shows the corresponding spectrum for starch film obtained on drying of 600 μl droplet with 9.5% starch concentration. Table 5.2 gives the positions of the prominent Raman peaks in this range for our samples. These peaks are attributed to different vibrational modes of the molecule [142, 143]. A comparison between Raman spectra of starch grains and starch film shows that most of these Raman peaks are at same Raman shift. This result implies that the starch grains and the dried films have very similar molecular configuration. It has been proposed that the FWHM of the peak at 478 cm^{-1}

decreases with increasing the starch crystallinity [144, 145]. The similarity in the width of this sharp peak for the native potato starch grains and the starch film found in our experiments implies that both of them possess similar amount of crystallinity. The peak at 942 cm^{-1} and the shoulder peak at 1150 cm^{-1} indicate the presence of glycosidic linkage between glucose units in starch.

5.3.7 Polarising optical microscopy studies

The starch films formed after drying were found to be birefringent. Therefore, the POM studies were performed to investigate the anisotropic optical properties of starch films by using an Olympus BX50 polarising optical microscope.

Orthoscopy studies

The films formed after drying of starch solution droplets are birefringent. Fig. 5.9a shows the POM texture of a starch film formed after drying a 10 μl droplet with 10.8 wt% of starch concentration. The dried starch films obtained in our experiments are found to be optically biaxial in nature. The three principal axes of the refractive indicatrix are oriented along the normal, radial and azimuthal directions of the dried circular starch films. The principal values of refractive indices along these directions are denoted as α, β and γ respectively. The circular starch films between crossed polarisers appear bright with a Maltese cross along the pass axis of polarisers. The black brushes of the Maltese cross divide the whole circular film into four quadrants and remain invariant on rotating the sample on the microscope stage. This observation implies that the principal indices β and γ are along the radial and azimuthal directions of the film respectively. The POM studies using a λ-plate (530 nm) were performed to determine the major and minor indices on the plane of film. The film appears black and white between crossed polarisers implying that the retardation of the film is in the first order of Levy chart. The introduction of the λ-plate with the slow axis at an angle of 45° with respect to the polariser changes the colour of first and third quadrants to yellow whereas second and fourth

quadrants become blue as shown in fig. 5.9b. These colours belong to the first and second order of the Levy chart respectively. The effective subtraction of the path differences in the first and third quadrants of the sample and the λ-plate produces the yellow color. On the other hand, the effective addition of the path differences in the second and fourth quadrants of the sample and the λ-plate produces the blue color. Therefore, it can be concluded from these observations that the principal refractive index γ along the azimuthal direction is greater than the other principle index β along the radial direction of the film.

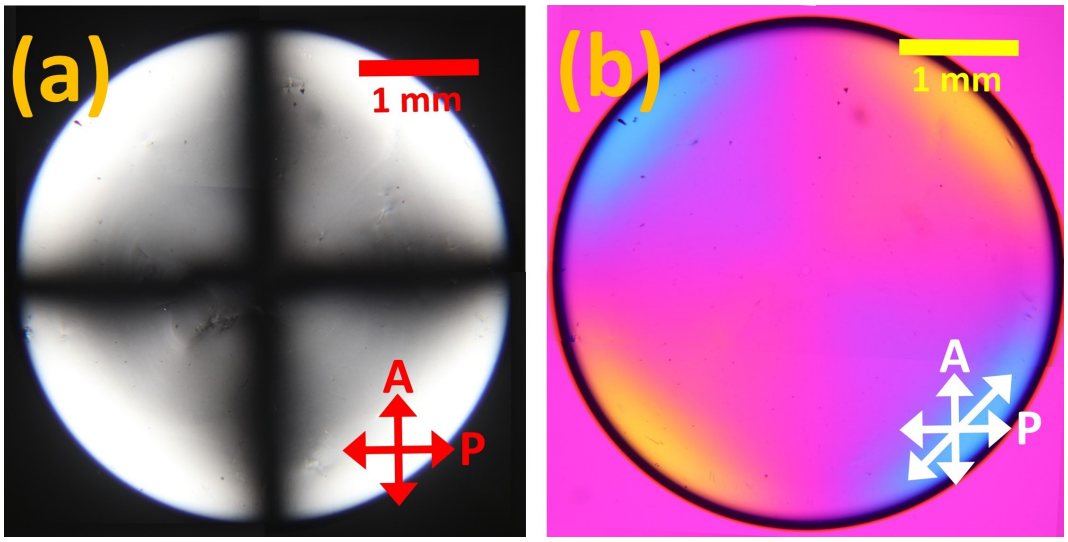


Figure 5.9: The POM images of the starch film (a) between crossed polarisers and (b) after inserting of a λ-plate with the slow axis at an angle of 45° with respect to the polariser.

The variation in the POM textures of a drying starch solution droplet was studied to investigate the growth of the film from its periphery. Fig. 5.10a-f show the POM textures of a section near the edge of a 150 μl droplet with 9.5 wt% of starch concentration at different time intervals after of its dropcasting on a glass substrate. Initially, the POM texture of the droplet appears dark due to the isotropic nature of the sample. After a certain time, the circular edge of the droplet starts to recede towards the center leaving a birefringent film at its peripheral region (see fig. 5.10a). This film appears bright between crossed polarisers. The width of this film along the radial direction increases with time on further drying as shown in fig. 5.10b-f. The intensity at a 66 $\times$ 66 μm^2 spot about 1 mm from the edge of the droplet

measured as function of time is shown in fig. 5.10g. This spot is indicated by the red dot in fig. 5.10a-f. The intensity was calculated by adding the red, blue and green intensities at the spot and then dividing by 3. Initially, the intensity was almost zero before the edge of the birefringent film appeared at the spot. Then the intensity increased sharply as the edge swept through the spot. The intensity almost saturated to a constant value as the edge of the film passed through the spot.

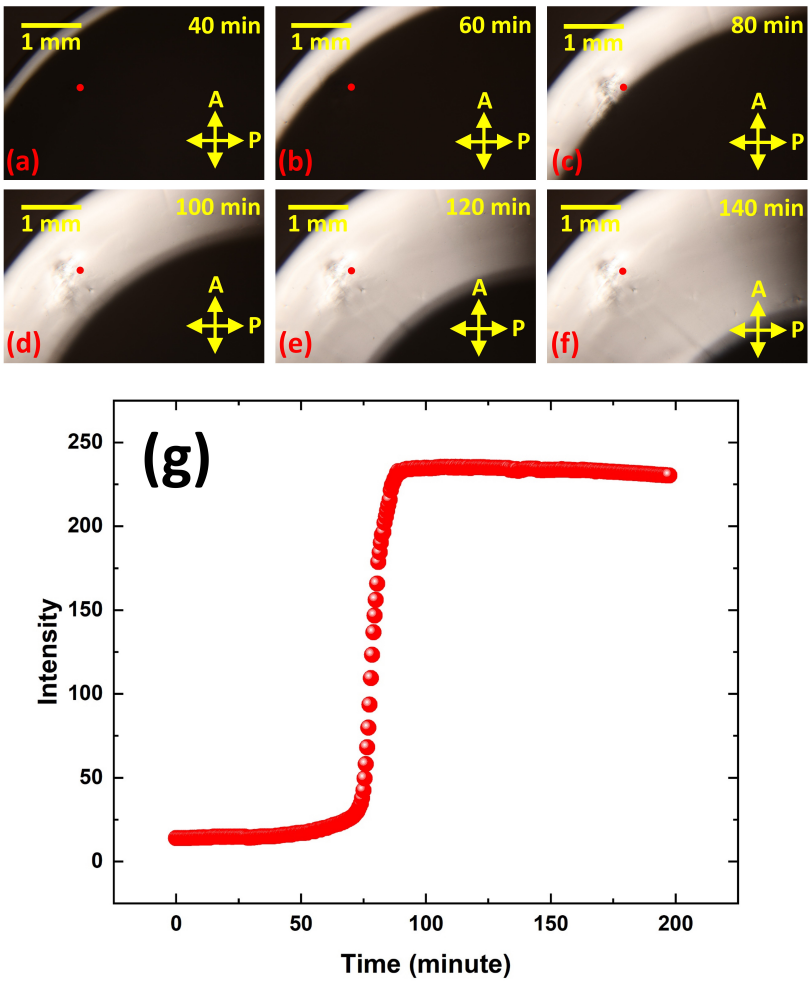


Figure 5.10: (a)-(f) The POM textures of a section near the edge of a 150 μl droplet with 9.5 wt% of starch concentration at different time intervals after of its dropcasting on a glass substrate. (g) The variation of intensity at a 66 $\times$ 66 μm^2 spot at about 1 mm away from droplet edge. The red dot on the images indicates the spot where the intensity was calculated.

Conoscopy studies

The conoscopic studies were performed to determine the optical nature of the dried starch films. The conoscopic studies show that the starch films are optically biaxial

except at its center. The center of the film is uniaxial in nature with the optic axis along the normal to the film. Fig. 5.11 shows the conoscopic figures of a starch film of diameter about 16 mm formed after drying a 600 μl droplet with 9.5 wt% of starch concentration. The conoscopic figures were recorded at the center of the film and 3 mm away from it. The center of the film between crossed polarisers appears dark in POM which implies that this central region is either optically isotropic or uniaxial with an optic axis along the normal to the film. The uniaxial nature of the central region of film was confirmed by the conoscopic studies. The bottom row in fig. 5.11 shows the conoscopic figures at the center of the film for three different orientations of the sample on the microscope rotation stage. The conoscopic figure at the center of the film has the black isogyres parallel to the crossed polarisers and the figure remains invariant on rotating the sample by $\pm 45^{\circ}$ on the microscope stage (see fig. 5.11 bottom row) confirming the optical uniaxiality of the central region of the film with an optic axis perpendicular to the film. The conoscopic studies using a λ-plate (530 nm) with its slow axis at 45° with respect to the polariser were performed to determine the sign of the birefringence. The interference colour in conoscopic figure of the film is in the first order of levy chart. The insertion of the λ-plate into the optical path changed the colour of the peripheral region in the first and third quadrants to yellow whereas the peripheral region of the second and fourth quadrants became blue as shown in the bottom row of fig. 5.11. In the yellow (blue) colored regions parallel (perpendicular) to the slow axis of the λ-plate, an effective subtraction (addition) of the path differences at the sample and the phase plate occurs. This observation clearly implies that the sign of the birefringence at the central region of the film is negative. Hence, the conoscopic studies confirm that the indicatrix ellipsoid at the center of the film has uniaxial oblate shape.

The top row in fig. 5.11 shows the conoscopic figures about 3 mm away from the center of the film for three different orientations of the sample on the microscope rotation stage. These conoscopic figures clearly demonstrate the biaxial nature of the film at this position. The conoscopic figures on rotating the film by 360°

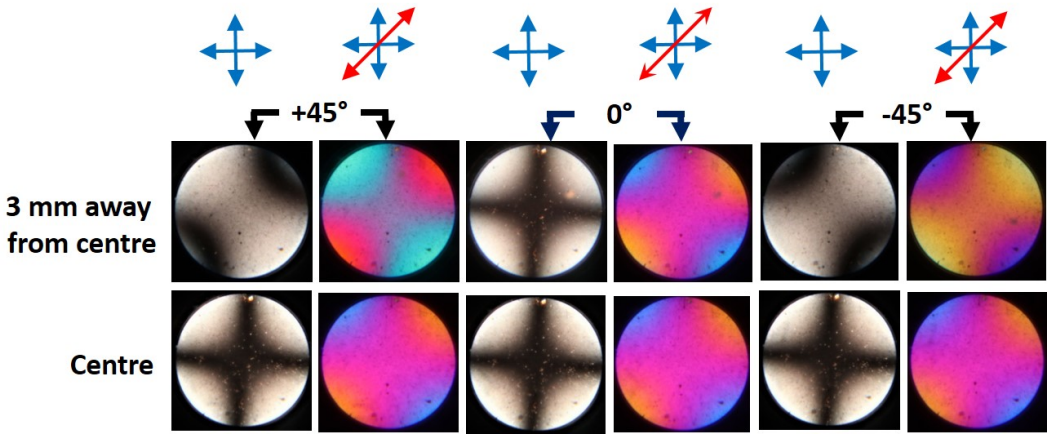


Figure 5.11: The conoscopic figures of starch film at its center (bottom row) and 3 mm away from its center (top row). The angle of the optic plane of the film with respect to the polariser and the presence of the λ-plate between the crossed polarisers are also indicated in the respective figures.

on the microscope stage show that the isogyres become crossed at four distinct positions with a difference of 90°. At ±45° with respect to the crossed positions, the isogyres separate and become hyperbolic as shown in the top row of fig. 5.11 which indicates the optical biaxiality of the film at this position. These hyperbolic isogyres containing the poles of the two optic axes at their apex are centered at the middle of the field of view. Further, the crossed positions of the isogyres are also at the center of the field of view. Therefore, these observations indicate that one of the principal index denoted as α and the optic plane containing both the optic axes are perpendicular to the film. Hence, the other two principal axes with indices β and γ respectively must be on the plane of the film. The orthoscopic studies as discussed above have confirmed that the index γ along azimuthal direction is greater than the index β along the radial direction of the film.

The conoscopic studies after inserting the λ-plate (530 nm) in the optical path were performed to determine the order of the principal indices α, β and γ at this biaxial part of the film. The insertion of the λ-plate for +45° orientation of the sample changed the colour in the peripheral region between the isogyres to blue whereas it became yellow at −45° orientation of the sample (see the top row of fig. 5.11). These results indicate that biaxial starch films are optically negative and $\alpha < \gamma$. Therefore, the starch films are biaxial with the three principal indices

$\alpha < \beta < \gamma$ and the optic plane in the biaxial region lies along the azimuthal direction and perpendicular to the film.

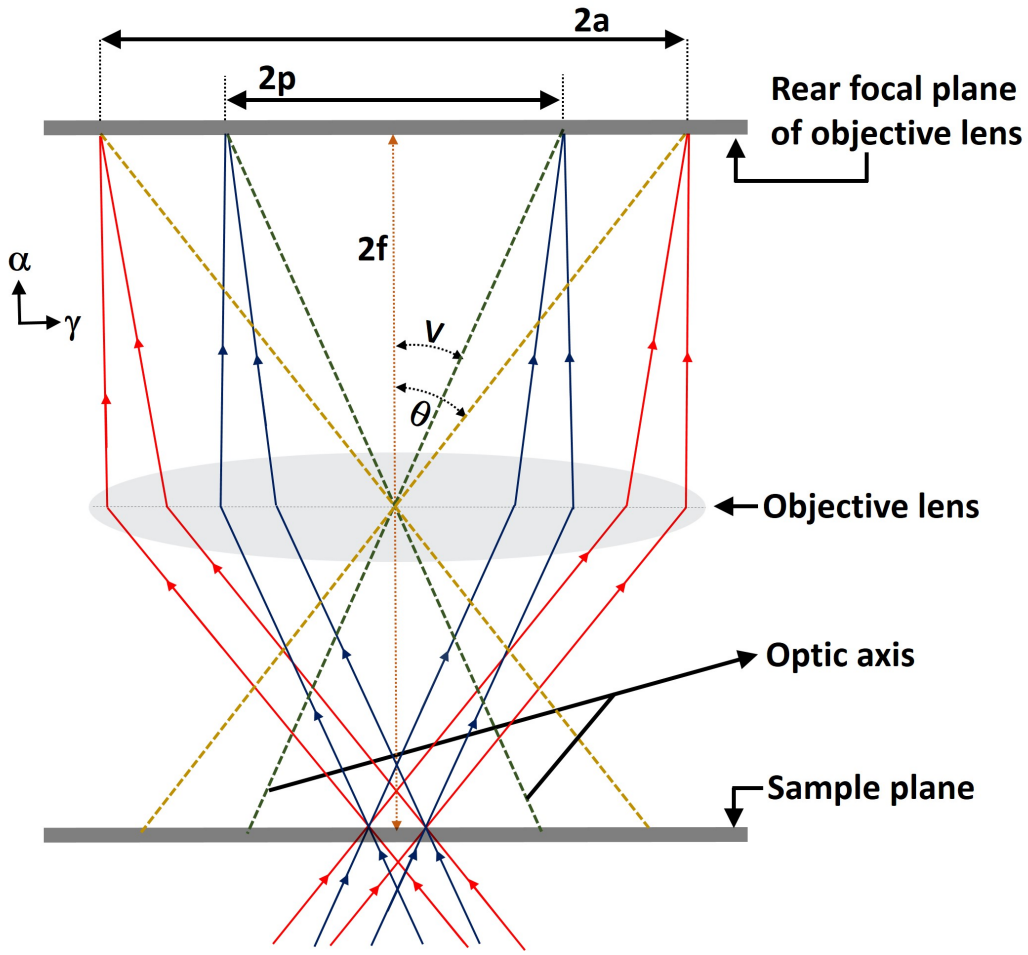


Figure 5.12: Schematic ray diagram of the conoscopic measurement setup.

Determination of acute axial angle

The acute axial angle ($2V$) between the two optic axes was calculated from the conoscopic figures. Fig. 5.12 shows the ray diagram of the conoscopic measurement setup. The diagram depicts the light rays in the $\alpha - \gamma$ plane of the sample containing both the optic axes. In this setting, the light rays from the illuminated part of the sample kept in the front focal plane of the objective lens are focused on its rear focal plane. Hence from fig. 5.12, it can be written as

$$\frac{a}{f} = \tan\theta \tag{5.2}$$

and,

$$\frac{p}{f} = \tan V \tag{5.3}$$

From eqn. 5.2 and eqn. 5.3, one can write,

$$\frac{p}{a} = \frac{\tan V}{\tan \theta} = \frac{\sin V}{\cos V} \times \frac{\cos \theta}{\sin \theta} \tag{5.4}$$

Since the numerical aperture $NA = n \times \sin \theta$ of the objective lens with 50X magnification is 0.5 and the refractive index $n = 1.0$ for the intervening air medium, $\theta = 30°$ in our setup. With V between 0° and 30°, $(\cos \theta / \cos V) \approx 1$ and we get

$$\boxed{\sin V = \frac{NA \times p}{a} = \frac{NA \times 2p}{2a}} \tag{5.5}$$

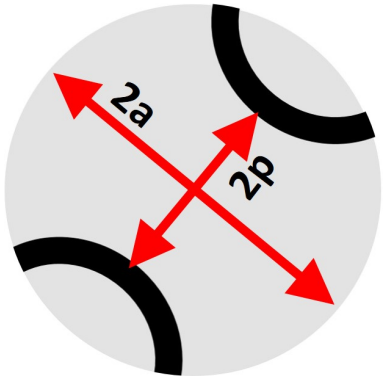


Figure 5.13: Schematic diagram of a conoscopic figure having two uncrossed hyperbolic isogyres depicting the distances $2p$ and $2a$.

Fig. 5.13 shows the schematic conoscopic figure of a biaxial sample where $2p$ is the distance between the poles of the optic axes and $2a$ is the diameter of the circular field of view. The acute axial angle $2V$ between the optic axis can be determined from eqn. 5.5 by measuring the ratio of $2p$ and $2a$.

The conoscopic figures at different positions along the the diameter of a starch film formed from 600 μl droplet with 9.5 wt% of initial starch concentration are shown in fig. 5.14a. The measurements were performed at an interval of 1 mm along the radial direction. The acute angle $(2V)$ between the two optic axes along the diameter of the film was calculated from these conoscopic figures by using eqn. 5.5.

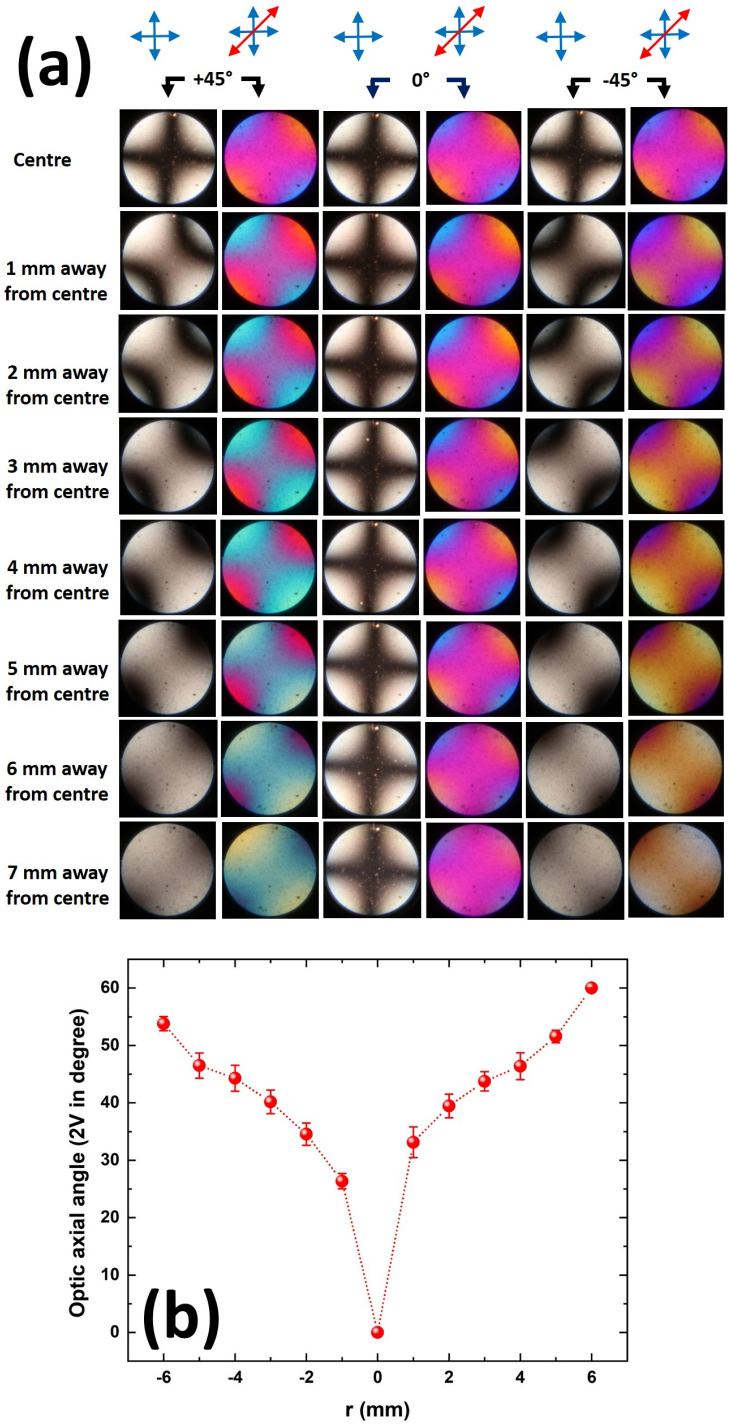


Figure 5.14: (a) Conoscopic figures at different positions along the radial direction of a starch film of radius about 8 mm formed from 600 μl starch solution with 9.5 wt% of starch concentration. The distance between two consecutive positions of measurement is 1 mm. (b) The variation of the optic axial angle ($2V$) along the radial direction of the film obtained from the conoscopic figures.

The variation of angle $2V$ along the radial direction of the film is shown in fig. 5.14b.

The angle $2V$ is zero at the uniaxial center and it increases monotonically towards

the edge of the film. The hyperbolic isogyres beyond 6 mm from the center of the film went out of the field view and the calculation of the acute axial angle beyond this limit was not possible.

5.3.8 Measurement of birefringence along the diameter of starch films

The POM studies discussed above clearly establish that dried starch films are optically biaxial in nature. We also measured the effective birefringence on the plane of these starch films. Though there are several reports of the mechanical and spectroscopic properties of these starch films [146–149], the measurements of the optical biaxiality of them have not been carried out. Clearly the anisotropic optical properties of these starch film arise due to the orientational order of starch bio-polymers during drying. Therefore, these measurements provide valuable insight on the structure of these films.

The effective retardation [$(\gamma - \beta) \times$ sample thickness)] in the plane of the film was measured using a home built setup with a photo elastic modulator (PEM). The detail of this experimental setup has been discussed in chapter 2. The effective retardation was measured at different positions along the diameter of the film at an interval of 0.1 mm. The thickness profile of the film along its diameter was also measured by following the procedure as discussed in section 5.3.3. The effective birefringence $(\gamma - \beta)$ at a point can be obtained by dividing the effective retardation by the corresponding thickness of the film.

Fig. 5.15a shows the variation of birefringence $(\gamma - \beta)$ along the diameter of a starch film formed after drying a 600 μl droplet with 9.5 wt% of starch concentration. The birefringence is maximum at the edge of the film and diminishes monotonically to zero towards its center. The measured birefringence at the center of the film is zero due to its uniaxial nature as discussed above. The birefringence profile along the radial direction from the center to the edge of the film can be divided into three parts with three different slopes. Initially the birefringence increases

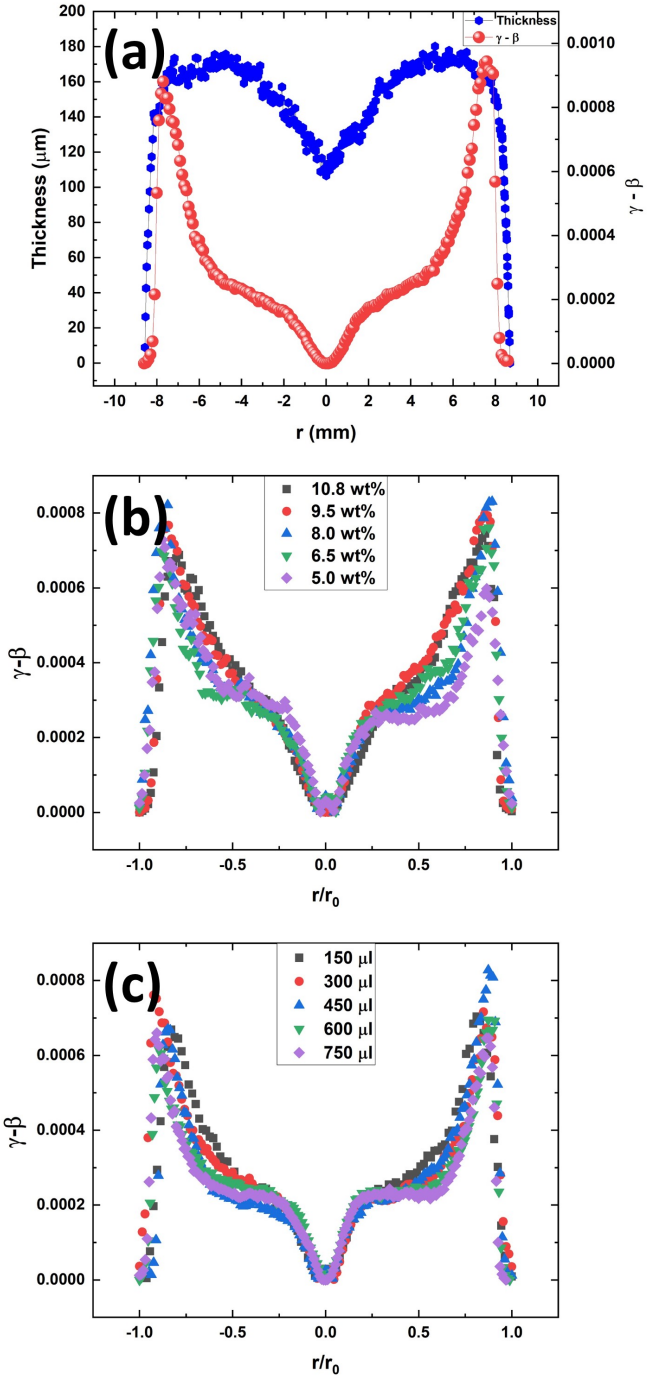


Figure 5.15: (a) The birefringence profile $(\gamma - \beta)$ along the diameter of a starch film obtained from a 600 μl droplet with 9.5 wt% starch concentration. Its thickness profile has also given in this figure. (b) The birefringence profiles $(\gamma - \beta)$ along the normalized radial direction of starch films formed from 300 μl droplets with different starch concentrations. (c) The birefringence profiles $(\gamma - \beta)$ along the normalized radial direction of starch films obtained from different volumes of droplets with 6.5 wt% initial starch concentration.

rapidly along the radially outward direction from its center. Then it increases with a relatively lower slope and again increases rapidly to the maximum value. Beyond this maximum point, the measured birefringence drops to zero rapidly at the edge. Fig. 5.15a also shows the corresponding thickness profile of the film along its radial direction.

The birefringence profiles of starch films obtained on drying the same volume of droplets but with different starch concentrations were measured to investigate the effects of initial starch concentration. Fig. 5.15b shows the birefringence profiles of films obtained on drying 300 μl droplets with different starch concentrations. The birefringence profile is plotted as a function of the normalized radial distance in the film. The normalization was performed on dividing the radial distance (r) by the radius of the film (r_0). These profiles with different concentrations have similar characteristic variation along the radial direction with three different slopes. But the slope in the middle part of the birefringence profile decreases with decreasing the initial starch concentration. The maximum values of birefringence at the edge of these films are close to each other independent of the initial starch concentrations of droplets.

The birefringence profiles of the starch films formed after drying different volumes of droplets but with same 6.5 wt% initial starch concentration were measured to study the effect of initial droplet volume. The birefringence profiles as a function of the normalized radial distance (r/r_0) of the starch films for different initial volume of the droplets are shown in fig. 5.15c. Though different initial volumes of the droplets produce films of different radii, the data in fig. 5.15c almost superpose on each other. The superposition of all these data indicates that the birefringence ($\gamma - \beta$) is a function of r/r_0 only for the other experimental conditions remaining the same. The maximum value of birefringence at the edge of these films have very similar values indicating that it neither depends on the initial starch concentration nor on the initial droplet volume.

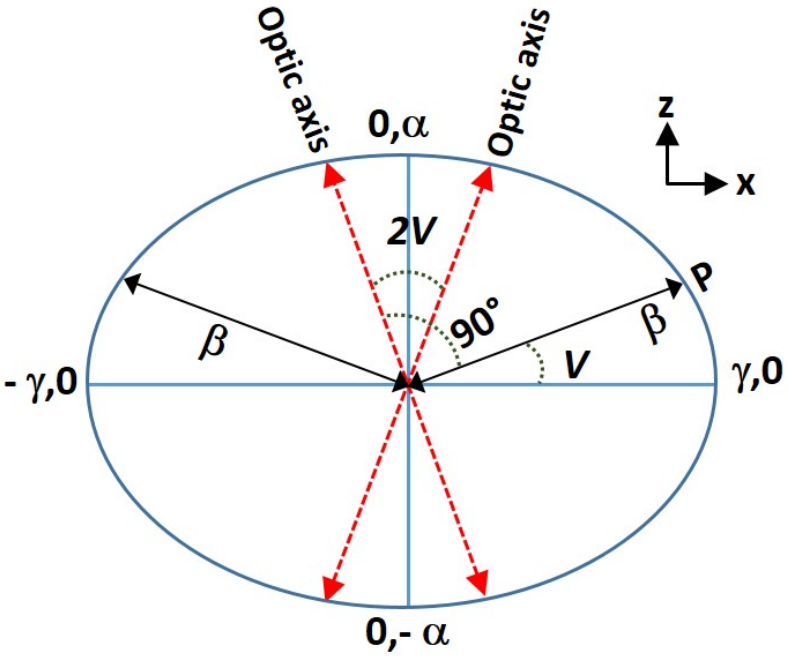


Figure 5.16: The index ellipse on the optic plane of starch film.

Measurement of $(\beta - \alpha)$

The POM studies as discussed in section 5.3.7 confirm the biaxial nature of the starch films away from the center. The three principle indices α, β and γ ($\alpha < \beta < \gamma$) are along the perpendicular, radial and azimuthal directions of the film respectively. The index ellipse on the optical plane is shown in fig. 5.16. The equation of this index ellipse can be written as

$$\frac{x^2}{\gamma^2} + \frac{z^2}{\alpha^2} = 1 \tag{5.6}$$

where γ and α are the major and minor indices respectively. The sections of the optical indicatrix perpendicular to optic axes are circular with radius β. Therefore, the length of the radius vector to the point P on the index ellipse in fig. 5.16 is the intermediate index β. Then using eqn. 5.6, it can be shown that

$$\tan^2 V = \frac{1 - \frac{\beta^2}{\gamma^2}}{\frac{\beta^2}{\alpha^2} - 1} \tag{5.7}$$

The principal refractive indices α, β and γ of starch film are expected to be of similar order of magnitude to that of water or glass. The measured value of

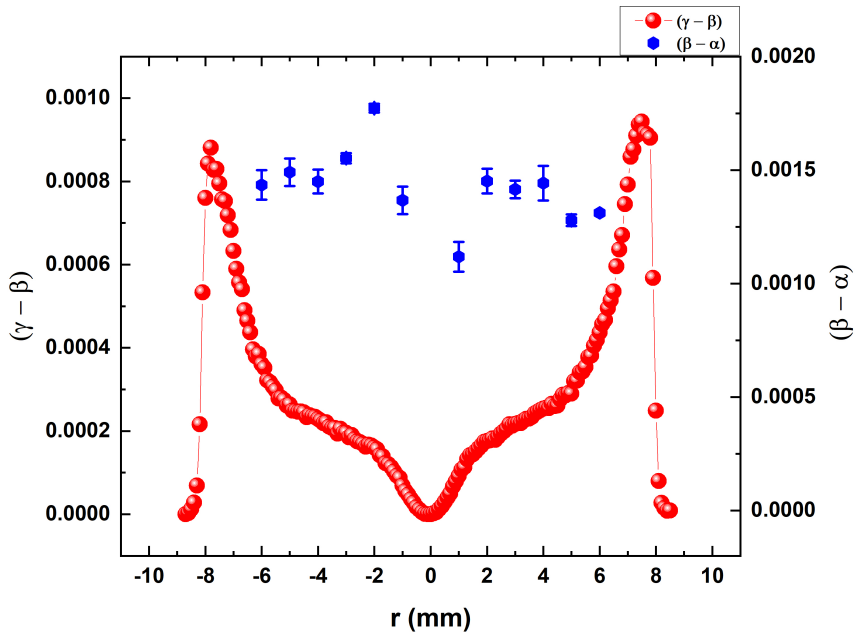


Figure 5.17: The variation of $(\gamma - \beta)$ and $(\beta - \alpha)$ along the diameter of a starch film obtained on drying of 600 μl droplet with 9.5 wt% starch concentration.

birefringence $(\gamma - \beta)$ of the starch films is found to be of order 10^{-4} which is very small compared to the principal values of the indices. As $60° > 2V > 30°$ in most part of the starch films (see fig. 5.14b), it implies that $(\beta - \alpha)$ also has similar order of magnitude as that of $(\gamma - \beta)$. Therefore, using $(\gamma - \beta) \ll \beta$ and $(\beta - \alpha) \ll \beta$, eqn. 5.7 can be approximated as

$$\boxed{\tan^2 V = \left[\frac{\gamma - \beta}{\beta - \alpha}\right]} \tag{5.8}$$

or

$$\boxed{(\beta - \alpha) = \left[\frac{\gamma - \beta}{\tan^2 V}\right]} \tag{5.9}$$

The variation of $(\gamma - \beta)$ along the diameter of a starch film formed from 600 μl solution droplet with 9.5 wt% starch concentration is shown in fig. 5.17. The axial angle $(2V)$ measured from the conoscopic textures along the same radial direction of this film is shown in fig. 5.14b. The calculated variation of $(\beta - \alpha)$ from eqn. 5.9 along the diameter of the film is shown in fig. 5.17. It can be seen from this figure that $(\gamma - \beta)$ varies considerably along the radial direction of the film but $(\beta - \alpha)$

remains almost constant.

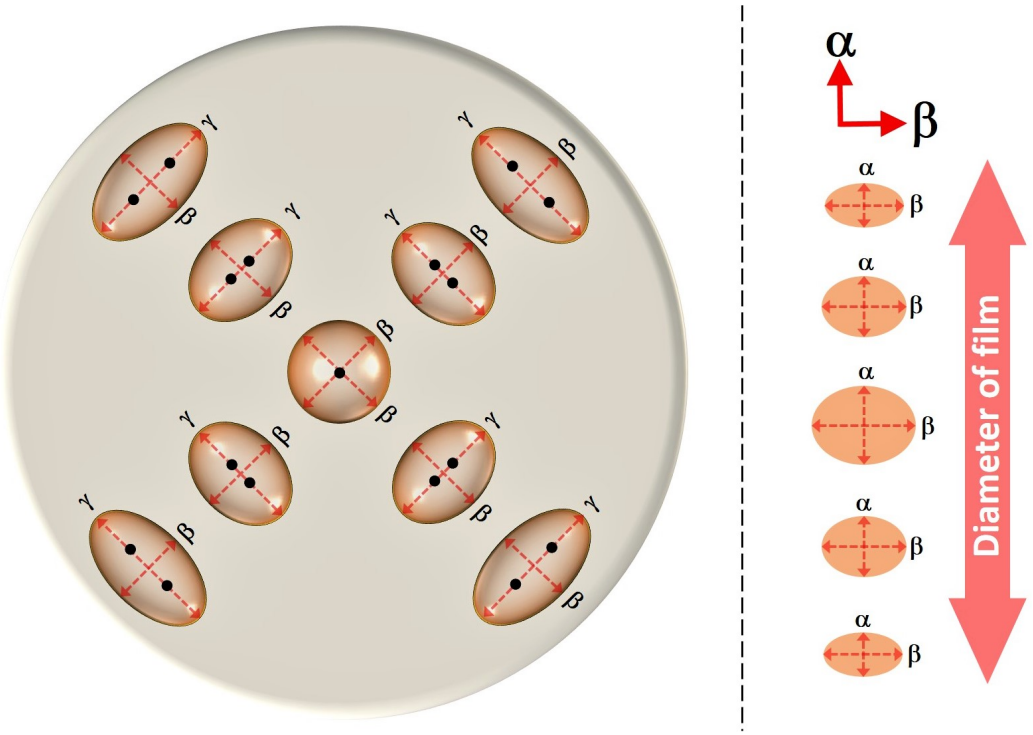


Figure 5.18: [Left] The index ellipsoids along the diameter of starch film. [Right] The variation of index ellipse containing the principal indices α and β along the diameter of the film.

The variation of indicatrix ellipsoid along the diameter of the starch film is schematically shown in fig. 5.18. The indicatrix in the biaxial part of the film is a general ellipsoid with three different principal indices α, β and γ along the normal, radial and azimuthal directions of the film respectively. The left hand side of fig. 5.18 shows the index ellipsoids at different parts of the film when viewed from the top. The intersection points between the optic axes and the ellipsoid in biaxial part of the film are indicated by a pair of black dots on each indicatrix in this diagram. The increasing acute angle between the two optic axes towards the edge of the film widens the separation between these dots along the radially outward direction. At the center of the film having uniaxial character, the index ellipsoid appears circular with the intersection point of optic axis at its center. The right hand side of fig. 5.18 shows the variation of index ellipse in the α–β plane along the diameter of the film. At the uniaxial center of the film, the birefringence is negative and the index ellipsoid has an oblate shape. The α and β are maximum at the center of the film and they

diminish monotonically towards the edge keeping their difference almost same.

5.3.9 Scanning electron microscopy (SEM) studies

The cryo-SEM studies of drying starch droplets were carried out to investigate the submicroscopic structures of the sample. It is found that the droplets with initial starch concentration higher than 9.5 wt% transform to gel within few minutes after dropcasting. The cryo-SEM studies were performed on these drying droplets to find the gel network structure developed in these droplets. The 300 μl droplets with 9.5 wt% starch concentration were dropcasted on plastic petridish and left to dry in air. It is found that these droplets generally take about 18 to 20 hours to dry completely at about 298 K and 45% - 50% humidity. The liquid nitrogen was poured in the plastic petridish to freeze the droplets after certain time from dropcasting. A frozen droplet was then removed from the plastic petridish and immediately transferred to the channel of an aluminum sample holder as shown in fig. 5.19a. The droplet was fixed vertically to the channel wall by using colloidal graphene conducting paste such that half of the droplet protruded out of the holder as shown schematically in fig. 5.19b. The sample with the holder was again dipped in liquid nitrogen and then transferred to the cryo-preparation chamber kept at 10^{-4} to 10^{-5} mbar pressure. The sample stage in this chamber was kept at 103 K. The sample was then heated to 183 K and kept at that temperature for 5 minutes to make it soft for cutting through its diameter. The cross sectional area of the sample was left for 15 minutes at this temperature and pressure for ice sublimation. Then the cross sectional area of the sample was sputter coated with platinum for 60 seconds. Finally, the sample was transferred to the microscope stage of SEM which was kept at temperature 83 K and pressure 10^{-5} to 10^{-6} mbar.

Fig. 5.20a,b show the cryo-SEM textures of a starch droplet with 9.5 wt% initial starch concentration after 10 minutes of its dropdasting. The textures clearly show the presence of a solid thin crust on the surface of the droplet (fig. 5.20a) and a cellular network inside the sample (fig. 5.20b). The solid crust forms due to the

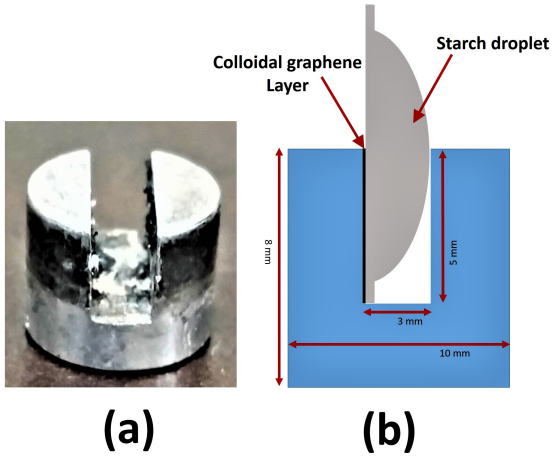


Figure 5.19: (a) Aluminum holder for cryo-SEM studies. (b) A schematic diagram showing the starch droplet in the aluminum holder.

drying from the surface and the cellular network is responsible for the gel property. The walls of the cellular structures are composed of starch bio polymers. In addition, the starch nano particles were found to float in water inside these cells. Similar gel network structure has also been observed during retrogradation of gelatinized starch sample [150–152].

As discussed in section 5.3.2, the droplet beyond a waiting time starts to recede from its initial pinned edge towards the center with the formation of a peripheral film. The edge of a 300 μl droplet with 9.5 wt% of starch concentration recedes about 3 mm towards the center after 14 hours of dropcasting. Fig. 5.20c shows the cross sectional SEM texture near the contact line of this droplet surrounded by the dried film on the SEM holder. The regions marked 1 and 2 in this figure correspond to the dried film outside and the gel just inside the droplet edge respectively. The the magnified view of region 1 as shown in fig. 5.20d is depicting the smooth texture of the film. On the other hand, the magnified view of region 2 as shown in fig. 5.20e is depicting the thread like network structure. This thread like networks of starch biopolymers ultimately give rise to the smooth texture of the film after complete drying.

Fig. 5.20f shows the cross sectional SEM texture near the interface of this droplet at its central region. Three different regions with three different textures can be

observed in this figure. A relatively dense crust forms on top of the droplet. Below the crust, a thread like network region is developed by the starch bio-polymers. The width of this region is large compared to that of the crust and has relatively lesser density than the crust. A cellular network structure with lowest density is observed below the thread like network region. It should be noted here that the thread like network is formed by the filaments of starch biopolymers whereas the cellular network is made of starch biopolymer membranes. The marked regions 3 and 4 near the interface and inside the droplet are shown in fig. 5.20g and fig. 5.20h respectively in higher magnification. Fig. 5.20g shows the smooth texture of the crust with thickness about 2.5 μm above the thread like network region. This texture of the crust is same as that found for the dried peripheral film shown in fig. 5.20d. The cellular network structure as shown in fig. 5.20h clearly reveals the starch membranes separating the cells. Therefore, the SEM studies confirm that at sufficient time after dropcasting, the cellular network region inside the droplet is surrounded by a thread like network region with intermediate density which in turn is covered by a relatively thinner solid elastic crust as schematically shown in fig. 5.21. It is apparent that the cellular network structure gives rise to the denser thread like network structure near the droplet interface which transforms to the dried film on further drying.

The biaxiality of the dried starch films can be explained by assuming that the starch filaments forming the thread like network structure observed experimentally are birefringent. These filaments near the circular contact line of the drying droplet tend to align themselves parallel to this line. This alignment of the starch filaments perhaps gives rise to the biaxial starch film with three principal indices α, β and γ along its perpendicular, radial and azimuthal directions respectively. The alignment tendency of these filaments along the azimuthal direction gives rise to the highest index γ along this direction at the edge of the film. The other two principal directions being experimentally not equivalent, give rise to the biaxility of the film away from the center. The gradual diminishing order of the filaments decreases the value of

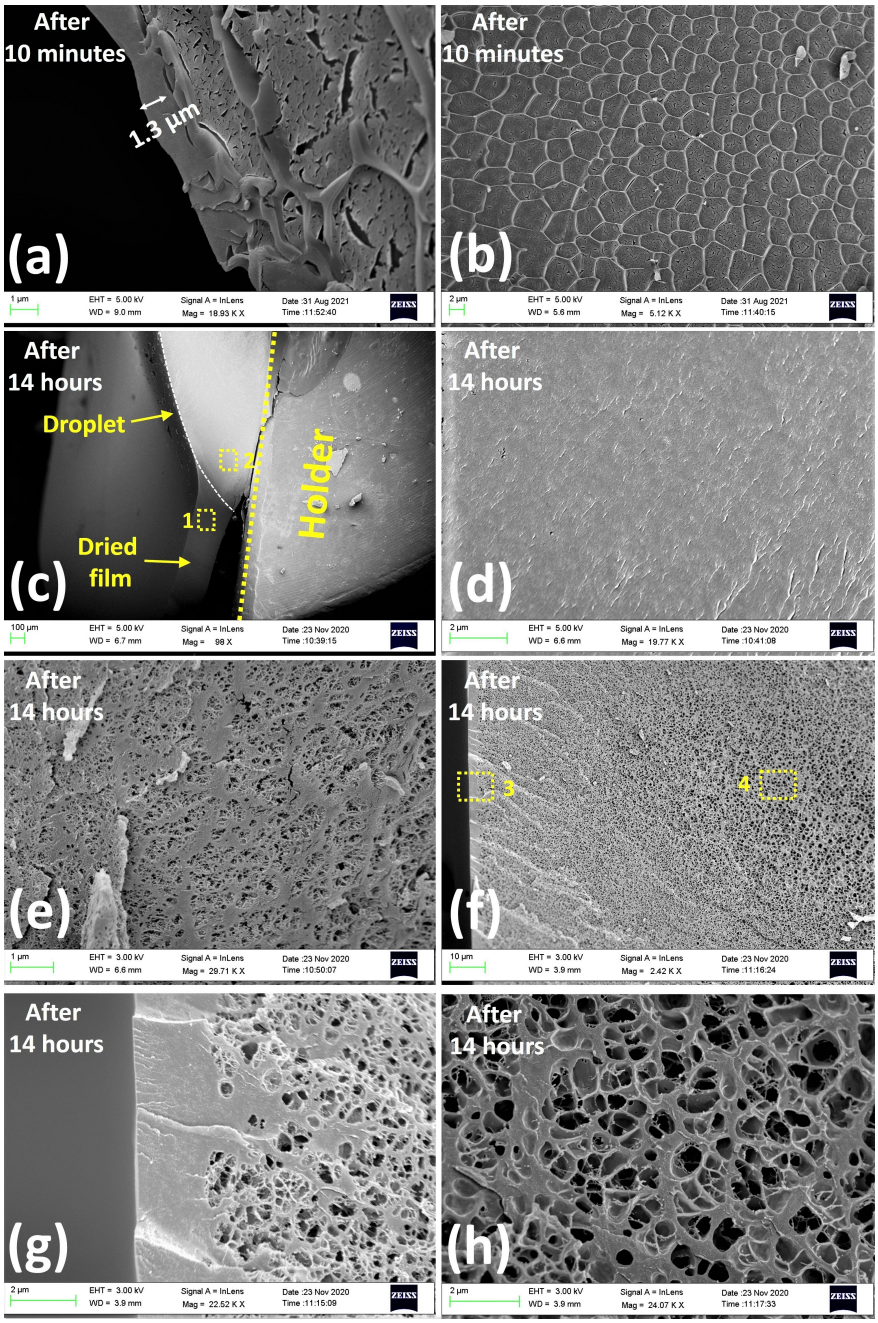


Figure 5.20: The Cryo-SEM textures of cross section of a 300 μl droplet with 9.5 wt% starch concentration at different time after dropcasting. (a) The crust formed on the surface of the droplet after 10 minutes. (b) The cellular network structure inside the droplet after 10 minutes. (c) The texture near the contact line of the droplet after 14 hours showing the droplet surrounded by the dried film on the SEM holder. (d) The magnified view of the marked region 1 showing the smooth texture of the dried starch film. (e) The magnified view of the marked region 2 showing the thread like network structure inside the droplet edge. (f) The SEM texture near the interface of the droplet at its central region after 14 hours. (g) The magnified view of the marked region 3 showing the crust on top of the droplet and the thread like network below it. (h) The magnified view of the marked region 4 showing the cellular network structure well inside the droplet.

the principal index γ monotonically along the radially inward direction of the film. As a consequence of this, the value of other two principal indices α and β increases simultaneously along the radially inward direction of the film keeping their difference constant as found experimentally.

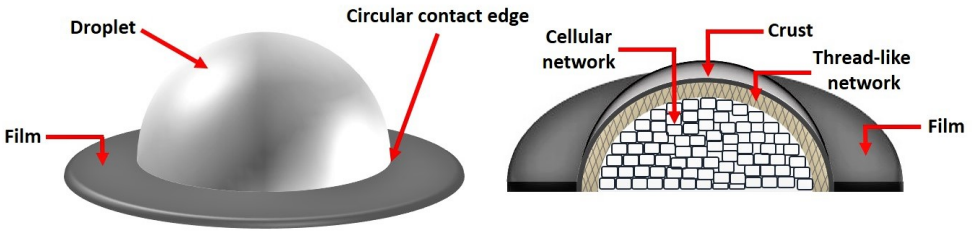


Figure 5.21: The schematic image of the droplet and droplet cross-section along with the peripheral film.

5.4 Conclusion

In this chapter, we have studied the drying dynamics of dropcasted gelatinized starch solution droplets at room temperature and humidity. Initially the droplets are pinned at its circular edge of contact to the substrate. The edge of the droplet starts to recede toward the center after a certain time of its dropcasting, leaving a transparent birefringent film from the initial pinned edge. The circular starch films formed after complete drying of droplets are azimuthally symmetric and show M-shaped thickness profiles along their diameter. These films are partially crystalline and look bright between crossed polarisers. The POM studies show that the films are optically biaxial except at its center where it is uniaxial with an optic axis perpendicular to film. In biaxial part of film, the three principal indices α, β and γ are along the normal, radial and azimuthal directions of the film respectively where $\alpha < \beta < \gamma$ and the film is optically negative. The optic plain containing both the optic axes is along the azimuthal direction and normal to the film. The effective birefrigence $(\gamma - \beta)$ on the plane of the film increases along the radially

outward direction whereas $(\beta - \alpha)$ as obtained from the conoscopic figures remains almost constant along the same direction. The cryo-SEM studies of droplets after certain time of dropcasting show a cellular network of starch biopolymers. This cellular network gives rise to the gelling property of the droplets. The evaporation of water near the interface of drying droplets leads to the formation of a water permeable elastic crust on top of it. This crust formation possibly gives rise to the starch films with a dimple at its center on complete drying of droplets. The SEM studies of droplets also show that at sufficient time after dropcasting, the cellular network region inside the droplet is surrounded by a thread like network region which in turn is covered by a relatively thinner crust. It is apparent that the cellular network structure gives rise to the thread like network structure near the droplet interface which transforms to the solid film on further drying. The starch filaments forming the thread like network structure as observed experimentally are possibly birefringent. The alignment of these filaments near the circular contact line of the drying droplets perhaps gives rise to the birefringence in the solid films.

Summary

In this thesis, two different types of materials are studied experimentally. The first system is a calamatic liquid crystal compound (8OCB) consisting of highly polar rod-like molecules. The crystal polymorphs of this compound formed from its supercooled smectic phase are studied in detail. It is observed that the most stable solid phase of this compound shows both banded and non-banded spherulitic growth from the supercooled smectic phase. The second system studied in this thesis is the starch films formed on drying droplets of gelatinized potato starch solution on a flat substrate.

In **chapter 1**, a brief introduction about calamatic liquid crystals, spherulitic growth and starch are given.

In **chapter 2**, the various experimental techniques used to study the samples are discussed.

In **chapter 3**, we study the two crystal polymorphs of 8OCB formed from its melt during cooling. We identify that one of these phases is metastable long parallelepiped or PP phase. The other stable solid phase is identified as commercial powder or CP phase. It is found that the CP phase is not a homogeneous phase. In this phase, the fibrillar nano crystallites with monoclinic lattice structure are embedded in a solid amorphous phase.

It is observed that the CP phase of 8OCB shows both banded and non-banded spherulitic growth from the supercooled smectic phase. Both of these spherulite domains show a spherical growth front which appears circular in quasi-two-dimensional geometry. In **chapter 4**, the banded and non-banded spherulitic growth of CP phase are studied in detail. In these spherulite domains, the radially aligned fibrillar crystallites are found to be embedded in a solid amorphous phase. The bands in the banded spherulite domain arise due to the periodic variation of the composition of the two different coexisting phases along the radial direction of the domain. This

variation gives rise to the alternating concentric crystallite-rich and crystallite-poor bands which appear as the concentric interference color bands between crossed polarisers. It is found that the banded spherulite of 8OCB is not a stable structure. It transforms irreversibly to the non-banded spherulite on heating and also on aging.

In **chapter 5**, we study mainly the structural and optical properties of circular starch films formed on drying droplets of gelatinized starch solutions dropcasted on a flat surface. It is found that the films are transparent in visible light and possess a semi-crystalline structure. These films are birefringent and appear bright between crossed polarisers. The circular films are found as optically uniaxial at their center with an optic axis normal to the film. Except center, the films are optically biaxial with three principal indices α, β and γ along the normal, radial and azimuthal direction respectively. The starch films are found to be optically negative in both the uniaxial and biaxial regions. Based on experimental results, we have found that (γ - β) decreases monotonically from the edge to the center of the films whereas (β - α) remains almost constant along the radial direction.

Bibliography

[1] P. E. Cladis, D. Guillon, F. R. Bouchet, and P. L. Finn, "Reentrant nematic transitions in cyano-octyloxybiphenyl (8OCB)," *Phys. Rev. A*, vol. 23, pp. 2594–2601, May 1981. [Online]. Available: https://link.aps.org/doi/10.1103/PhysRevA.23.2594

[2] P. E. Cladis, R. K. Bogardus, W. B. Daniels, and G. N. Taylor, "High-pressure investigation of the reentrant nematic - bilayer-smectic-A transition," *Phys. Rev. Lett.*, vol. 39, pp. 720–723, Sep 1977. [Online]. Available: https://link.aps.org/doi/10.1103/PhysRevLett.39.720

[3] Leadbetter, A.J., Frost, J.C., Gaughan, J.P., Gray, G.W., and Mosley, A., "The structure of smectic a phases of compounds with cyano end groups," *J. Phys. France*, vol. 40, no. 4, pp. 375–380, 1979. [Online]. Available: https://doi.org/10.1051/jphys:01979004004037500

[4] K. Hori, M. Kurosaki, H. Wu, and K. Itoh, "Two Crystal Forms of 4′-octyloxy-4-cyanobiphenyl (8OCB)," *Acta Crystallographica Section C*, vol. 52, no. 7, pp. 1751–1754, Jul 1996. [Online]. Available: https://doi.org/10.1107/S0108270196003447

[5] K. HORI, "Crystalline polymorphs of higher homologues of 4-alkoxy-4′-cyanobiphenyl, *n*OCB (n=8,9,10 and 12)," *Liquid Crystals*, vol. 26, no. 1, pp. 37–43, 1999. [Online]. Available: https://doi.org/10.1080/026782999205515

[6] A. G. Shtukenberg, Y. O. Punin, E. Gunn, and B. Kahr, "Spherulites," *Chemical Reviews*, vol. 112, no. 3, pp. 1805–1838, 2012, pMID: 22103741. [Online]. Available: https://doi.org/10.1021/cr200297f

[7] P. de Gennes and J. Prost, *The Physics of Liquid Crystals*, ser. International Series of Monogr. Clarendon Press, 1993. [Online]. Available: https://books.google.co.in/books?id=0Nw-dzWz5agC

[8] F. Reinitzer, "Beiträge zur kenntniss des cholesterins," *Monatshefte für Chemie und verwandte Teile anderer Wissenschaften*, vol. 9, no. 1, pp. 421–441, 1888.

[9] R.-P. Pan, C.-F. Hsieh, C.-L. Pan, and C.-Y. Chen, "Temperature-dependent optical constants and birefringence of nematic liquid crystal 5CB in the terahertz frequency range," *Journal of Applied Physics*, vol. 103, no. 9, p. 093523, 2008.

[10] P. Barois, J. Pommier, and J. Prost, *Frustrated Smectics*. New York, NY: Springer New York, 1992, pp. 191–234. [Online]. Available: https://doi.org/10.1007/978-1-4612-0917-1_6

[11] Y. Yamamura, R. Tsuchiya, S. Fujimura, M. Hishida, and K. Saito, "Odd–even effect on nematic smad phase boundary and smad structure in homologous binary systems of cyanobiphenyl mesogens: 4-alkyl-4′-cyanobiphenyl (*n*CB) and 4-alkoxy-4′-cyanobiphenyl (*n*OCB)," *The Journal*

of Physical Chemistry B, vol. 121, no. 6, pp. 1438–1447, 2017, pMID: 28124910. [Online]. Available: https://doi.org/10.1021/acs.jpcb.6b12977

[12] P. E. Cladis, R. K. Bogardus, and D. Aadsen, "High-pressure investigation of the reentrant nematic bilayer smectic-A transition," *Phys. Rev. A*, vol. 18, pp. 2292–2306, Nov 1978. [Online]. Available: https://link.aps.org/doi/10.1103/PhysRevA.18.2292

[13] K. Hori, Y. Koma, M. Kurosaki, K. Itoh, H. Uekusa, Y. Takenaka, and Y. Ohashi, "Crystalline polymorphism and phase transition behavior of mesogenic 4-heptyloxy-4′-cyanobiphenyl (7OCB)," *Bulletin of the Chemical Society of Japan*, vol. 69, no. 4, pp. 891–897, 1996. [Online]. Available: https://doi.org/10.1246/bcsj.69.891

[14] M. Kuribayashi and K. Hori, "Crystal structures of 4-cyano-4-hexylbiphenyl (6CB) and 4-cyano-4-heptylbiphenyl (7CB) in relation to odd-even effects," *Liquid Crystals*, vol. 26, no. 6, pp. 809–815, 1999. [Online]. Available: https://doi.org/10.1080/026782999204499

[15] A. Jakli, I. Janossy, and A. Vajda, "Polymorphic crystalline forms of 8OCB," *Liquid Crystals*, vol. 27, no. 8, pp. 1035–1038, 2000. [Online]. Available: https://doi.org/10.1080/02678290050080779

[16] L. Walz, Paulus, and W. Haase, "Crystal and molecular structures of four mesogenic 4′-alkoxy-4-cyanobiphenyls," *Zeitschrift für Kristallographie - Crystalline Materials*, vol. 180, no. 1-4, pp. 97–112, 1987. [Online]. Available: https://doi.org/10.1524/zkri.1987.180.14.97

[17] C. Fehr, P. Dieudonné, J. L. Sauvajol, and E. Anglaret, "Raman investigation of stable and metastable states of $4-\text{octyl}-4'$-cyanobiphenyl confined in porous silica matrices," *Phys. Rev. E*, vol. 67, p. 061706, Jun 2003. [Online]. Available: https://link.aps.org/doi/10.1103/PhysRevE.67.061706

[18] P. Mandal and S. Paul, "X-ray studies on the mesogen 4′-n-pentyloxy-4-biphenylcarbonitrile (5OCB) in the solid crystalline state," *Molecular Crystals and Liquid Crystals*, vol. 131, no. 3-4, pp. 223–235, 1985. [Online]. Available: https://doi.org/10.1080/00268948508085045

[19] B. Crist and J. M. Schultz, "Polymer spherulites: A critical review," *Progress in Polymer Science*, vol. 56, pp. 1–63, 2016. [Online]. Available: https://www.sciencedirect.com/science/article/pii/S0079670015001288

[20] B. Lotz and S. Z. Cheng, "A critical assessment of unbalanced surface stresses as the mechanical origin of twisting and scrolling of polymer crystals," *Polymer*, vol. 46, no. 3, pp. 577–610, 2005. [Online]. Available: https://www.sciencedirect.com/science/article/pii/S003238610400713X

[21] G. Lofgren, "An experimental study of plagioclase crystal morphology; isothermal crystallization," *American Journal of Science*, vol. 274, no. 3, pp. 243–273, 1974. [Online]. Available: https://www.ajsonline.org/content/274/3/243

[22] R. Coish and L. A. Taylor, "The effects of cooling rate on texture and pyroxene chemistry in dsdp leg 34 basalt: A microprobe study," *Earth and Planetary Science Letters*, vol. 42, no. 3, pp. 389–398, 1979. [Online]. Available: https://www.sciencedirect.com/science/article/pii/0012821X79900487

[23] R. J. Kirkpatrick, "Kinetics of crystal growth in the system $CaMgSi_2O_6$-$CaAl_2SiO_6$," *American Journal of Science*, vol. 274, no. 3, pp. 215–242, 1974. [Online]. Available: https://www.ajsonline.org/content/274/3/215

[24] I. Minkoff and W. C. Nixon, "Scanning electron microscopy of graphite growth in iron and nickel alloys," *Journal of Applied Physics*, vol. 37, no. 13, pp. 4848–4855, 1966. [Online]. Available: https://doi.org/10.1063/1.1708149

[25] J. Bisault, G. Ryschenkow, and G. Faivre, "Spherulitic branching in the crystallization of liquid selenium," *Journal of Crystal Growth*, vol. 110, no. 4, pp. 889–909, 1991. [Online]. Available: https://www.sciencedirect.com/science/article/pii/002202489190647N

[26] R. Beck and J.-P. Andreassen, "Spherulitic growth of calcium carbonate," *Crystal Growth & Design*, vol. 10, no. 7, pp. 2934–2947, 2010. [Online]. Available: https://doi.org/10.1021/cg901460g

[27] Y. Oaki and H. Imai, "Amplification of chirality from molecules into morphology of crystals through molecular recognition," *Journal of the American Chemical Society*, vol. 126, no. 30, pp. 9271–9275, 2004, pMID: 15281817. [Online]. Available: https://doi.org/10.1021/ja048661+

[28] A. Thomas, E. Rosseeva, O. Hochrein, W. Carrillo-Cabrera, P. Simon, P. Duchstein, D. Zahn, and R. Kniep, "Mimicking the growth of a pathologic biomineral: Shape development and structures of calcium oxalate dihydrate in the presence of polyacrylic acid," *Chemistry – A European Journal*, vol. 18, no. 13, pp. 4000–4009, 2012. [Online]. Available: https://chemistry-europe.onlinelibrary.wiley.com/doi/abs/10.1002/chem.201102228

[29] W. H. F. Talbot, "III. On the optical phenomena of certain crystals," *Philosophical Transactions of the Royal Society of London*, vol. 127, pp. 25–27, 1837. [Online]. Available: https://royalsocietypublishing.org/doi/abs/10.1098/rstl.1837.0005

[30] D. Brewster, "XLIII.—On circular crystals," *Transactions of the Royal Society of Edinburgh*, vol. 20, no. 4, p. 607–623, 1853.

[31] H. D. Keith and F. J. Padden, "A phenomenological theory of spherulitic crystallization," *Journal of Applied Physics*, vol. 34, no. 8, pp. 2409–2421, 1963. [Online]. Available: https://doi.org/10.1063/1.1702757

[32] H. Keith and F. Padden, "Twisting orientation and the role of transient states in polymer crystallization," *Polymer*, vol. 25, no. 1, pp. 28–42, 1984. [Online]. Available: https://www.sciencedirect.com/science/article/pii/0032386184902647

[33] A. G. Shtukenberg, J. Freudenthal, and B. Kahr, "Reversible twisting during helical hippuric acid crystal growth," *Journal of the American Chemical Society*, vol. 132, no. 27, pp. 9341–9349, 2010, pMID: 20405919. [Online]. Available: https://doi.org/10.1021/ja101491n

[34] A. G. Shtukenberg, X. Cui, J. Freudenthal, E. Gunn, E. Camp, and B. Kahr, "Twisted mannitol crystals establish homologous growth mechanisms for high-polymer and small-molecule ring-banded spherulites," *Journal of the American Chemical Society*, vol. 134, no. 14, pp. 6354–6364, 2012, pMID: 22413815. [Online]. Available: https://doi.org/10.1021/ja300257m

[35] W. Pisula, M. Kastler, D. Wasserfallen, T. Pakula, and K. Müllen, "Exceptionally long-range self-assembly of hexa-peri-hexabenzocoronene with dove-tailed alkyl substituents," *Journal of the American Chemical Society*, vol. 126, no. 26, pp. 8074–8075, 2004, pMID: 15225022. [Online]. Available: https://doi.org/10.1021/ja048351r

[36] X. Cui, A. L. Rohl, A. Shtukenberg, and B. Kahr, "Twisted aspirin crystals," *Journal of the American Chemical Society*, vol. 135, no. 9, pp. 3395–3398, 2013, pMID: 23425247. [Online]. Available: https://doi.org/10.1021/ja400833r

[37] A. Shtukenberg, J. Freundenthal, E. Gunn, L. Yu, and B. Kahr, "Glass-crystal growth mode for testosterone propionate," *Crystal Growth & Design*, vol. 11, no. 10, pp. 4458–4462, 2011. [Online]. Available: https://doi.org/10.1021/cg200640g

[38] T.-F. Lin, R.-M. Ho, C.-H. Sung, and C.-S. Hsu, "Helical morphologies of thermotropic liquid-crystalline chiral schiff-based rod-coil amphiphiles," *Chemistry of Materials*, vol. 18, no. 23, pp. 5510–5519, 2006. [Online]. Available: https://doi.org/10.1021/cm061666g

[39] J. L. Hutter and J. Bechhoefer, "Three classes of morphology transitions in the solidification of a liquid crystal," *Phys. Rev. Lett.*, vol. 79, pp. 4022–4025, Nov 1997. [Online]. Available: https://link.aps.org/doi/10.1103/PhysRevLett.79.4022

[40] J. L. Hutter *et al.*, "Banded spherulitic growth in a liquid crystal," *Journal of Crystal Growth*, vol. 217, no. 3, pp. 332–343, 2000. [Online]. Available: https://www.sciencedirect.com/science/article/pii/S0022024800004796

[41] J. M. Schultz, "Self-induced field model for crystal twisting in spherulites," *Polymer*, vol. 44, no. 2, pp. 433–441, 2003.

[42] A. Toda, T. Arita, and M. Hikosaka, "Three-dimensional morphology of pvdf single crystals forming banded spherulites," *Polymer*, vol. 42, no. 5, pp. 2223–2233, 2001.

[43] D. Bassett and A. Hodge, "On lamellar organization in certain polyethylene spherulites," *Proceedings of the Royal Society of London. A. Mathematical and Physical Sciences*, vol. 359, no. 1696, pp. 121–132, 1978.

[44] D. C. Bassett, A. M. Hodge, and A. Keller, "On the morphology of melt-crystallized polyethylene. III. spherulitic organization," *Proceedings of the Royal Society of London. A. Mathematical and Physical Sciences*, vol. 377, no. 1768, pp. 61–71, 1981. [Online]. Available: https://royalsocietypublishing.org/doi/abs/10.1098/rspa.1981.0115

[45] Y. Okabe and T. Kyu, "Spatio-temporal growth of broken spiral and concentric ringed spherulites in blends of poly(vinylidene fluoride) and ethylene-vinylacetate copolymers," *Polymer*, vol. 45, no. 25, pp. 8485–8490, 2004. [Online]. Available: https://www.sciencedirect.com/science/article/pii/S0032386104009656

[46] H. Uesaka and R. Kobayashi, "Pattern formation in the crystallization of ascorbic acid," *Journal of Crystal Growth*, vol. 237-239, pp. 132–137, 2002, the thirteenth international conference on Crystal Growth in conj unction with the eleventh international conference on Vapor Growth and Epitaxy. [Online]. Available: https://www.sciencedirect.com/science/article/pii/S0022024801018929

[47] Y. Li, H. Huang, T. He, and Z. Wang, "Coupling between crystallization and evaporation dynamics: Periodically nonlinear growth into concentric ringed spherulites," *Polymer*, vol. 54, no. 24, pp. 6628–6635, 2013. [Online]. Available: https://www.sciencedirect.com/science/article/pii/S0032386113008756

[48] Y. Yamazaki, M. Kikuchi, A. Toda, J.-i. Wakita, and M. Matsushita, "Dynamical properties in uniform and periodic growth modes of ascorbic acid crystal domain from thin solution film," *Journal of the Physical Society of Japan*, vol. 83, no. 6, p. 064002, 2014. [Online]. Available: https://doi.org/10.7566/JPSJ.83.064002

[49] Y. Li, H. Huang, Z. Wang, and T. He, "Tuning radial lamellar packing and orientation into diverse ring-banded spherulites: Effects of structural feature and crystallization condition," *Macromolecules*, vol. 47, no. 5, pp. 1783–1792, 2014. [Online]. Available: https://doi.org/10.1021/ma402579d

[50] Y. Li, Z. Wang, Q. Gu, and X. Wu, "Enhance understanding of rhythmic crystallization in confined evaporating polymer solution films: from environment to solution film and then to one period," *RSC Adv.*, vol. 6, pp. 45 241–45 249, 2016. [Online]. Available: http://dx.doi.org/10.1039/C6RA02803A

[51] Y. Li, Z. Wang, and T. He, "Morphological control of polymer spherulites via manipulating radial lamellar organization upon evaporative crystallization: A mini review," *Crystals*, vol. 7, no. 4, 2017. [Online]. Available: https://www.mdpi.com/2073-4352/7/4/115

[52] J. Wei, L. Wu, H. Zhu, Y. Li, and Z. Wang, "Formation of well-organized, concentric-ringed spherulites of four-arm star symmetric PEO-b-PCL via confined evaporative crystallization," *CrystEngComm*, vol. 22, pp. 7016–7024, 2020. [Online]. Available: http://dx.doi.org/10.1039/D0CE01183E

[53] B. Fang, J. Wei, S. Qiu, J. Zhu, L. Wu, and Y. Li, "Unusually negative, single ring-banded spherulites of poly(ethylene adipate) formed via controlled stepwise evaporative crystallization," *Journal of Crystal Growth*, vol. 575, p. 126372, 2021. [Online]. Available: https://www.sciencedirect.com/science/article/pii/S002202482100347X

[54] S. Pérez, P. M. Baldwin, and D. J. Gallant, "Chapter 5 - structural features of starch granules I," in *Starch (Third Edition)*, third edition ed., ser. Food Science and Technology, J. BeMiller and R. Whistler, Eds. San Diego: Academic Press, 2009, pp. 149–192. [Online]. Available: https://www.sciencedirect.com/science/article/pii/B9780127462752000057

[55] S. Wang and L. Copeland, "Molecular disassembly of starch granules during gelatinization and its effect on starch digestibility: a review," *Food & function*, vol. 4, no. 11, pp. 1564–1580, 2013.

[56] S. Wang, C. Li, L. Copeland, Q. Niu, and S. Wang, "Starch retrogradation: A comprehensive review," *Comprehensive Reviews in Food Science and Food Safety*, vol. 14, no. 5, pp. 568–585, 2015.

[57] D. J. Gallant, B. Bouchet, and P. M. Baldwin, "Microscopy of starch: evidence of a new level of granule organization," *Carbohydrate polymers*, vol. 32, no. 3-4, pp. 177–191, 1997.

[58] T. Y. Bogracheva, V. Morris, S. Ring, and C. Hedley, "The granular structure of C-type pea starch and its role in gelatinization," *Biopolymers: Original Research on Biomolecules*, vol. 45, no. 4, pp. 323–332, 1998.

[59] A. Buléon, C. Gérard, C. Riekel, R. Vuong, and H. Chanzy, "Details of the crystalline ultrastructure of C-starch granules revealed by synchrotron microfocus mapping," *Macromolecules*, vol. 31, no. 19, pp. 6605–6610, 1998.

[60] W. Shujun, Y. Jinglin, G. Wenyuan, P. Jiping, L. Hongyan, and Y. Jiugao, "Granule structural changes in native chinese yam (dioscorea opposita thunb var. anguo) starch during acid hydrolysis," *Carbohydrate polymers*, vol. 69, no. 2, pp. 286–292, 2007.

[61] C. Wei, F. Qin, W. Zhou, H. Yu, B. Xu, C. Chen, L. Zhu, Y. Wang, M. Gu, and Q. Liu, "Granule structure and distribution of allomorphs in C-type high-amylose rice starch granule modified by antisense RNA inhibition of starch branching enzyme," *Journal of Agricultural and Food Chemistry*, vol. 58, no. 22, pp. 11 946–11 954, 2010.

[62] A. Imberty, H. Chanzy, S. Pérez, A. Bulèon, and V. Tran, "The double-helical nature of the crystalline part of A-starch," *Journal of molecular biology*, vol. 201, no. 2, pp. 365–378, 1988.

[63] A. Imberty and S. Perez, "A revisit to the three-dimensional structure of B-type starch," *Biopolymers: Original Research on Biomolecules*, vol. 27, no. 8, pp. 1205–1221, 1988.

[64] J. W. Donovan, "Phase transitions of the starch–water system," *Biopolymers: Original Research on Biomolecules*, vol. 18, no. 2, pp. 263–275, 1979.

[65] P. J. Jenkins and A. M. Donald, "Gelatinisation of starch: a combined SAXS/WAXS/DSC and SANS study," *Carbohydrate research*, vol. 308, no. 1-2, pp. 133–147, 1998.

[66] J. Carlstedt, J. Wojtasz, P. Fyhr, and V. Kocherbitov, "Understanding starch gelatinization: The phase diagram approach," *Carbohydrate Polymers*, vol. 129, pp. 62–69, 2015.

[67] T. A. Waigh, M. J. Gidley, B. U. Komanshek, and A. M. Donald, "The phase transformations in starch during gelatinisation: a liquid crystalline approach," *Carbohydrate Research*, vol. 328, no. 2, pp. 165–176, 2000.

[68] B. Zhang, S. Dhital, B. M. Flanagan, and M. J. Gidley, "Mechanism for starch granule ghost formation deduced from structural and enzyme digestion properties," *Journal of agricultural and food chemistry*, vol. 62, no. 3, pp. 760–771, 2014.

[69] M. R. Debet and M. J. Gidley, "Why do gelatinized starch granules not dissolve completely? roles for amylose, protein, and lipid in granule "ghost" integrity," *Journal of Agricultural and Food Chemistry*, vol. 55, no. 12, pp. 4752–4760, 2007.

[70] C. G. Biliaderis, C. M. Page, T. J. Maurice, and B. O. Juliano, "Thermal characterization of rice starches: A polymeric approach to phase transitions of granular starch," *Journal of Agricultural and Food Chemistry*, vol. 34, no. 1, pp. 6–14, 1986.

[71] I. Evans and D. Haisman, "The effect of solutes on the gelatinization temperature range of potato starch," *Starch-Stärke*, vol. 34, no. 7, pp. 224–231, 1982.

[72] X. Zhou, R. Wang, S.-H. Yoo, and S.-T. Lim, "Water effect on the interaction between amylose and amylopectin during retrogradation," *Carbohydrate Polymers*, vol. 86, no. 4, pp. 1671–1674, 2011.

[73] J. Longton and G. LeGrys, "Differential scanning calorimetry studies on the crystallinity of ageing wheat starch gels," *Starch-Stärke*, vol. 33, no. 12, pp. 410–414, 1981.

[74] J.-L. Putaux, A. Buleon, and H. Chanzy, "Network formation in dilute amylose and amylopectin studied by tem," *Macromolecules*, vol. 33, no. 17, pp. 6416–6422, 2000.

[75] P. Ambigaipalan, R. Hoover, E. Donner, and Q. Liu, "Retrogradation characteristics of pulse starches," *Food Research International*, vol. 54, no. 1, pp. 203–212, 2013.

[76] M. Miles, V. Morris, and S. Ring, "Some recent observations on the retrogradation of amylose," *Carbohydrate Polymers*, vol. 4, no. 1, pp. 73–77, 1984.

[77] S. Kim, J.-H. Kang, and K. B. Song, "Development of a sword bean (canavalia gladiata) starch film containing goji berry extract," *Food and Bioprocess Technology*, vol. 13, no. 5, pp. 911–921, 2020.

[78] N. Nikvarz, G. R. Khayati, and S. Sharafi, "Bio-based ultraviolet protective packaging film preparation using starch with incorporated date palm syrup," *Materials Chemistry and Physics*, vol. 270, p. 124794, 2021. [Online]. Available: https://www.sciencedirect.com/science/article/pii/S0254058421005770

[79] D. Yun, H. Cai, Y. Liu, L. Xiao, J. Song, and J. Liu, "Development of active and intelligent films based on cassava starch and chinese bayberry (myrica rubra sieb. et zucc.) anthocyanins," *RSC Adv.*, vol. 9, pp. 30 905–30 916, 2019. [Online]. Available: http://dx.doi.org/10.1039/C9RA06628D

[80] M. G. A. Vieira, M. A. da Silva, L. O. dos Santos, and M. M. Beppu, "Natural-based plasticizers and biopolymer films: A review," *European polymer journal*, vol. 47, no. 3, pp. 254–263, 2011.

[81] E. Brini, C. J. Fennell, M. Fernandez-Serra, B. Hribar-Lee, M. Lukšič, and K. A. Dill, "How water's properties are encoded in its molecular structure and energies," *Chemical Reviews*, vol. 117, no. 19, pp. 12 385–12 414, 2017, pMID: 28949513. [Online]. Available: https://doi.org/10.1021/acs.chemrev.7b00259

[82] K. A. Sharp, *Water: Structure and Properties*. American Cancer Society, 2001. [Online]. Available: https://novel-coronavirus.onlinelibrary.wiley.com/doi/abs/10.1038/npg.els.0003116

[83] K. Hori, M. Kuribayashi, and M. Iimuro, "Intra- and intermolecular interactions in mesogenic cyano compounds," *Phys. Chem. Chem. Phys.*, vol. 2, pp. 2863–2868, 2000. [Online]. Available: http://dx.doi.org/10.1039/B000567N

[84] L. M. Babkov, O. V. Gorshkova, E. V. Gabrusyonok, G. A. Puchkovskaya, and I. N. Khakimov, "Phase transitions, conformational lability, and intermolecular interactions in alkoxycyanobiphenyls," *Journal of Structural Chemistry*, vol. 36, pp. 739–746, 1995.

[85] G. J. Brownsey and A. J. Leadbetter, "Incommensurate coexistent density fluctuations in liquid-crystal phases of cyano compounds," *Phys. Rev. Lett.*, vol. 44, pp. 1608–1611, Jun 1980. [Online]. Available: https://link.aps.org/doi/10.1103/PhysRevLett.44.1608

[86] K. Hori, Y. Koma, A. Uchida, and Y. Ohashi, "Crystal structures of 6OCB and 7OCB," *Molecular Crystals and Liquid Crystals Science and Technology. Section A. Molecular Crystals and Liquid Crystals*, vol. 225, no. 1, pp. 15–22, 1993. [Online]. Available: https://doi.org/10.1080/10587259308036213

[87] J. Tanno, K. Itoh, A. Tsuji, and K. Hori, "Infrared spectroscopic study on the crystalline polymorphism and phase transition behavior of mesogenic 4-heptyloxy-4′-cyanobiphenyl," *Journal of Molecular Structure*, vol. 379, no. 1, pp. 121 – 134, 1996. [Online]. Available: http://www.sciencedirect.com/science/article/pii/0022286095092072

[88] K. Hori, Y. Iwai, M. Yano, R. Orihara-Furukawa, Y. Tominaga, E. Nishibori, M. Takata, M. Sakata, and K. Kato, "Phase relationships of crystalline polymorphs of mesogenic 4-cyano-4′-heptyloxybiphenyl (7OCB) and 4-cyano-4′-octyloxybiphenyl (8OCB)," *Bulletin of the Chemical Society of Japan*, vol. 78, no. 7, pp. 1223–1229, 2005. [Online]. Available: https://doi.org/10.1246/bcsj.78.1223

[89] P. Wu and W. Lee, "Phase and dielectric behaviors of a polymorphic liquid crystal doped with graphene nanoplatelets," *Applied Physics Letters*, vol. 102, no. 16, p. 162904, 2013. [Online]. Available: https://doi.org/10.1063/1.4802839

[90] J. Jiang, E. Zhuravlev, Z. Huang, L. Wei, Q. Xu, M. Shan, G. Xue, D. Zhou, C. Schick, and W. Jiang, "A transient polymorph transition of 4-cyano-4′-octyloxybiphenyl (8OCB) revealed by ultrafast differential scanning calorimetry (UFDSC)," *Soft Matter*, vol. 9, pp. 1488–1491, 2013. [Online]. Available: http://dx.doi.org/10.1039/C2SM27012A

[91] J. Jadżyn and G. Czechowski, "Dielectric studies of nematic-smectic A-reentrant nematic transition in the 8OCB/6OCB mixtures," *Liquid Crystals*, vol. 4, no. 2, pp. 157–163, 1989. [Online]. Available: https://doi.org/10.1080/02678298908029068

[92] A. Takase, S. Sakagami, and M. Nakamizo, "Conformational change of liquid crystalline ethyl-4′-n-octyloxy biphenyl carboxylate at the liquid crystal phase transitions," *Japanese Journal of Applied Physics*, vol. 17, no. 9, pp. 1495–1498, sep 1978. [Online]. Available: https://doi.org/10.1143/jjap.17.1495

[93] K. Merkel, R. Wrzalik, and A. Kocot, "Calculation of vibrational spectra for cyanobiphenyl liquid crystals," *Journal of Molecular Structure*, vol. 563-564, pp. 477 – 490, 2001. [Online]. Available: http://www.sciencedirect.com/science/article/pii/S0022286000008917

[94] R. Mishra, A. Bhattacharjee, D. Bhattacharjee, K. N. Singh, B. Gogoi, and P. R. Alapati, "Temperature-dependent vibrational spectroscopic studies of pure and gold nanoparticles dispersed 4-n-hexyloxy-4′-cyanobiphenyls," *Liquid Crystals*, vol. 45, no. 9, pp. 1333–1341, 2018. [Online]. Available: https://doi.org/10.1080/02678292.2018.1441457

[95] C. Wang, R. Thomann, J. Kressler, Y. Thomann, K. Crämer, B. Stühn, P. Svoboda, and T. Inoue, "Morphology of banded spherulites in poly(ε-caprolactone)/ poly(styrene-ran-acrylonitrile) blends," *Acta Polymerica*, vol. 48, pp. 354 – 362, 03 1997.

[96] C.-Y. Sun, M. A. Marcus, M. J. Frazier, A. J. Giuffre, T. Mass, and P. U. P. A. Gilbert, "Spherulitic growth of coral skeletons and synthetic aragonite: Nature's three-dimensional printing," *ACS Nano*, vol. 11, no. 7, pp. 6612–6622, 2017, pMID: 28564539. [Online]. Available: https://doi.org/10.1021/acsnano.7b00127

[97] U. Al-Atar, A. A. Bokov, D. Marshall, J. M. H. Teichman, B. D. Gates, Z.-G. Ye, and N. R. Branda, "Mechanism of calcium oxalate monohydrate kidney stones formation: Layered spherulitic growth," *Chemistry of Materials*, vol. 22, no. 4, pp. 1318–1329, 2010. [Online]. Available: https://doi.org/10.1021/cm901751g

[98] P. S. Chow, X. Y. Liu, J. Zhang, and R. B. H. Tan, "Spherulitic growth kinetics of protein crystals," *Applied Physics Letters*, vol. 81, no. 11, pp. 1975–1977, 2002. [Online]. Available: https://doi.org/10.1063/1.1506208

[99] J. E. Coleman, B. J. Allan, and B. L. Vallee, "Protein spherulites," *Science*, vol. 131, no. 3397, pp. 350–352, 1960. [Online]. Available: https://www.science.org/doi/abs/10.1126/science.131.3397.350

[100] M. R. H. Krebs, C. E. MacPhee, A. F. Miller, I. E. Dunlop, C. M. Dobson, and A. M. Donald, "The formation of spherulites by amyloid fibrils of bovine insulin," *Proceedings of the National Academy of Sciences*, vol. 101, no. 40, pp. 14 420–14 424, 2004. [Online]. Available: https://www.pnas.org/content/101/40/14420

[101] F. Catalina and L. Cifuentes, "Calcium oxalate: Crystallographic analysis in solid aggregates in urinary sediments," *Science*, vol. 169, no. 3941, pp. 183–184, 1970. [Online]. Available: https://www.science.org/doi/abs/10.1126/science.169.3941.183

[102] J. Chen and D. Yang, "Rhythmic growth of ring-banded spherulites in blends of liquid crystalline methoxy-poly(aryl ether ketone) and poly(aryl ether ether ketone)," *Journal of Polymer Science Part B: Polymer Physics*, vol. 45, no. 22, pp. 3011–3024, 2007. [Online]. Available: https://onlinelibrary.wiley.com/doi/abs/10.1002/polb.21124

[103] J. Chen *et al.*, "Phase behavior and rhythmically grown ring-banded spherulites in blends of liquid crystalline poly(aryl ether ketone) and poly(aryl ether ether ketone)," *Macromolecules*, vol. 38, no. 8, pp. 3371–3379, 2005. [Online]. Available: https://doi.org/10.1021/ma047904f

[104] A. Shtukenberg, E. Gunn, M. Gazzano, J. Freudenthal, E. Camp, R. Sours, E. Rosseeva, and B. Kahr, "Bernauer's bands," *ChemPhysChem*, vol. 12, no. 8, pp. 1558–1571, 2011. [Online]. Available: https://chemistry-europe.onlinelibrary.wiley.com/doi/abs/10.1002/cphc.201000963

[105] E. M. Woo, G. Lugito, and C.-E. Yang, "Analysis of crystal assembly in banded spherulites of phthalic acid upon solvent evaporation," *CrystEngComm*, vol. 18, pp. 977–985, 2016. [Online]. Available: http://dx.doi.org/10.1039/C5CE02043C

[106] T. Kajiya, W. Kobayashi, T. Okuzono, and M. Doi, "Controlling the drying and film formation processes of polymer solution droplets with addition of small amount of surfactants," *The Journal of Physical Chemistry B*, vol. 113, no. 47, pp. 15 460–15 466, 2009, pMID: 19921951. [Online]. Available: https://doi.org/10.1021/jp9077757

[107] T. Kajiya, D. Kaneko, and M. Doi, "Dynamical visualization of "coffee stain phenomenon" in droplets of polymer solution via fluorescent microscopy," *Langmuir*, vol. 24, no. 21, pp. 12 369–12 374, 2008, pMID: 18844390. [Online]. Available: https://doi.org/10.1021/la8017858

[108] T. Kajiya, E. Nishitani, T. Yamaue, and M. Doi, "Piling-to-buckling transition in the drying process of polymer solution drop on substrate having a large contact angle," *Phys. Rev. E*, vol. 73, p. 011601, Jan 2006. [Online]. Available: https://link.aps.org/doi/10.1103/PhysRevE.73.011601

[109] I. I. Smalyukh, O. V. Zribi, J. C. Butler, O. D. Lavrentovich, and G. C. L. Wong, "Structure and dynamics of liquid crystalline pattern formation in drying droplets of DNA," *Phys. Rev. Lett.*, vol. 96, p. 177801, May 2006. [Online]. Available: https://link.aps.org/doi/10.1103/PhysRevLett.96.177801

[110] S. Maheshwari, L. Zhang, Y. Zhu, and H.-C. Chang, "Coupling between precipitation and contact-line dynamics: Multiring stains and stick-slip motion," *Phys. Rev. Lett.*, vol. 100, p. 044503, Jan 2008. [Online]. Available: https://link.aps.org/doi/10.1103/PhysRevLett.100.044503

[111] R. Duggal, F. Hussain, and M. Pasquali, "Self-assembly of single-walled carbon nanotubes into a sheet by drop drying," *Advanced Materials*, vol. 18, no. 1, pp. 29–34, 2006. [Online]. Available: https://onlinelibrary.wiley.com/doi/abs/10.1002/adma.200500625

[112] S. Zhang, Q. Li, I. A. Kinloch, and A. H. Windle, "Ordering in a droplet of an aqueous suspension of single-wall carbon nanotubes on a solid substrate," *Langmuir*, vol. 26, no. 3, pp. 2107–2112, 2010, pMID: 19772351. [Online]. Available: https://doi.org/10.1021/la902642f

[113] Q. Li, Y. T. Zhu, I. A. Kinloch, and A. H. Windle, "Self-organization of carbon nanotubes in evaporating droplets," *The Journal of Physical Chemistry B*, vol. 110, no. 28, pp. 13 926–13 930, 2006, pMID: 16836343. [Online]. Available: https://doi.org/10.1021/jp061554c

[114] Y. Zhao, G. Cavallaro, and Y. Lvov, "Orientation of charged clay nanotubes in evaporating droplet meniscus," *Journal of colloid and interface science*, vol. 440, pp. 68–77, 2015.

[115] C. Querner, M. D. Fischbein, P. A. Heiney, and M. Drndić, "Millimeter-scale assembly of cdse nanorods into smectic superstructures by solvent drying kinetics," *Advanced Materials*, vol. 20, no. 12, pp. 2308–2314, 2008.

[116] A. Martín, C. Schopf, A. Pescaglini, J. J. Wang, and D. Iacopino, "Facile formation of ordered vertical arrays by droplet evaporation of Au nanorod organic solutions," *Langmuir*, vol. 30, no. 34, pp. 10 206–10 212, 2014.

[117] Z. S. Davidson, Y. Huang, A. Gross, A. Martinez, T. Still, C. Zhou, P. J. Collings, R. D. Kamien, and A. Yodh, "Deposition and drying dynamics of liquid crystal droplets," *Nature communications*, vol. 8, no. 1, pp. 1–7, 2017.

[118] G. Chu and E. Zussman, "From chaos to order: evaporative assembly and collective behavior in drying liquid crystal droplets," *The Journal of Physical Chemistry Letters*, vol. 9, no. 16, pp. 4795–4801, 2018.

[119] R. D. Deegan, O. Bakajin, T. F. Dupont, G. Huber, S. R. Nagel, and T. A. Witten, "Capillary flow as the cause of ring stains from dried liquid drops," *Nature*, vol. 389, no. 6653, pp. 827–829, 1997.

[120] R. D. Deegan *et al.*, "Contact line deposits in an evaporating drop," *Phys. Rev. E*, vol. 62, pp. 756–765, Jul 2000. [Online]. Available: https://link.aps.org/doi/10.1103/PhysRevE.62.756

[121] F. Parisse and C. Allain, "Drying of colloidal suspension droplets: experimental study and profile renormalization," *Langmuir*, vol. 13, no. 14, pp. 3598–3602, 1997. [Online]. Available: https://doi.org/10.1021/la951521g

[122] M. Haw, M. Gillie, and W. Poon, "Effects of phase behavior on the drying of colloidal suspensions," *Langmuir*, vol. 18, no. 5, pp. 1626–1633, 2002.

[123] J. Shi, L. Yang, and C. D. Bain, "Wetting and drying of aqueous droplets containing nonionic surfactants CnEm," *Langmuir*, vol. 37, no. 14, pp. 4091–4101, 2021, pMID: 33797926. [Online]. Available: https://doi.org/10.1021/acs.langmuir.0c03479

[124] S. J. Gokhale, J. L. Plawsky, and P. C. Wayner, "Spreading, evaporation, and contact line dynamics of surfactant-laden microdrops," *Langmuir*, vol. 21, no. 18, pp. 8188–8197, 2005, pMID: 16114921. [Online]. Available: https://doi.org/10.1021/la050603u

[125] N. Basu and R. Mukherjee, "Evaporative drying of sodium chloride solution droplet on a thermally controlled substrate," *The Journal of Physical Chemistry B*, vol. 124, no. 7, pp. 1266–1274, 2020, pMID: 31990551. [Online]. Available: https://doi.org/10.1021/acs.jpcb.9b08809

[126] M. D. Choudhury, T. Dutta, and S. Tarafdar, "Pattern formation in droplets of starch gels containing nacl dried on different surfaces," *Colloids and Surfaces A: Physicochemical and Engineering Aspects*, vol. 432, pp. 110–118, 2013.

[127] D. Brutin, B. Sobac, B. Loquet, and J. Sampol, "Pattern formation in drying drops of blood," *Journal of fluid mechanics*, vol. 667, pp. 85–95, 2011.

[128] H. M. Gorr, J. M. Zueger, D. R. McAdams, and J. A. Barnard, "Salt-induced pattern formation in evaporating droplets of lysozyme solutions," *Colloids and Surfaces B: Biointerfaces*, vol. 103, pp. 59–66, 2013.

[129] A. Pal, A. Gope, A. S. Athair, and G. S. Iannacchione, "A comparative study of the drying evolution and dried morphology of two globular proteins in deionized water solutions," *RSC Advances*, vol. 10, no. 29, pp. 16 906–16 916, 2020.

[130] T. Yakhno, O. Sedova, A. Sanin, and A. Pelyushenko, "On the existence of regular structures in liquid human blood serum (plasma) and phase transitions in the course of its drying," *Technical Physics*, vol. 48, no. 4, pp. 399–403, 2003.

[131] L. Pauchard and C. Allain, "Stable and unstable surface evolution during the drying of a polymer solution drop," *Phys. Rev. E*, vol. 68, p. 052801, Nov 2003. [Online]. Available: https://link.aps.org/doi/10.1103/PhysRevE.68.052801

[132] L. Pauchard. and C. Allain, "Mechanical instability induced by complex liquid desiccation," *Comptes Rendus Physique*, vol. 4, no. 2, pp. 231–239, 2003. [Online]. Available: https://www.sciencedirect.com/science/article/pii/S1631070503000276

[133] L. Pauchard *et al.*, "Buckling instability induced by polymer solution drying," *EPL (Europhysics Letters)*, vol. 62, no. 6, p. 897, 2003.

[134] S. Arai *et al.*, "Skin formation and bubble growth during drying process of polymer solution," *The European Physical Journal E*, vol. 35, no. 7, pp. 1–9, 2012.

[135] S. Arai and M. Doi, "Anomalous drying dynamics of a polymer solution on a substrate," *The European Physical Journal E*, vol. 36, no. 6, pp. 1–6, 2013.

[136] T. Okuzono, K. Ozawa, and M. Doi, "Simple model of skin formation caused by solvent evaporation in polymer solutions," *Physical review letters*, vol. 97, no. 13, p. 136103, 2006.

[137] D. Stevens and G. Elton, "Thermal properties of the starch/water system part I. measurement of heat of gelatinisation by differential scanning calorimetry," *Starch-Stärke*, vol. 23, no. 1, pp. 8–11, 1971.

[138] H. Liu, J. Lelievre, and W. Ayoung-Chee, "A study of starch gelatinization using differential scanning calorimetry, x-ray, and birefringence measurements," *Carbohydrate Research*, vol. 210, pp. 79–87, 1991.

[139] J. lin Jane, K. sum Wong, and A. E. McPherson, "Branch-structure difference in starches of A- and B-type x-ray patterns revealed by their naegeli dextrins," *Carbohydrate Research*, vol. 300, no. 3, pp. 219–227, 1997. [Online]. Available: https://www.sciencedirect.com/science/article/pii/S0008621597000566

[140] N. W. Cheetham and L. Tao, "Variation in crystalline type with amylose content in maize starch granules: an x-ray powder diffraction study," *Carbohydrate Polymers*, vol. 36, no. 4, pp. 277–284, 1998. [Online]. Available: https://www.sciencedirect.com/science/article/pii/S0144861798000071

[141] D. Domene-López, J. García-Quesada, I. Martin-Gullon, and M. G. Montalbán, "Influence of starch composition and molecular weight on physicochemical properties of biodegradable films," *Polymers*, vol. 11, p. 1084, 06 2019.

[142] E. Pigorsch, "Spectroscopic characterisation of cationic quaternary ammonium starches," *Starch - Stärke*, vol. 61, no. 3-4, pp. 129–138, 2009. [Online]. Available: https://onlinelibrary.wiley.com/doi/abs/10.1002/star.200800090

[143] R. Kizil, J. Irudayaraj, and K. Seetharaman, "Characterization of irradiated starches by using FT-Raman and FTIR spectroscopy," *Journal of Agricultural*

and Food Chemistry, vol. 50, no. 14, pp. 3912–3918, 2002, pMID: 12083858. [Online]. Available: https://doi.org/10.1021/jf011652p

[144] P. M. Fechner, S. Wartewig, P. Kleinebudde, and R. H. Neubert, "Studies of the retrogradation process for various starch gels using Raman spectroscopy," *Carbohydrate Research*, vol. 340, no. 16, pp. 2563–2568, 2005. [Online]. Available: https://www.sciencedirect.com/science/article/pii/S0008621505004106

[145] B. J. Bulkin, Y. Kwak, and I. C. Dea, "Retrogradation kinetics of waxy-corn and potato starches; a rapid, Raman-spectroscopic study," *Carbohydrate Research*, vol. 160, pp. 95–112, 1987. [Online]. Available: https://www.sciencedirect.com/science/article/pii/0008621587803051

[146] R. A. Talja, H. Helén, Y. H. Roos, and K. Jouppila, "Effect of various polyols and polyol contents on physical and mechanical properties of potato starch-based films," *Carbohydrate polymers*, vol. 67, no. 3, pp. 288–295, 2007.

[147] H. Abral, A. Basri, F. Muhammad, Y. Fernando, F. Hafizulhaq, M. Mahardika, E. Sugiarti, S. Sapuan, R. Ilyas, and I. Stephane, "A simple method for improving the properties of the sago starch films prepared by using ultrasonication treatment," *Food Hydrocolloids*, vol. 93, pp. 276–283, 2019. [Online]. Available: https://www.sciencedirect.com/science/article/pii/S0268005X1831539X

[148] O. V. López and M. A. García, "Starch films from a novel (Pachyrhizus ahipa) and conventional sources: Development and characterization," *Materials Science and Engineering: C*, vol. 32, no. 7, pp. 1931–1940, 2012. [Online]. Available: https://www.sciencedirect.com/science/article/pii/S092849311200255X

[149] G. P. Singh, S. P. Bangar, T. Yang, M. Trif, V. Kumar, and D. Kumar, "Effect on the properties of edible starch-based films by the incorporation of additives: A review," *Polymers*, vol. 14, no. 10, p. 1987, 2022.

[150] Y. Wu, Q. Lin, Z. Chen, W. Wu, and H. Xiao, "Fractal analysis of the retrogradation of rice starch by digital image processing," *Journal of Food Engineering*, vol. 109, no. 1, pp. 182–187, 2012.

[151] R. Utrilla-Coello, L. A. Bello-Perez, E. Vernon-Carter, E. Rodriguez, and J. Alvarez-Ramirez, "Microstructure of retrograded starch: quantification from lacunarity analysis of SEM micrographs," *Journal of Food Engineering*, vol. 116, no. 4, pp. 775–781, 2013.

[152] S. Charoenrein, O. Tatirat, K. Rengsutthi, and M. Thongngam, "Effect of konjac glucomannan on syneresis, textural properties and the microstructure of frozen rice starch gels," *Carbohydrate polymers*, vol. 83, no. 1, pp. 291–296, 2011.